BROADBAND DIELECTRIC SPECTROSCOPIC AND DFT INVESTIGATIONS OF SOLUBILITY LIMITED GLASS-FORMING PHARMACEUTICALS

Thesis submitted to the
University of Calicut for the partial fulfillment of
the requirements for the award of the degree of

DOCTOR OF PHILOSOPHY IN PHYSICS

Under the Faculty of Science

by

ABOOTHAHIR AFZAL

DEPARTMENT OF PHYSICS
UNIVERSITY OF CALICUT
KERALA, INDIA 673 635

JUNE 2021

BROADBAND DIELECTRIC SPECTROSCOPIC AND DFT INVESTIGATIONS OF SOLUBILITY LIMITED GLASS FORMING PHARMACEUTICALS

Ph.D. Thesis in Physics

Author:

Aboothahir Afzal

Department of Physics

University of Calicut

Calicut University (PO) – 673635, Kerala, India.

Email: abahyn@gmail.com

Under the guidance of

Dr. Mohamed Shahin Thayyil
Assistant Professor
Department of Physics
University of Calicut
Calicut University (P.O.) – 673635, Kerala, India.
Email: shahin@uoc.ac.in

UNIVERSITY OF CALICUT
DEPARTMENT OF PHYSICS

Dr. Mohamed Shahin Thayyil
Assistant professor
Department of Physics

Calicut University P.O
Kerala, India. 673 635
Tel: 0494-2407416(O)
+919961824725(M)
Email: shahin@uoc.ac.in

CERTIFICATE

Certified that the work presented in the thesis, entitled **'Broadband Dielectric Spectroscopic and DFT investigations of Solubility Limited Glass forming Pharmaceuticals'** is based on the authentic record of research work carried out by Mr. Aboothahir Afzal under my guidance in the Department of Physics, University of Calicut, Calicut University P.O., Kerala-673635, during 2014 -2021, and as per my knowledge, this work has not been included in any other thesis submitted previously for the award of any degree in any other University .

Calicut University

23-6- 2020

Dr. Mohamed Shahin Thayyil

DR. MOHAMED SHAHIN THAYYIL
ASST. PROFESSOR, DEPARTMENT OF PHYSICS
UNIVERSITY OF CALICUT 673635, KERALA (INDIA)

DECLARATION

Certified that the research work presented in this thesis, entitled **'Broadband Dielectric Spectroscopic and DFT investigations of Solubility Limited Glass forming Pharmaceuticals'** is based on the original research work done by me under the supervision and guidance of Dr. Mohamed Shahin Thayyil, Assistant professor, Department of physics, University of Calicut, University P.O, Kerala-673635 and and as per my knowledge, has not been included in any other thesis submitted previously for the award of any degree.

University of Calicut

23rd June 2021

Aboothahir Afzal

ACKNOWLEDGEMENT

First of all, I thank Almighty God for all His blessings. I owe my deepest sense of gratitude to my research supervisor, Dr.Mohamed Shahin Thayyil for his guidance, mentorship, faith, encouragement, and unwavering support throughout my research. He is a kind and social personality and was always motivating, supportive, insightful, and inspiring to me. He is also worth special acknowledgement for providing a research environment that promotes independent thought and creativity. I am indebted for his invaluable suggestions, advice, and support throughout my Ph.D. work which helped me to improve my skill sets and ability to think creatively. I would like to give a special thanks to the head of the Department, Dr.C.D.Ravikumar, and former HOD Prof. (Dr.) P Vinod Kumar for their substantial support and cooperation. I am also thankful to all the former heads of the Department, the research advisory committee members, and other faculty members of the Department of Physics, the University of Calicut for their valuable suggestions and support during my research period.

I would like to thank Directorate of Collegiate Education, Govt. of Kerala for providing me National Internship under FLAIR program under Dr.Ajit Kulkarni, Professor, Department of Metallurgical Engineering and Materials Science, IIT Bombay. I express my gratitude to Dr .C. Yohannan Panicker, Associate Prof. (Retd.), Dr. Saheer. V.C. and Dr. Nasarul Islam throughout my research period for suggestions for doing Quantum computational DFT research works.

I acknowledge with gratitude all the teachers, researchers and the non-teaching staff in the Department of Physics of University of Calicut. I thank Central Sophisticated Instrumental Facility (CSIF) of the University of Calicut for providing experimental facilities and computer workstation. I thank the Department of Metallurgical Engineering and Materials Science, IIT Bombay especially Prof. Dr. Ajith Kulkarni, Dr. Jayant Kolte and Mr. Samayendra for supporting in doing BDS experiments.

I am much fortunate to have co-researchers, Prof. P. A. Siva Ramakrishnan, Dr. Sailaja Urpayil, Mr. Nighil Nath M. P, Dr. K. P. Safna Hussan, Dr. Sahra T. P,

Dr. K.K. Thasneema, Mr. M.K. Sulaiman,Mrs.Ashifa, Mrs.Saifunnisa and Mr. Binish who have given valuable knowledge for data analysis. I also remember the help from my students Abinu A.J, Sourav, and Anjana Anand. I thank the University Grants Commission for providing me UGC Minor research project, Director of Collegiate Education Kerala, Govt. Arts and Science College Calicut and T.M. Govt. College Tirur for providing me UGC Minor research project and permission for faculty improvement program. I thank my colleagues and students in the Department of Physics in Govt. Arts and Science College Calicut and T.M. Govt. College Tirur for their support and cooperation.

I would also like to thank my non-professional entourage without whom none of this work would have been possible. I express my deep and sincere gratitude to my parents, Mr. S.M. Abdul Khadar and S. Fathima Beevi, my wife Hyrunisa M.I, my children Aysha Siddiqa, Saeed Anwar, and Kadheeja, and my siblings Mr. Arshad Mohammed, Mr. Mohamed Althaf, and Mr. CA. Asif Arfath who were a constant source of encouragement and support in all time.

Aboothahir Afzal

Dedicated to my parents and teachers

ABSTRACT

Much scientific and intellectual effort has gone into improving our understanding of the fundamental properties of amorphous materials to reap the benefits of their undeniable advantages in pharmaceutical applications in recent years. Preparing an amorphous substance with high free energy can be an exciting approach for improving the solubility and dissolution rate of poorly water-soluble active pharmaceutical ingredients(APIs). A significant commercial disadvantage of amorphous systems is their thermodynamic instability, which is followed by increased molecular mobility, both of which contribute to unfavourable drug re-crystallization. As a result, a thorough understanding of the critical factors that influence the physical stability of amorphous drugs is critical from both a theoretical and functional perspective. The physical instability of amorphous pharmaceuticals and our inability to predict their crystallization tendency is a barrier to their use as dosage forms. The main aim of this work is to advance a fundamental understanding of the roles of specific molecular mobility (global or local) on the physical instability of amorphous pharmaceuticals. The different types of molecular motions in the supercooled liquid and glassy states were comprehensively characterized using broadband dielectric spectroscopy (BDS), which will possibly empower the progress of effective tactics to stabilize amorphous pharmaceuticals. Comparison of glassy dynamics of anticancer alkaloids, brucine and colchicine, acetohexamide, piroxicam , acemetacin and bezafibrate was investigated. Molecular mobility with polymer additive in fenofibrate was studied and is compared with that of pure fenofibrate and bezafibrate. Coupling between translational and rotational motions is observed in acetohexamide and piroxicam.

One of the most difficult challenges in theoretical physics is gaining a thorough understanding of the phenomenon of glass transition and glassy dynamics, as there is currently no theory of glass transition. Because of the diverse complex structures of the samples studied in this work, the knowledge gained from this work will provide new insights to researchers working on the glass transition problem. Moreover, the origin of the experimentally observed secondary relaxations in these drugs was identified theoretically by the DFT method. The Density Functional Theory (DFT) method has evolved as a powerful and very reliable tool and is extensively used for the chemical

characterization of a molecule.The chemical characterization of bioactive molecules, particularly alkaloids, provides useful information to the pharmaceutical industry. The structural and reactive behaviour of the molecule can be identified using advanced FTIR and Raman spectrometers as well as quantum computational tools. Because the literature lacked a comprehensive spectroscopic characterization of the anticancer drugs brucine and colchicine, vibrational spectral investigations were performed on brucine and colchicine molecules using theoretical predictions of optimised structure, natural bond orbital analysis (NBO), vibrational wavenumbers, and IR and Raman intensities.

CONTENTS

LIST OF FIGURES

LIST OF TABLES

CHAPTER 1
GENERAL INTRODUCTION

1.1 Introduction

New drug discovery methods such as high-throughput screening and combinatorial chemistry have led to the identification of a large number of highly target-selective and potent new drug candidates[1,2]. Even though these techniques enable rapid identification of new lead drug molecules, a majority of these compounds (80-90%) are practically insoluble in water[3]. On average, 30%-40% of newly discovered drug candidates are found to be poorly water-soluble [4]. This poses a major challenge in the effective oral delivery of these compounds. According to the United States Pharmacopeia, a compound is considered insoluble if 1 part of solute dissolves only in 10,000 or more parts of solvent [3,5]. For a drug to be systemically effective following oral administration, drug absorption into the systemic circulation is a prerequisite[6,7]. There are two main barriers to oral drug absorption - dissolution in the gastrointestinal (GI) fluid followed by permeation across the gastrointestinal membrane[6,8,9]. These two barriers, solubility and permeability form the basis of the Biopharmaceutical Classification System (BCS)[10] and are shown in Figure 1.1 [3]. The pharmaceuticals already in commercial use and pipeline as per the BCS system are shown in table 1.1[3]. The BCS system has been also used as a tool in drug development to flag those pharmaceuticals which should not be considered for the clinical test unless necessary formulation strategies are employed[11]. For instance, a BCS Class II (permeable but comparatively insoluble) drug will not be a good candidate for clinical use unless some strategies to improve solubility or the dissolution rate are applied. Different systems are in place that aims to work with an API based on the BCS category for a specific drug delivery technique[12]. However, most approaches remain fragmented in their methods, ignoring commercial and biological factors that are relevant. Also, BCS may serve as an important tool for efficient drug production in conjunction with other details. It is a common notion that a first in human (FIH) drug dosage form should be designed to maximize its bioavailability. The FIH dosage type should be a logical step towards marketing, not just an interruption in order to facilitate acquisition of data.

Despite various strategies and intelligent protocols to solve this serious issue, a good number of APIs fail to fulfill this test, mainly due to poor water solubility[10]. Therefore, ensuring the necessary water solubility of drugs is the Herculean task to be

accomplished for achieving efficient absorption and desired therapeutic effects and is one of the prominent aspects of the drug development process[13–15]. BCS classification predicts the rate-limiting step in the intestinal absorption process and permeability through GI membrane on oral drug administration[16] and hence it has generated a remarkable impact on the entire pharmaceutical industry, in drug discovery, development, and regulation[16]. The seriousness of the situation is clear from the fact that about 40% of drug candidates in the pipeline for the market approval, and 90% of molecules in the drug discovery pipeline are poorly water-soluble. Realizing this, several solubility enhancement methods are already in practice, on modifying the API' via physical and chemical routes [17–19].

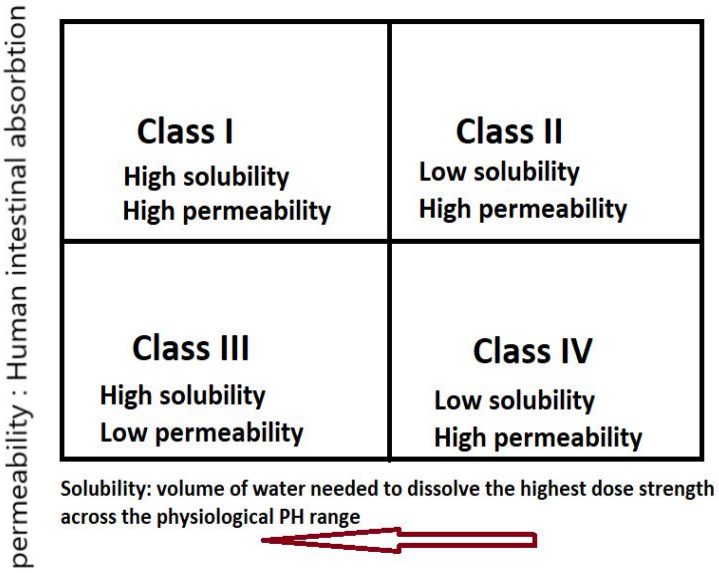

Figure 1.1 BCS classification of drugs. Arrow represents the direction of solubility

Table- 1.1 BCS classification System of drugs in the market and in the pipeline (as of 2011)[3]

BCS Class	Solubility	Permeability	% Marketed drugs	% In pipeline
I	High	High	35	5-10
II	Low	High	30	60-70
III	High	Low	25	5-10
IV	Low	Low	10	10-20

Physical and chemical modifications of the drug, as well as other techniques including particle size reduction, crystal engineering, salt-forming, solid dispersion, surfactant, spray-drying, co-grinding and so on, are some of the various tactics in practice to increase the solubility of poorly soluble drugs [17]. Among these methods, preparation of low water-soluble API's in amorphous or co-amorphous phase with a conformer[20] is of particular interest and is slowly emerging as an effective approach and has gained significant attention over the past decades [21]. The amorphous form of a drug exhibit significant improvement in the dissolution rate and bioavailability compared to its crystalline counterpart [3,22]. The solubility advantage over the most stable crystalline form was predicted to be between 10 and 1,600-fold by treating each amorphous drug as an equilibrium super-cooled liquid or a pseudo-equilibrium glass. The apparent solubility enhancement (theoretical or measured) is likely to influence in-vitro and in-vivo dissolution behaviour, even for partially amorphous materials [23]. The amorphous pharmaceuticals have higher free energy, low density, and more entropy[24] than its crystalline counterpart and hence more solubility, manifold faster drug absorption, faster dissolution rate, and better mechanical properties [22,25,26] and has been noted for many drugs [23]. For example, an order of magnitude increase in the dissolution rate of amorphous itraconazole as compared to its crystalline form was reported in the literature [27].

The amorphous phase is a metastable state with a higher free energy E_{am} than the crystalline state E_{cr}. A phase transition towards the crystalline phase is caused by this energy difference, but lowering E_{am} may not improve stability[28]. Furthermore, the amorphous phase's stability is dominated by atom mobility, which is represented by the activation energy E_a[29]. Amorphous APIs are thermodynamically unstable, that is they are prone to revert to a crystallized state[30], a more thermodynamically stable state due to the high energy associated with its solid-state form[21]. This instability leads to recrystallization driven by a thermodynamic drive to decrease the energy of the system and return to an equilibrium state leading to decreased physical stability as well as loss of the benefits arising from the amorphous state. Therefore, the advantage of amorphous pharmaceuticals comes with a cost[23]. Recrystallization may occur during storage, raising serious concerns about their industrial viability [31].

Extensive attempts were made to understand the causes of physical instability in amorphous pharmaceuticals [4,32]. Many factors contribute to the limited physical stability of amorphous APIs, including the method of amorphization, water content, the presence of isomers, chemical purity, configuration entropy, specific surface area, surface mobility, and molecular mobility of the system[25,27,30,31,33–37]. It is worth highlighting that the latter factor is believed to be the most important [38–41]. The significance of the molecular dynamics in determining physical stability and crystallization rate of amorphous substances is emphasized by the Classical Nucleation Theory (CNT)[42], where the nucleation rate (I) and the crystal growth(U) are expressed by the following equations

$$I(T,P) = C_1 \exp\left(-\frac{W*(T,p)}{K_B T}\right) \times \exp\left(-\frac{\Delta G(T,p)}{K_B T}\right) \quad (1.1)$$

$$U(T,P) = C_2\left[1 - exp\left(-\frac{\Delta G*(T,p)}{K_B T}\right)\right] \times exp\left(\left(-\frac{\Delta E(T,p)}{K_B T}\right)\right) \quad (1.2)$$

In this k_B is the Boltzmann's constant, T is the temperature, W^* denotes the thermodynamic barrier to nucleation, ΔG^* is the thermodynamic driving force for crystallization, where ΔG and ΔE represent the kinetic factor for nucleation and crystal growth, respectively. The appearance of the kinetic factor in the above equations shows that both nucleation rate and crystal growth are directly dependent on the system's molecular dynamics. The Boltzmann constant is k_B, the temperature is T, the thermodynamic barrier to nucleation is W*, the thermodynamic driving force for crystallization is G*, and the nucleation and crystal growth kinetic factors are G and E, respectively. The presence of the kinetic factor in the above equations shows that both nucleation rate and crystal growth are directly dependent on the system's molecular dynamics. As a result, understanding the relaxing processes associated with amorphous materials' molecular mobility is critical for determining their physical stability. In contrast, it should be emphasized that the temperature dependence of nuclear and crystal growth plays a critical role in determining the overall crystallization rate. Greater undercooling (i.e., the difference between T_m and T_g) contributes to an increase in the nuclear driving force in this context. This process comes from the decreased molecular mobility that occurs when the temperature drops and the viscosity increases.

As a result, the rates of nuclear and crystal growth are increased by temperature and then decreased to a maximum.

There is, however, no known theory that connects the form of relaxation phenomenon to amorphous phase stability. The crystallisation kinetics of various glass-forming liquids were found to be linked to structural relaxation and local mobility. Nonetheless, it is widely assumed that storing amorphous materials at temperatures well below Tg, where molecular mobility is greatly reduced, reduces the risk of drug recrystallization. Several study studies have examined the potential association between physical instability and molecular mobility [32]. Bhardwaj et al. established that the global mobility revealed as structural or α-relaxation is strongly correlated to the physical stability of amorphous itraconazole and trehalose[41,43] and for indomethacin, felodipine, flopropione, and celecoxib in the supercooled state
($T > T_g$)[44,45]. Though, amorphous pharmaceuticals are generally stored in the glassy state ($T < T_g$). Therefore, it is important from a practical point of view to understand the role of structural mobility on stability. Moreover, it is reported that local molecular mobility revealed as secondary relaxations below the glass transition temperature can also influence stability[46]. Therefore, for complete characterization of the amorphous pharmaceutical, the measurement of molecular mobility below T_g is necessary.

In our opinion, any predictive approach should take into account the influence of global and local motions. The molecular mobility, the property required to keep the system amorphous and account for the life span of the system can also cause crystallization [47]. For the last couple of decades, this subject has been a research focus for both pharmaceutical and chemical scientists[48]. Higher mobility is often held responsible for the increased instability in the amorphous state. Therefore, current research efforts are aimed at reducing molecular mobility to enhance physical stability[34,37,43]. On this account, discovering a safer temperature zone where crystallization trends are the least and the amorphous state is maintained is an intuitive approach. On this basis, the upper-temperature limit for safer storage is commonly estimated roughly by subtracting 50K from the glass transition temperature (T_g) (Kauzmann temperature T_K), where the intermolecular mobility is believed to cease[48].

Molecular mobility of amorphous drugs was estimated experimentally in the glass and supercooled liquid states by various methods viz. differential scanning

calorimetry (DSC) (enthalpy relaxation)[47], NMR spectroscopy (spin−lattice relaxation)[49], dielectric spectroscopy (dipolar relaxation)[50], and by estimating the associated time for various molecular processes. Out of these techniques, broadband dielectric spectroscopy (BDS) is greeted to be the finest in terms of its affluence, high sensitivity, and accessible broad dynamic range for monitoring the dynamics. BDS technique uses ac impedance for data measurement and can give a clear quantitative picture on charge transport and rotational fluctuations of molecular dipoles in a solid or liquid system[51] in the frequency range of 10^{-6} to 10^{12} Hz and in a wide temperature range (123K to 700K)[52,53]. Time-domain dielectric techniques such as isothermal depolarization and thermally stimulated current [54,55] have been employed to characterize molecular motions in glassy pharmaceuticals. Different relaxations occurring below and above T_g can be studied simultaneously by varying temperature and/or elevating pressures and a wealth of information can be extracted. Above T_g, a noticeable structural or α-relaxation originating from cooperative reorientation motions of molecules, which move to higher frequencies on elevating the temperature. Temperatures below T_g, the α-relaxation become slower and goes beyond experimental timescales, while fast local motions, originating from inter or intramolecular processes would be more active within our frequency/time window, designated as β, γ, δ relaxations. Often the intermolecular secondary relaxations are not visible in the dielectric measurements of most of the samples. Taking into account its fundamental importance, researchers have carried out dielectric experiments at high pressure as well as a test in an apolar host of high T_g since the classic discovery by two pioneering scientists, Johari and Goldstein. It is noted that many pharmaceutical products have a narrow α dispersion, restricting JG β-relaxation visibility as a separate dielectric window. To resolve the conundrum, molecular dynamics of the binary system having lower molecular weight among fibrate drugs as a probe in a test apolar host to understand the effect of mixing polymers in the stability of amorphous pharmaceuticals[56,57]. Above all, the extensively derived information from this comprehensive investigations can have many crucial links to the resolution of the yet unresolved theory of glass transition and the further progress of allied subjects such as polymers, metallic glasses, colloids, ionic liquids, plastic crystals, etc[54,55,57–59].

Even though research on glass-forming substances and the glass transition phenomenon has a long history, the slowing down of dynamics expressed in various properties in various systems such as ionic liquids, pharmaceuticals, biomolecules, biopolymers, metallic glasses, colloids, and so on has remained an unresolved problem in condensed matter physics[60]. The existence of a variety of glass-formers with widely varying chemical compositions and physical structures, which give rise to diverse thermodynamic and dynamic properties to be considered, adds to the problem's difficulty. However, these various properties are advantageous in practical applications. Ionic liquids stand out among these because the ionic conductivity relaxation occurs concurrently with the structural relaxation. While the former causes calorimetry to detect the nominal glass transition T_g due to its relaxation time, the latter causes another glass-like transition at temperature T_g where the conductivity relaxation time exceeds the experimental observation time-scale. Because the two processes are not identical and have different correlation functions, their dynamics differ and can be separated. As a result, any relationship between the two types of relaxations in glass-forming ionic liquids is of current interest in terms of significantly enriching knowledge about the fundamentals, and paving the way for tuning properties for practical applications [58]. The many-body cooperative nature of structural and conductivity relaxations was observed in some glassy systems[61,62]. As a result, several research communities are interested in studying secondary dipolar and secondary ionic conductivity relaxations, as well as their connections to primary relaxations. With this in mind, we investigated both structural and conductivity relaxations in some pharmaceuticals to characterize the translational rotational coupling phenomenon.

The activation energy of the observed secondary relaxations in glass formers could be determined by experimental methods like BDS, but no such tool is available until now, to give sufficient information that can help to identify the relevant part of the molecule whose motion originates the observed secondary relaxation in its glassy state. Schamme *et al.* successfully identified the part of quinidine molecule whose local motion originates the observed secondary relaxation by DFT calculations using the concept of potential energy surfaces on performing dihedral scan[63].

The fundamental goal of my work is to gain a fundamental insight into the possible mechanisms governing molecular dynamics of glassy pharmaceuticals of

different classes like phytochemicals, synthetic drugs having diverse molecular structures, and to give insight to researchers engaged in glass transition problem.

Predicting and comprehending the properties of a chemical compound is crucial from a scientific and academic standpoint. Similarly, both from a technological and academic perspective, the conduct of real-world material structures is important. Theoretical problems related to these structures are very complex. Quantum chemical computational approaches have proven to be an effective tool for resolving complex chemical problems and mechanisms. It has become a valuable way to investigate materials to make observations about the structure and properties of molecules and solids before performing complicated or costly experiments. Quantum mechanical techniques can now be specifically extended to a variety of scientific applications thanks to astronomical advancements in computer hardware and related achievements. The numerical computation of molecular electronic structures using ab initio, DFT, and semi-empirical techniques is the subject of computational quantum studies. Computational methods, especially ab initio and DFT, have emerged as important tools for studying the molecular structure, stability, and reaction mechanisms. It has become a valuable way to investigate materials to make observations about the structure and properties of molecules and solids before performing complicated or costly experiments. Quantum mechanical techniques can now be specifically extended to a variety of scientific applications, thanks to astronomical advancements in computer hardware and related achievements. The numerical computation of molecular electronic structures using ab initio, DFT, and semi-empirical techniques is the subject of computational quantum studies. Computational methods, especially ab initio and DFT, have become important tools in the study of structural, stability, and reaction problems in molecules[64,65].

The high computational speed of molecular mechanics allows it to be used in procedures that require a large number of energy assessments, such as molecular dynamics, conformational energy seeking, and docking. In recent years, the computational analysis of chromatographic separations has grown in importance. It contains valuable information about chromatographic separation mechanisms and stationary phase architecture. Hatice Ozdemir used computation tools to analyze the chromatographic separations of chiral benzimidazole from sulphoxides[66]. Macrolide

antibiotics have long been known to play an important role in therapeutics, particularly as new pathogens arise. Salah Belaidi *et al*. used molecular mechanics to study the conformational properties of dissymmetric macrolide antibiotics [67]. The molecular mechanics' simulation approach is well adapted for microscopically investigating many-particle structures, and thus bridges the theoretical and experimental worlds. Molecular mechanics was used to analyzing the geometrical structure of the sea anemone[68].

Cancer is increasingly becoming the world's most significant health problem. Resistance to current anticancer drugs leaves the testing door open in the hunt for newer anticancer molecules. Cancer is the world's second leading cause of death and reported 9.6 million deaths in 2018 [69]. The rising burden of cancer worldwide calls for an alternative treatment solution. However, the window passage has narrowed since finding a molecule that can selectively inhibit the proliferation of abnormal cells while having little to no effect on normal cells has become more difficult. As a result, numerous laboratories are still looking for anticancer agents. Recently, there has been a rise in interest in the use of phytochemicals with the potential for cancer chemoprevention [70]. Herbal medicines, drugs made from phytochemicals offer a very viable alternative to western cancer medicine [71–74]. Many researchers have reported potentially beneficial effects on cancer progression and may modify chemotherapy-induced toxicities [75]. A vast number of clinical trials have shown the benefit of natural therapies in conjunction with traditional therapeutics on the longevity, immune regulation, and quality of life (QOL) of patients with cancer[76]. Even though a very large number of phytochemicals having anticancer properties remain unexplored [77] like the alkaloids available commonly in Asian countries, i.e. brucine and colchicine [78] are alkaloids reported to have anti-cancerous effects [79,80]. This motivated me to perform quantum computational calculations for characterizing structural, vibrational, and electronic properties on brucine and colchicine.

Molecular docking studies of two alkaloids were performed. In molecular docking, the computer-generated 3D structure of small ligands is docked into a receptor protein structure in a variety of orientations, conformations, and positions. This approach can help with drug development and medicinal chemistry by revealing molecular recognition. Docking has become an important component of computer-

assisted drug design and development. The semi-flexible or static handling of targets and ligands is a drawback of traditional docking methods. Over the last decade, developments in the fields of analytical, proteomics, and genomics have led to the advancement of various docking methods that take into account the flexibility of protein-ligand interactions and their differences. On these grounds, we have focused our attention on the characterization of two unexplored anti-cancerous alkaloids brucine and colchicine by quantum computational methods.

1.2 Literature review

The dielectric relaxation study of amorphous acetaminophen was conducted in 2005 by G. P. Johari *et al*. The dielectric permittivity and dielectric loss spectra of amorphous and supercooled acetaminophen were measured in the frequency range 10 Hz-0.4 MHz[81]. The findings demonstrate shortcomings in the methods for the physical stability estimation based on thermal studies. The molecular dynamics in the supercooled liquid and glassy states of amorphous ibuprofen were studied by BDS in 2008[82]. Ibuprofen was found to have a complex relaxation map including two secondary relaxations, γ which is non-Johari-Goldstein type (intramolecular), and β which is Johari-Goldstein in nature (intermolecular). The temperature dependence of the relaxation time of the α-process does not obey a single VFT law. Instead, two VFTH regimes are observed separated by a crossover temperature, T_B = 265 K. Adrjanowicz *et al.* also conducted studies on dielectric relaxation and also crystallization kinetics of amorphous ibuprofen at ambient and elevated pressure[83]. The crystallization kinetic studies revealed an extension in crystallization time and induction time under high pressure compared to that crystallized at ambient pressure, which was due to the shift of the optimal nucleation and crystal growth process to higher temperatures with pressure.

T. El Goresy *et al.* studied amorphous nifedipine and an equimolar binary mixture of nifedipine and acetaminophen were studied by dielectric spectroscopy in its supercooled liquid and its glassy state[84]. The α-relaxation process of the binary mixture occurs at a significantly lower temperature as compared to pure nifedipine and the supercooled liquid states were characterized by a relatively large steepness index m. A. C. Rodrigues *et al.* studied the molecular mobility of amorphous S-flurbiprofen using BDS[85]. The fragility or steepness index was calculated as m = 113, classifying S-flurbiprofen as a fragile glass former. K Adrjanowicz *et al.* in 2010 determined the

structural α-relaxation times deep in the glassy state of the pharmaceutical, Telmisartan using the approach suggested by Casalini and Roland[86]. The values of structural relaxation time were compared with those predicted by the coupling model (CM).
Z. Wojnarowska *et al.* performed broadband dielectric measurements on the pharmaceutical indomethacin at ambient and elevated pressure and characterized its molecular mobility in its supercooled liquid and glassy states[87]. Molecular dynamics studies were carried out on the antibiotics-azithromycin, clarithromycin, and roxithromycin-in their supercooled liquid and glassy forms by using dielectric spectroscopy[88]. Several relaxation processes of different molecular origins were reported.

Z. Wojnarowska *et al*. studied the molecular dynamics of a common local anesthetic drug, lidocaine hydrochloride, and its water mixtures by using BDS. From the calorimetric measurements, it was observed that even a small addition of water causes a significant effect on the relaxation dynamics of the analyzed protic ionic liquid[89]. The physical stability of a group of amorphous drugs after storage above and below the glass transition temperature and its relationship to glass-forming ability was studied[90] by A. Alhalaweh *et al.* They resolved that glass transition temperature was feebly correlated to physical stability and stated that molecular properties have a significant impact on the glass-forming ability and glass stability. U. Sailaja *et al.* studied the molecular dynamics of nizatidine and perphenazine[91], fenofibrate[92] using BDS in 2016. U. Sailaja *et al.* also conducted dielectric spectroscopic investigations on amorphous captopril[93]. The sample was found to be highly unstable in the amorphous state. Molecular relaxation studies on amorphous ketoprofen using BDS over a wide temperature and frequency range were done by Sailaja *et.al*.

J. Knapik-Kowalczuk *et al.* studied the physical stability of pure amorphous probucol and also studied the physical stability of amorphous probucol by mixing it with atorvastatin as a crystallization inhibitor[94]. Z. Wojnarowska *et al.* carried out dielectric measurements of pharmaceuticals, procaine hydrochloride and procainamide hydrochloride-which are glass-forming as well as ionically conducting materials, to study the dynamics of the conductivity relaxation. They pointed the vital importance of β-conductivity relaxation as it is crucial as the precursor of the α-conductivity relaxation[95], analogous to the relation found between the Johari-Goldstein

β-relaxation and the structural *α*-relaxation in non-ionic glass-forming systems.

K.Ad Janowicz *et al.* studied the molecular dynamics of the pharmaceutical Posaconazole[96] in the supercooled liquid and glassy states. G. Shete *et al.* investigated the dielectric relaxation of amorphous hesperetin using dielectric spectroscopy and also assessed the crystallization kinetics of amorphous hesperetin[97] above the glass transition temperature. Amorphous hesperetin exhibited both structural *α*-relaxation and more local *β*-relaxation. With the help of dielectric spectroscopy,

K. Grzybowska *et al*. investigated the molecular dynamics and crystallization tendency of amorphous celecoxib[36]. This study stated that structural relaxation seems

to be responsible for the devitrification of celecoxib if stored at room temperature. Molecular dynamics and structural properties on the crystallization tendency of three 1,4-dihydropyridine derivatives, namely nifedipine, nisoldipine, and nimodipine[98] were studied in their supercooled states using DSC and BDS. Isothermal crystallization kinetics of supercooled nifedipine and nimodipine were also investigated using BDS and found that nimodipine exhibits much slower crystallization in comparison to nifedipine. The amorphous drug-drug system of nifedipine-nimodipine was found to be stable and thus nimodipine act as an effective crystallization inhibitor for nifedipine.

Dantuluri *et al.* studied the role of *α*-relaxation toward isothermal crystallization of amorphous celecoxib using dielectric relaxation spectroscopy[45].

K. Kolodziejczyk *et al.* investigated molecular relaxations and crystallization kinetics of amorphous sildenafil[99] in both supercooled liquid and glassy state. Safna *et.al* we studied both the structural and the conductivity relaxations in an ionically conducting salt, sodium ibuprofen, and in amlodipine besylate and reported the presence of translational rotational coupling in these glass formers[58,62]. In 2016, Schamme *et.al*. conducted a comprehensive molecular relaxation study of amorphous Quinidine through BDS experiments and theoretical density functional theory (DFT) calculations[63]. The origin of secondary relaxation was identified theoretically by DFT by exploring potential energy surfaces by performing a dihedral scan.

M.C. Flores *et al.* has reported the molecular modelling studies of bromopyrrole alkaloids as potential antimalarial compounds: a DFT approach was reported in 2018[100].

Instead of individual wave functions for each electron, the DFT approximates

the interaction system of electrons by using a function to describe the electron density[101]. The total electron density is used in DFT, and the electrons are "placed" in non-interacting Kohn-Sham (KS) orbitals[102]. Large molecules can be calculated using the DFT method because the potential is based on three spatial coordinates rather than 3N degrees of freedom. DFT's application to chemical systems has recently gotten a lot of attention, thanks to improvements in the prediction of the molecular force field, vibrational frequencies (and thus thermodynamic parameters), dipole moments, and polarizability data, as well as a faster convergence time than traditional quantum mechanical correlation methods. As a result, the force field derived from DFT calculations can be combined with spectroscopic data to assign observed frequencies and refine molecular force[103]. Structural, vibrational, UV–vis, quantum-chemical properties, molecular docking, and anti-cancer activity study of annomontine and N-hydroxyannomontine β-carboline alkaloids: A combined experimental and DFT approach was reported in 2015 by Costa *et al*., where a complete characterization of alkaloids was done by spectroscopy and DFT methods[104]. Quinoline derivatives as possible lead compounds for anti-malarial drugs: Spectroscopic, DFT, and MD study was reported by Panicker *et al*.[105]. As a result, the force field derived from DFT calculations can be combined with spectroscopic data to assign observed frequencies and refine the molecular force field under investigation. Various laboratories are also looking for anticancer agents. Benzimidazole has recently been documented to have antitumor, anti-proliferative, and anticancer properties by various authors all over the world[106,107]. Combining FT-IR and FT-Raman spectroscopy with ab initio/DFT is proving to be an effective method for vibrational assignment and studying the structure and properties of complex molecules[108].

1.3 Glass transition

Glass is one of the oldest materials used by humans[109]. In the last half-century, the appearance of numerous new types of glasses as metal alloys, polymers, simple liquids, and other materials has made such materials ubiquitous and of immeasurable importance to material engineering and science. However, the theory of the nature of glass and the glass transition remains the most difficult and intriguing unsolved problem in solid-state theory [110]. Significant theoretical and experimental

advances in recent years, however, have rekindled interest in the physics of glasses, raising the prospect of a breakthrough in understanding of the glassy state [51].

Glass is a non-crystalline solid with molecular order and physical properties that differ from their crystalline counterparts. While the atomic structure of glass is similar to that of a supercooled liquid, it behaves as a solid below the glass transition temperature (T_g). The theory of glass transition is a topic of constant interest in the scientific community, and the theory of glass transition is still not widely accepted and completely satisfying. Research on the glass transition and amorphous structural materials has been significant in the fields of pharmaceuticals, medical, food, electronics, metallurgy, geoscience, nanoscience, and energy sources.

Crystallisation occurs when a liquid is cooled below its melting point; if the cooling rate is fast enough to overcome crystallisation, the liquid becomes supercooled, and with further cooling, it becomes glass. Glasses are a fascinating material due to their dual nature, i.e., the mechanical properties of solids and the molecular disorder characteristics of liquids. The glass transition temperature is the temperature at which a liquid changes from a liquid to a glassy state (T_g). T_g causes molecular motion to slow to a hundred-second time scale, and below T_g, molecular rearrangement is too slow, causing molecules to fail to reach their equilibrium positions. The liquid state is transformed into a metastable state known as supercooled liquid below the point of crystallisation (liquid-like state). As the temperature drops further, the viscosity increases sharply until it reaches a specific viscosity close to that of solids (the universal 1013 Poise), corresponding to a relaxation time of 100 seconds. The temperature at which this viscosity is reached is known as the glass transition temperature, abbreviated as T_g. When the characteristic temperature T_g is reached, the characteristic time scale required to balance the supercooled liquid exceeds the experimental time scale, and the system loses thermodynamic equilibrium, resulting in a glassy state. This glassy state has liquid-like structures, but lacks long-range structural order, and their macroscopic behaviour is more like that of a solid. Heat capacity, volume, entropy, enthalpy, viscosity, and thermal expansion coefficient, among other thermodynamic quantities, change dramatically during the transition from liquid to glass. Figure 1.2 shows the variation of specific heat capacity at constant pressure with temperature during glass transition illustrates the origin of the glass transition phenomenon in an amorphous solid.

In the figure,the volume and enthalpy of the crystalline state increases with increase in temperature. On reaching the melting temperature (T_m), volume and enthalpy values show a rapid discontinuity as shown in figure 1.2 due to a first-order transition from the crystalline state to the liquid state. On the other hand, if the liquid is cooled at a faster rate sufficiently enough to avoid crystallization, values of H and V follow the normal trend of the liquid state toward the supercooled liquid. On further cooling to reach the T_g , a gradual decrease of H and V values up to the sharp change in slope is observed. Below T_g, values of H and V are higher for the glassy state than for the original crystalline state.

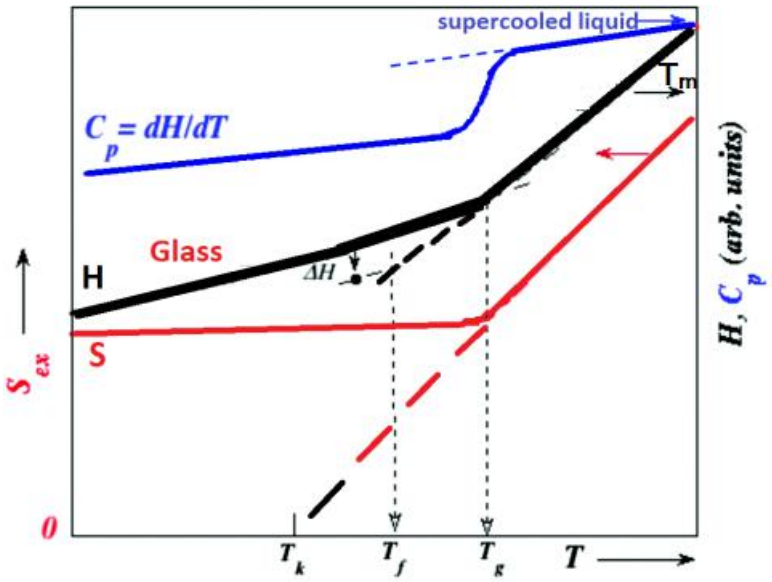

Figure 1.2 Variation of specific heat, entropy, and enthalpy on cooling a liquid

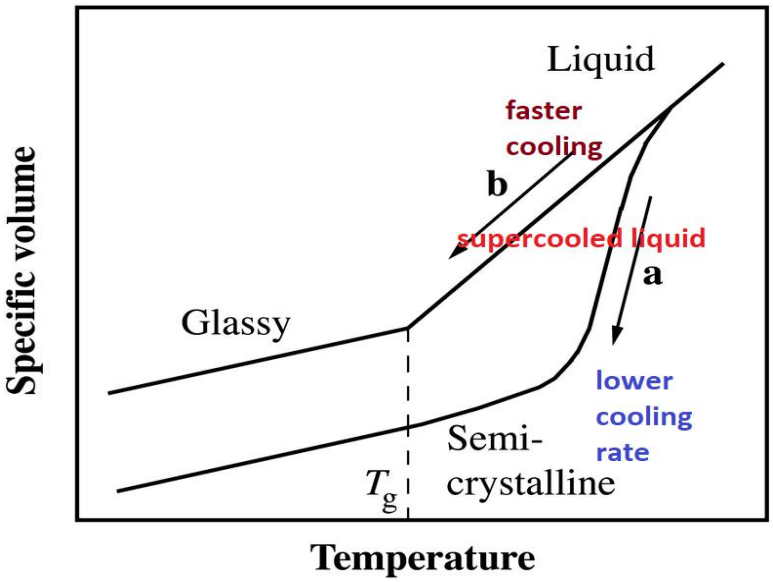

Figure 1.3 specific volume vs. temperature on cooling a liquid

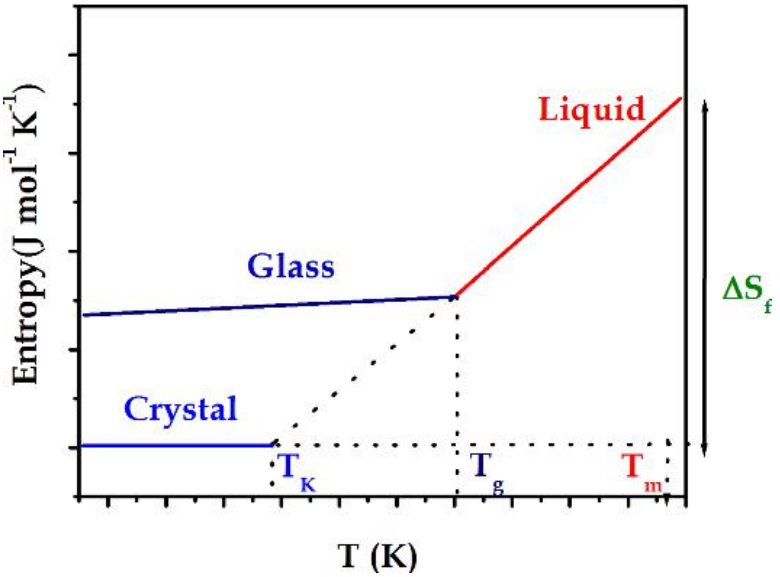

Figure 1.4 Variation of entropy at constant pressure on cooling a liquid to form a crystal and a glass

These physical quantities change during glass transition in a narrow temperature interval defined by a single temperature value called glass transition temperature T_g, which is traditionally calculated by the intersection of the liquid and the glassy curve, as shown in figure 1.3. Alternatively, T_g is also known as the temperature at which the viscosity is approximately 10^{13} Poise[111] or the temperature at which the structural relaxation time occurs in the order of 10^2s. The glass

transformation is a complex phenomenon[112] whose fundamental origin is not yet understood and a general theory of glass transition is still under development[113]. Several features of the temperature-dependent behaviour of glass-forming materials can also be observed in the way they react to a pressure variation, according to recent high-pressure studies on the liquid-glass transition.

The effect of isothermal compression on molecular motions is similar to that of isobaric cooling, and using pressure as an additional thermodynamical variable can be a useful tool for testing theories that claim to explain glass transition. The glass transformation has been debated as to whether it is a kinetic or a thermodynamic phenomenon. According to kinetic theory[114], the glass transition occurs when the characteristic time of molecular motion equals or exceeds the experimental characteristic time scale. This provides clear evidence that the glass transition is a strictly kinetic phenomenon. The glass transition, on the other hand, is a second-order phase transition in thermodynamic theory, meaning that it is continuous over enthalpy, entropy, and volume but discontinuous at specific heat capacity, compressibility, and coefficient of thermal expansion, which are second derivatives of Gibbs free energy or volume. However, Ehrenfrest relations[115] for a second-order phase transition show that

$$\frac{dTg}{dP} = T_g V \frac{\Delta\alpha_p(T_g)}{\Delta C_P(T_g)} \tag{1.3}$$

$$\frac{dTg}{dP} = \frac{\Delta K_T(T_g)}{\Delta\alpha_P(T_g)} \tag{1.4}$$

Where α_P is the thermal expansion coefficient at constant pressure, Cp is the specific heat capacity at constant pressure, K_T is isothermal compressibility coefficient, V and P are the volume and pressure of the systems respectively. For any parameter, Δ indicates the difference between the value measured in the liquid and glass phases. Equations 1.3 and 1.4 are obtained imposing the continuity of the entropy and the volume from the liquid to glass respectively. In a true phase transition, the product Π in the Prigogine- Defay ratio [116] shown in equation (1.5) must be equal to 1.

$$\Pi = \frac{\Delta K_T \Delta C_P}{T_g V \Delta\alpha_P^2} \tag{1.5}$$

For polymeric glasses the ratio Π is generally between 2 and 5, therefore, the glass transition is not a true second phase transition. On the other hand, the kinetic nature of the glass transition is also supported by the observed dependence of T_g on the cooling rate. The slower a liquid is cooled, the longer the time available at each temperature for changing its structure, and hence the liquid, cooled with a high cooling rate falls out of the equilibrium before. Consequently, T_g increases with the cooling rate. The properties of glass, therefore, depend on its cooling history. In practice, the dependence of T_g on the cooling rate is weak, and the transformation range is narrow so that T_g is an important material characteristic.

The interpretation of glass transition is difficult because of its dynamic and thermodynamics nature, its dynamic nature is by its dependence on T_g. i.e., if the liquid is cooled faster then the value of T_g will be greater and vice versa. Also, the glass transition is observed when the characteristic time of molecular motion becomes of the same order or greater than the characteristic time of experiments, for example, the reciprocal of the cooling rate in heat capacity measurements. On the other hand, the thermodynamic nature of the glass transition is mainly derived as a consequence of the dependence of T_g on the cooling rate. The extrapolated entropy of the supercooled liquid should become less than that of the glass and also less than zero at $T > 0K$, which is the basis of a thermodynamic paradox known as the Kauzmann paradox[117]. To avoid an entropy crisis, the existence of an (ideal) thermodynamic transition at T_k was proposed, where the entropy of the supercooled liquid stops decreasing and remains constant at zero. The “laboratory” glass transition is defined as the temperature range where many dynamical processes become “arrested” in the experimental time scale, whereas the “ideal” glass transition is a true thermodynamic phase transition between two different states of matter, according to the thermodynamic interpretation. In this context, the laboratory transition is nothing more than the kinetic expression of the thermodynamic glass transition that occurs at T_k.

As a result, various configuration states linked to various thermal histories may emerge. The kinetic nature of the glass transition results in a competition between structural relaxation time scales and experiment time scales. The kinetic nature of T_g is revealed by its dependence on the cooling rate. A high T_g value is obtained by a rapid cooling rate, whereas a low T_g value is obtained by a slow cooling rate. Furthermore, a

holistic view of the glass transition from a physical standpoint avoids the Kauzmann paradox and the entropy catastrophe. The entropy of the liquid S is greater than that of the crystalline state at melting temperature. Because a liquid's heat capacity C_p is greater than that of a solid, entropy is higher in a liquid. As the heat capacity, C_p of a liquid is higher than a solid, entropy of the liquid decreases faster than the crystal's one according to:

$$S = \int_0^T \frac{C_P}{T}\, dT \tag{1.6}$$

The curves of the liquid and crystalline states converge at a certain temperature, known as the "Kauzmann temperature," or T_K. The entropy of the liquid (disordered state) falls below that of the crystalline state (ordered state) below this temperature, resulting in negative configurational entropy. However, from a thermodynamic perspective, this condition is still unsatisfactory. Entropy is always positive according to thermodynamic rules. As a result, with the crystal's enthalpy nullifying at 0 K, the liquid's enthalpy cannot be lower than that of the crystal's. The paradox of Kauzmann is the name given to this case. Since T_K is experimentally inaccessible and can only be calculated by extrapolations, it remains a hot topic of debate.

1.4 Relaxation in glasses

The relaxation effect in physics refers to the return of a macroscopic system to thermodynamic equilibrium after an external perturbation is removed. For example, a system can be perturbed from its equilibrium state by a variety of mechanical, electrical, and magnetic stresses, and the energy from the external source can be dissipated in the system in characteristic time-regions determined by the glassy system's molecular structure. These are the relaxation mechanisms in which the external stress induces configuration re-arrangement of atomic or molecular constituents of the glass, which must be minimal in comparison to, say, the electrical forces acting between the constituent particles. The volume or enthalpy of the system can be determined in some cases, while the conductivity or optical density at frequencies characteristic of specific subunits of the glass structure can be determined in others. Much can be learned about the complex relationship between the various elements of the glass system, as well as the various energy and volume-changing processes, from the correlation and

comparisons of these various types of experiments. It is commonly observed that the amorphous state reduces its excess entropy and enthalpy during storage without potentially recrystallizing. The amorphous state tends to reach a lower energetic state while maintaining its disordered state, which is known as "relaxation." As a result, amorphous solids show the ability to slowly anneal w when held at temperatures below T_g. So, at below T_g, amorphous solids show the ability to anneal slowly with a thermodynamic restructuring (implying a loss of free energy, enthalpy, and entropy) to reach supercooled liquid values, in figure 1.5.

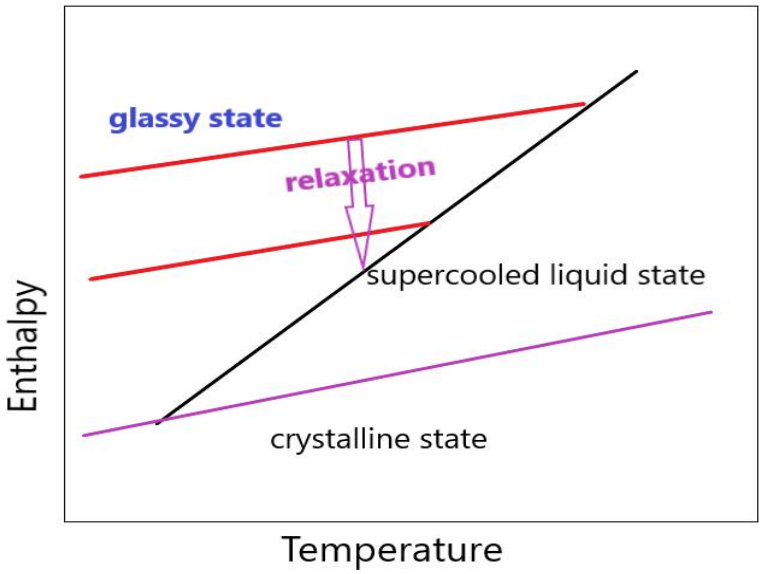

Figure 1.5 Enthalpy vs. temperature on glass transition showing relaxation

Furthermore, these characteristic relaxations are of importance as they are highly temperature-dependent varying over 13-15 orders of magnitude between T_g and Tm, unlike resonant frequency. They are named successively by the Greek alphabets by the order of frequency of their occurrence and are classified as follows.

(i) Collective, co-operative molecular movements involving the rearrangement of molecular groups or segmental movements in polymer chains are permitted at the longest time scale. In this case, the dynamics is controlled by the α relaxation, also referred to as the structural relaxation, which is the main universal dynamic process associated with the glass transition. Figure 1.6 depicting the situation in the vicinity of T_g with the alpha-peak located at a rather low alphabet. Increasing the temperature will quickly shift the α relaxation peak to higher frequencies.

(ii) The molecular motions are non-cooperative at shorter times. This process is present even in the viscous liquid state or in the glass state and is generally more localized and activated, and due to the disturbed structure of the glass, a large distribution of the barrier energy can be present. As shown in figure 1.6, various dynamic features can be observed in glass-forming systems. In some systems, an excess wing appears in the high-frequency peak, while in other systems, a slow peak appears. It's worth noting that, in comparison to the dominant-peak, the amplitudes of all these processes beyond the α-process are quite small. Despite this, there has been a lot of interest in understanding their microscopic origins in recent years.

(iii) At some THz a second loss peak shows up that can be identified with the called boson peak (bp) known from neutron and light scattering [3]. The boson peak is a universal feature of glass systems materials and corresponds to the vibrational density of the state.

The characteristic relaxation time, which represents the most likely time, or the average time, which is the area below the peak curve of the various relaxation spectra, is the most important parameter of a single relaxation process. The main feature of structural- and secondary- relaxations will be introduced and discussed in the sections that follow. We'll also go over the properties of the various secondary relaxations found in glassy systems, ranging from intramolecular degrees of freedom to those that are more intermolecular and thus universal. Indeed, the latter's properties are of particular interest because they may provide useful hints as to which features must be reproduced by a complete theory of the glass transition.

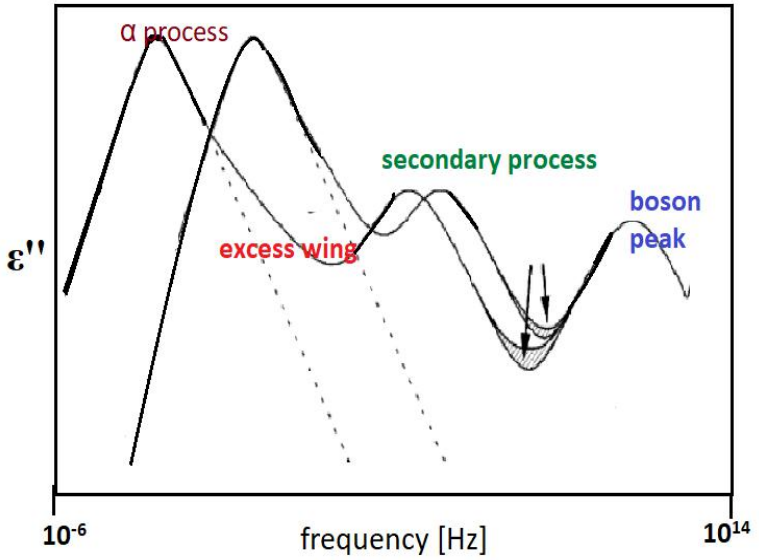

Figure 1.6 Schematic view of the different relaxation loss spectra in the glass-forming system. Showing an excess wing and a glass former with well-resolved β relaxation.

Upon storage, it is often noted that the amorphous state decreases its excess of entropy and enthalpy without leading to potential recrystallization[118]. This phenomenon is known as "relaxation" as the amorphous state tends to reach a lower energetic state while maintaining its disordered state. Therefore, when held at temperatures below T_g, amorphous solids demonstrate a capability to slowly anneal with a thermodynamic restructuring (implying loss of free energy, enthalpy, and entropy) to reach values expected for the supercooled liquid, as illustrated in figure 1.6.

1.4.1 The structural relaxation

The process of structural relaxation in supercooled liquids slows down more quickly as it approaches the glass transition, and it is more affected by vitrification. As a result, the glass transition is defined as the temperature range in which structural relaxation motions occur on the order of 10^2 seconds. The viscosity is another property that is closely linked to the characteristic time for molecular rearrangement. The viscosity can be expressed as $\eta = G\tau$, where G is the shear modulus and τ is the relaxation time. G is only weakly dependent on temperature, η, therefore, gives a direct measure of a typical relaxation time scale τ in supercooled liquids. The temperature where η reaches the value 10^{13} Poise is defined as the glass transition temperature T_g. In terms of operation, this corresponds to relaxation time scales of the order of hundreds of seconds or more for typical G values. With the temperature, the structural-relaxation

process, which is the most common dynamical process associated with the glass transition shifts rapidly to higher frequencies. In certain glass-forming systems, an excess wing is found in the high-frequency power-law flank of the -peak, while in others, the relaxation mechanism leads to secondary relaxations. The structural α-relaxation process[84], which is the main common dynamical process associated with the glass transition, shifts rapidly to higher frequencies with increasing temperature. In some glass-forming systems, an excess wing is observed in the high-frequency power-law flank of the α-peak, while in some systems further relaxation process leads to additional peaks named as secondary relaxations or β-peak (or γ, δ…..relaxations if there are more than one). The amplitudes of all these processes further than the α-process are relatively small compared to the universal α-relaxation. At frequencies around some THz, another loss peak shows up that can be acknowledged with the so-called boson peak identified from neutron and light scattering. The boson peak is a universal characteristic of glass-forming systems and corresponds to the vibrational density of the state[119]. Non-exponential relaxation patterns and non-Arrhenius temperature dependence of the characteristic time scale are the most prominent features of -relaxation caused by the structural disorder.

(a) Dynamic heterogeneity and non-exponentiality: Unlike a simple Debye relaxation phenomenon, which uses a simple exponential function to describe the dielectric response of a system of noninteracting molecular dipoles rotating in a non-polar viscous setting. Experiments have shown that the response of glass-forming compounds, as well as a variety of solid dielectric materials, exhibits a stretched exponential response over a broad period. For a wide range of materials, the structural relaxation as a function of time is best represented by the empirical extended exponential or the Kohlrausch-Williams-Watts style [120] decay given by

$$\varphi(t) = \varphi(0)\exp\left(-\left(\frac{t}{\tau_{kww}}\right)\right)^{\beta_{kww}} \tag{1.7}$$

The quantities $\varphi(t)$ and $\varphi(0)$ are the dynamic response at time t and 0, respectively, after a perturbation, while τ_{KWW} is a characteristic relaxation time, the exponent β is the stretching parameter and is generally in the range between 0 and 1. For simple Debye relaxation[121] behaviour, the response is an exponential function with β=1. The

deviations from simple exponential to the stretched exponential of the time dependence of the relaxation functions when a liquid is supercooled could be related to two reasons. The first reason is, at lower temperatures, the cooperativity effect becomes more pronounced as density increases. As a result, the long-time dependence of the relaxation functions should have a greater temperature dependence as the glass transition approaches, and the motion should become more cooperative as molecular packing increases, which explains the stretching of the structural relaxation. The propensity of the relaxation function to become exponential as the temperature increases, as expressed by the increase, which in some cases reaches the limiting value, is a general characteristic of structural-relaxation[122]. This effect is typically explained by the fact that at relatively high temperatures, this effect is usually explained by the fact that at high temperatures, cooperative effects on dynamics become less important, and structural relaxation reflects molecular motions that are nearly independent.

The second reason is, in condensed matter, dynamic heterogeneity is now recognized as a fundamental feature of the slow dynamics of super-cooled fluids and glasses. In terms of dynamics, heterogeneity refers to the presence of fast and slow relaxing modes. These dynamically distinct domains are thought to be on the order of a few nanometres in size. In a glass-forming system, some molecules have fast motions while others have much slower motions, acting as cages for the faster. This picture is dynamic in the sense that due to mutual interactions; the fast molecules could become slow and vice versa a few moments later (usually on the time scale of structural relaxation). In most cases, fast and slow molecules are grouped in domains. One might be tempted to explain the stretched exponentiality of relaxation in glass-forming systems by assuming that relaxation occurs exponentially in each spatial domain but with a different relaxation time in each domain: averaging over the ensembles should result in a distribution of relaxation times. Ediger and colleagues[123] proposed a spatially heterogeneous model of translational and rotational diffusion in supercooled liquids, based on the temperature behaviour of the two quantities reported in the $T_g<T<1.2T_g$ region. Translational diffusion was found to be less temperature-dependent than rotational diffusion. According to Ediger, the decoupling could be caused by the different importance of fast and slow motions on translational and rotational

diffusion[124,125], respectively: thus, if spatial heterogeneity is reflected in a given distribution of relaxation times for the α relaxation, the wider the distribution, the stronger the decoupling between translational and rotational diffusion. Some experimental evidence for organic glass-formers (for example, tris-naphthyl benzene (TNB), where the width of the relaxation peak (and thus the distribution of relaxation times) was found to be temperature-independent over a broad temperature range[126], while a decoupling between translational and rotational relaxation times was found to be temperature-independent over the same range. The coupling model (CM)[127] proposes that decoupling of translational and rotational diffusion in glass-forming liquids is a special case of a more general phenomenon, in which different dynamic observables weigh the many-body relaxation differently and have different coupling parameters n (i.e., different degrees of intermolecular cooperativity) that enter into the stretch exponents β_{KWW} of their Kohlrausch correlation functions but also in the temperature-dependent of the considered observable. Another characteristic feature of the structural α-relaxation process is the deviation of its temperature dependence[128] from the Arrhenius law, which is the general expected behaviour for thermally activated processes.

$$\tau = \tau_{\infty}\exp\left(\frac{\Delta E}{k_B T}\right) \tag{1.8}$$

For fragile glasses, the temperature dependence of the α- relaxation time can be described empirically with the Vogel-Fulcher-Tammann[129] equation given by eqn.1.8 and eqn.1.9.

$$f_{\alpha} = f_0^{\alpha} e^{(-B/T-T_0)} \tag{1.9}$$

For fragile glasses, the temperature dependence of the α- relaxation time can be described empirically with the Vogel-Tammann-Fulcher (VTF) law given by (1.10).

$$\tau(T) = \tau_0^{\alpha}\exp\left(\frac{DT_0}{T-T_0}\right) \tag{1.10}$$

The extent of this deviation from Arrhenius's behaviour is incredibly different for different glass-forming materials. Oldekop and later Laughlin and Uhlmann[130] were the first to use T_g as a corresponding state parameter for liquid viscosity η to

compare the flow behaviour of different liquids. Angell [100] was the first who recognized the significance of the Laughlin-Uhlmann plot as a means to classify the transport properties of glass-formers. Fragile glasses show a bent curve in the normalized activation plot log(τ) versus T_g /T, which indicates that on decreasing T, the apparent activation energy increases. Now, the expressions strong and fragile are often used to express the curvature or location of either log η or log τ of the glass formers in the Oldekop-Laughlin- Uhlmann-Angell (OLUA) plot. Typical fragility plot or Angell plot for strong and fragile liquids are shown in figure 1.7.

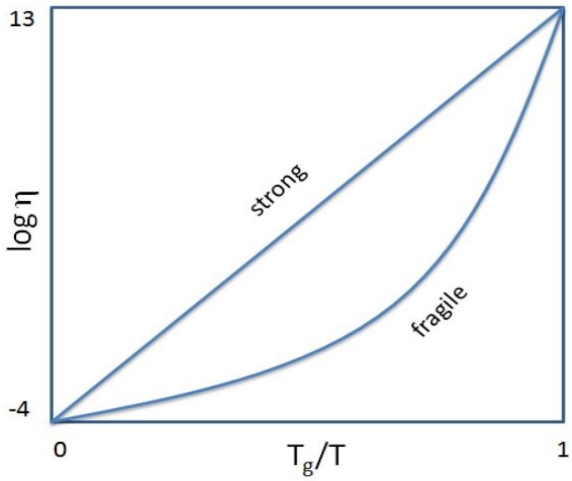

Figure 1.7 Typical Angel's plot

The fragility or steepness index, m can be calculated from VFT fit and is defined as the slope of the relaxation time curve vs. T_g / T at the glass transition temperature T_g in the Oldekop-Laughlin-Uhlmann-Angell (OLUA) plot, given by

$$m = \frac{d \log \tau}{d(\frac{T_g}{T})} \Big/_{T=T_g} \tag{1.11}$$

The classical value of m is between 50 and 150 for fragile systems, (for instance m=140 for cis-Polyisoprene), and m are between 16 and 20 for strong systems, for instance, m=20 for GeO_2 and SiO_2. Of course, there is a continuity of systems with intermediate fragility. All experimental evidence indicates the complex dependence of the structural relaxation time on the temperature. Several experimental and numerical simulation results reported that the slowing down of the dynamics on approaching T_g and the increasing of the apparent activation energy could be related to the onset of cooperative motions, involving molecules on an increasing correlation length. If the value of m is less than 45 then such system belongs to strong liquids and if m is greater than 75 such system belongs to fragile liquids in fragile liquids near the glass transition

temperature, molecular mobility changes rapidly with temperature indicating weak thermodynamic stability and consecutively leads to a larger tendency toward crystallization of amorphous systems.

1.4.2 Secondary relaxations

Molecular motions in glass-forming materials are hampered as they approach the supercooled liquid state as they cool from liquid state. In the glass transition area, this slowing ranges from picoseconds (10^{-12} s) to nearly a hundred seconds. In the supercooled liquid state, materials frequently exhibit multiple relaxation processes. Because of its physical nature, the molecule mobility responsible for the glass transition is referred to as "global mobility." Because they typically appear at a lower frequency in a dielectric relaxation profile, such molecular mechanisms are also known as structural or α - relaxation. As a result, estimating it in the glassy state is important. One of the simplest methods based on the master curve approach cannot be mentioned in the context of the temperature dependence of structural relaxation times in the glassy state predictions. Indeed, this method can be applied to the region below T_g to determine the time scale of structural relaxation in the glassy state. At temperatures above T_g, dielectric loss spectra corresponding to the α process were chosen to estimate α - relaxation times below T_g. To match the high-frequency side of the spectra collected below T_g with the low-frequency side, the latter is shifted horizontally to temperatures close to and below T_g. It's worth noting that other forecasts exist.

The structure of the liquid becomes "frozen" as it cools, and the system becomes glassy. The time scale of structural relaxation below T_g is excessively long when it is far from equilibrium. As a result, molecular dynamics of relaxation in glassy materials take a long time, and only predictions of relaxation times are possible nowadays. As a result, only secondary relaxations resulting from some local molecular motions are usually measured experimentally in the glassy state. Although is an unknown quantity below the glass transition, understanding the time scale of relaxation below T_g is critical for selecting appropriate storage conditions for amorphous materials to avoid crystallization and chemical instability. It is well known that glass-forming liquids, in addition to the α- relaxation, show secondary β- relaxations in the glassy state, which in dielectric loss spectra appears as a broad peak, more often symmetrical slowly moving at a lower frequency on decreasing temperature, Microscopically, two

different mechanisms can contribute to the β process: firstly, motions of molecular subunits that can relax independently from the whole molecules (intramolecular origin). Besides, in some other systems, the observed secondary relaxation reflects the motion of the whole molecule (intermolecular secondary relaxation).

In simple glass-forming systems with no internal degree of freedom, Johari and co-workers discovered a specific type of intermolecular secondary relaxation process [39]. Two approaches to elucidating the origin of these intermolecular secondary relaxations have been proposed. The reason for the Johari-Goldstein (JG) β-process, according to Johari, is the concept of islands of mobility, which are isolated regions of loosely packed molecules caged in a glassy matrix. As a result, only molecules within these regions have enough space in the glassy state to execute the relatively fast and independent motions that appear as α-relaxation[131]. Williams and Watts later proposed a completely different explanation[132]. In contrast to Johari's theory, they proposed that the β-process could be attributed to a faster, small-angle (thermally-activated) reorientation motion of all molecules and have a homogeneous nature. In some small molecular glass formers, JG β-relaxation is present but unresolved, because it is sandwiched between the more intense α-relaxation and a faster but non-JG secondary γ-relaxation. Thayyil *et al*. showed in benzophenone and dimethyl phthalate that by dissolving either glass former in a host with a much higher glass transition temperature, the α-relaxation moved further from the γ-relaxation[133].

The linear temperature dependence of the secondary relaxations is well described by the Arrhenius equation at temperatures below the glass transition temperature when the structural relaxation process moved out of the frequency interval of the measurement.

$$f_\beta = f_0^\beta \exp\left(-\frac{\Delta E_\beta}{RT}\right) \tag{1.12}$$

where R is the gas constant (R = 8.314 J mol^{-1} K^{-1}), f_β is the pre-exponential factor related to the lattice vibrational frequency and ΔE_β is the activation energy to overcome the energy barrier.

1.5 Amorphous pharmaceuticals

Synthetic chemists' main aim has been to ensure the crystalline form of every active pharmaceutical ingredient (API) incorporated into pharmaceutical products over the years. A three-dimensional long-range order and close packing of molecules in the crystal lattice provide solid-state stability as well as chemical and structural purity. An API built for oral administration in a solid dosage form must have adequate aqueous solubility to have reasonable oral bioavailability. The well-known Noyes-Whitney equation[134] can be used to determine the rate of dissolution.

$$\frac{dC}{dt} = k_D A(C_S - C_t) \tag{1.13}$$

with dC/dt representing the dissolution rate, k_D representing the dissolution rate constant, A representing the total surface area of the drug particles available for dissolution, C_s representing the drug's aqueous saturation solubility, and C_t representing the concentration dissolved at time t. In the Noyes-Whitney equation, the dissolution rate is proportional to the surface area of the solute particle and the drug's solubility, with all other variables, kept constant.

As a result, pharmaceuticals with low aqueous solubility should have low dissolution rates, resulting in poor oral bioavailability. The role of aqueous solubility in oral absorption was highlighted by the establishment of the Biopharmaceutics Classification System (BCS) [10]. Due to solubility problems, a large number of medications have been relegated to the II and IV grades in recent years. This tends to be linked to an increase in the number of molecules with greater average molecular weights (Mw), higher melting temperatures, and higher hydrophobicity. As a result, solubility enhancement methods have been developed based on chemical and physical modifications to increase the rate of drug dissolution. The surface area of drug particles and solubility in aqueous media of poorly water-soluble crystalline APIs could be refined using the Noyes-Whitney equation to improve dissolution rates. Three methods are commonly used to ensure a higher dissolution rate: The use of structurally disordered physical forms of the considered solid (i) formulation and processing,
(ii) chemical alteration, and (iii) use of structurally disordered physical forms of the considered solid[135]. To increase the specific surface area, one technique is to reduce the particle size of the crystalline raw material (down to the nanometre scale) (i.e., total surface area per unit of mass). To boost the solubility of hydrophobic compounds,

solubilizers (e.g., cyclodextrins) may be applied to the formulation and processing steps. Dissolution rates can be increased by chemical synthesis by producing more strongly water-soluble crystalline salts or co-crystals[3]. This viewpoint is only true if the dissolved form of the drug is held supersaturated in contrast to the crystalline form of the compound. Finally, approaches aimed at changing, reducing, or annihilating the crystal lattice energy could increase apparent solubility. According to this perspective, liquid molecules have a higher solubility than their crystalline counterparts. Furthermore, crystal defects have been documented to serve as defect localities to increase dissolution rate[136]. As a result, creating the amorphous shape of a pharmaceutical component by completely suppressing long-range three-dimensional order in crystals will significantly increase apparent solubility and dissolution rates. Moreover, by theoretical methods, it is estimated that when recrystallization during dissolution is minimal and the maximum solubility enhancement is obtained by an amorphous substance relative to its crystalline form for structurally diverse insoluble drugs [137].

1.6 Molecular mobility and physical stability of amorphous pharmaceuticals

Several studies revealed that there is a correlation between molecular mobility in the supercooled liquid state and glassy states of amorphous APIs and their physicochemical stability. For trimethyl benzene and 1,2-diphenylbenzene, Ngai *et al.* previously demonstrated a partial coupling between crystallization rate and structural relaxation time[138]. Recently researchers discovered a strong link between the structural relaxation time and the onset of crystallization above T_g [139,140]. D. Zhou *et al.* reported that the physical stability of five structurally diverse amorphous compounds is most closely related to the configurational entropy and the molecular mobility. The other thermodynamic driving forces, H_c and G_c, tend to be relatively weak predictors of crystallization under the conditions investigated. As a result, examining T_g and T_K as well as configurational entropy and molecular mobility values as a function of temperature should be part of an initial feasibility evaluation for amorphous formulations. The most stable compounds are those with high T_g's, high configurational entropy barriers, high T_K, and low molecular mobilities. Mehta *et al.* in 2016[141] reported that in the supercooled state, the structural relaxation time was linked to the

characteristic crystallization time. In the glassy state, however, a close connection was not found. In both glassy indomethacin and celecoxib, there was a greater association between the JG relaxation time and physical instability,plasticization of the JG relaxation may be a viable strategy for improving physical stability.

1.7 Spectroscopy and Pharmaceuticals: Computational approaches

Each chemical compound has a distinct absorbance pattern or chemical fingerprint that can be used in pharmaceutical analysis to ensure the composition, quantity, and quality of prepared pharmaceuticals. In pharmacology labs, there are two common absorption spectroscopy techniques: UV/Visible Spectroscopy and Fourier Transformation Infrared (FTIR). FT-IR, FT Raman, UV-VIS, and NMR spectroscopy, in combination with computational and Raman spectroscopy, are versatile instruments in pharmaceutics and bio pharmaceutics[142], with a wide range of applications ranging from drug formulation characterization to elucidation of kinetic processes in drug delivery. Raman spectroscopy is quickly becoming one of the most common analytical measurement tools in the pharmaceutical industry, with applications ranging from raw material verification to drug production process monitoring to product quality control[143]. A Raman spectrum is a wavelength distribution of peaks corresponding to molecular vibrations unique to the sample being studied, similar to an infrared spectrum. Chemicals, such as narcotics, may be classified and quantified by the frequency and intensity of their peaks. In practice, a laser is concentrated into the sample, and the inelastically scattered radiation (Raman) is collected optically and guided into a spectrometer, which separates the wavelengths.

Infrared spectroscopy has proved to be a useful tool for analyzing pharmaceutical formulations. Both qualitative and quantitative data can be analyzed using these spectroscopic techniques. It has immense potential in the field of pharmaceuticals. Current drug applications cover a wide range of topics in the pharmaceutical industry, including fast identifiable proof of mixtures in the investigation of product combinations, dynamic fixings, and excipients, the detection of foreign substances, the representation of detailed products, the discovery of fake and debasing drug objects, and the comprehension of mixing steps as well as the identification of fake and debasing drug items. Eliasson et al. demonstrated that it can be used in the quantitative, non-invasive probing of the bulk content of pharmaceutical

products contained within capsules from the production line. Advanced process analysis schemes may use Raman methodologies to evaluate tablet content, track polymorphism transitions, and so on. The Raman technique is often preferred over infrared for studying inorganic systems since it can be used for aqueous solutions.

UV-visible spectroscopy is a valuable tool for determining the quantity of a single, well-defined element. Due to the direct linear relationship between absorbance and concentration and the relative simplicity of measuring UV-Visible light, UV-visible spectroscopy is the basis for thousands of quantitative analytical methods. This method is widely used to assess pharmaceutical product stability and monitor drug quality in manufacturing facilities. Drug interactions with different types of ions, as well as the effect of storage conditions on the drug, can be studied using UV-Vis spectral approaches. The area of spectroscopy has increased in importance as a result of the use of advanced methods for handling electromagnetic radiation and data processing. In chemical studies of pharmaceutical drugs, NMR spectroscopy, especially proton NMR, carbon-13 NMR, deuterium NMR, and phosphorous-31 NMR, is commonly used. Chemists may use the peaks of nuclear magnetic resonance spectra to determine the composition of a variety of substances. It can be a very selective technique, distinguishing between atoms within a molecule or a group of similar molecules that differ only in their local chemical environment.

Given the enormous growth in computational capacity and the increasing availability of high-performance computing systems, it would be naive to assume that either of the life sciences fields could advance or even thrive without the use of computational modelling. Furthermore, computational methods are needed, comprehensive, and widespread in one of the most diverse and interdisciplinary fields of research, pharmacy, which incorporates fundamental principles of physical and organic chemistry, physics, engineering, biochemistry, biology, and medicine. However, the interdisciplinarity of pharmaceutical sciences, as well as the widespread use of analytical methods in them, has resulted in a narrowing of specialization, even among scientists who use molecular modelling in their daily work. As a result, one of the goals of this review was to compile and present the most recent developments and applications in a very specific branch of molecular modelling methods, namely DFT (density functional theory) periodic calculations used in pharmaceutical sciences[144].

Density functional theory (DFT) has emerged as a QM method[145] that is both rigorous and efficient enough to be used for pharmaceutical problems in the last five years. DFT is a popular method for describing biologically relevant molecular systems accurately and efficiently at a low computational cost.

1.8 Objectives and thesis overview

As previously stated, the physical instability (recrystallization) of amorphous pharmaceuticals is correlated to their molecular mobility. A safe temperature zone is to be designed where the molecular mobility is least to ensure the safe storage of amorphous pharmaceuticals. This work primarily aims to focus on amorphous pharmaceuticals as a solution to the problem of the low solubility of drugs which is the biggest problem of the pharmaceutical industry. The goals of this work can be summarised as follows.

1. Estimating the thermal stability by determining glass transition temperature of some selected API's using DSC
2. To gain a fundamental understanding of the molecular mobility in supercooled and glassy pharmaceuticals and to characterize its amorphous state
3. To estimate safe storage conditions for amorphous APIs.
4. To study the structural and conductivity relaxations in some selected glassy pharmaceuticals and to understand the correlation between these two types of relaxations
5. To identify the origin of experimentally observed secondary relaxations by quantum computational methods
6. To provide deep insights to researchers involved in the glass transition problem as the samples selected in this study are diverse in structure and nature,
7. To characterize anticancerous phytochemical alkaloids brucine and colchicine by vibrational spectroscopy and DFT methods for various applications.

The thesis is organized as follows. Chapter 1 gives a general introduction about glass, relaxation phenomena in glassy systems, classification of pharmaceuticals based on solubility and permeability, and the challenge of low soluble drugs faced by the present pharmaceutical industry, advantages of amorphous drugs, instability of amorphous state, and the various factors affecting its instability. Moreover, chapter 1

discusses the theoretical identification of the origin of the secondary relaxation and the spectroscopic characterization of biopharmaceuticals by computational DFT methods. Chapter 2 discusses the theoretical and experimental overview and materials used for this study. Chapter 3 discusses the molecular dynamics and characterization in the supercooled liquid and glassy phases of amorphous pharmaceuticals, brucine, colchicine, and acemetacin and the stability of its amorphous phase. Chapter 4 discusses a comparative study of molecular dynamics in the supercooled liquid and glassy states of pure bezafibrate, fenofibrate, and binary mixture of fenofibrate with polystyrene. Chapter 5 discusses the molecular dynamics in the supercooled liquid and glassy states of acetohexamide and discusses the correlation between the structural and conductivity relaxations which is translational-rotational coupling in acetohexamide. Chapter 6 discusses the molecular dynamics in the supercooled and glassy piroxicam where structural relaxation is masked by dc conductivity and the use of modulus formalism to analyze dielectric relaxation. Chapter 7 discusses vibrational spectroscopic studies, DFT investigations, and molecular docking of anticancerous alkaloids, brucine, and colchicine. The overall conclusion and plans of the work are presented in Chapter 8.

References

[1] M.R. Yadav, New drug discovery: Where are we heading to? J. Adv. Pharm. Technol. Res. 4 (2013) 2–3. https://doi.org/10.4103/2231-4040.107493.

[2] A. Carnero, High throughput screening in drug discovery, Clin. Transl. Oncol. 8 (2006) 482–490. https://doi.org/10.1007/s12094-006-0048-2.

[3] N.J. Babu, N. Jagadeesh Babu, A. Nangia, Solubility Advantage of Amorphous Drugs and Pharmaceutical Cocrystals, Cryst. Growth Des. 11 (2011) 2662–2679. https://doi.org/10.1021/cg200492w.

[4] S.A. Fouad, F.A. Malaak, M.A. El-Nabarawi, K.A. Zeid, A.M. Ghoneim, Preparation of solid dispersion systems for enhanced dissolution of poorly water-soluble diacerein: In-vitro evaluation, optimization, and physiologically based pharmacokinetic modelling, PLoS One. 16 (2021) e0245482. https://doi. org/10.1371/ journal.pone.0245482.

[5] The United States pharmacopeia, nineteenth revision. Prepared and Published

by the United States Pharmacopeial Convention, Inc., Distributed by Mack Publishing Co., 20th & Northampton Sts., Easton, PA 18042, 1974.1 824pp. 21.5×28cm. Price $25.00, J. Pharm. Sci. 64 (1975) 1266–1267. https://doi.org/10.1002/jps.2600640740.

[6] J.B. Dressman, G.L. Amidon, C. Reppas, V.P. Shah, Dissolution testing as a prognostic tool for oral drug absorption: immediate release dosage forms, Pharm. Res. 15 (1998) 11–22. https://doi.org/10.1023/a:1011984216775.

[7] L.X. Yu, G.L. Amidon, A compartmental absorption and transit model for estimating oral drug absorption, Int. J. Pharm. 186 (1999) 119–125. https://doi.org/10.1016/s0378-5173(99)00147-7.

[8] Y. Zhang, L.Z. Benet, The Gut as a Barrier to Drug Absorption, Clin. Pharmacokinet. 40 (2001) 159–168. https://doi.org/10.2165/00003088-200140030-00002.

[9] M.N. Martinez, G.L. Amidon, A Mechanistic Approach to Understanding the Factors Affecting Drug Absorption: A Review of Fundamentals, J. Clin. Pharmacol. 42 (2002) 620–643. https://doi.org/10.1177/00970002042006005.

[10] G.L. Amidon, H. Lennernäs, V.P. Shah, J.R. Crison, A Theoretical Basis for a Biopharmaceutic Drug Classification: The Correlation of in Vitro Drug Product Dissolution and in Vivo Bioavailability, Pharm. Res. 12 (1995) 413–420. https://doi.org/10.1023/A:1016212804288.

[11] M.S. Ku, Use of the Biopharmaceutical Classification System in early drug development, AAPS J. 10 (2008) 208–212. https://doi.org/10.1208/s12248-008-9020-0.

[12] Wu, CY., Benet, L. Predicting Drug Disposition via Application of BCS: Transport/Absorption/ Elimination Interplay and Development of a Biopharmaceutics Drug Disposition Classification System. *Pharm Res* 22**,** 11–23 (2005). https://doi.org/10.1007/s11095-004-9004-4

[13] Daniela A.S. Agostinho, Ana R. Jesus, Ana B.P. Silva, José M.S.S. Esperança, Alexandre Paiva, Ana R.C. Duarte, Patrícia M. Reis, Improvement of new dianionic ionic liquids vs monoanionic in solubility of poorly water-soluble

drugs, J. Pharm. Sci. (2021). https://doi.org/10.1016/j.xphs.2021.01.014.

[14] Kawabata Y, Wada K, Nakatani M, Yamada S, Onoue S, Formulation design for poorly water-soluble drugs based on biopharmaceutics classification system: Basic approaches and practical applications, Int. J. Pharm. 420 (2011) 1–10. https://doi.org/10.1016/j.ijpharm.2011.08.032.

[15] S. Gupta, R. Kesarla, A. Omri, Formulation Strategies to Improve the Bioavailability of Poorly Absorbed Drugs with Special Emphasis on Self-Emulsifying Systems, ISRN Pharm. 2013 (2013). https://doi.org/10.1155/2013/848043.

[16] A. Dahan, J.M. Miller, G.L. Amidon, Prediction of solubility and permeability class membership: provisional BCS classification of the world's top oral drugs, AAPS J. 11 (2009) 740–746. https://doi.org/10.1208/s12248-009-9144-x.

[17] K.T. Savjani, A.K. Gajjar, J.K. Savjani, Drug Solubility: Importance and Enhancement Techniques, ISRN Pharm. 2012 (2012) 1–10. https://doi.org/10.5402/2012/195727.

[18] K.P.S. Hussan, M. Shahin Thayyil, S.K. Deshpande, T. V Jinitha, V.K. Rajan, K.L. Ngai, Synthesis and molecular dynamics of double active pharmaceutical ingredient-benzalkonium ibuprofenate, J. Mol. Liq. 223 (2016) 1333–1339. https://doi.org/10.1016/j.molliq.2016.09.054.

[19] A. Schittny, J. Huwyler, M. Puchkov, Mechanisms of increased bioavailability through amorphous solid dispersions: a review, Drug Deliv. 27 (2020) 110–127. https://doi.org/10.1080/10717544.2019.1704940.

[20] S. Du, W.S. Li, Y.R. Wu, Y. Fu, C. Yang, J. Wang, Comparison of the physical and thermodynamic stability of amorphous azelnidipine and its coamorphous phase with piperazine, RSC Adv. 8 (2018) 32756–32764. https://doi.org/10.1039/C8RA05535A.

[21] B. Schammé, N. Couvrat, P. Malpeli, E. Dudognon, L. Delbreilh, V. Dupray, É. Dargent, G. Coquerel, Transformation of an active pharmaceutical ingredient upon high-energy milling: A process-induced disorder in Biclotymol, Int. J. Pharm. 499 (2016) 67–73. https://doi.org/10.1016/j.ijpharm.2015.12.032.

[22] B.C. Hancock, G. Zografi, Characteristics and Significance of the Amorphous State in Pharmaceutical Systems, J. Pharm. Sci. 86 (1997) 1–12. https://doi.org/10.1021/js9601896.

[23] B.C. Hancock, M. Parks, What is the true solubility advantage for amorphous pharmaceuticals?, Pharm. Res. 17 (2000) 397–404. https://doi.org/10.1023/a:1007516718048.

[24] P. Gupta, G. Chawla, A.K. Bansal, Physical Stability and Solubility Advantage from Amorphous Celecoxib: The Role of Thermodynamic Quantities and Molecular Mobility, Mol. Pharm. 1 (2004) 406–413. https://doi.org/10.1021/mp049938f.

[25] R. Zallen, The Physics of Amorphous Solids, (1998). https://doi.org/10.1002/9783527617968.

[26] L. Yu, Amorphous pharmaceutical solids: preparation, characterization and stabilization, Adv. Drug Deliv. Rev. 48 (2001) 27–42. https://doi.org/10.1016/s0169-409x(01)00098-9.

[27] K. Six, G. Verreck, J. Peeters, M. Brewster, G. Van den Mooter, Increased Physical Stability and Improved Dissolution Properties of Itraconazole, a Class II Drug, by Solid Dispersions that Combine Fast- and Slow-Dissolving Polymers, J. Pharm. Sci. 93 (2004) 124–131. https://doi.org/10.1002/jps.10522.

[28] B. Kalkan, S. Sen, S.M. Clark, Nature of phase transitions in crystalline and amorphous GeTe-Sb2Te3 phase change materials, J. Chem. Phys. 135 (2011) 124510. https://doi.org/10.1063/1.3643327.

[29] S. Raoux, C.T. Rettner, J.L. Jordan-Sweet, A.J. Kellock, T. Topuria, P.M. Rice, D.C. Miller, Direct observation of amorphous to crystalline phase transitions in nanoparticle arrays of phase change materials, J. Appl. Phys. 102 (2007) 94305. https://doi.org/10.1063/1.2801000.

[30] A. Karagianni, K. Kachrimanis, I. Nikolakakis, Co-Amorphous Solid Dispersions for Solubility and Absorption Improvement of Drugs: Composition, Preparation, Characterization and Formulations for Oral Delivery, Pharmaceutics. 10 (2018) 98. https://doi.org/10.3390/pharmaceutics10030098.

[31] K. Kawakami, Crystallization Tendency of Pharmaceutical Glasses: Relevance to Compound Properties, Impact of Formulation Process, and Implications for Design of Amorphous Solid Dispersions, Pharmaceutics. 11 (2019) 202. https://doi.org/10.3390/pharmaceutics11050202.

[32] C. Bhugra, M.J. Pikal, Role of Thermodynamic, Molecular, and Kinetic Factors in Crystallization from the Amorphous State, J. Pharm. Sci. 97 (2008) 1329–1349. https://doi.org/https://doi.org/10.1002/jps.21138.

[33] B. Karolewicz, A. Górniak, D.M. Marciniak, I. Mucha, Molecular Mobility and Stability Studies of Amorphous Imatinib Mesylate, Pharmaceutics. 11 (2019) 304. https://doi.org/10.3390/pharmaceutics11070304.

[34] C. Bhugra, S. Rambhatla, A. Bakri, S.P. Duddu, D.P. Miller, M.J. Pikal, D. Lechuga-Ballesteros, Prediction of the onset of crystallization of amorphous sucrose below the calorimetric glass transition temperature from correlations with mobility, J. Pharm. Sci. 96 (2007) 1258–1269. https://doi.org/10.1002/jps.20918.

[35] K. Kothari, V. Ragoonanan, R. Suryanarayanan, Influence of Molecular Mobility on the Physical Stability of Amorphous Pharmaceuticals in the Supercooled and Glassy States, Mol. Pharm. 11 (2014) 3048–3055. https://doi.org/10.1021/mp500229d.

[36] K. Grzybowska, M. Paluch, A. Grzybowski, Z. Wojnarowska, L. Hawelek, K. Kolodziejczyk, K.L. Ngai, Molecular dynamics and physical stability of amorphous anti-inflammatory drug: celecoxib, J. Phys. Chem. B. 114 (2010) 12792–12801. https://doi.org/10.1021/jp1040212.

[37] Y. Aso, S. Yoshioka, S. Kojima, Molecular mobility-based estimation of the crystallization rates of amorphous nifedipine and phenobarbital in poly(vinylpyrrolidone) solid dispersions, J. Pharm. Sci. 93 (2004) 384–391. https://doi.org/10.1002/jps.10526.

[38] S.L. Shamblin, B.C. Hancock, Y. Dupuis, M.J. Pikal, Interpretation of relaxation time constants for amorphous pharmaceutical systems, J. Pharm. Sci. 89 (2000). https://doi.org/10.1002/(SICI)1520-6017(200003)89:3<417::AID-JPS12>3.0.CO;2-V.

[39] G.P. Johari, M. Goldstein, Viscous Liquids and the Glass Transition. II. Secondary Relaxations in Glasses of Rigid Molecules, J. Chem. Phys. 53 (1970) 2372–2388. https://doi.org/10.1063/1.1674335.

[40] G.P. Johari, Intrinsic mobility of molecular glasses, J. Chem. Phys. 58 (1973) 1766–1770. https://doi.org/10.1063/1.1679421.

[41] S.P. Bhardwaj, K.K. Arora, E. Kwong, A. Templeton, S.-D. Clas, R. Suryanarayanan, Correlation between molecular mobility and physical stability of amorphous itraconazole, Mol. Pharm. 10 (2013) 694–700. https://doi.org/10.1021/mp300487u.

[42] D.W. Oxtoby, Homogeneous nucleation: theory and experiment, J. Phys. Condens. Matter. 4 (1992) 7627–7650. https://doi.org/10.1088/0953-8984/4/38/001.

[43] S.P. Bhardwaj, R. Suryanarayanan, Molecular Mobility as an Effective Predictor of the Physical Stability of Amorphous Trehalose, Mol. Pharm. 9 (2012) 3209–3217. https://doi.org/10.1021/mp300302g.

[44] C. Bhugra, R. Shmeis, S.L. Krill, M.J. Pikal, Prediction of Onset of Crystallization from Experimental Relaxation Times. II. Comparison between Predicted and Experimental Onset Times, J. Pharm. Sci. 97 (2008) 455–472. https://doi.org/10.1002/jps.21162.

[45] A.K.R. Dantuluri, A. Amin, V. Puri, A.K. Bansal, Role of α-Relaxation on Crystallization of Amorphous Celecoxib above Tg Probed by Dielectric Spectroscopy, Mol. Pharm. 8 (2011) 814–822. https://doi.org/10.1021/mp100411v.

[46] S. Bhattacharya, R. Suryanarayanan, Local Mobility in Amorphous Pharmaceuticals—Characterization and Implications on Stability, J. Pharm. Sci. 98 (2009) 2935–2953. https://doi.org/https://doi.org/10.1002/jps.21728.

[47] A. Newman, J.E. Hastedt, M. Yazdanian, New directions in pharmaceutical amorphous materials and amorphous solid dispersions, a tribute to Professor George Zografi – Proceedings of the June 2016 Land O'Lakes Conference, AAPS Open. 3 (2017). https://doi.org/10.1186/s41120-017-0017-6.

[48] H. Tanaka, Relation between Thermodynamics and Kinetics of Glass-Forming Liquids, Phys. Rev. Lett. 90 (2003). https://doi.org/10.1103/physrevlett.90.055701.

[49] G.R. Thuduppathy, R. Blake Hill, Applications of NMR Spin Relaxation Methods for Measuring Biological Motions, Methods Enzymol. (2004) 243–264. https://doi.org/10.1016/s0076-6879(04)84015-1.

[50] T.A. Ezquerra, J. Majszczyk, F.J. Baltà-Calleja, E. López-Cabarcos, K.H. Gardner, B.S. Hsiao, Molecular dynamics of the \ensuremath{\alpha} relaxation during crystallization of a glassy polymer: A real-time dielectric spectroscopy study, Phys. Rev. B. 50 (1994) 6023–6031. https://doi.org/10.1103/PhysRevB.50.6023.

[51] F. Kremer *et al.,* Broadband dielectric spectroscopy, Springer, Berlin; New York, 2003.

[52] S.P. Bhardwaj, R. Suryanarayanan, Use of dielectric spectroscopy to monitor molecular mobility in glassy and supercooled trehalose, J. Phys. Chem. B. 116 (2012) 11728–11736. https://doi.org/10.1021/jp303317p.

[53] F. Kremer, Dielectric spectroscopy – yesterday, today and tomorrow, J. Non. Cryst. Solids. 305 (2002) 1–9. https://doi.org/https://doi.org/10.1016/S0022-3093(02)01083-9.

[54] J. Alie, J. Menegotto, P. Cardon, H. Duplaa, A. Caron, C. Lacabanne, M. Bauer, Dielectric study of the molecular mobility and the isothermal crystallization kinetics of an amorphous pharmaceutical drug substance, J. Pharm. Sci. 93 (2004) 218–233. https://doi.org/10.1002/jps.10520.

[55] N.T. Correia, J.J. Ramos, M. Descamps, G. Collins, Molecular mobility and fragility in indomethacin: a thermally stimulated depolarization current study, Pharm. Res. 18 (2001) 1767–1774. https://doi.org/10.1023/a:1013339017070.

[56] K. Kothari, V. Ragoonanan, R. Suryanarayanan, The Role of Drug–Polymer Hydrogen Bonding Interactions on the Molecular Mobility and Physical Stability of Nifedipine Solid Dispersions, Mol. Pharm. 12 (2015) 162–170. https://doi.org/10.1021/mp5005146.

[57] A. Afzal, M.S. Thayyil, P.A. Sivaramakrishnan, S. Urpayil, S. Capaccioli, Molecular dynamics in the supercooled liquid and glassy states of bezafibrate and binary mixture of fenofibrate, J. Non. Cryst. Solids. 550 (2020) 120407. https://doi.org/10.1016/j.jnoncrysol.2020.120407.

[58] K.P. Safna Hussan, M.S. Thayyil, A. Poulose, K.L. Ngai, Glassy Dynamics and Translational–Rotational Coupling of an Ionically Conducting Pharmaceutical Salt-Sodium Ibuprofen, J. Phys. Chem. B. 123 (2019) 7764–7770. https://doi.org/10.1021/acs.jpcb.9b06478.

[59] K.K Thasneema, M.S. Thayyil, T. Rosalin, K.K. Elyas, T. Dipin, P.K. Sahu, N.S. Krishna Kumar, V.C. Saheer, M. Messali, T. Ben Hadda, Thermal and spectroscopic investigations on three phosphonium based ionic liquids for industrial and biological applications, J. Mol. Liq. 307 (2020) 112960. https://doi.org/https://doi.org/10.1016/j.molliq.2020.112960.

[60] K.L. Ngai, Why the glass transition problem remains unsolved?, J. Non. Cryst. Solids. 353 (2007) 709–718. https://doi.org/https://doi.org/10.1016/j.jnoncrysol.2006.12.033.

[61] K. Ngai L., Structural relaxation and conductivity relaxation in glassy ionics, J. Phys. IV Fr. 02 (1992) C2-61-C2-73. https://doi.org/10.1051/jp4:1992207.

[62] Safna Hussan K. P, M.S. Thayyil, S.K. Deshpande, J. T. V, M. K, K.L. Ngai, Molecular dynamics and the translational–rotational coupling of an ionically conducting glass-former: amlodipine besylate, RSC Adv. 8 (2018) 20630–20636. https://doi.org/10.1039/C8RA01544A.

[63] B. Schammé, M. Mignot, N. Couvrat, V. Tognetti, L. Joubert, V. Dupray, L. Delbreilh, E. Dargent, G. Coquerel, Molecular Relaxations in Supercooled Liquid and Glassy States of Amorphous Quinidine: Dielectric Spectroscopy and Density Functional Theory Approaches, J. Phys. Chem. B. 120 (2016) 7579–7592. https://doi.org/10.1021/acs.jpcb.6b04242.

[64] J. Cao, Q. Ren, F. Chen, T. Lu, Comparative study on the methods for predicting the reactive site of nucleophilic reaction, Sci. China Chem. 58 (2015) 1845–1852. https://doi.org/10.1007/s11426-015-5494-7.

[65] J. Lorenc, I. Bryndal, M. Marchewka, E. Kucharska, T. Lis, J. Hanuza, Crystal

and molecular structure of 2-amino-5-chloropyridinium hydrogen selenate—its IR and Raman spectra, DFT calculations and physicochemical properties, J. Raman Spectrosc. 39 (2008) 863–872. https://doi.org/https://doi.org/10.1002/jrs.1925.

[66] H. Can, A Computational Investigation for the Chiral Chromatographic Separation of benzimidazole type sulphoxides, Turkish J. Chem. 27 (2003) 553–564.

[67] S. Belaidi, A. Dibi, M. Omari, A conformational exploration of dissymmetric macrolides antibiotics, Turkish J. Chem. 26 (2002) 26,491-500.

[68] L. Demir, N.M. Godjaev, Conformational analysis of Pol-RFamide II (Glu(1)-Trp(2)-Leu(3)-Lys(4)-Gly(5)-Arg(6)-Phe(7)-NH_2) heptapeptide, 26 (2002) 825–831.

[69] F. Bray, J. Ferlay, I. Soerjomataram, R.L. Siegel, L.A. Torre, A. Jemal, Global cancer statistics 2018: GLOBOCAN estimates of incidence and mortality worldwide for 36 cancers in 185 countries, CA. Cancer J. Clin. 68 (2018) 394–424. https://doi.org/https://doi.org/10.3322/caac.21492.

[70] N. Mollakhalili Meybodi, A.M. Mortazavian, A. Bahadori Monfared, S. Sohrabvandi, F. Aghaei Meybodi, Phytochemicals in Cancer Prevention: A Review of the Evidence, Iran. J. Cancer Prev. 10 (2017) e7219. https://doi.org/10.17795/ijcp-7219.

[71] A.-K. Yang, S.-M. He, L. Liu, J.-P. Liu, Q. Wei, S. Zhou, Herbal Interactions with Anticancer Drugs: Mechanistic and Clinical Considerations, Curr. Med. Chem. 17 (2010) 1635–1678. https://doi.org/10.2174/092986710791111279.

[72] N. Islam, S. Niaz, T. Manzoor, A.H. Pandith, Theoretical investigations into spectral and non-linear optical properties of brucine and strychnine using density functional theory, Spectrochim. Acta. A. Mol. Biomol. Spectrosc. 131 (2014) 461–470. https://doi.org/10.1016/j.saa.2014.04.089.

[73] A.G. Desai, G.N. Qazi, R.K. Ganju, M. El-Tamer, J. Singh, A.K. Saxena, Y.S. Bedi, S.C. Taneja, H.K. Bhat, Medicinal plants and cancer chemoprevention, Curr. Drug Metab. 9 (2008) 581–591. https://doi.org/10.2174/138920008785821657.

[74] B. Patwardhan, D. Warude, P. Pushpangadan, N. Bhatt, Ayurveda and

traditional Chinese medicine: a comparative overview, Evid. Based. Complement. Alternat. Med. 2 (2005) 465–473. https://doi.org/10.1093/ecam/neh140.

[75] Shu-Yi Yin, Wen-Chi Wei, Feng-Yin Jian, Ning-Sun Yang, "Therapeutic Applications of Herbal Medicines for Cancer Patients", Evidence-Based Complementary and Alternative Medicine, vol. 2013, Article ID 302426, 15 pages, (2013). https://doi.org/10.1155/2013/302426.

[76] K. Hedigan, Herbal medicine reduces chemotherapy toxicity, Nat. Rev. Drug Discov. 9 (2010) 765. https://doi.org/10.1038/nrd3280.

[77] S. Shukla, A. Mehta, Anticancer potential of medicinal plants and their phytochemicals: a review, Brazilian J. Bot. 38 (2015). https://doi.org/10.1007/s40415-015-0135-0.

[78] A. Kumar, P.R. Sharma, D.M. Mondhe, Potential anticancer role of colchicine-based derivatives: an overview., Anticancer. Drugs. 28 (2017) 250–262. https://doi.org/10.1097/CAD.0000000000000464.

[79] J.-M. Qin, P.-H. Yin, Q. Li, Z.-Q. Sa, X. Sheng, L. Yang, T. Huang, M. Zhang, K.-P. Gao, Q.-H. Chen, J.-W. Ma, H.-B. Shen, Anti-tumor effects of brucine immuno-nanoparticles on hepatocellular carcinoma, Int. J. Nanomedicine. 7 (2012) 369–379. https://doi.org/10.2147/IJN.S27226.

[80] M. Serasanambati, S.R. Chilakapati, P.K. Manikonda, J.R. Kanala, D.R. Chilakapati, Anticancer effects of brucine and gemcitabine combination in MCF-7 human breast cancer cells, Nat. Prod. Res. 29 (2015) 484–490. https://doi.org/10.1080/14786419.2014.951932.

[81] G.P. Johari, S. Kim, R. Shanker, Dielectric Studies of Molecular Motions in Amorphous Solid and Ultraviscous Acetaminophen, J. Pharm. Sci. 94 (2005) 2207–2223. https://doi.org/10.1002/jps.20455.

[82] A.R. Brás, J.P. Noronha, A.M.M. Antunes, M.M. Cardoso, A. Schönhals, F. Affouard, M. Dionísio, N.T. Correia, Molecular Motions in Amorphous Ibuprofen As Studied by Broadband Dielectric Spectroscopy, J. Phys. Chem. B. 112 (2008) 11087–11099. https://doi.org/10.1021/jp8040428.

[83] K. Adrjanowicz, K. Kaminski, Z. Wojnarowska, M. Dulski, L. Hawelek, S. Pawlus, M. Paluch, W. Sawicki, Dielectric Relaxation and Crystallization Kinetics of Ibuprofen at Ambient and Elevated Pressure, J. Phys. Chem. B. 114 (2010) 6579–6593. https://doi.org/10.1021/jp910009b.

[84] R. Böhmer, T. Goresy, Dielectric relaxation processes in solid and supercooled liquid solutions of acetaminophen and nifedipine, J. Phys. Condens. Matter. 19 (2007). https://doi.org/10.1088/0953-8984/19/20/205134.

[85] A.C. Rodrigues, M.T. Viciosa, F. Danède, F. Affouard, N.T. Correia, Molecular Mobility of Amorphous S-Flurbiprofen: A Dielectric Relaxation Spectroscopy Approach, Mol. Pharm. 11 (2014) 112–130. https://doi.org/10.1021/mp4002188.

[86] K. Adrjanowicz, M. Paluch, K. Ngai, Determining the structural relaxation times deep in the glassy state of the pharmaceutical Telmisartan, J. Phys. Condens. Matter. 22 (2010) 125902. https://doi.org/10.1088/0953-8984/22/12/125902.

[87] Z. Wojnarowska, K. Adrjanowicz, P. Wlodarczyk, E. Kaminska, K. Kaminski, K. Grzybowska, R. Wrzalik, M. Paluch, K.L. Ngai, Broadband Dielectric Relaxation Study at Ambient and Elevated Pressure of Molecular Dynamics of Pharmaceutical: Indomethacin, J. Phys. Chem. B. 113 (2009) 12536–12545. https://doi.org/10.1021/jp905162r.

[88] K. Adrjanowicz, D. Zakowiecki, K. Kaminski, L. Hawelek, K. Grzybowska, M. Tarnacka, M. Paluch, K. Cal, Molecular dynamics in supercooled liquid and glassy states of antibiotics: azithromycin, clarithromycin and roxithromycin studied by dielectric spectroscopy. Advantages given by the amorphous state., Mol. Pharm. 9 (2012) 1748–1763. https://doi.org/10.1021/mp300067r.

[89] Z. Wojnarowska, K. Grzybowska, L. Hawelek, A. Swiety-Pospiech, E. Masiewicz, M. Paluch, W. Sawicki, A. Chmielewska, P. Bujak, J. Markowski, Molecular Dynamics Studies on the Water Mixtures of Pharmaceutically Important Ionic Liquid Lidocaine HCl, Mol. Pharm. 9 (2012) 1250–1261. https://doi.org/10.1021/mp2005609.

[90] A. Alhalaweh, A. Alzghoul, D. Mahlin, C.A.S. Bergström, Physical stability of drugs after storage above and below the glass transition temperature: Relationship to glass-forming ability, Int. J. Pharm. 495 (2015) 312–317. https://doi.org/https://doi.org/10.1016/j.ijpharm.2015.08.101.

[91] U. Sailaja, M. Shahin Thayyil, N.S. Krishna Kumar, G. Govindaraj, K.L. Ngai, Molecular mobility in the supercooled and glassy states of nizatidine and perphenazine, Eur. J. Pharm. Sci. 99 (2017) 147–151. https://doi.org/ https://doi.org/ 10.1016/ j.ejps.2016.11.024.

[92] U. Sailaja, M.S. Thayyil, N.S.K. Kumar, G. Govindaraj, Molecular dynamics of amorphous pharmaceutical fenofibrate studied by broadband dielectric spectroscopy., J. Pharm. Anal. 6 (2016) 165–170. https://doi.org/10.1016/ j.jpha.2014.09.003.

[93] S. Urpayil, M .Shahin Thayyil, Dielectric and Spectroscopic Investigations of Amorphous Captopril, IOSR J. Pharm. 2 (2012) 479–484. https://doi.org/ 10.9790/3013-0230479484.

[94] J. Knapik-Kowalczuk, Z. Wojnarowska, M. Rams-Baron, K. Jurkiewicz, J. Cielecka-Piontek, K.L. Ngai, M. Paluch, Atorvastatin as a Promising Crystallization Inhibitor of Amorphous Probucol: Dielectric Studies at Ambient and Elevated Pressure, Mol. Pharm. 14 (2017) 2670–2680. https://doi.org/ 10.1021/acs.molpharmaceut.7b00152.

[95] Z. Wojnarowska, A. Swiety-Pospiech, K. Grzybowska, L. Hawelek, M. Paluch, K.L. Ngai, Fundamentals of ionic conductivity relaxation gained from study of procaine hydrochloride and procainamide hydrochloride at ambient and elevated pressure., J. Chem. Phys. 136 (2012) 164507. https://doi.org/ 10.1063/1.4705274.

[96] K. Adrjanowicz, K. Kaminski, P. Wlodarczyk, K. Grzybowska, M. Tarnacka, D. Zakowiecki, G. Garbacz, M. Paluch, S. Jurga, Molecular Dynamics of the Supercooled Pharmaceutical Agent Posaconazole Studied via Differential Scanning Calorimetry and Dielectric and Mechanical Spectroscopies, Mol. Pharm. 10 (2013) 3934–3945. https://doi.org/10.1021/mp4003915.

[97] G. Shete, K.S. Khomane, A.K. Bansal, Molecular Relaxation Behaviour and Isothermal Crystallization above Glass Transition Temperature of Amorphous Hesperetin, J. Pharm. Sci. 103 (2014) 167–178. https://doi.org/https://doi.org/10.1002/jps.23766.

[98] J. Knapik-Kowalczuk, W. Tu, K. Chmiel, M. Rams-Baron, M. Paluch, Co-Stabilization of Amorphous Pharmaceuticals—The Case of Nifedipine and Nimodipine, Mol. Pharm. 15 (2018) 2455–2465. https://doi.org/10.1021/acs.molpharmaceut.8b00308.

[99] K. Kolodziejczyk, M. Paluch, K. Grzybowska, A. Grzybowski, Z. Wojnarowska, L. Hawelek, J. Ziolo, Relaxation Dynamics and Crystallization Study of Sildenafil in the Liquid and Glassy States, Mol. Pharm. 10 (2013). https://doi.org/10.1021/mp300479r.

[100] M.C. Flores, E.A. Márquez, J.R. Mora, Molecular modelling studies of bromopyrrole alkaloids as potential antimalarial compounds: a DFT approach, Med.Chem.Res. 27 (2018) 844–856.https://doi.org/10.1007/s00044-017-2107-3.

[101] W.J. Hehre, A Guide to Molecular Mechanics and Quantum Chemical Calculations, Wavefunction, 2003.

[102] E.J. Baerends, O. V Gritsenko, A Quantum Chemical View of Density Functional Theory, J. Phys. Chem. A. 101 (1997) 5383–5403. https://doi.org/10.1021/jp9703768.

[103] C. James, C. Ravikumar, V.S. Jayakumar, I. Hubert Joe, Vibrational spectra and potential energy distributions for 1-benzyl-1H-imidazole by normal coordinate analysis, J. Raman Spectrosc. 40 (2009) 537–545. https://doi.org/https://doi.org/10.1002/jrs.2160.

[104] R.A. Costa, E.S.A. Junior, G.B.P. Lopes, M.L.B. Pinheiro, E. V Costa, D.P. Bezerra, K. Oliveira, Structural, vibrational, UV–vis, quantum-chemical properties, molecular docking and anti-cancer activity study of annomontine and N-hydroxyannomontine β-carboline alkaloids: A combined experimental and DFT approach, J. Mol. Struct. 1171 (2018) 682–695. https://doi.org/https://doi.org/10.1016/j.molstruc.2018.06.054.

[105] B. Sureshkumar, Y.S. Mary, C.Y. Panicker, S. Suma, S. Armaković, S.J.

Armaković, C. Van Alsenoy, B. Narayana, Quinoline derivatives as possible lead compounds for anti-malarial drugs: Spectroscopic, DFT and MD study, Arab. J. Chem. 13 (2020) 632–648. https://doi.org/https://doi.org/10.1016/j.arabjc.2017.07.006.

[106] M.M. Ramla, M.A. Omar, A.-M.M. El-Khamry, H.I. El-Diwani, Synthesis and antitumor activity of 1-substituted-2-methyl-5-nitrobenzimidazoles, Bioorg. Med. Chem. 14 (2006) 7324–7332. https://doi.org/https://doi.org/10.1016/j.bmc.2006.06.033.

[107] Y.-H. Yang, M.-S. Cheng, Q.-H. Wang, H. Nie, N. Liao, J. Wang, H. Chen, Design, synthesis, and anti-tumor evaluation of novel symmetrical bis-benzimidazoles, Eur. J. Med. Chem. 44 (2009) 1808–1812. https://doi.org/https://doi.org/10.1016/j.ejmech.2008.07.021.

[108] P.B. Nagabalasubramanian, S. Periandy, S. Mohan, Ab initio HF and DFT simulations, FT-IR and FT-Raman vibrational analysis of α-chlorotoluene, Spectrochim. Acta Part A Mol. Biomol. Spectrosc. 77 (2010) 150–159. https://doi.org/https://doi.org/10.1016/j.saa.2010.04.043.

[109] P. Lunkenheimer, U. Schneider, R. Brand, A. Loid, Glassy dynamics, Contemp. Phys. 41 (2000) 15–36. https://doi.org/10.1080/001075100181259.

[110] P.W. Anderson, Through the Glass Lightly, Science (80-.). 267 (1995) 1611 LP – 1611. https://doi.org/10.1126/science.267.5204.1611-e.

[111] R.S. Stearns, I.N. Duling, R.H. Johnson, Relationship of Glass Transition Temperature to Viscosity-Temperature Characteristics of Lubricants, I&EC Prod. Res. Dev. 5 (1966) 306–313. https://doi.org/10.1021/i360020a002.

[112] M.G. Abiad, M.T. Carvajal, O.H. Campanella, A Review on Methods and Theories to Describe the Glass Transition Phenomenon: Applications in Food and Pharmaceutical Products, Food Eng. Rev. 1 (2009) 105–132. https://doi.org/10.1007/s12393-009-9009-1.

[113] L.-M. Wang, R. Liu, W.H. Wang, Relaxation time dispersions in glass forming metallic liquids and glasses, J. Chem. Phys. 128 (2008) 164503. https://doi.org/10.1063/1.2904559.

[114] T.S. Chow, Molecular kinetic theory of the glass transition, Polym. Eng. Sci. 24 (1984) 1079–1086. https://doi.org/https://doi.org/10.1002/pen.760241403.

[115] P.B. Moin, Ehrenfest equations for second-order phase transition under hydrostatic and uniaxial stresses, Phase Transitions. 89 (2016) 1074–1077. https://doi.org/10.1080/01411594.2016.1146951.

[116] J.W.P. Schmelzer, I. Gutzow, The Prigogine-Defay ratio revisited, J. Chem. Phys. 125 (2006) 184511. https://doi.org/10.1063/1.2374894.

[117] F.H. Stillinger, P.G. Debenedetti, T.M. Truskett, The Kauzmann Paradox Revisited, J. Phys. Chem. B. 105 (2001) 11809–11816. https://doi.org/10.1021/jp011840i.

[118] K.A. Graeser, J.E. Patterson, J.A. Zeitler, T. Rades, The Role of Configurational Entropy in Amorphous Systems, Pharmaceutics. 2 (2010) 224–244. https://doi.org/ 10.3390/pharmaceutics2020224.

[119] N. Tomoshige, H. Mizuno, T. Mori, K. Kim, N. Matubayasi, Boson peak, elasticity, and glass transition temperature in polymer glasses: Effects of the rigidity of chain bending, Sci. Rep. 9 (2019) 19514. https://doi.org/10.1038/s41598-019-55564-2.

[120] G. Williams, D.C. Watts, Non-symmetrical dielectric relaxation behaviour arising from a simple empirical decay function, Trans. Faraday Soc. 66 (1970) 80–85. https://doi.org/10.1039/TF9706600080.

[121] R.M. Hill, L.A. Dissado, Debye and non-Debye relaxation, J. Phys. C Solid State Phys. 18 (1985) 3829–3836. https://doi.org/10.1088/0022-3719/18/19/021.

[122] J.C. Mauro, Y.Z. Mauro, On the Prony series representation of stretched exponential relaxation, Phys. A Stat. Mech. Its Appl. 506 (2018) 75–87. https://doi.org/https://doi.org/10.1016/j.physa.2018.04.047.

[123] M. Ediger, Ediger, M. D. Spatially Heterogeneous Dynamics in Supercooled Liquids. Ann. Rev. Phys. Chem. 51, 99-128, Annu. Rev. Phys. Chem. 51 (2000) 99–128. https://doi.org/10.1146/annurev.physchem.51.1.99.

[124] K. V Edmond, M.T. Elsesser, G.L. Hunter, D.J. Pine, E.R. Weeks, Decoupling of rotational and translational diffusion in supercooled colloidal fluids, Proc. Natl. Acad. Sci. 109 (2012) 17891 LP – 17896. https://doi.org/10.1073/pnas.1203328109.

[125] S. Vivek, E. Weeks, Decoupling of translational and rotational diffusion in quasi-2D colloidal fluids, J. Chem. Phys. 147 (2017). https://doi.org/10.1063/1.4996733.

[126] R. Richert, K. Duvvuri, L.-T. Duong, Dynamics of glass-forming liquids. VII. Dielectric relaxation of supercooled tris-naphthylbenzene, squalane, and decahydroisoquinoline, J. Chem. Phys. 118 (2003) 1828–1836. https://doi.org/10.1063/1.1531587.

[127] K.L. Ngai, Alternative Explanation of the Difference between Translational Diffusion and Rotational Diffusion in Supercooled Liquids, J. Phys. Chem. B. 103 (1999) 10684–10694. https://doi.org/10.1021/jp990554s.

[128] M. Paluch, S. Pawlus, C.M. Roland, Pressure and Temperature Dependence of the α-Relaxation in Poly(methyltolylsiloxane), Macromolecules. 35 (2002) 7338–7342. https://doi.org/10.1021/ma020587x.

[129] R. Levit, J.C. Martinez-Garcia, D.A. Ochoa, J.E. García, The generalized Vogel-Fulcher-Tamman equation for describing the dynamics of relaxor ferroelectrics, Sci. Rep. 9 (2019) 12390. https://doi.org/10.1038/s41598-019-48864-0.

[130] E.D. Zanotto, D.R. Cassar, The microscopic origin of the extreme glass-forming ability of Albite and B2O3, Sci. Rep. 7 (2017) 43022. https://doi.org/10.1038/srep43022.

[131] M. Vogel, E. Rössler, Slow β process in simple organic glass formers studied by one-and two-dimensional 2H nuclear magnetic resonance. I, Chem. Phys. - CHEM PHYS. 114 (2001) 5802–5815. https://doi.org/10.1063/1.1351159.

[132] K. Ngai, P. Lunkenheimer, C. Leon, U. Schneider, R. Brand, A. Loidl, Nature and properties of the Johari–Goldstein-relaxation in the equilibrium liquid state of a class of glass-formers, J. Chem. Phys. 115 (2001) 1405–1413. https://doi.org/10.1063/1.1381054.

[133] M.S. Thayyil, S. Capaccioli, D. Prevosto, K.L. Ngai, Is the Johari-Goldstein β-relaxation universal? Philos. Mag. 88 (2008) 4007–4013. https://doi.org/10.1080/14786430802270082.

[134] A. Dokoumetzidis, V. Papadopoulou, P. Macheras, Analysis of dissolution data using modified versions of Noyes-Whitney equation and the Weibull function, Pharm. Res. 23 (2006) 256–261. https://doi.org/10.1007/s11095-006-9093-3.

[135] A. Newman, Pharmaceutical amorphous solid dispersions, 2015.

[136] S.P. Chamarthy, R. Pinal, The nature of crystal disorder in milled pharmaceutical materials, Colloids Surfaces A Physicochem. Eng. Asp. 331 (2008) 68–75. https://doi.org/https://doi.org/10.1016/j.colsurfa.2008.06.040.

[137] S.B. Murdande, M.J. Pikal, R.M. Shanker, R.H. Bogner, Solubility Advantage of Amorphous Pharmaceuticals: II. Application of Quantitative Thermodynamic Relationships for Prediction of Solubility Enhancement in Structurally Diverse Insoluble Pharmaceuticals, Pharm. Res. 27 (2010) 2704–2714. https://doi.org/ 10.1007/s11095-010-0269-5.

[138] K.L. Ngai, J.H. Magill, D.J. Plazek, Flow, diffusion and crystallization of supercooled liquids: Revisited, J. Chem. Phys. 112 (2000) 1887–1892. https://doi.org/10.1063/1.480752.

[139] M. Mehta, S.P. Bhardwaj, R. Suryanarayanan, Controlling the physical form of mannitol in freeze-dried systems, Eur. J. Pharm. Biopharm. 85 (2013) 207–213. https://doi.org/https://doi.org/10.1016/j.ejpb.2013.04.010.

[140] S. Bhattacharya, R. Suryanarayanan, Molecular Motions in Sucrose-PVP and Sucrose-Sorbitol Dispersions: I. Implications of Global and Local Mobility on Stability, Pharm.Res.28 (2011) 2191–2203. https://doi.org/10.1007/s11095-011-0447-0.

[141] M. Mehta, V. Ragoonanan, G.B. McKenna, R. Suryanarayanan, Correlation between Molecular Mobility and Physical Stability in Pharmaceutical Glasses, Mol. Pharm. 13 (2016) 1267–1277. https://doi.org/10.1021/ acs.molpharmaceut. 5b00853.

[142] B. Chandralekha, R. Hemamalini, S. Muthu, S. Sevvanthi, Spectroscopic (FT-IR, FT-RAMAN, NMR, UV–Vis) investigations, computational analysis and molecular docking study of 5-bromo-2-hydroxy pyrimidine, J.Mol.Struct. 1218 (2020)128494.https://doi.org/https://doi.org/10.1016/j.molstruc.2020. 128494.

[143] C. Shende, W. Smith, C. Brouillette, S. Farquharson, Drug stability analysis by

Raman spectroscopy, Pharmaceutics. 6 (2014) 651–662. https://doi.org/10.3390/pharmaceutics6040651.

[144] A.H. Mazurek, Ł. Szeleszczuk, D.M. Pisklak, Periodic DFT Calculations—Review of Applications in the Pharmaceutical Sciences, Pharm. . 12 (2020). https://doi.org/10.3390/pharmaceutics12050415.

[145] M. Hoffmann, J. Rychlewski, Density Functional Theory (DFT) and Drug Design, in: 2002: pp. 1767–1803. https://doi.org/10.1142/9789812775702_0058.

CHAPTER 2
THEORETICAL AND EXPERIMENTAL OVERVIEW

2.1 Introduction

Despite years of research into various theories and models to clarify the fundamental existence of the glass transition, the phenomenon of the glass transition remains a mystery [1]. Even though several models have been developed to explain dynamical slowing in the vicinity of the glass transition, none of them has been effective in capturing all of its aspects. In terms of optimal storage conditions, evaluating T_g is an important part of amorphous solids classification, and its value must be determined in detail. The transition to the glass state has an impact on the system's physical properties, especially the dynamics of relaxation of certain macroscopic observables including polarization and density fluctuation. It's vital to be able to examine the dynamics of relaxation through several observables because it helps you to equate their complex properties and personalize the universal characteristics.

Amorphous pharmaceuticals is considered to be a promising solution to the problem of low solubility of poorly water soluble pharmaceuticals. In the amorphous state, molecular mobility, which includes both global and local motions, has been proposed as a major factor governing crystallization as well as accelerating chemical reactivity[2]. Global motions, also known as primary, structural, or α-relaxation motions, are cooperative. Local motions or secondary relaxations are fast non-cooperative motions that originate from a part of a molecule or involve the entire molecule. This study focuses solely on structural relaxation, with a particular emphasis on the glassy state.

The structure evolves continuously towards equilibrium in the glassy state, and the relaxation time is a measure of the system's mobility. Physical aging is a term that is used to describe this phenomenon. It has long been known that structural relaxation affects material properties in polymers, ceramics, and gels. Several excellent reviews have been written on the theoretical and phenomenological aspects of structural relaxation. In the pharmaceutical literature, this topic has recently received a lot of attention. In the supercooled state, several groups have found a link between relaxation time and crystallization behaviour. Amorphous pharmaceuticals must be stored below the glass transition temperature to maintain their desired stability. As a result, assessing such correlations in a glassy state is extremely useful. However, experimentally characterizing structural relaxation is difficult due to the extremely long-timescale of

these motions and the non-ergodic nature of glasses. It's also important to understand that structural relaxation is non-linear, non-exponential, and time-dependent. Calorimetric approaches, which are widely used in pharmaceuticals, do not always capture the consequences of these properties. Mao *et al*. [3] recently developed a simulation model to estimate relaxation times based on heat capacity measurements. This, however, does not provide a direct indication of relaxation time. Direct experimental measurement of structural relaxation time is required to investigate the potential correlation between structural relaxation and other properties of practical interest. This work, on the other hand, is extremely difficult because it necessitates the ability and willingness to use a range of experimental methods to quantify different observables. Broadband dielectric spectroscopy is used in this study to measure the relaxation dynamics of polarization caused in the device by an external electric field, and it is sensitive to the orientation polarization due to permanent molecular dipoles. Furthermore, two anti-cancerous alkaloids brucine and colchicine are characterized by experimental and theoretical DFT methods. This chapter is divided into two parts. The first part is devoted to the description of the theoretical approaches for dielectric spectroscopy and DFT, and the second part is devoted to the experimental approaches.

2.2 Theoretical models of dielectric relaxation

Two methods were mainly proposed: free volume and entropy-based models. In general, free-volume models acknowledge that molecules need free space in their vicinity to rearrange. As a result, as the temperature drops, the amount of free space available for molecules to rearrange decreases.

2.2.1 Free volume approach

Doolittle proposed the idea of the free volume in 1951[4]. The slowing of molecular motion on cooling is explained by the decrease in free volume when you approach the glass transition area. Doolittle simplified this character by using the equation that relates viscosity and free volume. The free volume f, available for translational molecular motion, is related to the internal mobility of molecular systems expressed as viscosity, according to this theory. Following that, within the free volume model, Doolittle's fluidity equation is given by

$$\eta = Ae^{B(\frac{V-V_f}{V_f})} \tag{2.1}$$

where η corresponds to the viscosity, A and B are the fitting parameters, V is the total specific volume and V_f is the free volume per molecule

Consider a glassy state, Let v represent the volume per molecule, and v_o represent the volume per molecule except for all other molecules. The excess volume, $v-v_o$, grows as the temperature rises. Packing restrictions place a significant energy penalty on any non-uniform redistribution of excess volume at very low temperatures. As a result of the increased anharmonicity in the vibrational motion of molecules around an essentially fixed value caused by thermal expansion, the excess volume is uniformly distributed. Furthermore, because the volume change is not accompanied by randomization of molecular motion, the entropy rises. Once $v-v_o$ reaches a critical value, any additional volume can be redistributed at random without incurring an energy penalty. The free volume v_f is the portion of the excess volume that can be distributed randomly without incurring an energy cost.

$$v - v_0 = v_f + \Delta v_c \tag{2.2}$$

where Δv_c is that part of the thermal expansion that cannot be randomly distributed. The entropy is increased significantly by the randomization of molecular motion caused by the redistribution of free volume. The ideal glass transition occurs when $v_f = 0$ and therefore $v - v_0 = \Delta v_c$. For laboratory transition, $v_f > 0$. In a dense liquid, molecules are encased in a cage formed by their immediate neighbours. Occasionally, spontaneous density fluctuations result in the formation of holes within a cage large enough to allow the trapped central molecules to be displaced. Only if another molecule occupies the hole before the first one can return to its original position can diffusive motion occur. The relationship between translational diffusion coefficient and free volume is the main result of Cohein-Turnbull theory. Denoting the free volume associated with a given molecule as v', the translational diffusion coefficient is written as a sum over all possible contributions from molecules having different available free volumes:

$$\mathbf{D} = \int_{\mathbf{v}^*}^{\infty} \mathbf{D(v)P(v')dv'} = \mathbf{gu} \int_{\mathbf{v}^*}^{\infty} \mathbf{a(v')p(v')dv'} \tag{2.3}$$

where D($v^{'}$) is the contribution to the translational diffusion coefficient due to molecules having free volume $v^{'}$ and $v^{'}$+ d$v^{'}$; a($v^{'}$) is the length scale indicative of the cage diameter corresponding to a molecule having free volume $v^{'}$, u is the thermal velocity [u≈$(\frac{K_BT}{m})^{\frac{1}{2}}$, with m the molecular mass]; g is a geometrical factor, and v^* is the minimum free volume capable of accommodating another molecule after the original displacement in the cage. The function P(v) is calculated as

$$\boldsymbol{P(v^{'}) = \frac{\gamma}{v_f}\exp\left(-\frac{\gamma v^{'}}{v_f}\right)} \tag{2.4}$$

Since D($v^{'}$) varies more slowly than $P(v^{'})$, and in general $v^{*} \gg v_f$, we can write

$$\boldsymbol{D = \int_{v^*}^{\infty} D(v)P(v^{'})dv^{'} \approx D(v^*)\int_{v^*}^{\infty} P(v)P(v^{'})dv^{'}} \tag{2.5}$$

$$\boldsymbol{= ga^* u exp\left(-\frac{\gamma v^{'}}{v_f}\right)}$$

Where, consistently with the interpretation given to v, we take a^* to be of the order of the molecular diameter. The free volume expression predicts that D has no more free volume available for random redistribution (v_f=0). Eq;(2.4)) is related to the empirical Doolittle equation, proposed originally to describe fluidity,η^{-1}

$$\boldsymbol{\eta^{-1} = A\exp\left(-\frac{bv_0}{v_f}\right)} \tag{2.6}$$

Where A and D are constants, v_0 and v_f are the occupied and free volume per molecule, respectively; and the implied inverse relationship between translational diffusion and viscosity follows from the Stokes-Einstein equation, D = $\frac{K_B T}{6\pi a\eta}$ in which a is the molecular diameter.

2.2.2 Adam-Gibb's Theory Approach

In practice, the free volume approach was used to explain strong temperature-dependent changes using the Williams-L and el-Ferry relationship [5](WLF). Free-volume models have received a lot of criticism because they ignore the role of thermodynamics. Not everything could be explained as a function of volume in this way. Furthermore, pressure experiments reveal that volume is not the only dominant

control variable[6]. The central idea of entropy-based systems, on the other hand, comes from the slowing down of relaxation dynamics as a result of the decrease in configurational entropy S_{conf} and, as a result, the number of available configurations. In 1965, Adam and Gibbs proposed a theory for the glass transition phenomena, assuming that the glass system can be divided into independent, distinguishable regions containing molecules that move cooperatively in dynamically cooperative regions (cooperative rearranging regions CRR), and that structural relaxation ordinates from the rearrangement of the molecules in this latter. The Adam and Gibbs approach [6,7] is the most widely used entropy-based model. They proposed that rearrangements over energy barriers of molecular units must be "cooperative," involving many molecular units that must increase with decreasing temperature, based on a theory in which S_{conf} governs structural relaxation. According to this theory, systems can be divided into independent, distinguishable, and equivalent regions containing molecules that move cooperatively, referred to as the "cooperative rearranging region" (CRR). As a result, structural relaxation is caused by the rearrangement of molecules in CRRs.

The cooperativity increases as the temperature approach the glass transition temperature, increasing the size of the CRRs and, as a result, a reduction in the number of configurations available (reduction of the configurational entropy Sc). The Adam-Gibbs theory links the increase in molecular relaxation time to a decrease in configurational entropy Sc as the cooperative rearranging regions expand[8]. At constant T, the system can be divided into N regions, each containing z molecules; additionally, n of these regions is assumed to be in a thermodynamic state that allows molecular cooperative rearrangement and can transform to a different configuration under the influence of energy fluctuation (Enthalpy), independent of its environment. A cooperative region with z molecules has a probability transition W(T) that can be expressed as:

$$\mathbf{W(T) = Aexp\left(-\frac{z\Delta\mu}{kT}\right)} \tag{2.7}$$

Where A is a normalizing factor, and $\Delta\mu$ is the difference between the chemical potential of molecules in the region where rearrangement is allowed and the region where it is not allowed. When the size of a single CRR exceeds a critical size z, the

majority of configurational transitions occur; as a result, the transition probability can be written as

$$\overline{\mathbf{W(T)}} = \bar{\mathbf{A}}\mathbf{exp}\left(-\frac{\mathbf{z^*\Delta\mu}}{\mathbf{kT}}\right) \tag{2.8}$$

$\bar{A}$ is an average proportionality, independent of the temperature. z^* depends on the thermodynamic parameters, and in particular on S_c. If the CRRs are weakly interacting, the macroscopic system's configurational entropy can be defined as the sum of each CRR's configuration: $S_c=N_sc$. Furthermore, if the system is made up of a mole of molecules, and each CRR is made up of z molecules, the number N of CRR in the system is Na/z, where Na is the Avogadro's number, and z=Ns/S. A critical value of the configurational entropy S_c is associated with the smallest size z that permits a configurational transition, which cannot be less than k ln2, because two distinct configurations are the minimum required for the rearrangement to occur. Therefore $z^*= N_a\, s_c^*/S_c$, inserting into eq (2.8), yields

$$\overline{\mathbf{W(T)}} = \bar{\mathbf{A}}\mathbf{exp}\left(-\frac{\mathbf{\Delta\mu S_C^*}}{\mathbf{k_B TS_c}}\right) = \bar{\mathbf{A}}\mathbf{exp}\left(-\frac{\mathbf{C_{AG}}}{\mathbf{TS_c}}\right) \tag{2.9}$$

This equation connects the increase in molecular relaxation with the increase in configurational entropy. Because configurational entropy is not an experimentally available quantity, a direct test of the model is not possible. Sc can be replaced by the excess of entropy of the supercooled liquid with respect to the crystal in the hypothesis that the vibrational contribution to the entropy of the supercooled liquid, Smelt, and the crystal S_{crst} or S_{glass} are the same (or the glass)[7]

Relaxation times of glass-forming liquids approaching the glass transition are often described by the Adam-Gibbs model[8] and are linked to the configurational entropy S_{conf} as:

$$\boldsymbol{\tau = \tau_0 e^{\left(\frac{C}{TS_{conf}(T)}\right)}} \tag{2.10}$$

Where τ_0 and C are constants. As the temperature drops, mutual rearranging regions become more prevalent, and the relaxation phenomenon necessitates an ever-increasing number of units. With this in mind, the loss of configurational entropy is expressed in an increase in cooperativity when cooling down. With this in mind, an

increase in cooperativity during cooling results in a loss in configurational entropy, which is manifested by an increase in relaxation time. Fundamental questions were posed in the same way as they were in the case of free-volume models[9].

The Two Order Parameter (TOP) model[10,11] also known as the principle of frustration toward crystallization, is the final approach we'll look at. Tanaka *et al*. proposed this model, which offers a novel explanation of the glass transformation. According to this model, as a supercooled liquid approaches the glass transition, it is more likely to transform into an equilibrium crystal with long-range ordering. The geometrical frustration between short-range and long-range ordering is the basis for this two-order parameter model. As a consequence, the anger effect acts as an impurity that prevents crystallization and boosts the nucleation-free barrier energy. The main difference between TOP and other models is that TOP views crystallization as a strategic phenomenon that plays an important role in the liquid-to-glass transition, while the models described previously valued amorphization as a result of increasing density.

2.2.3 Debye model

The dielectric constant, also known as relative permittivity, is a measure of the distortion or polarisation of a material's electric charge distribution caused by the application of an electric field. It is determined by the frequency of the applied field and the material's polarizability. At low frequencies, dipoles follow the field, and the orientation polarisation achieves equilibrium, resulting in a high dielectric permittivity. The mobility of the dipoles increases as the applied frequency of the field rises, and a phase lag between the applied field and dipole orientation develops owing to intermolecular interactions. This causes the dielectric material to absorb electrical energy from a source, which is then lost as heat, increasing the dielectric loss. As a result, as the frequency of the applied field increases, so does the dielectric permittivity. When the applied field's frequency is sufficiently high, the molecular dipoles rotate as rapidly as they can, causing a peak in the dielectric loss. The frequency that corresponds to this peak is known as the dielectric relaxation frequency. Dielectric dispersion is the change in dielectric permittivity and dielectric loss with frequency over a broad spectrum of frequencies of the applied electric field.

Furthermore, when the temperature rises, the dielectric permittivity of a dielectric material normally decreases because the disorderliness of the molecular dipoles increases. Each dipole's rotational motion reflects a relaxation period, which is an essential parameter in dielectric spectroscopy. The relaxation might be caused by the motion of a whole molecule or a functional group linked to a larger molecule. The relaxation time is determined by intermolecular interactions and molecular size, and it decreases inversely with temperature since all molecule motions become quicker at higher temperatures. The dielectric relaxation behaviour of glass-forming systems can be explained using various models such as Debye, Cole-Cole, Cole-Davidson, and Havriliak-Negami models[12]. Debye argued that the relaxation rate of a dipolar system in non-equilibrium grows linearly with the distance from equilibrium. The Debye model is appropriate for systems with a single relaxation period[13]. He mathematically explained the nature of dielectric dispersion, i.e., dielectric constant fluctuation with frequency and absorption for polar materials by a single relaxation time. The equation gives the relationship for complex permittivity at angular frequency.

$$\boldsymbol{\varepsilon^{'} = \varepsilon^{'}(\omega) - i\varepsilon^{''}(\omega) = \varepsilon_{\infty} + \frac{\varepsilon_0 - \varepsilon_{\infty}}{1 + i\omega\tau}} \qquad (2.11)$$

where ε_∞ is the high-frequency dielectric constant, ε_0 is the static dielectric constant and τ is the macroscopic relaxation time. This is the familiar Debye dispersion equation. The characteristic shapes of real and imaginary parts of ε^* against the frequency of the outer electrical field $\upsilon = \omega/2\pi$ for this model are plotted in figure 2.1. The imaginary part exhibits an asymmetric peak with a maximum value at $\omega_{max}\ \tau = 1$ and has an amplitude given by $\boldsymbol{\varepsilon^{''}_{max} = {(\varepsilon_0 - \varepsilon_{\infty})}/{2}}$

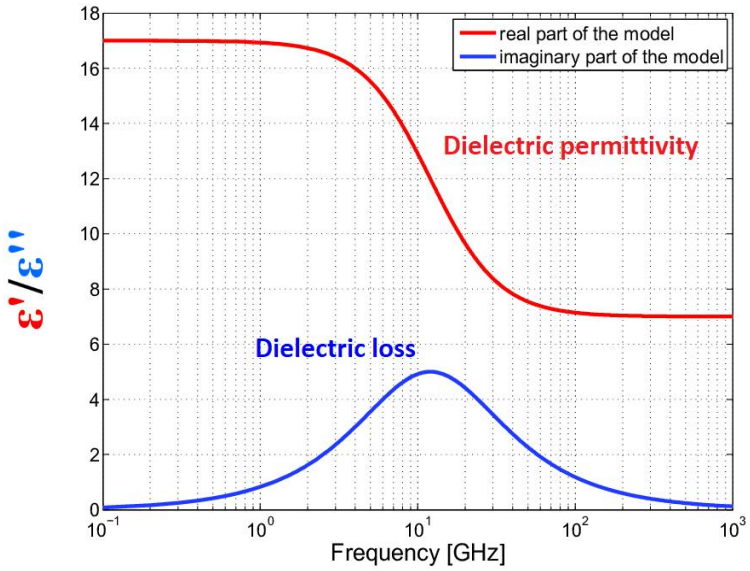

Figure 2.1 Frequency dependence of the real (ε') and imaginary (ε") parts of permittivity in the Debye process

The plot of the imaginary part of permittivity on the vertical axis *vs*. the real part of permittivity on the horizontal axis is known as the Cole-Cole plot. The Cole-Cole plot of the Debye relaxations assumes the shape of an asymmetric semi-circular arc with a center at $(\frac{(\varepsilon_0+\varepsilon_\infty)}{2}, 0)$ and radius $\frac{(\varepsilon_0-\varepsilon_\infty)}{2}$. Debye model response is observed in very few materials and for more complex systems such as polymers, this model fails to represent experimental data.

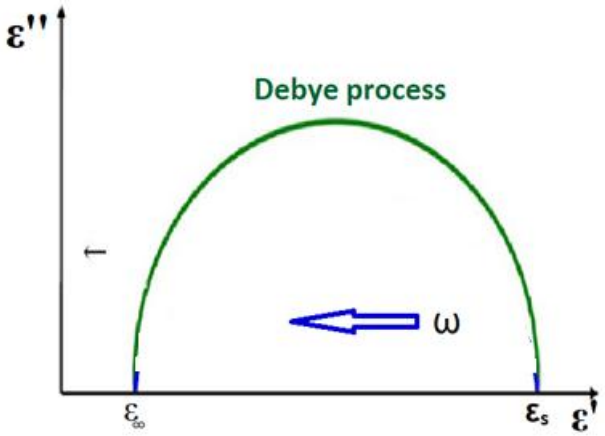

Figure 2.2. Cole-Cole plot for Debye process

Most recorded dielectric responses in most systems are non-Debye in nature, with a larger, asymmetric spectrum or bearing the hallmarks of both[14]. Shape functions such as Cole-Cole (CC), Cole-Davidson (CD), and Havriliak-Negami (HN) are commonly used to characterize them.

2.2.4 Cole-Cole model

Experiments on long-chain polar molecules revealed a depressed or expanded semicircle, which could only be explained by putting a fractional power in the imaginary component of the Debye function, as proposed by K.S. Cole and R.H. Cole[15]. The center of the semi-circle is below the abscissa, not above it. This was seen in practically all secondary relaxations in complicated systems. This may also be described in terms of the distribution of relaxation durations of dipoles with small variations. The complex dielectric function is defined as follows:

$$\varepsilon^*(\omega) - \varepsilon_\infty = \frac{\varepsilon_0 - \varepsilon_\infty}{1 + (i\omega\tau)^{1-\alpha}} \tag{2.12}$$

where α is the relaxation time distribution parameter which measures the broadening of the loss curve. The value of α lies between 0 and 1, *i.e.,* $0 < \alpha < 1$. When $\alpha = 0$, the Cole-Cole model reduces to the Debye model. When $\alpha > 0$, the relaxation is stretched, *i.e., it* extends over a wider range on a logarithmic ω scale than Debye relaxation.

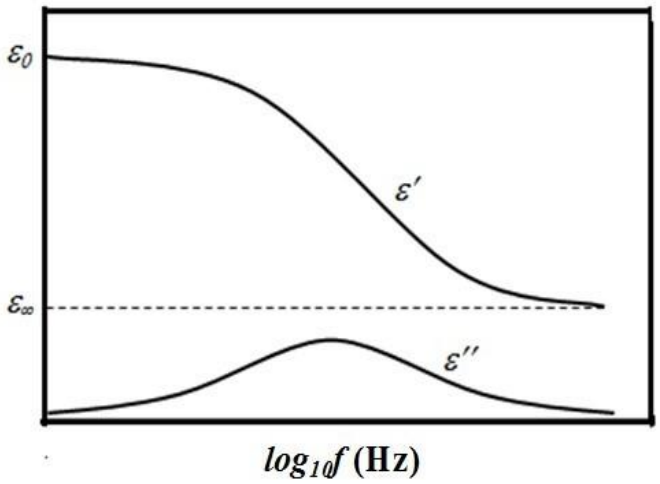

Figure 2.3. Frequency dependence of the real (ε') and imaginary (ε'') parts of dielectric permittivity in a Cole-Cole process.

In this model also the loss curve is symmetric, but in Cole-Cole relaxations, the value of s decreases more slowly near the relaxation frequencies as compared to Debye relaxation.

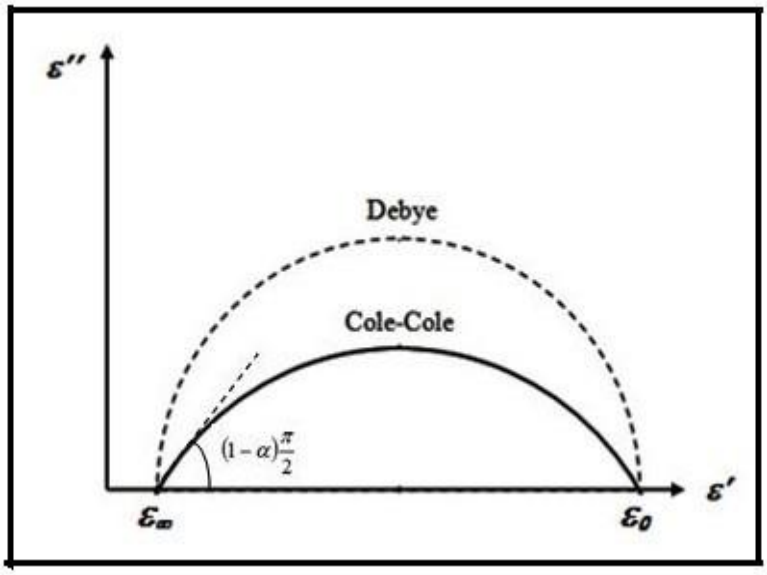

Figure 2.4. Cole-Cole plot for Cole-Cole process

2.2.5 Cole-Davidson model

Most of the supercooled glass-forming system show a skewed arc with a high-frequency straight line and a low-frequency circular arc, where the spectra could only be explained by introducing a fractional power to the denominator, put forwarded by Davidson and Cole[16] given by

$$\varepsilon^*(\omega) - \varepsilon_\infty = \frac{\varepsilon_0 - \varepsilon_\infty}{(1+(i\omega\tau))^\beta} \tag{2.13}$$

The above equation is known as the Cole-Davidson equation[17]. β is the shape parameter whose value changes between $0 < \beta < 1$. When $\beta = 1$, the above equation becomes the Debye equation and for values $\beta < 1$, the arc is skewed to the right. The frequency dependence of real and imaginary parts of permittivity is shown in figure 2.5. From the figure, it can be seen that the loss curve is asymmetric near relaxation frequencies. The Cole-Cole plot for the Cole-Davidson process is shown in figure 2.6.

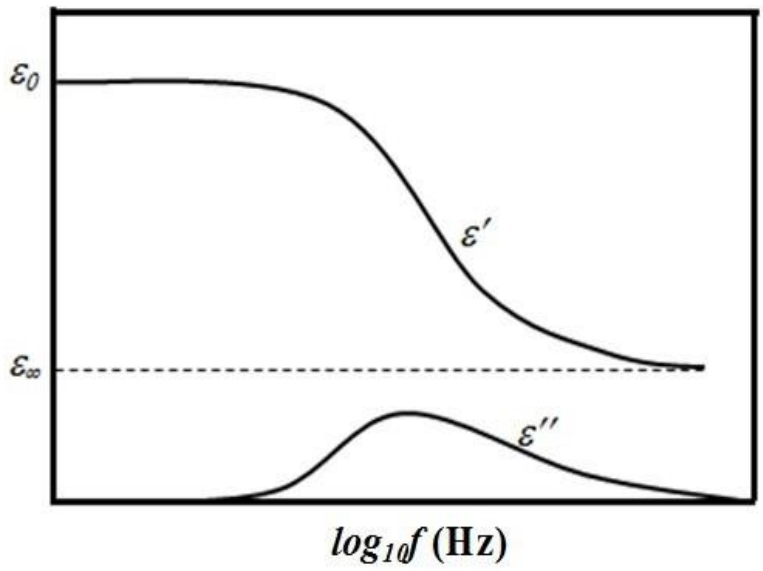

Figure 2.5. Frequency dependence of the real (ε') and imaginary (ε'') parts of dielectric permittivity in a Cole-Davidson process

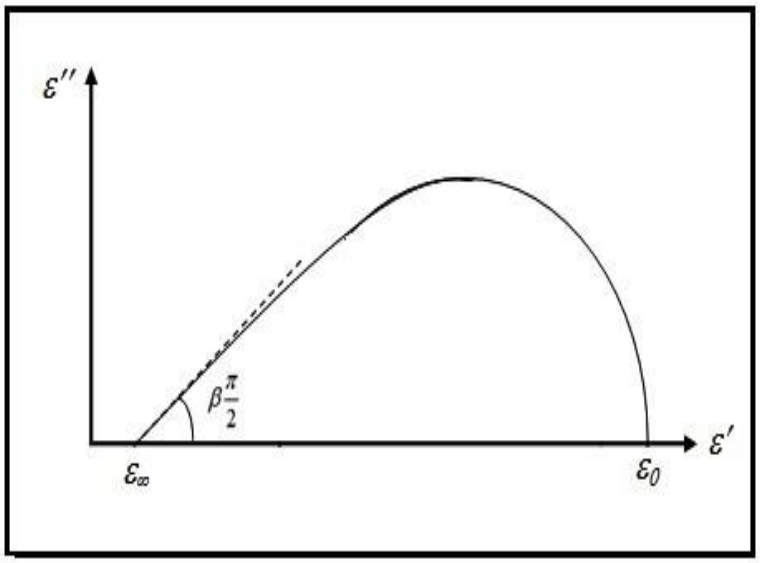

Figure 2.6. Cole-Cole plot for Cole-Davidson process

2.2.6 Havriliak-Negami model

Havriliak-Negami relaxation model [18] accounts for both the broadness and asymmetry of the dielectric dispersion curve. The model was initially employed to describe the dielectric relaxation of some polymers by adding two exponential parameters to the Debye equation,

$$\boldsymbol{\varepsilon^*_{HN}(\omega) = \varepsilon_\infty + \frac{\Delta\varepsilon}{\left(1+(i\omega\tau_{HN})^{1-\alpha_{HN}}\right)^{\beta_{HN}}}} \tag{2.14}$$

The exponents α and β are the shape parameters that describe the width or broadness and the asymmetry of the corresponding spectra respectively. Also $\Delta\varepsilon = \varepsilon_0 - \varepsilon_\infty$. For $\alpha = 0$ and $\beta = 1$, the Havriliak -Negami (HN) equation reduces to the Debye equation. Also, for $\beta = 1$, the HN equation reduces to the Cole-Cole equation and for $\alpha = 0$ to the Cole- Davidson equation. Most of the dielectrics possess conductivity due to the motion of charges, which gives rise to the conduction current and additionally polarizes the dielectric. Adding the contribution dc conductivity σ, the dielectric permittivity can be expressed as

$$\boldsymbol{\varepsilon^*_{HN}(\omega) = \varepsilon' - i\varepsilon''}$$

$$\boldsymbol{= \varepsilon_\infty + \sum_K \left(\frac{\Delta\varepsilon}{(1+(i\omega\tau_{HNk})^{1-\alpha_{HNk}})^{\beta_{HNk}}}\right) - i\left(\frac{\sigma}{\omega\varepsilon_0}\right)^s} \quad (2.15)$$

where s characterizes the conduction process. The conductivity term increases within absorbed moisture or in the case of polymers, the onset of dc conductivity at the higher temperature, dramatically increases the loss factor at lower frequencies. The conductivity term added to the imaginary part of the HN fit function can be subtracted from it after the fit. The use of Σ in the above equation stands for the summation over multiple relaxations. The characteristic relaxation time τ_{HN} is related to the frequency of maximal loss f_{max}. The relaxation time τ can be calculated using the equation

$$\boldsymbol{\tau = \tau_{HN} \times \left[\sin\left(\frac{\alpha_{HN}\pi}{2+2\beta_{HN}}\right)\right]^{-1/\alpha_{HN}} \left[\sin\left(\frac{\alpha_{HN}\pi\beta_{HN}}{2+2\beta_{HN}}\right)\right]^{1/\alpha_{HN}}} \quad (2.16)$$

For the secondary relaxation process, $\beta_{HN} = 1$, and thus HN function becomes the Cole-Cole function. Frequency dependence of the real (ε') and imaginary (ε'') parts of dielectric permittivity in HN model and Cole-Cole plot for typical HN relaxation are shown in figure 2.7 and 2.8, respectively.

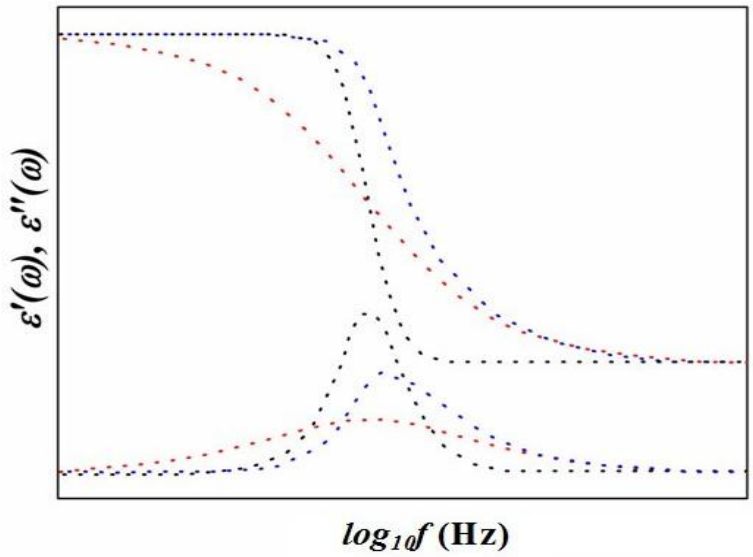

Figure 2.7. Frequency dependence of the real (ε′) and imaginary (ε″) parts of dielectric permittivity in HN model. The black dotted line shows the HN function with α = 0 and β = 1 (Debye), red dotted line denotes HN function with α = 0.6 and β = 1 (Cole-Cole) and blue dotted line denotes HN function with α = 0 and β = 0.4 (Cole-Davidson).

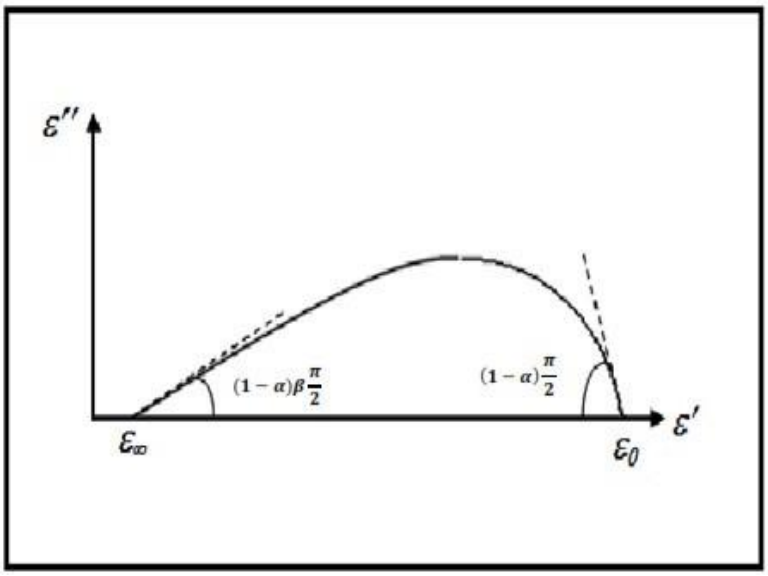

Figure 2.8. Cole-Cole plot for HN relaxation

2.2.7 Coupling model

Glass-forming substances are made up of units with complicated interactions. As a result, structural relaxation of glass-formers is a many-body relaxation problem, which is still unsolved in statistical mechanics, and thus glass transition is an unsolved problem as well[19]. The effect of mutual interaction is often taken into account in conventional theories and models of glass transition using a mean-field approach, i.e., by averaging the effect of the surrounding molecules on the relaxing one. The many-body

relaxation dynamics have a lot of experimental support [5,19,20]. K.L. Ngai's Coupling Model [21] on the other hand, isn't a complete solution to the many-body relaxation problem. Nonetheless, its predictions can explain the properties of structural relaxation resulting from many-body relaxation, as well as their relationships to the Johari-Goldstein secondary relaxation, which is its precursor. There is a temperature-independent time t_c in the coupling model that separates non-cooperative dynamics characterized by a single exponential from cooperative dynamics characterized by stretched exponential. A schematic description of the dynamic evolution can be described as following: at very short time $t < t_c$, molecules units relax independently with the correlation function [22].

$$\emptyset(\boldsymbol{t}) = \boldsymbol{exp}(-\frac{\boldsymbol{t}}{\boldsymbol{\tau_0}}) \tag{2.17}$$

Characterized by the independent (primitive or non-cooperative) relaxation time τ_0, which present the inverse of the rate $W_{0=}\tau_0^{-1}$ at which the molecule starts to relax, however, starting at t_e, the many molecule dynamics prevent all attempts by molecules to be successful at the same time, resulting in faster and slower relaxing molecules or heterogeneous dynamics. When the effect is averaged, it is equivalent to the slowing down of τ_0^{-1} by another multiplicative factor, which is time-dependent. According to Ngai's Coupling model, the relaxation time of JG secondary relaxation (τ_{JG}) and that of primitive relaxation ($\tau 0$) are correlated. The CM predicts a correlation of relaxation time of JG secondary process $\tau_{JG}(T)$ from α relaxation times. The primitive relaxation time τ_0 calculated from the equation (3.8), corresponds to the relaxation times of the hidden secondary process [23][24].

$$\boldsymbol{\tau_{JG}(T) = \tau_0(T) = (t_c)^n(\tau_\alpha(T)^{1-n}} \tag{2.18}$$

where t_c is equal to 2 ps for molecular glass formers and ($n=1-\beta_{KWW}$) is the coupling parameter. In particular, the slowing down factor $f(t)^{-1}$ was found to be dependent on time according to a sublinear power law, and hence $w(t) \propto t^{-n}\tau_0^{-1}$, where n is the coupling parameter of the CM and $0 < n < 1$. The stronger the slowing effect of the many-molecules dynamics, the larger the coupling parameter n, and vice versa, the greater the extent of dynamic heterogeneity. As a result, the model's corresponding

correlation function is the Kohlrausch stretched exponential function[25,26] which only holds for t >> tc.

$$\emptyset(\boldsymbol{t}) = \mathbf{exp}\left[-\left(\frac{\boldsymbol{t}}{\boldsymbol{\tau_\alpha}}\right)^{\mathbf{1-n}}\right] \tag{2.19}$$

and the cross-over at t_c leads to a relation between τ_α and τ_0 given by

$$\boldsymbol{\tau_\alpha} = [\boldsymbol{t_c^{-n}\tau_0}]^{\mathbf{1-n}} \tag{2.20}$$

There are experimental evidence [20,27,28] and numerical simulations [29,30] that the cross-over from the primitive relaxation to Kohlrausch relaxation is at $t_c \approx 2$ps for molecular systems. For molecular systems, the cross-over from primitive relaxation to Kohlrausch relaxation is at $t_c = 2$ps, according to experimental evidence and numerical simulations. The experiments were carried out at temperatures above Tg, where time becomes short, on the order of ten picoseconds or less. K.L. Ngai [21,31] predicted and demonstrated the relationship between the independent (primitive) relaxation time of the coupling model and the JG-relaxation time. The similarities in the two relaxation processes, such as their local nature, involvement of almost the entire molecule, common properties, and the fact that both serve as the precursor to the - relaxation, suggest a link between $\tau_0(T, P)$ and $\tau_{JG}(T, P)$ and this is should be valid for different temperature and pressure conditions. Surprisingly, where JG is derived from experiment and 0 is calculated, this relationship holds for a wide range of small molecular and polymeric glass-formers [32,33]. The CM has been used to investigate blend dynamics, polymer viscoelasticity, and ionic conductors. Different mechanisms for identifying the Johari-Goldstein secondary relaxation have been proposed, the first of which was proposed by Johari and supports the idea of an island of mobility, and the second of which was proposed by Goldstein and states that essentially all molecules contribute to the JG relaxation and the motions are dynamically and spatially heterogeneous. Surprisingly, this relationship holds for a wide range of small molecular and polymeric glass-formers, where JG is derived from the experiment and τ_0 is calculated [23,34,35]. Blend dynamics, polymer viscoelasticity, and ionic conductors have all been studied using the CM[35]. It was mentioned that different mechanisms have been proposed to identify the Johari-Goldstein secondary relaxation, the first of which was proposed by Johari and supports the idea of an island of mobility, and the second of which was proposed by Goldstein and states that essentially all molecules contribute to the JG relaxation and

the motions are dynamically and spatially heterogeneous. The coupling model explanation of the JG relaxation could help resolve the various points of view on its existence held by Johari and others. It's important to note that JG relaxation takes longer than t_c, particularly in molecular glass-forming systems where many molecule dynamics start at t_c=2ps.

It was stated that different mechanisms have been proposed to describe the Johari-Goldstein secondary relaxation, the first of which was proposed by Johari and supports the concept of an island of mobility, and the second of which was proposed by Goldstein and states that essentially all molecules contribute to the JG relaxation and the motions are dynamically and spatially heterogeneous. The JG relaxation's coupling model description can aid in resolving the various points of view on its existence held by Johari and others. It's important to note that JG relaxation usually takes longer than t_c, particularly in molecular glass-formers, where many-molecule dynamics begin at t_c=2ps. When $t_c << \tau_0 << \tau_\alpha$, the molecules are all caged for a short time, and then a progressive growth of cooperativity occurs as more molecules become able to reorient independently. Many of the molecules in the $t_c << \tau_0 << \tau_\alpha$ region try to relax independently, but not all of them succeed due to interactions with or restrictions imposed by the surrounding molecules. If molecular interactions are negligible, the most likely relaxation time JG, linked to the few molecules that have the chance to independently reorient, should be close to 0, the primitive relaxation time of independent reorientation. Although the primitive and JG relaxation processes are not identical, they are somewhat related. To evaluate the estimation of CM in glass-forming systems, the check of correspondence between JG relaxation time and the primitive relaxation time τ_0 is critical. To test the prediction of CM in glass-forming systems, it is critical to check for correspondence between JG relaxation time and the primitive relaxation time τ_0.

2.2.8 Kohlraush-William-Watts (KWW) fit

The instability of amorphous pharmaceuticals during their shelf-life is an important concern for pharmaceutical scientists as well as for the industry. Amorphous phase stability depends on the degree of deformation or structural perturbation of molecules in the amorphous phase. The degree of structural deformation can be assessed through the degree of nonexponentiality in the structural relaxation curves at

different temperatures in the supercooled liquid phase. The dielectric loss spectra above T_g in most glass formers normally are non-exponential due to the distribution of molecular relaxation times indicating their dynamic heterogeneity. The dielectric loss spectrum above T_g of glass formers is modeled by Kohlrausch-Williams-Watts's function. The Kohlrausch–Williams–Watts (KWW) function (Eq. 2.14) has been used to describe non-exponential relaxation processes within various amorphous pharmaceuticals[36,37]

$$\boldsymbol{\phi(t) = \exp\left(-\frac{t}{\tau_{KWW}}\right)^{\beta_{KWW}}} \tag{2.21}$$

Where $\phi(t)$ is the relaxation function, τ_α is the structural relaxation time and β_{KWW} is the stretched exponential parameter and is related to the distribution of molecular relaxation times and is a relevant criterion in predicting the safe shelf life of amorphous pharmaceuticals. The Kohlraush-William-Watts (KWW) function [38] describes the non-exponential behaviour of dielectric relaxation and is used to find the asymmetrical stretching parameter β_{KWW} which measures the asymmetric distribution of relaxation time and its deviation from Debye relaxation (β_{KWW} =1). The breadth of the structural relaxation peak was described using the stretching parameter β_{KWW} ($0 < \beta_{KWW} \leq 1$) which can be determined by fitting the α-peak in the frequency domain by the one-sided Fourier transform of the KWW function. The value of fractional exponent β_{KWW} which is a measure of the width of the dielectric loss curves, β_{KWW} = 1-n = 1 corresponds to the ideal Debye relaxation and is considered as a parameter to describe the distribution of molecular motion Moreover, the β_{KWW} parameter is consistent in the life expectancy of amorphous systems.

According to Shamblin's criterion [39], β_{KWW} has a very important role in predicting the stability or shelf life of amorphous APIs. If β_{KWW} decreases, the distribution of molecular relaxation becomes more non-exponential and hence stability decreases. If β_{KWW} is closer to 1, it indicates a narrow distribution of structural relaxation time, and hence that amorphous system is considered to be stable. While, if β_{KWW} value is lower, it represents a larger distribution of α-relaxation times and also leads to localized molecular mobility and crystallization tendency. A high value of β_{KWW} means narrow distribution of structural relaxation time which in turn indicates better shelf life and hence a smaller chance of amorphous API to crystallize.

Conversely, a lower value of β_{KWW} means larger distribution of the structural relaxation times which indicates faster localized molecular motions, which accelerates crystal nucleation criterion[39]. Taking one side Fourier transform of the Kohlrausch−Williams−Watts (KWW) function is common for analyzing the dielectric data[38].

2.3 Computational Chemistry

Computational chemistry is a branch of chemistry that utilizes computer simulations to help in the resolution of chemical problems. It calculates the structures and properties of molecules and solids using theoretical chemistry methods integrated into powerful computer programs. It is needed because, except for recent findings involving the hydrogen molecular ion , the quantum many-body problem cannot be solved analytically, let alone in closed form. Although computational findings are typically used to supplement the knowledge obtained from chemical experiments, they can also be used to predict chemical phenomena that have yet to be observed. It's widely used in drug and material development. Structure (i.e., the expected positions of the constituent atoms), absolute and relative (interaction) energies, electronic charge density distributions, dipoles and higher multipole moments, vibrational frequencies, reactivity, or other spectroscopic quantities, and collision cross sections with other particles are all examples of such properties. Static and dynamic conditions are also protected by the approaches used. In all instances, the amount of computing time and other resources (such as memory and disc space) required to study the device grows exponentially with its complexity. Almost any aspect of a material can be subjected to a qualitative or approximate quantitative analysis. Structure (i.e., expected atomic positions), absolute and relative (interaction) energies, electronic charge density distributions, dipoles and higher multipole moments, vibrational frequencies, reactivity, or other spectroscopic quantities, and cross-sections for collisions with other particles are examples of such properties. Both static and dynamic situations are covered by the methods used. With the size of the system being studied, computer time and other resources (such as memory and disc space) increase rapidly. A single molecule, a group of molecules, or a solid can make up that system. The accuracy of computational chemistry methods varies from very approximate to extremely precise; the latter is usually only possible for small systems. Quantum mechanics and fundamental physical constants are used exclusively in ab-initio methods. Because they use additional

empirical parameters, other methods are referred to as empirical or semi-empirical. Approximations are used in both ab initio and semi-empirical approaches. These include simplified first-principles equations that are easier or faster to solve, approximations that limit the size of the system (for example, periodic boundary conditions), and fundamental approximations to the underlying equations that are required to achieve any solution to the problem. Most ab initio calculations, for example, use the Born–Oppenheimer approximation, which greatly simplifies the underlying Schrödinger equation by assuming that the nuclei remain stationary throughout the calculation. As the number of approximations is reduced, ab initio methods should eventually converge to the exact solution of the underlying equations. However, it is impossible to eliminate all approximations in practice, and residual error is unavoidable. The goal of computational chemistry is to keep the calculations tractable while minimizing residual error. In some cases, the electronic structure of molecules is less important than their long-term phase space behaviour.

In protein conformational studies and protein-ligand binding thermodynamics, this is the case. To enable longer simulations of molecular dynamics, classical approximations to the potential energy surface are used, typically with molecular mechanics force fields, because they are computationally less intensive than electronic calculations. In addition, cheminformatics employs more empirical (and computationally less expensive) methods such as machine learning based on physicochemical properties. Predicting the binding affinity of drug molecules to a given target is a common problem in cheminformatics. Predicting binding specificity, off-target effects, toxicity are among the other issues.

2.3.1 Ab-Initio Methods

Mathematical modelling based on Schrodinger's equation is used in ab-initio. The energy of the molecule, its vibrational frequencies, its thermodynamic properties, and the values of its molecular orbitals, to name a few, can all be calculated using ab initio methods using several constants such as the speed of light, Planck's constant, and the masses of the electrons and nuclei. The accuracy with which calculations are performed is the primary advantage of ab-initio methods. The ab-initio method is used when a physicist needs to know a property that most closely matches experimental data or most closely approximates a theoretical prediction. Ab-initio is thought to be the

most accurate and precise of all the molecular modelling methods currently available. Currently, these methods are mostly used on small molecular systems. The majority of computational chemists believe that the upper limit for ab initio methods is around 50 atoms. This limitation prevents biologists from studying biologically important proteins and molecules, which are typically thousands of atoms in size.

2.3.2 Density Functional Theory (DFT)

Density Functional Theory (DFT) calculations quickly became a standard tool for a wide range of materials modelling problems in physics, chemistry, materials science, and a variety of engineering disciplines. In recent years, there has been an increased interest in using theoretical conformational calculations or molecular dynamics simulations to understand the physical nature of complex transitions at the atomic level, which is sometimes combined with experimental studies. This section aims to give you an overview of how to use density functional theory (DFT) calculations in the context of molecular dynamics. Here, we'll present some key quantum mechanics insights that underlie DFT. Hohenberg and Kohn[40] proposed the DFT [41] in their work. According to Zeigler, the use of DFT in ab initio calculations of molecular properties has increased dramatically recently[42]. This is due to the development of new and more accurate density functionals, as well as the increased efficiency and availability of DFT codes, as well as DFT computations with superior accuracy-to-effort ratio when compared to other ab initio methodologies[43]. Chacon Villalba et al. published a density functional theory-based quantum chemistry vibrational study (DFT)[44]. Many DFT methods like B3LYP, B3P86, B3PW91, BH and H, BH, and HLYP are available. The density functional method used in this study is B3LYP. The hybrid Becke 3 Lee – Yang – Parr correlational function is represented by the B3LYP. As suggested by Becke, this function is a hybrid of exact (HF) exchange with local and gradient corrected exchange and correlation terms. Becke[45] proposed and tested exchange-correlation functionals.

Consider the following scenario, in which the properties of a collection of atoms are described. The major physical properties of these atoms are their energy and, more importantly, how their energy is altered when they move around. Atomic nuclei are much heavier than individual electrons when applying quantum mechanics to molecules. As a result, we can solve the equations that depict electron motion for fixed

positions of atomic nuclei. The goal is to find the lowest energy electron configuration for a set of electrons moving in the domain of a set of nuclei. The ground state of electrons is the lowest energy configuration or state. As a result, the Born–Oppenheimer approximation assumes that the motion of atomic nuclei and electrons in a molecule can be broken down into separate mathematical problems. We can formulate the ground-state energy E depending on the positions of these nuclei, E (R_I,..., R_X), by considering X nuclei at positions ranging from R_I to R_X. The adiabatic potential energy surface of the atoms is the name for this function. Once we've calculated this potential energy surface, the next question is: "How does the molecular energy of the material change as atoms move around?" In general, the time-independent Schrödinger equation is written as:

$$\mathbf{H\Psi} = \boldsymbol{E_n \psi_n} \tag{2.22}$$

Where H stands for the Hamiltonian operator corresponding to total energy and is a set of Hamiltonian solutions. Each of these solutions has an eigenvalue, E_n, which is a real number that fulfills the eigenvalue equation. The Hamiltonian operator has a simple form in the case of a hydrogen atom, and the Schrödinger equation can be solved exactly. It is more difficult to solve a more complex context where multiple electrons interact with multiple nuclei, and this will not be addressed here.

For the Hamiltonian considered in this section, Ψ is the electronic wave function, which is a function of each of the N electrons' spatial coordinates (electron spin is neglected in this description). So far, we've:

$$\mathbf{\Psi = \Psi}(\boldsymbol{r_I}, \ldots, \boldsymbol{r_N}) \tag{2.23}$$

Even if the electron wave function is a function of each of the coordinates of all N electrons, the product of individual electron wave functions can be used to approximate Ψ:

$$\mathbf{\Psi = \Psi_I(r)\Psi_{II}(r), \ldots, \Psi_N(r)} \tag{2.24}$$

The electron-electron interaction is a crucial component in calculating the total energy of the system using the Hamiltonian. As a result, the above-mentioned individual electron wave function, Ψ(r), cannot be found without also taking into account the individual electron wave functions associated with all other electrons. The Schrödinger equation is a many-body problem in general. Direct observation of the

wave function for a random set of coordinates is not possible from an experimental standpoint. The probability that the N electrons are at a specific set of coordinates, r_1,..r_N, is the component that can be quantified in principle. This probability is equal to:

$$\boldsymbol{\rho(r) = \psi^*(r_1, r_2, r_3 \ldots\ldots r_N)} \tag{2.25}$$

We can also define a related quantity, n, that appears to be the density of electrons at a specific point in space n(r). This can be thought of as a function of the individual electron wave functions as follows: The asterisk indicates a complex conjugate.

$$\mathbf{n(r)} = \sum \boldsymbol{\psi_i^*(r) * \psi_i(r)} \tag{2.26}$$

The important point here is that the electron density, n(r), contains a wealth of information that can be physically observed from the Schrödinger equation's full wave function solution. Density functional theory is based on two fundamental mathematical theorems proved by Hohenberg and Kohn, as well as Kohn and Sham's mid-1960s derivation of a set of equations. The stationary ground-state energy E from the Schrödinger equation is a unique function of the electron density, according to the first proved theorem by Hohenberg and Kohn[40].

Let's start by defining the term "functional." A function (f) is a mathematical formula that maps one set of numbers to another

$$\boldsymbol{y = f(x)} \tag{2.27}$$

As a result, a functional (F) is a mapping between a set of functions and a set of numbers. This follows the equation, where E[ρ] is the function of the electronic density:

$$\boldsymbol{E[\rho] = \int (\rho(\vec{r}))d^3n} \tag{2.28}$$

By specifying that the ground-state energy E can be expressed as E[n(r)], where n(r) is the electron density, Hohenberg, and Kohn's theorem can be rewritten and strengthened. The term "density functional theory" was coined to describe this field. As a result, the ground state density $\rho_0(r)$, determines all properties of the many-body system. Each property is a function of the ground state density $\rho_0(r)$, written as f [ρ_0] by the same reasoning.

Even though the first theorem establishes that an electron density functional exists and can be used to solve the Schrödinger equation, it has a major flaw in that it does not state what the function is. In accord with the first proposed theorem, Hohenberg–Kohn theorem defined a second one by implementing an important characteristic of the functional. For all electron systems, a universal function for the energy E[ρ] of the density ρ(r) can be defined. The exact ground state density ρ(r) is the density that minimizes this functional.

The second theorem's functional could be expressed in terms of single-electron wave functions, $\Psi(r)$. These wave functions determine the electron density, n(r), according to Eq. (2.18). As a result, the energy functional can be written as follows:

$$\mathbf{E[\rho(\{\varphi i\})]} \;=\; \mathbf{E[\Psi i]} \;=\; \boldsymbol{E_{known}[\Psi_i]} \;+\; \boldsymbol{E_{XC}[\Psi i]} \qquad (2.29)$$

where φ_i are the Kohn-Sham orbitals, $E_{known}[\Psi_i]$ are known terms and $E_{XC}[\Psi_i]$ are everything else. The electron kinetic energies, Coulomb interactions between electrons and nuclei, Coulomb interactions between pairs of electrons, and Coulomb interactions between pairs of nuclei are all covered by the term $E_{known}[\Psi_i]$. The exchange-correlation functional, $[\Psi_i]$, is the other term in the complete energy functional.

It includes a definition of all quantum mechanical effects of electron-electron repulsion, as well as a kinetic energy adjustment. As a result, it is the functional that contains all of the unknowns. Kohn and Sham demonstrated that finding the right electron density can be formulated in an accessible form to find minimum energy solutions of the total energy functional. This one entails the solution of a set of equations involving only a single electron in each equation. The following is an overview of Kohn-Sham equations:

$$\left[-\frac{\boldsymbol{\hbar^2}}{\boldsymbol{2m}}\boldsymbol{\nabla^2} + \boldsymbol{V(r)} + \underbrace{\boldsymbol{V_H(r)} + \boldsymbol{V_{XC}(r)}}_{\textbf{Kohn-Sham potential}}\right]\boldsymbol{\Psi_i(r)} = \boldsymbol{\varepsilon_i}\boldsymbol{\Psi_i(r)} \qquad (2.30)$$

Three parameters, V, V_H, and V_{XC}, are involved in the left part of the equation. The interaction between an electron and a collection of atomic nuclei is defined by the letter V. The Hartree potential is denoted by V_H, and it depicts the Coulomb repulsion between an electron and the total electron density. Finally, V_{XC} depicts the

contributions to exchange and correlation. The Hartree potential, or the potential due to the electron density distribution, must be defined to solve the Kohn–Sham equations. However, we need to know the electron density to define the Hartree potential. However, we need to know the single-electron wave functions to calculate the electron density. Access to wave functions, on the other hand, necessitates the solution of Kohn–Sham equations. As outlined, breaking this pattern is done iteratively [46].

1. Make an educated guess about the electron density, n(r), and the orbitals, φ_i
2. To find the single-particle wave functions, $\Psi_i(r)$, solve the Kohn–Sham equations using the Kohn–Sham potential and the trial electron density n(r).
3. Calculate the electron density using the single-particle wave functions defined by Kohn–Sham.

$$\boldsymbol{n_{KS}(r)} = \sum_{\boldsymbol{i}} \boldsymbol{\Psi_i^*}\,\boldsymbol{(r)\Psi_i(r)} \tag{2.31}$$

At step 1, compare the electron density calculated, $n_{KS}(r)$, with the electron density used in solving the Kohn–Sham equations, n(r). The ground-state electron density is determined if both densities are the same. The system's total energy can be calculated. If the two densities are not equal, the initial estimate of electron density must be updated in some way. After that, the process starts all over again from step 2. To summarise, all that is required for a complete determination of all molecular properties is knowledge of density.

2.3.3 Geometry optimization

To perform a DFT calculation, you'll need to be familiar with both the system and the method. The former necessitates a starting structure as well as knowledge of charge and spin multiplicity. The latter is made up of a functional and a foundation. Let us begin by describing the overall setup for a system's modelling method. We must first establish the starting molecular structure before we can study. To calculate molecular energy, different methods (ab initio, semi-empirical, or molecular mechanics) could be used. By optimizing the geometry and computing the selected properties with adapted methods (relative energies, reaction pathway), an optimal structure could be obtained.

The goal of optimization is to link a molecule's energy to its geometry. The potential energy surface will be built as a result of this (PES). It expresses the energy of

a system (typically a group of atoms) in terms of the atoms' positions. PES is an important instrument for studying molecular geometry and chemical reaction dynamics, as well as exploring structure properties (e.g., finding the minimum energy shape of a molecule). As a result, PES defines the structure-energy relationship as follows[47]:

$$\boldsymbol{E_{tot} = T\{p_i\} + V\{R_I\}} \tag{2.32}$$

$T\{p_i\}$ is the kinetic energy that is dependent on momenta, and $V\{R_I\}$ is the potential energy that is dependent on coordinates? As a result, although this equation gives the energy of a single nuclear configuration, a PES is composed of several points. Geometry optimization and energy computation can also be done using many methods. The methods are described below in order of increasing precision from the least precise to the most precise (this goes hand in hand with calculation time). The "ball-and-spring" solution is used in force fields or Molecular Mechanics (MM); the electronic structure is ignored. Force fields, i.e., functional structure and parameter sets used to measure the potential energy, are used to calculate the system's potential energy.

The molecule is defined as a series of charged points (atoms) connected by springs using this process (bonds). Semi-empirical molecular orbital methods are the second approach we plan to present. To streamline the computation process, this approach uses quantum methods with approximate parameters, which are normally derived from experimental results. These methods include qualitative representations of molecular structures that are satisfactory. They can only be used for elements and interactions that have been parameterized, however. Finally, ab initio methods, which allow for a complete quantum mechanical treatment of the electronic wave function, are still used. The DFT method, which is used to analyze the electronic structure, falls into this asset class. Chemical reactions and transition states, as well as mechanical, optical, and magnetic properties, are all positive factors. The computational limit of about 250 atoms is the system's key limitation (as simulation time grows as N^3 where N is the number of electrons).

2.3.4 Choosing functionals and basis sets

Over time, several different types of basis sets for describing molecular orbitals have been created[48]. The most commonly used of all the itemized basis sets comes from John Pople's group in the form of X-YZ_g[49]. The number of primitive Gaussians

in each basis function is defined by X. Y and Z, on the other hand, mean that valence orbitals are made up of two different basis functions. The presence of two numbers after the hyphens indicates that the basis set is split-valence. Here is a list of split-valence basis sets of this kind that are widely used: 3-21G, 3-21G* (polarized), 3-21+G (diffuse functions), 3-21+G* (with polarization and diffuse functions), 6-31G, 6-31G*, 6-31+G*, 6-31G(3df, 3pd), 6-311G, 6-311G* and 6- 311+G*. As a result, both of these foundation functions allow the electronic definition to be improved. Local-density approximation (LDA) can be considered when choosing a low level of theory. This method relies solely on the importance of the electronic density at each point in space when determining local density (e.g., SVWN functional). We progress from the generalized gradient approximation (GGA) (e.g., BLYP or PBE) considering density gradients to the meta-generalized gradient approximation (meta-GGA) (e.g., TPSS or M06L) endorsing the explicit dependency on kinetic energy density by gradually raising the level of theory. The global (e.g., B3LYP or PBE0) and range-separated (e.g., B97XD or CAM-B3LYP) sections of the above theory scale denoted as hybrid functionals are separated. It makes an explicit dependency on occupied orbitals by using a class of approximations to the exchange-correlation energy functional. Completely non-local functionals, such as B2PLYP, allow an explicit dependency on unoccupied orbitals at the higher level of theory.

2.3.5 Frontier molecular orbital characterization

All chemical interactions, according to classical chemical theory, are either electrostatic (polar) or orbital (covalent) in nature. Covalent interactions in quantum chemistry are caused by orbital overlap. The energy eigenvalues of two orbitals determine their interaction. As a result, energies associated with the highest occupied molecular orbital (E_{HOMO}) and the lowest unoccupied molecular orbital (E_{LUMO}) are frequently used as 2-dimensional descriptors. E_{HOMO}, for example, could model the covalent basicity of a hydrogen bond acceptor, while E_{LUMO} could model the covalent acidity of a hydrogen bond donor's proton[50].

Further interpretation is possible because the HOMO energy is related to the ionization potential and is a measure of the molecule's tendency to be attacked by electrophiles. Correspondingly, the LUMO energy is related to the electron affinity and is a measure of a molecule's tendency to be attacked by nucleophiles[51]. Transition

state formation also involves interaction between the frontier orbitals of reacting species, according to frontier molecular orbital theory. The HOMO-LUMO gap, or the energy difference between the HOMO and the LUMO, is a crucial stability metric[52]. A large HOMO-LUMO gap indicates a molecule's high stability, as measured by its lower reactivity in chemical reactions. The HOMO-LUMO energy gap has been used to derive the concept of chemical hardness[53]. Frontier orbital electron densities can also be used to characterize donor-acceptor interactions in great detail. According to the frontier electron reactivity theory, the majority of chemical reactions occur at the position and orientation where the HOMO and LUMO of the respective reactants can overlap the most. The HOMO or nucleophilic density of a donor molecule is critical to the reaction, while the LUMO or electrophilic density of an acceptor molecule is crucial. As a result, the electron densities of HOMO and LUMO can be used as 3-dimensional descriptors. As electrophilic and nucleophilic atomic frontier electron densities, these densities are transformed into global 2-dimensional descriptors. The interaction of a compound with the electrophilic center of another reagent is described by the electrophilic atomic frontier electron density. The interaction of a compound with the nucleophilic centre at the other reagent is described by the nucleophilic frontier electron density. Frontier electron densities, on the other hand, can only be used to describe the reactivity of different atoms within a single molecule. Frontier electron densities must be normalized by the energy of the corresponding frontier molecular orbitals, defined as the indices of atomic frontier electron density, in order to compare the reactivities of different molecules. The super delocalizability is another indicator of a molecule's proclivity to be attacked by an electrophile or nucleophile. It's linked to the atom's electron density and can be thought of as a measure of the affinity of occupied and unoccupied orbitals in chemical reactions. It's possible to distinguish between electrophilic and nucleophilic localizability once more. The former refers to a compound's interaction with another reagent's electrophilic centre. The interaction of a compound with the nucleophilic centre at the other reactant is described by the nucleophilic localizability.

2.3.6 Natural bond orbital analysis

NBO analysis is based on a method for optimally transforming a given wave function into localized form, which corresponds to the chemist's Lewis structure

picture's one-center ("lone pairs") and two-center ("bonds") elements. The input atomic orbital basis set is transformed into natural bond orbitals using natural atomic orbitals (NAOs) and natural hybrid orbitals (NHOs) in NBO analysis (NBOs). The NBOs obtained in this way are consistent with the widely used Lewis model, which localizes two-center bonds and lone pairs. Natural bond orbital analysis, a unique property of computational methods, allows us to visualize both electron orbitals and population analysis intuitively [54]. NBO analysis is based on the transformation of multi-electron wavefunctions of molecules into a localized form that corresponds to a single-center [Lone pair (LP)] and two-centered [natural bond and antibonding orbitals (BD and BD*, respectively) element. It provides a detailed understanding of the intramolecular and intermolecular orbital interactions in molecules between the filled donor and empty acceptor NBOs, allowing us to perform a quantitative evaluation and draw a qualitative conclusion about the substituent's donor-acceptor properties. NBO analysis was used to determine the bond orders of the molecules under investigation.

2.3.7 Spectral characterization

Because of its utility, the density functional theory (DFT) has become a powerful tool in computational chemistry. This technique emerged as a commanding implementation for spectroscopic analysis of chemical entities. DFT calculations are now required for interpreting experimental spectra of complex molecules because they can predict frequencies and spectral intensities. In the last decade, a lot of progress has been made in developing new DFT approaches that can be used in existing quantum-chemical computational programs[55]. Theoretical computation of vibrational frequencies has become practically essential for experimental spectroscopists in recent years, as it aids in the assignment and interpretation of experimental infrared/Raman spectra, particularly in difficult and uncertain cases. Many studies previously used the HF method to calculate vibrational frequencies, but it has long been known that this method frequently miscalculates these frequencies to the point of being alarming. The main contributors to error are found to be insufficient handling of electron correlation and anharmonicity of the vibrations[56]. DFT largely eliminated the errors because theoretical computations aided in the interpretation of experimental findings, demonstrating that theoretical data can be nearly attained at the harmonic level using DFT. Different density functional approaches can be used to calculate optimized

geometry, IR intensities, vibrational frequencies, and Raman scattering activities[57]. DFT-based new methods are developed that are appropriate for the satisfactory hypothetical interpretation of NMR spectra of various chemical and biochemical systems, taking into account NMR spectroscopy. Magnetic resonance parameters, such as shielding tensors, nuclear spin-spin coupling parameters, hyperfine tensors, and g-tensors, are influenced by local geometrical and electronic structures. A practical approximation of the real system is depicted by a model system in which 50–100 atoms are treated with ab initio techniques for NMR parameter speculations. DFT has risen to the forefront of the field of calculating NMR parameters in recent years as a result of its ability to include electron correlation effects in a very efficient manner[58]. Quantum chemists are increasingly interested inaccurate calculations of excited-state properties, and as a result, they are developing novel solutions for these properties. The advancement of computations based on the time-dependent density functional theory (TDDFT) in recent years has sparked interest in the calculations of electronic structures in excited states. The time-dependent concept of electronic spectroscopy provides a commanding method for performing exact quantum mechanical calculations of the intervalence absorption spectrum[59]. Since the time development of the wave-packet can be tracked and inferred[60], a corporeal picture of the effects of the coupling of electronic and nuclear motions became available by employing calculations in the time realm. Because electronic spectra are frequently calculated with TD-DFT, the technique's many successes have recently been revised. This technique can calculate vertical excitation energies, absorption wavelengths, and oscillator strength[61].

2.3.8 Vibrational spectroscopy by DFT

The impact of vibrational spectroscopy as an analytical tool can be seen in a variety of fields. The basic interpretation of vibrational spectra is the qualitative association of bands with specific structures or chemical groups. In contrast to nuclear magnetic resonance, where nuclear spin is associated with a single peak or multiplet, the observed bands in vibrational spectra are the result of the combined motion of all of the nuclei in the sample. There are only 3N-6 experiential fundamental bands for N nuclei, and the matrix of internuclear force interactions, i.e., the second derivative matrix in harmonic approximation, currently has (3 N-6) (3 N -5)/2 exclusive terms. Because many bands are not observed, such as overtones, combination bands, and

nonconformities from the harmonic approximation, the extraction of force constants from vibrational frequencies is still an unsolved mathematical problem[62]. The discovery of effective codes provides a possible solution to the problem of calculating the ground state's potential energy surface. Calculating vibrational spectra will benefit from a technique that precisely determines bonding as well as intermolecular interactions. DFT approaches accurately calculate the ground state properties and potential energies; thus, DFT excellently and proficiently calculates the vibrational spectra from the first principles[57]. When using DFT models to characterize the bonding, the absolute values of the frequencies are high in comparison to experimental values, allowing comparison with experimental trends. The limitations of the harmonic approximation are frequently a leading cause of divergence between theory and experiment, so DFT methods provide sufficient accuracy for normal mode calculations. Following the success of the method applied to small molecules, it is reasonable to broaden the approach by including molecular interactions. Anharmonicity and hydrogen bonding, both of which result in a lower frequency for a specific normal mode than projected by harmonic approximation, can be reasons for inconsistency[63].

Calculation of vibrational frequencies using a molecular system [7]. When force is proportional to displacement, for example, when springs are considered Hookean, equations of motion are easily solved, and vibrational frequencies are associated with force constants and atom masses. For example, the frequency of a simple molecule like CO, which has only one spring, is calculated as in Eq.

$$\boldsymbol{v} = \frac{\mathbf{1}}{\mathbf{2}\boldsymbol{\pi}} \sqrt{\frac{\boldsymbol{k}}{\boldsymbol{\mu}}} \tag{2.33}$$

Where k is the spring constant and μ is the reduced mass of carbon and oxygen atoms. Geometry optimization is required before frequency calculations, as these calculations are only valid at fixed points on the potential energy surface. The following is how molecular harmonic vibrational frequencies are now calculated

$$\boldsymbol{v_k} = \frac{\boldsymbol{\lambda_k^{1/2}}}{\mathbf{2}\boldsymbol{\pi}} \tag{2.34}$$

Six of the k values derived from Eq. (9 will be zero, resulting in six frequencies with zero value, which corresponds to the molecule's three translational and three

rotational degrees of freedom. Because equilibrium geometry never originates with infinite precision, it is possible to find six vibrational frequencies with values close to zero in practice. The remaining 36 vibrational frequencies correspond to molecular-harmonic vibrations.

2.3.9 Time-dependent density functional theory (TD-DFT)

Classic DFT is concerned with the ground stationary state, whereas applications such as UV-vis spectroscopy, photochemistry, NLO, and others include electronically excited states or time-dependent electronic characteristics, which are consistent with time-dependent density functional theory (TD-DFT). Formal TD-DFT can be traced back to a classic paper by Runge and Gross[64], which strained to solidify previous efforts on the same topic. As a result, Runge- Gross TD-DFT[65] is two decades younger than Hohenberg Kohn-Sham's theory[40], which, as previously stated, is about the stationary ground state. The Runge-Gross paper proposed four theorems. The Runge-Gross theorem states that time-dependent charge density, $\rho_r(r,t)$, in conjunction with preliminary wave function $\psi(0)$, regulates external potential up to an additive function of time. Electronic spectra are based on a variety of chemical and physical molecular properties. Because many stimulating chemical problems are included in both the ground and excited states of molecules, different chemical and physical effects can be easily investigated computationally by modifying the spectral characteristics of molecules. DFT provided an effective explanation for ground-state properties of atoms, molecules, and solids; thus, the DFT formalism must be extended to excited states to designate photochemical and photophysical procedures[65]. As a result, time-dependent DFT (TD-DFT) is established as an operative tool for excited-state calculations because it provides a first-principles technique for calculating excitation energies and various response-related characteristics in a density functional outline. A molecule's valence-MO-valence-MO single electronic excitations can be designated as valence-MO-valence-MO single electronic excitations and replicated in spectra. For multiple energy calculations, such as using spin-orbital number I to the empty spin-orbital number, excited determinant energies are required (j). As a result, specific states are denoted by the symbols $\pi \rightarrow \pi^*$, $n \rightarrow \pi^*$ transitions. The process of concluding wave functions for these states is sometimes smoothed by the relative ease of character. Calculating the dynamic answer of charge density suggests a rigorous approach to

time-dependent DFT formalism simplification. In the typical dipole approximation, the poles of dynamic polarizability regulate excitation energies, allowing the determination of the electronic excitation spectrum. The poles' strengths are provided by oscillator strengths (fi) or transition dipole moments which are both commonly referred to as optical transition intensity.

2.3.10 Global descriptive parameters

The conceptual DFT-based global reactivity and the local reactivity descriptors are useful quantities to understand the global reactivity and the local site selectivity, respectively. Reliable calculation of global reactivity descriptors is important in conceptual DFT, as these values are used as input for understanding the relationships between structure, stability, and reactivity as well as for QSAR/QSPR/QSTR development[33]. The ionization potential and electron affinity of selected molecules are used in the working equations for calculating the various global reactivity descriptors. Total electronic energy calculations on the N-1, N, and N + 1 electron systems at the neutral geometry are used to compute the ionization potential and electron affinity. Chemical potential (μ) is defined by the first-order partial derivatives of total energy (E) concerning the number of electrons (N) at constant external potential, V(r), and global hardness (η) is defined by the second partial derivatives of total energy (E) concerning the number of electrons (N) at constant external potential, V(r). Chemical potential (μ) and chemical hardness (η) is generally calculated using the following equations

$$\boldsymbol{\mu \approx -\frac{1}{2}\,(I.P + E.A)} \tag{2.35}$$

$$\boldsymbol{\eta \approx \frac{1}{2}\,(I.P - E.A)} \tag{2.36}$$

where I.P = ionization potential and E.A = electron affinity. Using the Koopmans' theorem in terms of the energies of frontier molecular orbitals, the chemical potential and chemical hardness are given by

$$\boldsymbol{\mu \approx -\frac{1}{2}\,(E_{HOMO} + E_{LUMO})} \tag{2.37}$$

$$\boldsymbol{\eta \approx \frac{1}{2}\,(E_{LUMO} - E_{HOMO})} \tag{2.38}$$

Electrophilicity[66] is a reactivity descriptor that allows for quantitative classification of a molecule's global electrophilic nature on a relative scale. The electrophilicity index was proposed by Parr *et al*. as a measure of energy loss due to maximum electron flow between donor and acceptor. The electrophilicity index was defined as

$$\boldsymbol{\omega = \frac{\mu^2}{2\eta}} \tag{2.39}$$

This index, according to this definition, measures a chemical species' willingness to accept electrons. A lower value of μ, ω characterizes a good, more reactive nucleophile, whereas a high value of μ, ω characterizes a good electrophile. When the system acquires an additional electronic charge from the environment, this new reactive index measures energy stabilization. These global quantities, along with mean polarizability values (α_v), be extremely useful and complementary tools for describing chemical reactivity. There are 27 tensor components in the microscopic first hyperpolarizability. However, in the case of a molecule with no symmetry, due to independent interchange of Cartesian coordinates, these 27 elements are reduced to 10 according to Kleinman symmetry for a second-harmonic generation.

The global hardness reflects the overall stability of the system. The chemical hardness fundamentally signifies the reluctance towards the deformation of the electron cloud of the atoms, ions, or molecules under small perturbation encountered during chemical processes. Chemical softness is the measure of the capacity of a molecule to receive electrons[67]; more precisely it is related to the groups or atoms present in that molecule and inversely proportional to chemical hardness. The chemical potential in DFT, measures escaping tendency of an electron from equilibrium, is accounted by the first derivative of energy to the number of electrons and is also the negative of electronegativity, which is a measure of the tendency to attract electrons in a chemical bond. The electrophilic index tells one about the strength of electrophilicity of the species. Global reactive descriptors can be calculated by two different methods, one is based on the difference in total electronic energy of the neutral molecule and its corresponding anion and cation, obtained from the geometry of the neutral molecule to keep the external potential constant and usually call it as ‘energy vertical’. The global properties are computed by using equations.

2.3.11 Non-linear optical properties

The computational method can also be used to study the interaction of electromagnetic fields in various media to produce new fields with different frequency, phase, amplitude, or other propagation characteristics than the incident fields. The polarization P induced in a medium by an external field F is given by

$$\boldsymbol{P = P_0 + \chi^{(1)F} + \chi^{2F^2} + \chi^{(3)F^3} + \ldots} \quad (2.40)$$

Where χ^n is the nth order susceptibility tensor of the bulk medium. The dipole moment of a molecule interacting with an electric field can be written as

$$\boldsymbol{\mu_i = \mu_i^0 + \alpha_{ij}F_jF_k + \left(\frac{1}{2}\right)\beta_{ijkl}F_jF_k + \left(\frac{1}{6}\right)\gamma_{ijkl}F_jF_kF_l + ..} \quad (2.41)$$

Where μ_i^0 is the permanent dipole moment and α_{ij}, β_{ijkl} , are tensor elements of the linear polarizability and first and second hyperpolarizabilities respectively.

Nonlinear optical effects may result from this interaction (NLO). The dipole moment, first static hyperpolarizability, and related properties of the molecules, such as α, β and Δα, and, can be computed computationally in this direction to study the NLO properties. The sum and mixing of different frequencies (including second harmonic generation) and optical rectification are caused by the second-order term of hyperpolarizability. The third harmonic generation and two photo resonances are caused by the third-order term. NLO's polarizability and hyperpolarizability can be expressed using tensors. The linear polarizability tensor, which is a 3x3 matrix with nine components, is shown below.

$$\boldsymbol{\alpha} = \begin{bmatrix} \boldsymbol{\alpha_{xx}} & \boldsymbol{\alpha_{xy}} & \boldsymbol{\alpha_{xz}} \\ \boldsymbol{\alpha_{yx}} & \boldsymbol{\alpha_{yy}} & \boldsymbol{\alpha_{yz}} \\ \boldsymbol{\alpha_{zx}} & \boldsymbol{\alpha_{zy}} & \boldsymbol{\alpha_{zz}} \end{bmatrix} \quad (2.42)$$

$$\boldsymbol{\alpha_{total}} = \frac{(\boldsymbol{\alpha_{xx} + \alpha_{xx} + \alpha_{xx}})}{\boldsymbol{3}} \quad (2.43)$$

Alternatively, the first hyperpolarizability, the quantity of interest, is a tensor with a 3x3 matrix, and the total hyperpolarizability is calculated by

$$\boldsymbol{\beta} = \sqrt{\left(\boldsymbol{\beta_{yyy} + \beta_{yzz} + \beta_{yxx}}\right)^2 + \left(\boldsymbol{\beta_{zzz} + \beta_{zxx} + \beta_{zyy}}\right)^2 + \left(\boldsymbol{\beta_{yyy} + \beta_{yzz} + \beta_{yxx}}\right)^2} \quad (2.44)$$

When the polarizability and hyperpolarizabilities of molecules are compared to one of the prototypical molecules, urea, the nonlinear optical activity of any molecule can be predicted.

DFT methods incorporating gradient corrected (nonlocal) exchange and correlation functional produce results that are comparable to, if not better than, ab initio correlated calculations while consuming less computer time. Because of the method's enormous success, we used a DFT-based hybrid functional with a 6-31G(d) basis throughout our computational study. In this study, torsional energy was calculated using the DFT/B3LYP methods with the 6-31G(d) basis set at 10° intervals between 0° and 180°. Static polarizability, first hyperpolarizability as a function of dihedral angle, and optical energy gap were calculated using DFT-B3LYP. Static polarizability, first hyperpolarizability as a function of dihedral angle, and optical energy gap were calculated using the DFT-B3LYP method with the 6-31G(d) basis set. All of the calculations were done with the Gaussian-09 programs.

2.3.12 Origin of secondary relaxation: DFT approach

The molecular dynamics in the glassy state and hence the activation energy of the observed secondary γ relaxation of glass formers could be determined by the experimental methods like BDS, but no experimental technique is available until now to give sufficient information that can help to identify the relevant part of the corresponding molecule whose motion originates the observed intramolecular secondary relaxation in its glassy system. Therefore, our experimental investigations [68] using BDS were complemented with quantum computational DFT calculations. Although the activation energy of the secondary relaxation (γ-relaxation) could be experimentally determined using dielectric spectroscopy measurements in this chapter, no evidence of the relevant part of the molecule moieties involved in the transition could be inferred directly. Indeed, the root of secondary relaxations has remained a mystery, with no clear answer available to date Secondary relaxations may occur as a result of multi-molecular intramolecular changes or as a result of a Johari-Goldstein process (which is not the case here). The use of theoretical conformational calculations or molecular dynamics simulations to understand the physical existence of the transition at the atomic level has grown in popularity in recent years sometimes combined with experimental studies [69–71]. Additional knowledge is sought to expose

the origin of secondary processes using measured energy barriers and dipole moments when necessary selected versatile end groups to relax following this synergetic approach. Schamme *et al.* successfully identified the origin of the secondary relaxation in quinidine by DFT methods [72]. All of these theoretical data were compared to experimental dielectric findings, and they were found to be in reasonable agreement (considering the experimental uncertainty). These calculations, on the other hand, did not take into account the molten state's average electrostatic behaviour (i.e. closer to the amorphous state).

Schamme *et al.* reported the successful identification of the relevant part of the quinidine molecule which originates the observed secondary relaxation by the quantum computational method using DFT[72]. We have done a similar approach for identifying the origin of the secondary relaxation in title compounds. Quantum computation was done using density functional theory (DFT) with Gaussian 09 software package at B3LYP/6–311 g(d,p) level of theory [73]. The initial geometry of the sample drugs was taken from the PubChem database[74,75] and optimized. From the optimized structures of neat systems, vibrational spectra were calculated. The simulation was further done for investigating side-chain rotation at different relaxed dihedral angle scans on different possible flexible end groups to obtain a potential energy scan. A dihedral angle corresponding to a flexible part of the molecule was continuously rotated in steps of 10o to a complete circle keeping the rest of the molecule optimized, and corresponding energy as well as dipole moment were calculated. The potential energy surface (PES) obtained corresponding to relaxed dihedral scan is used, and the energy change of different potential energy barriers are matched with determined activation energy of secondary relaxation. On repeating this process on different flexible end groups, the relevant molecular side group and the range of dihedral angles corresponding to the expected potential barrier are identified using DFT calculations using Gaussian 09 package[73]. The relevant flexible part of the title molecules that originates the observed secondary relaxation was determined by the exploration of the associated potential energy barriers using the relaxed dihedral scan method [49]. All the DFT calculations were performed in the gas phase and transition states (TS), minima (Min) were identified along with the energy of the potential barrier[76], using the interface Gauss view 05[77] and calculated by using Gaussian 09 package [78].

2.3.13 Molecular docking

Docking is a computer program that predicts the best location for a ligand within a target protein's active site. The grid was specified using the glide ligand docking wizard, and the minimized protein and ligands were chosen for docking. HTVS (High Throughput Virtual Screening), SP (Standard Precision), and XP (Extreme Precision) were chosen over the other two docking procedures (Extra Precision). The XP procedure was chosen for this project because it is the most powerful and discriminating procedure. Docking was done with flexible molecules after the grid and ligands were in place, and proteins were used as rigid molecules. Docking is a molecular modelling technique that predicts one molecule's preferred orientation to another when they are bound together to form a stable complex. Molecular docking is an important tool in structural molecular biology and computer-assisted drug design. The preferred orientation can be used to predict the strength of an affinity between two molecules. Molecular docking is one of the most widely used methods in structure-based drug design because of its ability to predict the binding conformation of small-molecule ligands to the appropriate target binding site. The understanding of fundamental biochemical processes and the rational design of drugs are both aided by the study of binding behaviour. Despite advances in technology and biological system knowledge, drug discovery remains a time-consuming, expensive, difficult, and inefficient process with a low rate of new therapeutic discovery. Because Wodak and Janin's concept of protein docking was later expanded to include interactions between macromolecules and small ligands, protein-protein docking predates protein-ligand (small molecule) docking. Even though there is a significant complication, dealing with flexibility in the binding process is much easier with small molecules. Despite the high computational cost, small molecules make treating binding flexibility much easier, and small molecule docking has become one of the most active research areas in computational drug discovery.

Molecular docking is an in-silico method for predicting the position of small molecules or ligands within the active site of their target protein. Binding pose prediction, bio affinity, and virtual screening are the three main objectives. Docking is a computational simulation of a candidate ligand binding to a receptor. It's a bond between the receptor and the ligand, or between the host and the guests, or between the

lock and the key. It assists in determining the lowest energy state of the receptor-ligand complex. Molecular docking is an important tool in the field of molecular modelling because it is a key component of pharmacodynamics. It aids in the understanding of how drugs work by interacting with protein receptors, as well as determining whether a candidate drug will interact with the target protein appropriately. Molecular docking is a computational chemistry tool that has a clear intuitive definition of finding the structure and binding energy of a protein-ligand complex when the spatial structures of the protein and the ligand are known. Finding the right molecules to modulate the functions of the desired protein, such as a therapeutic target, would be simple with an instrument that can accurately and reliably predict protein-ligand structure. The world of drug discovery and biotechnological applications would have been very different if such instruments had been available. The following are the four major steps involved in docking:

- Protein preparation
- Ligand preparation
- Receptor grid generation
- Glide-ligand docking

Before docking programs can work, the receptor and ligand structures must be carefully prepared. The protein data bank was used to obtain the structures of the proteins used in this study. The protein preparation wizard is used to make proteins. Before they can be used as docking receptors, all protein structures must be pre-processed. Pre-processing operations include the addition of hydrogen atoms, the assignment of atomic charges, and the removal of water molecules that aren't involved in ligand binding. Missing chains and loops can be added if necessary. PROPKA PH 7.0 was used to optimize pre-processed protein and then minimized with OPSL3 force field function, which is followed by a convergence of heavy atoms to RMSD0.3Å. They were used after the samples' optimized structures were converted to mol2 extension structures. The imported structures can be edited using the Schrödinger Maestro's 2D sketcher option. The ligands can then be prepared with the ligprep wizard in the OPLS3 force field. The structures' tautomers were all created. The molecules were then subjected to conformational changes to find the most stable conformer while using the least amount of energy. Creating receptor grids is an important step in the

molecular docking process. As we all know, the grid represents the physical properties of the receptor's volume, especially at the active site. A three-dimensional grid with a maximum size of 20 x 20 x 20 and 0.5 spacing was created using the glide receptor grid generation wizard. The receptor grid generation wizard has enough options to apply any type of constraint, including precision constraints, H-bond constraints, and so on.

2.4 Materials

Table 2.1 List of samples

Name	IUPAC name	Molar mass	Melting point [K]	Water solubility
Brucine	2,3-dimethoxystrychnidin-10-one	394.46 g/mol	451	Insoluble
Colchicine	(1E)-N-[(7S)-1,2,3,10-Tetramethoxy-9-oxo-5,6,7,9-tetra hydro benzo[a]heptalen-7-yl] ethanimidic acid	399.437 g/mol	429	100 mg/mL
Acemetacin	2-[2-[1-(4-chlorobenzoyl)-5- methoxy-2-methylindol-3-yl] acetyl] oxyaceticacid	415.826 g/mol	424	62.4 [ug/mL]
Acetohexam-ide	1-(4-acetylphenyl)sulfonyl-3-cyclohexylurea	324.4 g/mol	463	less than 1 mg/mL at 64° F (NTP, 1992)
Piroxicam	4-Hydroxy-2-methyl-N-(2-pyridinyl)-2H-1,2-benzothiazine-3-carboxamide 1,1-dioxide	331.3 g/mol	474	<1 mg/mL MedChem Express HY-B0253
Griseofulvin	2S,6'R)- 7-chloro- 2',4,6-trimethoxy- 6'-methyl-3H,4'H-spiro [1-benzofuran- 2,1'-cyclohex[2]ene]- 3,4'-dione	352.8 g/mol	493	less than 1 mg/mL at 70° F (NTP, 1992)

Bezafibrate	2-(4-{2-[(4-chlorobenzoyl)amino]ethyl}phenoxy)-2-methylpropanoic acid	361.82 g·mol−1	459	1.55e-03 g/L
Polystyrene800	$[CH_2CH(C_6H_5)]n$	800 g·mol−1	-	-

The list of samples used in the work is listed in Table 2.1. All of the chemicals and materials used were analytical grade and did not require any additional purification. All the samples (>95% purity) were purchased from Sigma Aldrich and were used without further purification.

2.5 Computational tools

In this study, the Gaussian 09W [79] package is used to optimize the structure and find similar parameters for a better understanding of the molecules. All other ab initio codes are measured against the Gaussian standard. The primary advantage of ab initio methods is the accuracy with which calculations are performed. When a researcher needs to know a property that most closely matches experimental data or approximates a theoretical prediction, the ab initio method is used. It is, in essence, the most precise and accurate molecular modelling method currently available. Researchers investigate the properties of molecules using ab initio methods, which are important in the pharmaceutical industry, materials science, and drug design. The Gaussian 09W package [79] program was used by several researchers.

The PubChem database was used to obtain the input structures for the computational calculations. The downloaded structures were converted to Gaussian input files using Open Babel, and GaussView-5.0 was used as an interface for further graphical manipulation. The Gaussian 09W program was used for all other computational calculations. In the respective working chapters, more information on the structures, level of theory, and basis set will be provided. All of the work's computational calculations are done on a Dell Precision T5610 workstation with an Intel Xeon CPU E5-2620 v2 @ 2.10 GHz and 32.0 GB RAM running Windows 10.

John Pople and his research group at Carnegie Mellon University initiated Gaussian 09W [79] program in 1970. In 1970, John Pople and his Carnegie Mellon

University research group launched the Gaussian 09W [54] program. Pople chose Gaussian orbitals over Slater-type orbitals to improve performance on the limited computing capacities of then-current computer hardware for Hartree–Fock calculations, hence the name "Gaussian." It uses fundamental laws of quantum mechanics to predict the energies, molecular structures, vibrational frequencies, and molecular properties of molecules and reactions in a wide range of chemical environments.

It can also be used to study stable species and compounds that are difficult or impossible to observe experimentally (e.g., short-lived intermediates and transition structures). Gaussian 09W generates accurate, reliable, and complete models across the entire periodic table, with a wide range of chemical conditions and problem sizes. Gaussian stands out from other computational tools like Chemcraft, ChemDraw, and Avogadro because of its flexibility and ease of use. The optimization algorithm in Gaussian will change the structure until changes in the gradient and structure on two consecutive iterations converge. Gauss View is a graphical user interface that allows us to prepare input for Gaussian and visually inspect the output generated by Gaussian. Gauss View is a front-end/back-end processor that aids in the use of Gaussian. It is not integrated with the computational module of Gaussian. Gaussian users benefit from Gauss View in three ways. First, Gauss View's advanced visualization feature allows us to quickly sketch in even very large molecules, then rotate, translate, and zoom in on them using simple mouse movements. It can also read PDB files, which are common molecule file formats. Schrödinger Maestro software is used for molecular modelling, simulation, and docking. Schrödinger is a leading provider of advanced molecular simulations and enterprise software solutions for drug discovery and material design that help to improve efficiency and speed up the process. Maestro comes with many measurement tools that allow you to precisely quantify a molecule's structural features. Superimposition tools can be used to compare structures in great detail. It has many viewing options to suit the needs of different applications. This program serves as an interface for several modelling programs, including protein preparation wizard, lig-prep, and glide.

2.6 Experimental Methods

We have used different experimental methods for thermal and dielectric characterization.

2.6.1 Thermal gravimetric analysis

Thermogravimetric analysis (TGA) is a thermal analysis technique that measures the amount of matter in a sample material as a function of time or temperature, or it is an analytic technique that monitors the sample's thermodynamic stability as a function of temperature, or it measures the weight of the sample material when heated or cooled. A sample pan is attached to a well-defined precision balance in TGA. The sample pan is placed inside the furnace and heated throughout the measurement process. During the experiment, the weight of the sample material is visualized. An inert gas, such as nitrogen, regulates the sample's environment and flows through it before exiting through an exhaust. Figures 2.9 and 2.10 show the schematic diagram and figure of the TGA instrument.

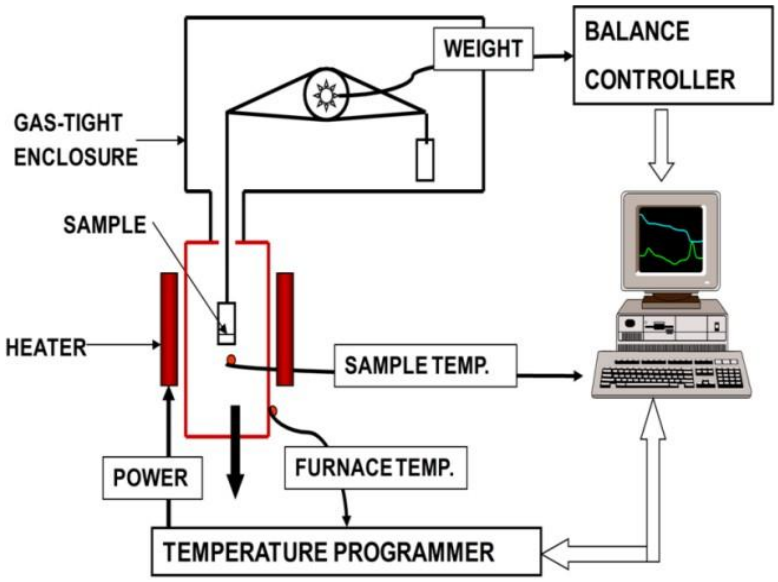

Figure 2.9 Schematic diagram of the thermogravimetric analyzer (TGA)

Figure 2.10 Thermogravimetric Analyzer (TGA)

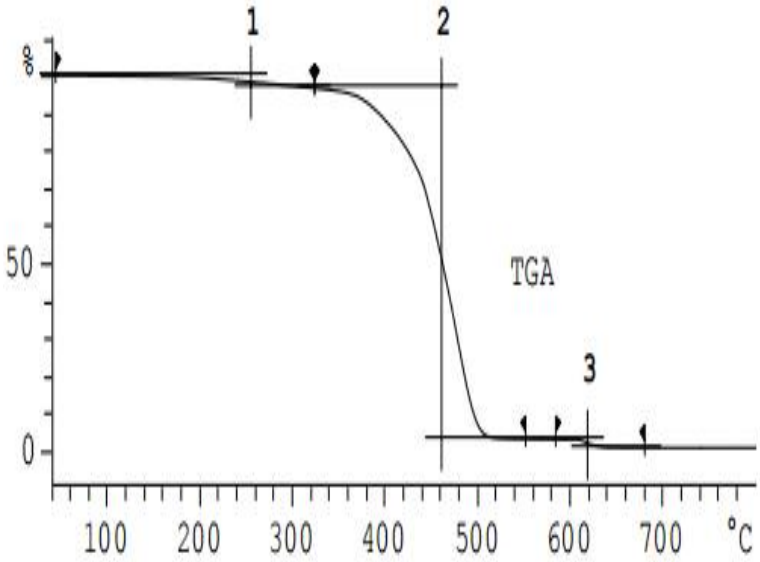

Figure 2.11 A typical TGA curve

Temperature or time is plotted on the X-axis, while weight loss or weight percentage is plotted on the y axis (see figure 2.11). From the lower to the higher temperature side, the curve is monitored. A gradual decrease in this curve indicates that the sample has lost weight or has been thermally degraded. Thermogravimetric analysis (TGA) was done by using TA Instruments Q500 TGA to ascertain the decomposition temperature.

2.6.2 Differential Scanning calorimetry (DSC)

Because of its dependability, simplicity, accuracy, and speed of operation, DSC is one of the most efficient methods of the thermal analysis technique. E.S. Watson and M.J.O Neill invented the DSC technique in 1960. It's a thermoanalytical technique that measures the difference in the amount of heat required to raise the temperature of a sample and a reference as a function of temperature. It is used to investigate the thermal properties of matter, such as phase transition temperatures, glass transition temperatures, crystallization temperatures, melting temperatures, and enthalpies associated with each phase transition. Two pans are used in this thermal analysis: one is the sample pan, and the other is the reference pan, both of which are kept at the same temperature throughout the experiment. The flow of heat (which increases linearly with time) into the sample or from the sample to the system is controlled by a specific program, and the output is monitored by the computer. DSC can be classified into two types based on their mode of operation: Heat flux DSC and power compensated DSC.

Both the sample and reference pans are kept at the same temperature throughout the measuring ranges in heat flux DSC. The sample is poured into the sample pan, which is then placed in the furnace alongside an empty sample pan. The furnace is then heated at a specific rate, with heat flowing through both the sample and reference pans. If a thermodynamic transition occurs in the sample, either heat from the system flows into the sample or heat is released from the sample to the system. The output of the DSC thermogram or DSC curve is the difference in heat flow between the reference and sample. The sample pan and reference pan are placed on separate furnaces in this power compensated DSC method, which keeps the data at a constant temperature throughout the measurement. The difference in thermal power between the sample and the reference is calculated as a function of time or temperature in this experiment. The use of a furnace is the main difference between heat flux and power compensated DSC. Both sample and reference pans are placed in the same furnace in heat flux DSC, but both sample and reference pans are placed in separate furnaces in power compensated DSC.

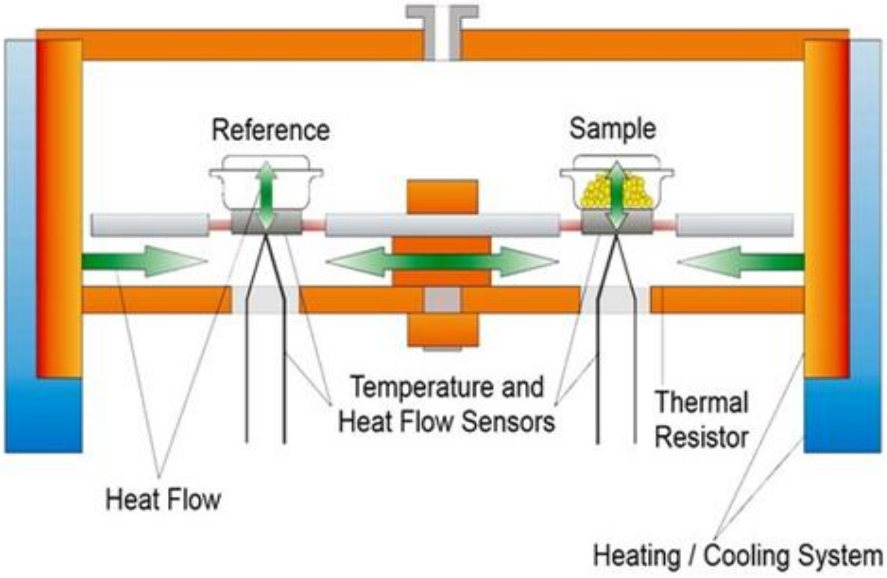

Figure 2.12 Schematic diagram of Heat flux DSC

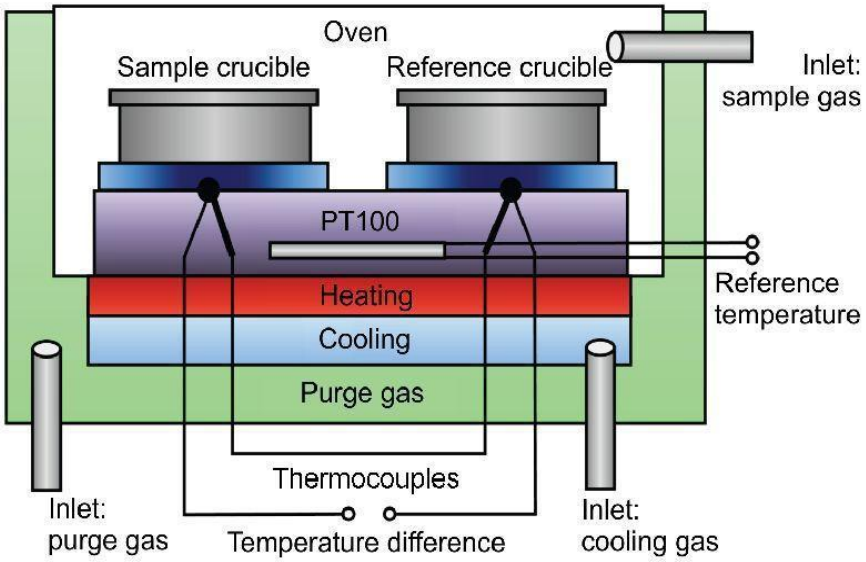

Figure 2. 13 Schematic diagrams of power compensated DSC

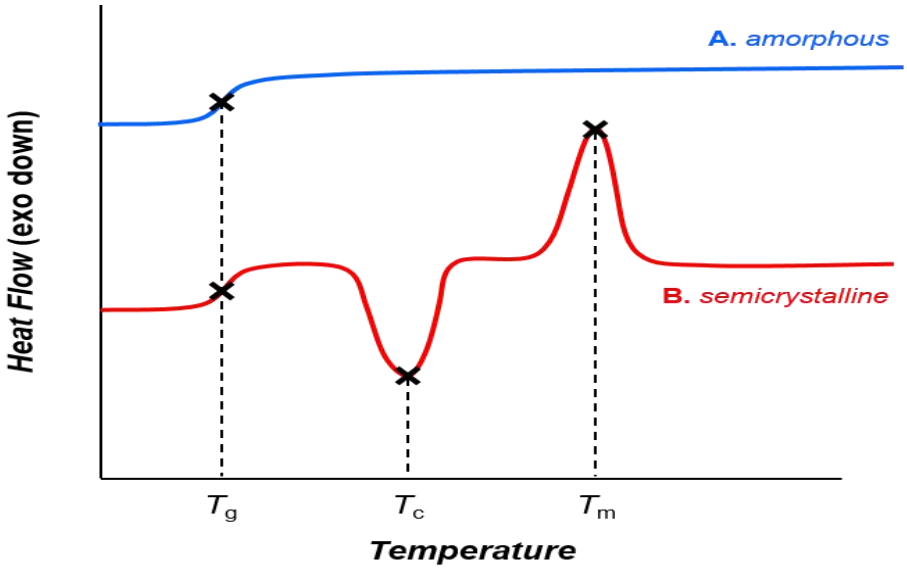

Figure 2.14 Different phase transitions of amorphous and semicrystalline materials

When a sample is heated, two distinct thermodynamic transitions are observed: endothermic process, which is a thermodynamic transition in which a substance absorbs a certain amount of energy in the form of heat; an exothermic process, which is a thermodynamic transition in which a substance absorbs a certain amount of energy in the form of heat. Melting, boiling, sublimation, and vaporization are examples of endothermic processes, whereas crystallization is an exothermic process in which an excessive amount of heat energy is released into the environment from the substance. A small shift in the baseline occurs in the DSC curve as a result of either endothermic or exothermic events occurring on the sample, depending on the sample history. Because it takes more energy to break the bonds between the molecules that make up the sample, the melting transition appears as an endothermic (upward) peak in the DSC curve. The crystallization event appears as an exothermic (downward) peak on the DSC curve because it releases an excess amount of energy into the system to bring the sample to a more thermodynamically stable state. Another small endothermic event is the glass transition, which appears as a small upward peak in the DSC thermogram or a small step-like change in the baseline. Furthermore, the glass transition is a purely kinetic arresting of the entire molecule at glass transition temperature via rapid cooling or heating of the sample at a specific rate, rather than a thermodynamic phenomenon. As a result, the glass transition temperature is strongly influenced by the rate of cooling or heating. During DSC measurements, different heating or cooling rates are provided to

gain a better understanding of glass transition phenomena. A DSC thermogram of a different class of materials (both heat flow and specific heat) is shown in figure 2.15.

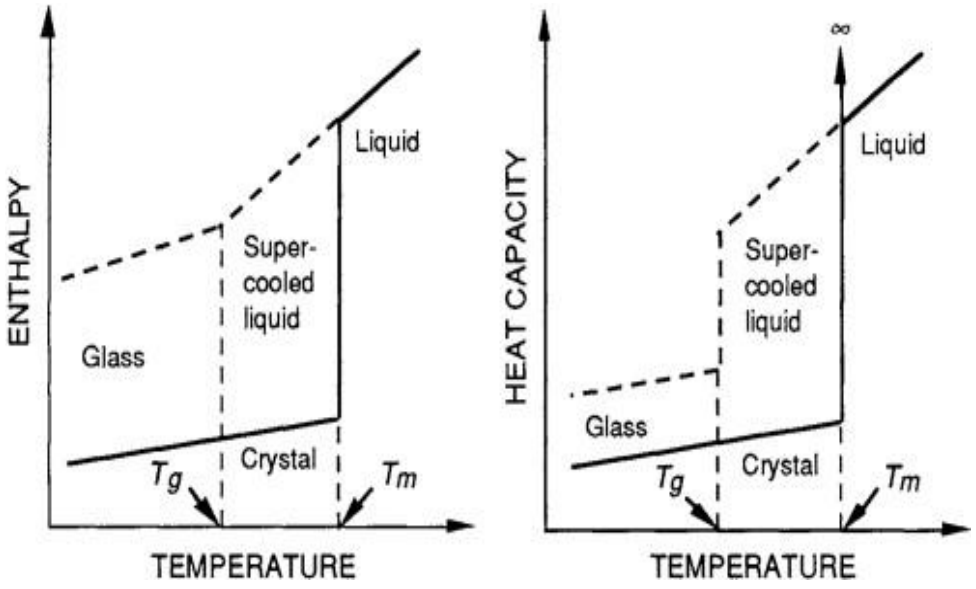

Figure 2.15 Variation of enthalpy and heat capacity on glass formation

DSC measurements were carried out with the help of DSC (Perkin Elmer 8000 series). As standards, high purity indium and zinc were used to calibrate the instrument. The sample is kept at the lowest temperature for few minutes (1-5min). The measurements were taken from deep glassy state to the irrespective melting temperatures with a heating rate of 10K/min. The transition temperatures at the set-out rate of heating are resolved from the DSC thermograms by using the software assigned by the constructor of the device. The sample was placed inside the sealed aluminum pan weighing 25 mg and was heated from room temperature to 5 K above the melting temperature at the heating rate of 10°C/min. Subsequently, the sample was cooled to room temperature at a cooling rate of 10°C/min. The quench-cooled sample was again heated at the heating rate of 10°C/min. Melting point and crystallization temperature were chosen as the peak maxima of the endotherm and exotherm peak respectively while glass transition temperature is taken as the onset of the endotherm peak. The DSC studies of bezafibrate and acetohexamide were performed by using a heat flux differential scanning calorimeter (TA Instruments DSC Q20 V24.11). The instrument was calibrated for temperature and specific heat using pure indium as standard. The sample was kept inside a sealed aluminum pan and heated to a few degrees above its melting temperature and kept for a while, cooled to a deep glassy state, and heated to

ascertain various transition temperatures. The rate of cooling and heating was maintained to be 10 K/min.

2.6.3 FT-IR spectroscopy

For the analysis of solids, liquids, and gases, Fourier transforms infrared spectroscopy (FT-IR) is an analytical tool used to quantitatively spot out the organic or inorganic functional groups in the unknown sample. The basic premise of FT-IR is that each molecular bond vibrates at a different frequency depending on the elements and types of bonds. This technique is used to determine how much-infrared radiation is absorbed by a sample material as a function of wavelength. These absorbed frequencies, according to quantum mechanics, correspond to specific molecular vibrations. The vibrating motion of the bond must change in its dipole moment with time to display the IR spectrum of a molecule. Figure 2.8 shows a schematic diagram for FT-IR spectroscopy.

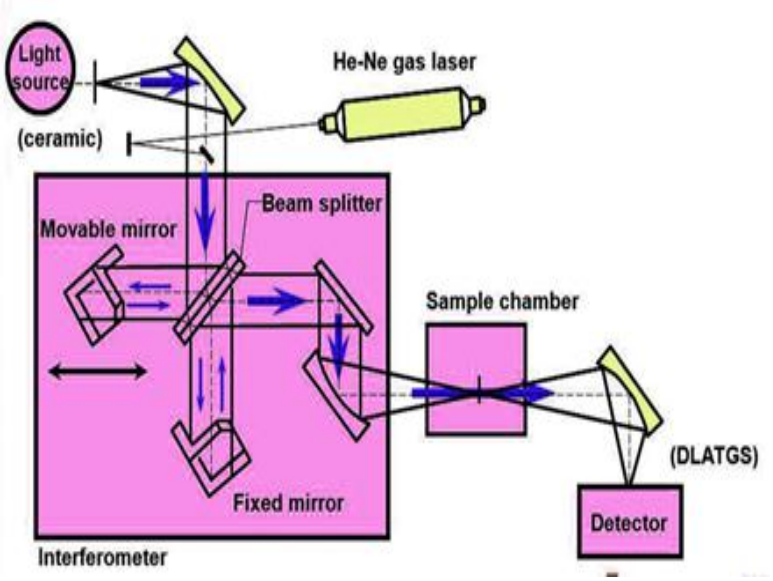

Figure 2.16 Ray diagram of FT-IR spectroscopy

The infrared radiation is allowed to fall on a beam splitter, where 50% of it will be reflected and the rest will be transmitted to a moving mirror, where it will be reflected again. The reflected beam moves towards the mirror and is then reflected on the beaming splitter at the same time. Thus, depending on the position of the moving mirror, the detector can detect two beams simultaneously with an interference pattern;

either constructive interference or destructive interference. Scanning the sinusoidal signal from the moving mirror for a specific frequency over a range can be used to investigate this. Within a fraction of a second, the corresponding Fourier spectrum is computed from the obtained interferogram. The sample techniques vary with the nature of samples; a gas cell with IR transparent window is used for the gaseous samples, two infrared transparent windows can be applied to liquid samples to squeeze it between the windows can be applied to liquid samples to squeeze it between the windows and KBr disc method can be used for the solid samples. The fundamental vibrations of IR vibrations were recorded between the region 4000 and 500 cm^{-1} on a JASCO FT-IR spectroscopy.

Even though this technique fails for some materials, such as films and rubber sheets, experimentalists prefer Attenuated total reflection in these cases (ATR). ATR is frequently used in conjunction with infrared spectroscopy; this quantitative approach allows samples to be examined directly in the solid or liquid state without the need for additional potassium bromide preparation (KBr). Total internal reflection, which results in an evanescent wave, is used in ATR-FTIR spectroscopy. Using a JASCO spectrometer at room temperature in the range of 4000 to 500°C, the attenuated total reflectance-Fourier transform infrared (ATR-FT-IR) spectra of all the film samples in this study were recorded.

2.6.4 FT-Raman spectroscopy

For the collection of spectral data, Raman spectrometers use one of two techniques: dispersion or Fourier Transform (FT). Because impurities are mixed in with the samples, dispersive Raman spectrometers produce interfacing fluorescence. Furthermore, the cost of such equipment, as well as its upkeep, is quite high. As a result, the FT-Raman spectrometer takes the place of the dispersive Raman spectrometer without producing sample fluorescence. The virtual state is lower and will overlap an upper electronic state because the sample is irradiated with a longer wavelength excitation laser. As a result, fluorescence interferences are greatly reduced, and Raman signals are distortion-free. Raman spectroscopy, as it is commonly known, measures intensity versus frequency. FT-Raman, on the other hand, is time-domain spectroscopy that measures the intensity of light at multiple frequencies at the same time. The Fourier transform is then used to convert this spectrum to a conventional spectrum. Fig.

2.9 depicts the FT-Raman spectrometer's block diagram. The source, interferometer, and detector are the three basic spectrometer components in an FT system. In the FT-Raman Spectrometer, lasers are commonly used as radiation sources. They are directional and intense, allowing for spectral recording down to 10 cm^{-1}
from the exciting line. Because most lasers operate at lower frequencies, the fluorescence is also expected to be lower. The most frequently used sources are He-Ne laser (632.8 nm), Argon ion laser (488 and 514.5 nm), Krypton laser (647.1, 568.2, 530.8, 520.8, 482.5, and 476.2 nm), and Ar-Kr mixed laser (488, 514.5, and 647.1 nm). In certain cases, red radiation is preferred to reduce the fluorescence and decomposition of the sample.

An interferometer is used in the FT-Raman spectrometer to create an interferogram, which "encodes" the Raman scattering's unique frequencies into a single signal. The interferometer uses a near-infrared (NIR)-optimized beam splitter to split the incoming Raman signal and scatter into two optical beams, one transmitted and one reflected. The reflected beam travels to a flat fixed mirror and reflects off of it. A flat moving mirror with a constant frequency and fixed motion also receive and reflects the transmitted beam. At the beam splitter, the two beams recombine. The two beams can interfere constructively or destructively depending on their path differences. The interference pattern is modulated by the moving mirror's constant frequency and fixed motion. Every data point (a function of the moving mirror position) in the resulting interferogram has information about every frequency of the Raman scatter collected from the sample. Signal averaging is quick and accurate because the signal can be measured quickly. The interferogram signals are detected by the detector and fed to the computer. It's a time-domain spectrum that records changes in detector response overtime during a mirror scan. The amplitude of the sinusoidal wave is reduced by an amount proportional to the amount of sample in the beam if the sample absorbs the signal at this frequency. The interferogram contains data from the entire Raman region where the detector responds. After calibrating the original data concerning the known wave number relationship, the required Raman shift is obtained. In photon counts, the plot represents the wavenumber and relative scattering intensity.

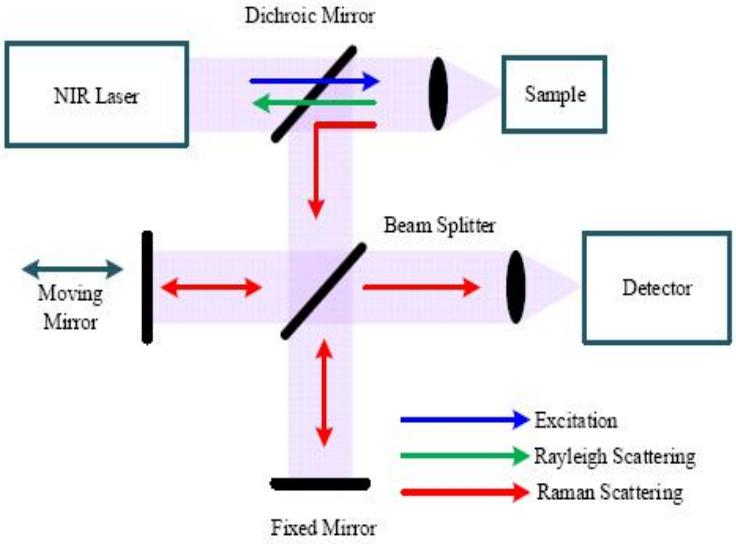

Figure 2.17 The block diagram of the FT-Raman spectrometer

2.6.5 UV-Visible spectroscopy

UV-Visible Spectroscopy is used as an analytical technique because it can be used to determine the strength and content of a substance as well as identify some functional groups present in molecules. For a variety of tasks, it is widely used in chemical and biochemical laboratories. It can be used to determine small amounts, such as trace metal content in alloys or the amount of a drug that reaches different parts of the body. The absorption of electromagnetic radiation by organic compounds with valence electrons that can be excited to higher energy levels causes the UV-Vis Spectrum. Because the spectra are the result of bonding electron excitation, the wavelength of the absorption peaks can be correlated with the type of bands in the compound under investigation. One or more broad speaks in the wavelength range of 200-400 nm make up the ultraviolet spectra. The region between 200 and 380 nm is known as the near UV region, while the region below 200 nm is known as the far or vacuum UV region. There are three types of electron orbitals in which valence electrons can be found. Single or bonding orbitals, double or triple bonding orbitals, and non-bonding orbitals are the different types of orbitals. Bonding orbitals have lower energy than non-bonding orbitals, and non-bonding orbitals have lower energy than bonding orbitals. When electromagnetic radiation of the correct frequency is absorbed, a transition occurs from one of the orbitals to an empty orbital, usually an antibonding orbital –σ* or π*. Most of the transitions from bonding orbitals are too

high a frequency, so most of the absorptions involve only π→π*, n→σ*, σ→σ* and n→ π* transitions. When the selection rules are applied, the first three transitions are usually allowed whereas the n→ π* transition is forbidden. Bands attributed to π→π* transitions are also called K-bands, which appear in molecules that contain conjugated π systems. R-bands also called forbidden bands to originate due to n→π* transition of a single chromophoric group and having at least one lone pair of electrons on the heteroatom. B-bands or Benzenoid bands arise due to π→ π*, transition in aromatic molecules. E or Ethylenic bands originate due to the electronic transitions in the benzenoid system of three ethylenic bonds which are inclosed cyclic conjugation [Kalsi 2002, Sharma1999].

Beer's Law and Lambert's Law are two laws that govern molecule absorption of flight. According to Beer's law, light absorption is proportional to concentration. Lambert's law states that the fraction of incident light absorbed is proportional to the total absorption of the optical path length, not to the intensity of the source. The Beer-Lamberts law is given by the equation A=Cl, where is the molar absorptivity or extinction coefficient and is a molecule characteristic, l is the optical path length in cm, and C is the concentration of the absorbing molecules in moles per litre.

The optical section of the spectrophotometer is made up of three basic modules: the light source, the dispersive system (combined in a monochromator), and the detector system. Depending on the instrument design, a sample compartment is inserted into the optical path either before or after the dispersive system. For the visible region of the system, an incandescent lamp with a tungsten filament housed in silica glass is used, and for the UV region, a deuterium arc lamp working under a slight pressure is used. For visible wavelengths, light-emitting diodes (LED) and xenon arc lamps have recently been used. A planar or concave grating, which is part of a monochromator assembly, disperses the light emitted by the source. Monochromators filter the light so that only light of a single wavelength reaches the detector, and photodiodes are used with them. Charged coupled devices (CCDs) use diffraction gratings to collect light of different wavelengths on different pixels. The detector converts the light intensity it receives into an electrical signal. A photomultiplier tube or a semiconductor detector is used, and the intensity of both is dependent on the wavelength. Detector technology has recently improved; the diode array detector

allows simultaneous detection across the entire range, allowing for rapid quantification of absorbing species. Single-beam or double-beam spectrophotometers are available. In a single-beam spectrophotometer, the blank solution's transmittance is set to 100 percent before each wavelength measurement. These spectrophotometers have a simple design, are inexpensive, and can be used for analysis if the wavelengths of measurements aren't changed very often. In UV-Vis spectrometric analysis, double beam spectrophotometers are the most commonly used instruments.

Figure 2.10 shows a schematic of the optical path. A prism or diffraction grating separates a beam of light from a visible or UV light source into its component wavelengths. A half-mirrored device divides each monochromatic beam into two equal intensity beams. The sample beam passes through a small transparent container (cuvette) containing a solution of the compound under investigation in a transparent solvent. The reference bream goes through an identical cuvette that only contains solvent. For work in the ultraviolet region, the cuvette is usually made of quartz. To minimize reflection loss, the best cells have windows that are perfectly normal to the direction of the beam. The cells' entrance and exit sides are made of plane-parallel surfaces. The radiation from the sample and reference cells is received by a photomultiplier tube, which produces photocurrent proportional to the incident radiation. Certain solid-state detectors are also used for this purpose. Microprocessors are incorporated or mostly computers are incorporated for the control and monitoring of entire sequences of operations.

This instrument uses two lamps: a tungsten lamp that covers the wavelength range of 350 to 1100 nm, and a deuterium lamp that covers the wavelength range of 190 to 350 nm. With the monochromator mounted onto a highly stable optical bench to ensure the integrity and trouble-free operation, this double beam instrument offers the very best in modern grating technology. The detector is a silicon photodiode, and the instrument can be used in scanning spectrum, kinetics, or quantitative modes. The Shimadzu UV-Probe software is used to control data acquisition and processing.

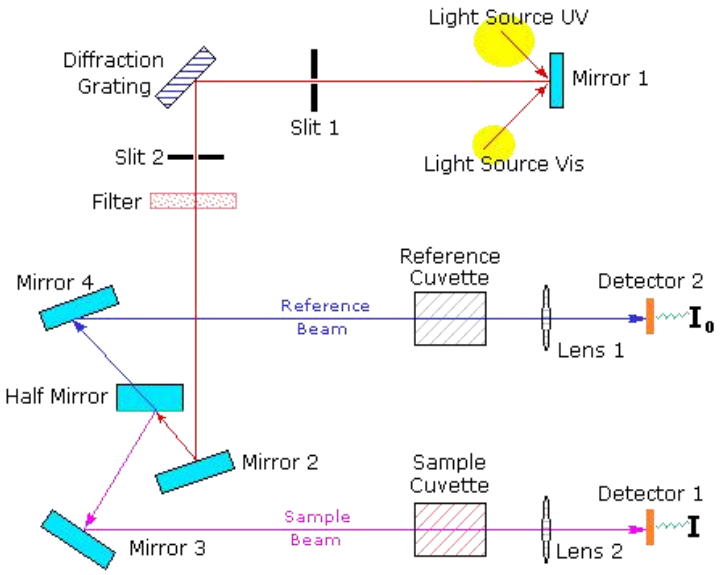

Figure 2.18 Optical path diagram of UV-Visible spectrophotometer

2.6.6 Broadband dielectric spectroscopy (BDS)

In the frequency domain, the interaction of an electromagnetic wave with a matter is well described using an experimental technique known as broadband dielectric spectroscopy (BDS) in the range of 10^{-2} to 10^{7} Hz. The primary goal of dielectric measurement of a sample over a broad frequency range is to investigate the electrical and dielectric properties of materials when they are exposed to a time-varying electric field. Because the electric field is directly coupled to the reorientation motion of a dipolar molecule as well as the translational motion of the charged species of the molecule, it is one of the most widely used experimental techniques for dielectric measurement. It can detect even minute phase transitions in the material under investigation due to its high sensitivity compared to other techniques. BDS can determine the material's complex impedance, from which we can derive several physical parameters such as complex dielectric permittivity, complex electric modulus, and complex conductivity, among others. As a function of frequency and temperature, molecular dynamics are investigated in terms of complex dielectric permittivity and complex electric modulus. When a dielectric material is sandwiched between two parallel plate capacitors and placed in a time-varying electric field, four different types of dielectric polarisation are induced:

1. Electronic polarization
2. Ionic polarization
3. Orientational polarization
4. Space charge or interfacial polarization.

By probing rotational fluctuations of molecular dipoles, charge transport, and ion hopping, BDS has been widely used as a versatile tool to investigate molecular dynamics. The composite information about the molecular ensemble and its dynamics can be deduced by extracting the impedance data and analyzing the dielectric function. This method allows us to investigate molecular motions on a variety of length scales, from fluctuations within a monomeric unit to the macromolecular level. Because dipoles provide the link between molecular motions and interactions with an external electric field, the presence of dipoles is a requirement for applying BDS to any system. This method can be used to investigate a wide range of systems containing monomers to polymers in various states, such as solids, liquids, glasses, rubbers, and so on. With advancements over the last few decades, this technique can now explore the system in an extremely wide frequency window of about 15 decades in a single click to explore the dynamics at different time scales while keeping the temperature and pressure constant. Figure 2.11 shows a schematic diagram of the BDS setup, which includes an alpha-beta analyzer, cryostat, and sample holder. This method determines the complex impedance of a capacitor with an empty capacitance C_0 and a sample material that fills it. Accurate measurements of electrode diameters (d) and sample thickness (l) are pre-requisite conditions for accuracy of the results and they will be used in the time of conversions between the different data representations (impedance, permittivity, conductivity, conductance, capacitance, etc.,). A sinusoidal voltage $E=E_0\exp(i\omega t)$ at a particular frequency ω is applied to the cell and the corresponding current as given below is measured across it.

$$\mathbf{I_s(t) = V\exp(j\omega t + \varphi)} \tag{2.45}$$

Where φ is the phase angle that depends upon the frequency and the properties of the sample. The phase angle (φ) is the difference in phase between the applied electric field and the current. The complex impedance of the material is then calculated as the ratio of an applied voltage to a complex current. The complex dielectric permittivity, complex electric modulus, complex conductivity, and so on can be derived and

expressed in the following form using this complex impedance. The circuit diagram and the schematic diagram are shown in Figures 2.12 and 2.13.

Figure 2.19 Broadband dielectric spectrometer- NoVo control (10^{-3}–10^{7}Hz)

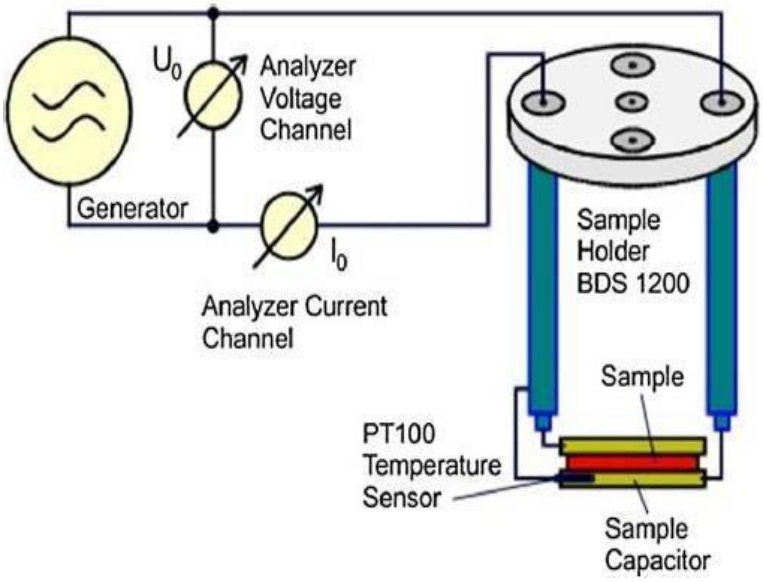

Figure 2.20 Circuit diagram of a broadband dielectric spectrometer

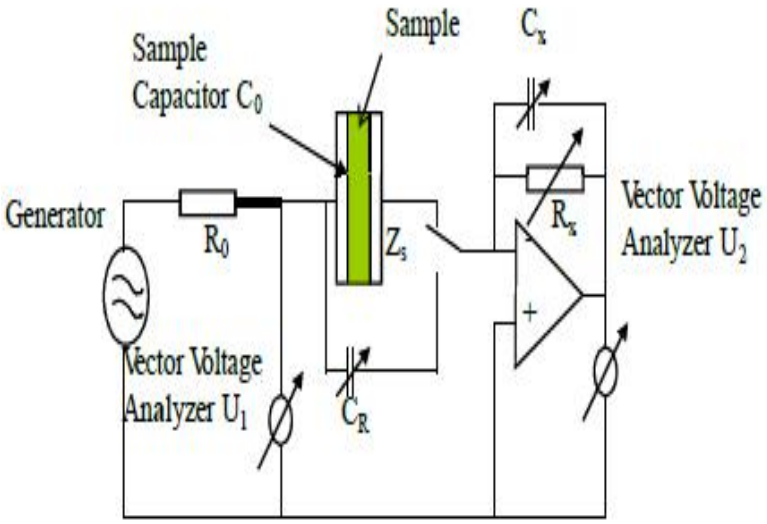

Figure 2.21 Schematic diagram of a broadband dielectric spectrometer

From the applied voltage and measured current, the value of the complex impedance can be calculated using the following equation

$$\mathbf{Z^*(\omega)} = \frac{\mathbf{V^*(\omega)}}{\mathbf{I^*(\omega)}} \tag{2.46}$$

The dielectric measurements of the capacitance C(ω) and the conductance G(ω) as a function of frequency are presented in terms of three equivalent forms: the complex conductivity, $\sigma^*(\omega)$, the complex permittivity $\varepsilon^*(\omega)$ and the complex electric modulus $M^*(\omega)$. They are equivalent because of their identities,

$$\mathbf{M^*(f)} = \frac{\mathbf{1}}{\boldsymbol{\epsilon}^*\mathbf{(\omega)}} = \frac{\mathbf{i\omega\varepsilon_0}}{\boldsymbol{\sigma}^*\mathbf{(\omega)}} \tag{2.47}$$

Where ε_0 is the permittivity of vacuum.

The complex permittivity can be calculated from the complex impedance as given below

$$\boldsymbol{\epsilon}^*\mathbf{(\omega)} = \boldsymbol{\varepsilon}^{'}\mathbf{(\omega)} - \mathbf{j}\boldsymbol{\varepsilon}^{''}\mathbf{(\omega)} = \frac{\mathbf{1}}{\mathbf{j\omega C_0 Z^*(\omega)}} \tag{2.48}$$

Permittivity is considered vital material parameters that measure, how much the molecules of that material oppose the applied electric field. The relative permittivity of a material compared to the permittivity of a vacuum is known as the dielectric constant of that material. The complex electric modulus is given as,

$$\mathbf{M^*(\omega) = M'(\omega) + jM''(\omega) = \frac{1}{\varepsilon^*(\omega)}} \tag{2.49}$$

It is a more direct way to exhibit the frequency dispersion of the primary α conductivity relaxation as done earlier for many ions conducting glass formers. In the case of conducting materials; either ionic or electric, the dielectric loss spectra are dominated by dc conductivity towards low frequencies arising from the conductivity contribution of the ions. Subsequently, the information on the structural relaxation often is not directly observable. The corresponding information available from the real part of permittivity will be masked by the electrode polarization at the same time. In such situations, modulus formalism can be used to overcome the problems above. The real and imaginary parts of M* can be related to ε* through the following relations.

$$\mathbf{M'(\omega) = \frac{\varepsilon'(\omega)}{(\varepsilon'(\omega))^2 + (\varepsilon''(\omega))^2}} \tag{2.50}$$

$$\mathbf{M''(\omega) = \frac{\varepsilon''(\omega)}{(\varepsilon'(\omega))^2+(\varepsilon''(\omega))^2}} \tag{2.51}$$

In this formalism, temperature-dependent peaks arise by suppressing the conductivity and electrode contributions, which can be assumed to be related to the translational ionic motions. The corresponding relaxation time of temperature-dependent peaks observed in modulus formalism can be called the conductivity relaxation time. Therefore, the data of some samples in this work were presented in electric modulus formalism since all the information regarding structural relaxations in the permittivity window were masked by the dc conductivity due to the hopping of ions in some samples. The main advantages of using electric modulus formalism for interpreting the relaxation phenomena are; large variations in the permittivity and loss at low frequencies and high temperatures are minimized. Moreover, the electrode polarization effects; difficulties occurring from the electrode nature, the electrode-specimen contact and the injection of space charges and absorbed impurities can be neglected in electric modulus. Subsequently, all the data were depicted in the modulus formalism and fitted with the Havriliak Negami equation.

$$\boldsymbol{M^*(i\omega) = M_\infty[1 - \int_0^\infty \exp(-i\omega t)(-\frac{d\varphi}{dt})]} \tag{2.52}$$

Whose Fourier transform is given by

$$\mathbf{M^*(\omega) = M_\infty + \frac{\Delta M}{(1 + (-i(\omega\tau_{HN})^{-1})^{1-\alpha})^{\beta}}} \tag{2.53}$$

Where α and β are shaping parameters and $\varphi(t)$ is the Kohlrausch-William-Watts (KWW) function.

$$\boldsymbol{\varphi(t) = \exp\left[-\left(\frac{t}{\tau_{\sigma\alpha}}\right)^{1-n}\right]} \tag{2.54}$$

Thus, the HN equation can be used to find out the temperature dependence of α- conductivity relaxation time, $\tau_{\sigma\alpha}$, frequency dispersion parameters, as well as dc conductivity term at various temperatures. Similarly, the skew asymmetric conductivity α-loss peak is well fitted by the Fourier transform of the Kohlrausch-William-Watts stretched exponential function as like done before for some pharmaceutical systems.

$$\mathbf{C(t) = \left\{-\left[\frac{t}{\tau_\sigma(T)}\right]^{1-n}\right\}} \tag{2.55}$$

Where $\tau_\sigma(T)$ is σ conductivity relaxation time, while the dc conductivity σ_{dc} can be calculated from mean conductivity relaxation time as given by

The plot of complex dielectric permittivity or complex electric modulus versus the frequency of the applied electric field depicts the materials' dielectric response. Complex dielectric spectra are the name for this type of graph. Because the frequency range of measurements in BDS is 10^{-2} to 10^7Hz, the dielectric spectra are dominated by orientational polarization and electrode polarization effects. A capacitor is formed by sandwiching a sample material between the upper and lower electrodes of the dielectric cell, which are separated by a Teflon spacer.

$$\boldsymbol{\epsilon^*(\omega) = \frac{1}{i\omega Z^*(\omega) C C_0}} \tag{2.56}$$

$$\boldsymbol{\sigma^*(\omega) = \frac{d}{Z^*(\omega) A}} \tag{2.57}$$

Where ω is the frequency of the applied electric field, $Z^*(\omega)$ is the complex impedance of the material under study, C_0 is the empty cell capacitance, d is the spacing of the electrodes of parallel plate capacitor and A is the area of the electrode. The circuit

diagrams and basic principles underlying inside a broadband dielectric spectrometer are elaborately illustrated in figures 2.14 and 2.15 respectively.

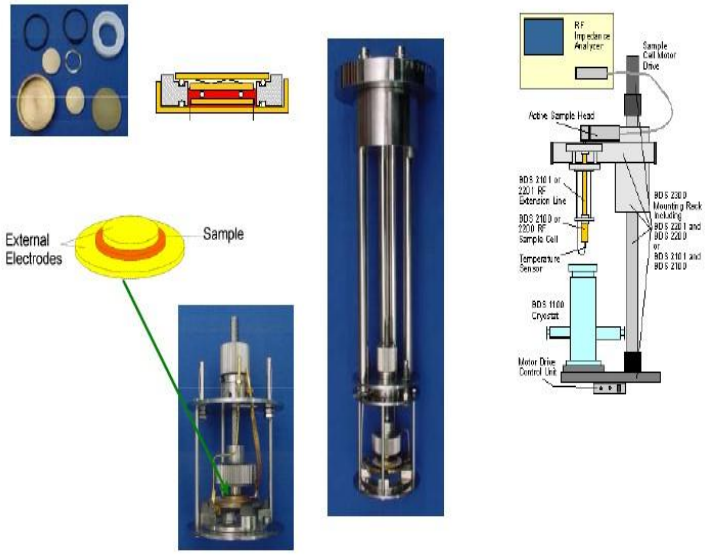

Figure 2.22 Novo-control quarto cryo system (93K to 573K)

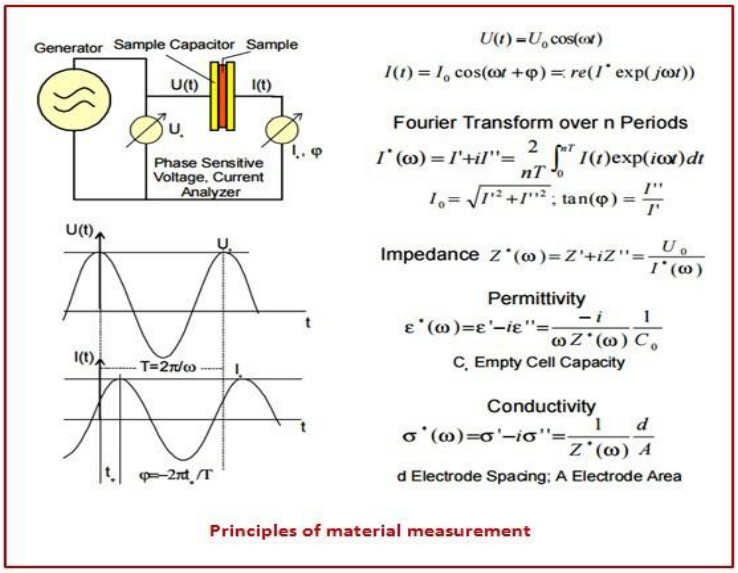

Figure 2.23 Basic principle of broadband dielectric spectroscopy

Isobaric measurements of the dielectric permittivity ε*(ω) = ε′(ω) − iε″(ω) were carried out using the Alpha analyzer (Novo-Control Technologies) over the frequency range from 1×10^{-2} to 1×10^{7} Hz at ambient pressure. Initially, the sample is kept between two stainless steel circular parallel plates separated with a narrow Teflon having an effective spacing of 0.1mm and having an effective diameter of 30mm. The sample was quickly supercooled down to its deep glassy state and at the time an ac

electric field of appropriate voltage is also applied and the measurements were done during heating by stabilizing the sample at the set point for about 600 minutes before taking measurement. From the measured complex impedance, all the relevant parameters like complex permittivity, complex electric modulus can be extracted. After performing the dielectric measurements on the sample, the real and imaginary part of the complex dielectric permittivity or complex electric modulus is plotted as a function of frequency. From these plots, various dielectric parameters are extracted. Each of the tested samples was placed between two stainless steel electrodes (Cylindrical shape, diameter 30 mm, gap 0.2 mm) and mounted on a cryostat maintained under dry nitrogen gas flow. Two poly Tetra Fluoro Ethylene strips were placed on the lower side of the crystalline sample. These strips prevent direct contact between the upper and lower electrodes when the sample is in a molten state and ensured constant thickness of the molten sample throughout the experiment. The temperature was controlled by QuatroSystem using a Nitrogen gas cryostat, with stability better than 0.1 K. Dielectric measurements were performed after its vitrification by heating the samples to the temperature of T_m+5K, and held for 10 minutes, then quench cooling the melt of the samples at 10K/min to 123.15K. The dielectric measurements were taken from 123.15K to a few degrees below melting temperature in different steps of increase in temperature. The fresh amorphous sample is prepared by quench cooling each time and the BDS instrument is calibrated by an empty cell. The dielectric data is fitted with winfit software provided by Novocontrol technologies.

Complex dielectric permittivity, [$\varepsilon^*(\omega) = \varepsilon'(\omega) - i\varepsilon''(\omega)$] in supercooled liquid and glassy phases of the samples are measured at different temperatures and the measured dielectric data was fitted by Havriliak - Negami (HN) given by equation (2.58)[18]

$$\boldsymbol{\varepsilon^*(\omega) = -\,i\left(\frac{\sigma_{dc}}{\omega\varepsilon_0}\right) + \varepsilon_\infty + \frac{\Delta\epsilon}{\left(1 + \left(i\omega\tau_{HN}\tau\right)^{(\alpha_{HN})}\right)^{\beta_{HN}}}} \qquad (2.58)$$

Where ε_∞ is the high-frequency limit of ε', $\Delta\varepsilon$ is the dielectric strength, and τ_{HN}_is the characteristic relaxation time of the medium, σ_{dc} is the dc conductivity, α and β are fractional shape parameters ($0 < \alpha < 1$ and $0 < \beta < 1$) which describe the symmetric and asymmetric broadening of the dielectric loss curves respectively The conductivity

contribution is represented by the first term is added to the imaginary part, where σ_0 is the conductivity due to the translational motion of the ions, ε_0 is the permittivity of vacuum and N is a fractional exponent. After fitting the conductivity contribution is subtracted from the dielectric data. The α relaxation time τ_α is obtained as τ_{max} calculated from the HN fit parameters, after subtracting the conductivity contribution.

Relaxation time is further calculated from the above parameters using the equation given by,

$$\tau = \tau_{HN} \times \left[sin\left(\frac{\alpha_{HN}\pi}{2+2\beta_{HN}}\right)^{-\frac{1}{\alpha_{HN}}} \left(sin\left(\frac{\alpha_{HN}\beta_{HN}\pi}{2+2\beta_{HN}}\right)^{\frac{1}{\alpha_{HN}}} \right) \right] \quad (2.59)$$

Fitting and analysis part of the dielectric data is performed by using a computer simulation programming employed via Havriliak -Negami empirical relation of the glass forming system and fitting parameters are deduced. By using the fitting parameters, the different types of plots are drawn as a function of either frequency or temperature, such as the Arrhenius diagram, map of dielectric strength, Angell plot, etc. Since structural relaxation strongly deviates from Arrhenius behaviour, the α relaxation peak is usually fitted by a non-linear curve via an empirical relation known as the Vogel-Fulcher-Taman equation or VFT. The nonlinear temperature dependence of the α process was fitted by the Vogel-Fulcher-Tamann (VFT) equation (Eq.3.3) [70, 24, 65].

$$\tau_\alpha = \tau_\infty \exp\left(\frac{DT_0}{T-T_0}\right) \quad (2.60)$$

where T is the absolute temperature, D is the strength parameter and T_0 is the VFT temperature (ideal glass transition temperature) at which all important molecular motion stops and relaxation time becomes infinity. From the VFT fit, the glass transition temperature, fragility, and activation energy for the α process are obtained. Glass transition temperature is obtained via a general definition i.e., the temperature at which relaxation time becomes 100 seconds and should correlate with those obtained from calorimetric measurement. Secondary relaxations display an Arrhenius or thermally activated behaviour and are fitted by using the Arrhenius equation. From the linear fit of secondary relaxation time, the activation energy for molecules to participate in this non-co-operative process is calculated. There exists another plot essentially

useful for the classification of glass-forming systems is known as the Angell plot, which is plotted as a function of T_g/T vs logarithm of relaxation time. From the Angell plot, the fragility index or steepness index is extracted by taking the slope of the Angell plot. Based on the value of the fragility index, systems are categorized into strong and fragile.

References

[1] M.G. Abiad, M.T. Carvajal, O.H. Campanella, A Review on Methods and Theories to Describe the Glass Transition Phenomenon: Applications in Food and Pharmaceutical Products, Food Eng. Rev. 1 (2009) 105–132. https://doi.org/10.1007/s12393-009-9009-1.

[2] S. Yoshioka, Y. Aso, Correlations between Molecular Mobility and Chemical Stability During Storage of Amorphous Pharmaceuticals, J. Pharm. Sci. 96 (2007) 960–981. https://doi.org/https://doi.org/10.1002/jps.20926.

[3] C. Mao, S.P. Chamarthy, R. Pinal, Time-Dependence of Molecular Mobility during Structural Relaxation and its Impact on Organic Amorphous Solids: An Investigation Based on a Calorimetric Approach, Pharm. Res. 23 (2006) 1906–1917. https://doi.org/10.1007/s11095-006-9008-3.

[4] A.A. Miller, ``Free Volume'' and the Viscosity of Liquid Water, J. Chem. Phys. 38 (1963) 1568–1571. https://doi.org/10.1063/1.1776922.

[5] M.L. Williams, R.F. Landel, J.D. Ferry, The Temperature Dependence of Relaxation Mechanisms in Amorphous Polymers and Other Glass-forming Liquids, J. Am. Chem. Soc. 77 (1955) 3701–3707. https://doi.org/10.1021/ja01619a008.

[6] G. Adam, J.H. Gibbs, On the Temperature Dependence of Cooperative Relaxation Properties in Glass-Forming Liquids, J. Chem. Phys. 43 (1965) 139–146. https://doi.org/10.1063/1.1696442.

[7] D. Prevosto, M. Lucchesi, S. Capaccioli, R. Casalini, P.A. Rolla, Correlation between configurational entropy and structural relaxation time in glass-forming liquids, Phys. Rev. B. 67 (2003) 174202. https://doi.org/10.1103/PhysRevB.67.174202.

[8] K.A. Graeser, J.E. Patterson, J.A. Zeitler, T. Rades, The Role of Configurational Entropy in Amorphous Systems, Pharmaceutics. 2 (2010) 224–244. https://doi.org/10.3390/pharmaceutics2020224.

[9] O. Yamamuro, I. Tsukushi, A. Lindqvist, S. Takahara, M. Ishikawa, T. Matsuo, Calorimetric Study of Glassy and Liquid Toluene and Ethylbenzene: Thermodynamic Approach to Spatial Heterogeneity in Glass-Forming Molecular Liquids, J. Phys. Chem. B. 102 (1998) 1605–1609. https://doi.org/ 10.1021/ jp973439v.

[10] H. Tanaka, Two-order-parameter model of the liquid–glass transition. I. Relation between glass transition and crystallization, J. Non. Cryst. Solids. 351 (2005) 3371–3384. https://doi.org/https://doi.org/10.1016/j.jnoncrysol. 2005.09.008.

[11] H. Tanaka, Relation between Thermodynamics and Kinetics of Glass-Forming Liquids, Phys. Rev. Lett. 90 (2003). https://doi.org/10.1103/ physrevlett. 90.055701.

[12] A.S. Volkov, G.D. Koposov, R.O. Perfil'ev, A. V Tyagunin, Analysis of Experimental Results by the Havriliak–Negami Model in Dielectric Spectroscopy, Opt. Spectrosc. 124 (2018) 202–205. https://doi.org/10.1134/ S0030400X18020200.

[13] P. Debye, Zur Theorie der spezifischen Wärmen, Ann. Phys. 344 (1912) 789–839. https://doi.org/https://doi.org/10.1002/andp.19123441404.

[14] E. [ORNL] Tuncer, J. [Universite I.T. Bellatar, M.E. [Universite I.T. Achour, C. [Universite de B. Brosseau, Broadband spectral analysis of non-Debye dielectric relaxation in percolating heterostructures, INTECH, New York, NY, USA, United States, 2011. https://www.osti.gov/biblio/1056893.

[15] K.S. Cole, R.H. Cole, Dispersion and Absorption in Dielectrics I. Alternating Current Characteristics, J. Chem. Phys. 9 (1941) 341–351. https://doi.org/ 10.1063/1.1750906.

[16] T.P. Iglesias, G. Vilão, J.C.R. Reis, An approach to the interpretation of Cole–Davidson and Cole–Cole dielectric functions, J. Appl. Phys. 122 (2017) 74102. https://doi.org/10.1063/1.4985839.

[17] T. Dotson, J. Budzien, J. McCoy, D. Adolf, Cole-Davidson dynamics of simple chain models, J. Chem. Phys. 130 (2009) 24903. https://doi.org/10.1063/1.3050105.

[18] S. Havriliak, S. Negami, A complex plane representation of dielectric and mechanical relaxation processes in some polymers, Polymer (Guildf). 8 (1967) 161–210. https://doi.org/https://doi.org/10.1016/0032-3861(67)90021-3.

[19] K. Ngai, The vestige of many-body dynamics in relaxation of glass-forming substances and other interacting systems, Philos. Mag. A-Physics Condens. Matter Struct. Defects Mech. Prop. - PHIL MAG A. 87 (2007) 357–370. https://doi.org/10.1080/14786430600900112.

[20] J. Colmenero, A. Arbe, G. Coddens, B. Frick, C. Mijangos, H. Reinecke, Crossover from Independent to Cooperative Segmental Dynamics in Polymers: Experimental Realization in Poly(Vinyl Chloride), Phys. Rev. Lett. 78 (1997) 1928–1931. https://doi.org/10.1103/PhysRevLett.78.1928.

[21] K.L. Ngai, Relation between some secondary relaxations and the α relaxations in glass-forming materials according to the coupling model, J. Chem. Phys. 109 (1998) 6982–6994. https://doi.org/10.1063/1.477334.

[22] K.L. Ngai, R.W. Rendell, Basic Physics of the Coupling Model: Direct Experimental Evidences, in: Supercooled Liq., American Chemical Society, 1997: pp. 4–45. https://doi.org/doi:10.1021/bk-1997-0676.ch004.

[23] K.L. Ngai, An extended coupling model description of the evolution of dynamics with time in supercooled liquids and ionic conductors, J. Phys. Condens. Matter. 15 (2003) S1107–S1125.

[24] M. Paluch, J. Knapik, Z. Wojnarowska, A. Grzybowski, K.L. Ngai, Universal Behaviour of Dielectric Responses of Glass Formers: Role of Dipole-Dipole Interactions, Phys. Rev. Lett. 116 (2016) 1–6. https://doi.org/10.1103/PhysRevLett. 116.025702.

[25] R. Kohlrausch, Theorie des elektrischen Rückstandes in der Leidener Flasche, Ann. Phys. 167 (1854) 56–82. https://doi.org/https://doi.org/10.1002/andp.18541670103.

[26] G. Williams, D.C. Watts, Non-symmetrical dielectric relaxation behaviour arising from a simple empirical decay function, Trans. Faraday Soc. 66 (1970) 80–85. https://doi.org/10.1039/TF9706600080.

[27] R. Zorn, A. Arbe, J. Colmenero, B. Frick, D. Richter, U. Buchenau, Neutron scattering study of the picosecond dynamics of polybutadiene and polyisoprene, Phys. Rev. E. 52 (1995) 781–795. https://doi.org/10.1103/PhysRevE.52.781.

[28] J. Colmenero, A. Arbe, A. Alegría, Crossover from Debye to non-Debye dynamical behaviour of the \ensuremath{\alpha} relaxation observed by quasielastic neutron scattering in a glass-forming polymer, Phys. Rev. Lett. 71 (1993) 2603–2606. https://doi.org/10.1103/PhysRevLett.71.2603.

[29] K.Y. Tsang, K.L. Ngai, Relaxation in interacting arrays of oscillators, Phys. Rev. E. 54 (1996) R3067–R3070. https://doi.org/10.1103/PhysRevE.54.R3067.

[30] K.Y. Tsang, K.L. Ngai, Dynamics of relaxing systems subjected to nonlinear interactions, Phys. Rev. E. 56 (1997) R17–R20. https://doi.org/10.1103/PhysRevE.56.R17.

[31] J.R. Macdonald, The Ngai coupling model of relaxation: Generalizations, alternatives, and their use in the analysis of non-Arrhenius conductivity in glassy, fast-ionic materials, J. Appl. Phys. 84 (1998) 812–827. https://doi.org/10.1063/1.368142.

[32] S.A. Reinsberg, X.H. Qiu, M. Wilhelm, H.W. Spiess, M.D. Ediger, Length scale of dynamic heterogeneity in supercooled glycerol near Tg , J. Chem. Phys. 114 (2001) 7299–7302. https://doi.org/10.1063/1.1369160.

[33] C.-Y. Wang, M.D. Ediger, How Long Do Regions of Different Dynamics Persist in Supercooled o-Terphenyl?, J. Phys. Chem. B. 103 (1999) 4177–4184. https://doi.org/10.1021/jp984149x.

[34] D. Prevosto, S. Capaccioli, M. Lucchesi, P.A. Rolla, K.L. Ngai, Dynamics of supercooled and glassy dipropyleneglycol dibenzoate as functions of temperature and aging: Interpretation within the coupling model framework, J. Chem. Phys. 120 (2004) 4808–4815. https://doi.org/10.1063/1.1646375.

[35] S. Sharifi, S. Capaccioli, M. Lucchesi, P. Rolla, D. Prevosto, Temperature and pressure dependence of secondary process in an epoxy system, J. Chem. Phys. 134 (2011) 44510. https://doi.org/10.1063/1.3518972.

[36] A. Afzal, M. Shahin Thayyil, M.K. Sulaiman, A.R. Kulkarni, Dielectric relaxation studies in super-cooled liquid and glassy phases of anti-cancerous alkaloid: Brucine, Indian J. Phys. 92 (2018) 565–573. https://doi.org/10.1007/s12648-017-1139-3.

[37] U. Sailaja, M. Shahin Thayyil, N.S. Krishna Kumar, G. Govindaraj, K.L. Ngai, Molecular mobility in the supercooled and glassy states of nizatidine and perphenazine, Eur. J. Pharm. Sci. 99 (2017) 147–151.

[38] G. Williams, D.C. Watts, Non-symmetrical dielectric relaxation behaviour arising from a simple empirical decay function, Trans. Faraday Soc. 66 (1970) 80–85.

[39] S.L. Shamblin, B.C. Hancock, Y. Dupuis, M.J. Pikal, Interpretation of relaxation time constants for amorphous pharmaceutical systems, J. Pharm. Sci. 89 (2000) 417–427.

[40] P. Hohenberg, W. Kohn, Inhomogeneous Electron Gas, Phys. Rev. 136 (1964) B864–B871. https://doi.org/10.1103/PhysRev.136.B864.

[41] G.S. Painter, Density functional description of molecular bonding within the local spin density approximation, J. Phys. Chem. 90 (1986) 5530–5535. https://doi.org/10.1021/j100280a011.

[42] T. Ziegler, Approximate density functional theory as a practical tool in molecular energetics and dynamics, Chem. Rev. 91 (1991) 651–667. https://doi.org/10.1021/cr00005a001.

[43] M. Johansson, V. Kaila, D. Sundholm, Ab Initio, Density Functional Theory, and Semi-Empirical Calculations, Methods Mol. Biol. 924 (2013) 3–27. https://doi.org/10.1007/978-1-62703-017-5_1.

[44] M.E. Chacón Villalba, E.L. Varetti, P.J. Aymonino, A new vibrational study of sodium nitroprusside dihydrate. II. A quantum chemistry vibrational study of the nitroprusside anion, [Fe(CN)5NO]2−, Spectrochim. Acta Part A Mol.

Biomol. Spectrosc. 55 (1999) 1545–1552. https://doi.org/https://doi.org/10.1016/S1386-1425(98)00339-4.

[45] A.D. Becke, Density functional calculations of molecular bond energies, J. Chem. Phys. 84 (1986) 4524–4529. https://doi.org/10.1063/1.450025.

[46] P. Jungwirth, Density Functional Theory. A Practical Introduction. By David Sholl and Janice A. Steckel., Angew. Chemie Int. Ed. 49 (2010) 485. https://doi.org/https://doi.org/10.1002/anie.200905551.

[47] G. Herzberg, H.C. Longuet-Higgins, Intersection of potential energy surfaces in polyatomic molecules, Discuss. Faraday Soc. 35 (1963) 77–82. https://doi.org/10.1039/ DF9633500077.

[48] K.L. Schuchardt, B.T. Didier, T. Elsethagen, L. Sun, V. Gurumoorthi, J. Chase, J. Li, T.L. Windus, Basis Set Exchange: A Community Database for Computational Sciences, J. Chem. Inf. Model. 47 (2007) 1045–1052. https://doi.org/10.1021/ci600510j.

[49] R. Ditchfield, W.J. Hehre, J.A. Pople, Self-Consistent Molecular-Orbital Methods. IX. An Extended Gaussian-Type Basis for Molecular-Orbital Studies of Organic Molecules, J. Chem. Phys. 54 (1971) 724–728. https://doi.org/10.1063/1.1674902.

[50] H. Sklenar, J. Jäger, Molecular structure–biological activity relationships on the basis of quantum-chemical calculations, Int. J. Quantum Chem. 16 (1979) 467–484. https://doi.org/https://doi.org/10.1002/qua.560160306.

[51] K. Tuppurainen, S. Lötjönen, R. Laatikainen, T. Vartiainen, U. Maran, M. Strandberg, T. Tamm, About the mutagenicity of chlorine-substituted furanones and halopropenals. A QSAR study using molecular orbital indices, Mutat. Res. Mol. Mech. Mutagen. 247 (1991) 97–102. https://doi.org/https://doi.org/10.1016/ 0027-5107(91)90037-O.

[52] D.L. Lewis, C.L. Farr, A.L. Farquhar, L.S. Kaguni, Sequence, organization, and evolution of the A+T region of Drosophila melanogaster mitochondrial DNA., Mol. Biol. Evol. 11 (1994) 523–538.

[53] G. Klopman, Chemical reactivity and the concept of charge- and frontier-controlled reactions, J. Am. Chem. Soc. 90 (1968) 223–234. https://doi.org/10.1021/ja01004a002.

[54] D.R. Leenaraj, I.H. Joe, Natural Bond Orbital Analysis and DFT Calculation of Non-opiod Analgesic Drug Lidocaine, Mater. Today Proc. 2 (2015) 969–972. https://doi.org/https://doi.org/10.1016/j.matpr.2015.06.018.

[55] J.M. Seminario, An introduction to density functional theory in chemistry, in: J.M. Seminario, P.B.T.-T. and C.C. Politzer (Eds.), Mod. Density Funct. Theory, Elsevier, 1995: pp. 1–27. https://doi.org/https://doi.org/10.1016/S1380-7323(05)80031-7.

[56] T.M. Watson, J.D. Hirst, Density Functional Theory Vibrational Frequencies of Amides and Amide Dimers, J. Phys. Chem. A. 106 (2002) 7858–7867. https://doi.org/10.1021/jp025551l.

[57] M.W. Wong, Vibrational frequency prediction using density functional theory, Chem. Phys. Lett. 256 (1996) 391–399. https://doi.org/https://doi.org/10.1016/0009-2614(96)00483-6.

[58] V.G. Malkin, O.L. Malkina, M.E. Casida, D.R. Salahub, Nuclear Magnetic Resonance Shielding Tensors Calculated with a Sum-over-States Density Functional Perturbation Theory, J. Am. Chem. Soc. 116 (1994) 5898–5908. https://doi.org/10.1021/ja00092a046.

[59] R.E. Stratmann, G.E. Scuseria, M.J. Frisch, An efficient implementation of time-dependent density-functional theory for the calculation of excitation energies of large molecules, J. Chem. Phys. 109 (1998) 8218–8224. https://doi.org/10.1063/1.477483.

[60] J. Alvarellos, H. Metiu, The evolution of the wave function in a curve crossing problem computed by a fast Fourier transform method, J. Chem. Phys. 88 (1988) 4957–4966. https://doi.org/10.1063/1.454707.

[61] E. Simoni, C. Reber, D. Talaga, J.I. Zink, Time-dependent theoretical treatment of intervalance absorption spectra. Exact calculations in a one-dimensional model, J. Phys. Chem. 97 (1993) 12678–12684. https://doi.org/10.1021/j100151a009.

[62] S. Franzen, Use of Periodic Boundary Conditions To Calculate Accurate β-Sheet Frequencies Using Density Functional Theory, J. Phys. Chem. A. 107 (2003) 9898–9902. https://doi.org/10.1021/jp035215k.

[63] A.P. Scott, L. Radom, Harmonic Vibrational Frequencies: An Evaluation of Hartree−Fock, Møller−Plesset, Quadratic Configuration Interaction, Density Functional Theory, and Semiempirical Scale Factors, J. Phys. Chem. 100 (1996) 16502–16513. https://doi.org/10.1021/jp960976r.

[64] E. Runge, E.K.U. Gross, Density-Functional Theory for Time-Dependent Systems, Phys. Rev. Lett. 52 (1984) 997–1000. https://doi.org/10.1103/PhysRevLett.52.997.

[65] E.K.U. Gross, W. Kohn, Time-Dependent Density-Functional Theory, in: P.-O.B.T.-A. in Q.C. Löwdin (Ed.), Density Funct. Theory Many-Fermion Syst., Academic Press, 1990: pp. 255–291. https://doi.org/https://doi.org/10.1016/S0065-3276(08)60600-0.

[66] R.G. Parr, W. Yang, Density functional approach to the frontier-electron theory of chemical reactivity, J.Am. Chem.Soc. 106 (1984) 4049–4050. https://doi.org/10.1021/ja00326a036.

[67] R.G. Pearson, Chemical hardness and density functional theory, J. Chem. Sci. 117 (2005) 369–377. https://doi.org/10.1007/BF02708340.

[68] U. Sailaja, M.S. Thayyil, N.S.K. Kumar, G. Govindaraj, Molecular dynamics of amorphous pharmaceutical fenofibrate studied by broadband dielectric spectroscopy., J. Pharm. Anal. 6 (2016) 165–170. https://doi.org/10.1016/j.jpha.2014.09.003.

[69] W. Kauzmann, The Nature of the Glassy State and the Behaviour of Liquids at Low Temperatures., Chem. Rev. 43 (1948) 219–256. https://doi.org/10.1021/cr60135a002.

[70] S. Havriliak, S. Negami, A complex plane representation of dielectric and mechanical relaxation processes in some polymers, Polymer (Guildf). 8 (1967) 161–210. https://doi.org/10.1016/0032-3861(67)90021-3.

[71] L. Chen, T. Okuda, X.-Y. Lu, H.-K. Chan, Amorphous powders for inhalation drug delivery., Adv. Drug Deliv. Rev. 100 (2016) 102–115. https://doi.org/10.1016/j.addr.2016.01.002.

[72] D. Turnbull, Under what conditions can a glass be formed?, Contemp. Phys. 10 (1969) 473–488. https://doi.org/10.1080/00107516908204405.

[73] M.J. Frisch, G.W. Trucks, H.B. Schlegel, G.E. Scuseria, M.A. Robb, J.R. Cheeseman, G. Scalmani, V. Barone, B. Mennucci, G.A. et. . Petersson, Gaussian 09, Gaussian, Inc. Wallingford,CT,. .

[74] National Center for Biotechnology Information (2021). PubChem Compound Summary for CID 39042, Bezafibrate. Retrieved June 1, 2021 from https://pubchem.ncbi.nlm.nih.gov/compound/Bezafibrate..

[75] National Center for Biotechnology Information. PubChem Compound Summary for CID 3339, Fenofibrate. https://pubchem.ncbi.nlm.nih.gov/compound/ Fenofibrate. Accessed June 1, 2021.

[76] K.P. Safna Hussan, M.S. Thayyil, M. Binesh, S.K. Deshpande, V.K. Rajan, Molecular dynamics in amorphous pharmaceutically important protic ionic liquid–benzalkonium chloride, J. Mol. Liq. 251 (2018) 487–491.

[77] J.M.M. R. Dennington, T.A. Keith, Gauss View, Version 5, in: Semichem Inc.,

[78] M.J. Frisch, G.W. Trucks, H.B. Schlegel, G.E. Scuseria, M.A. Robb, J.R. Cheeseman, G. Scalmani, V. Barone, B. Mennucci, G.A. et. . Petersson, Gaussian 09, Gaussian, Inc. Wallingford,CT, . .

[79] M.J. Frisch, G.W. Trucks, H.B. Schlegel, G.E. Scuseria, M. a. Robb, J.R. Cheeseman, G. Scalmani, V. Barone, G. a. Petersson, H. Nakatsuji, X. Li, M. Caricato, a. V. Marenich, J. Bloino, B.G. Janesko, R. Gomperts, B. Mennucci, H.P. Hratchian, J. V. Ortiz, a. F. Izmaylov, J.L. Sonnenberg, Williams, F. Ding, F. Lipparini, F. Egidi, J. Goings, B. Peng, A. Petrone, T. Henderson, D. Ranasinghe, V.G. Zakrzewski, J. Gao, N. Rega, G. Zheng, W. Liang, M. Hada, M. Ehara, K. Toyota, R. Fukuda, J. Hasegawa, M. Ishida, T. Nakajima, Y. Honda, O. Kitao, H. Nakai, T. Vreven, K. Throssell, J. a. Montgomery Jr., J.E. Peralta, F. Ogliaro, M.J. Bearpark, J.J. Heyd, E.N. Brothers, K.N. Kudin, V.N. Staroverov, T. a. Keith, R. Kobayashi, J. Normand, K. Raghavachari, a. P.

Rendell, J.C. Burant, S.S. Iyengar, J. Tomasi, M. Cossi, J.M. Millam, M. Klene, C. Adamo, R. Cammi, J.W. Ochterski, R.L. Martin, K. Morokuma, O. Farkas, J.B. Foresman, D.J. Fox, G16_C01, (2016) Gaussian 16, Revision C.01, Gaussian, Inc., Wallin.

CHAPTER 3

THERMAL AND DIELECTRIC STUDIES OF BRUCINE, COLCHICINE, AND ACEMETACIN IN SUPERCOOLED AND GLASSY STATES

Reproduced in part with the permission of **Aboothahir Afzal** *et.al* from the following publications

1. Dielectric relaxation studies in super-cooled liquid and glassy phases of anti-cancerous alkaloid: Brucine, **Aboothahir Afzal**, M Shahin Thayyil, M K Sulaiman, and A R Kulkarni. Indian Journal of Physics, Volume 92, Issue 5, pp.565-573 Pub Date: May 2018, DOI: 10.1007/s12648-017-1139-3.

2. Dielectric spectroscopic studies in supercooled liquid and glassy states of Acemetacin, Brucine, and Colchicine. **Aboothahir Afzal**, M. Shahin Thayyil, P.A. Sivaramakrishnan, M.K. Sulaiman, K.P. Safna Hussan, C. Yohannan Panicker, K.L. Ngai, Journal of Non-Crystalline solids, 2019, DOI: https://doi.org/10. 1016/j.jnoncrysol.2019.01.008

3.1 Introduction

Amorphous pharmaceuticals are a promising solution for drugs having low water solubility [1]. The amorphous API's tendency to revert to their stable crystalline state will lead to losing the benefits of increased solubility [2]. Recent study focuses on critical factors that causes this instability over time, like molecular mobility and crystallization tendency[3,4]. Crystal growth rate and global mobility are usually coupled, ie,cooperative molecular motion linked to dynamic glass transition [5–7]. In the amorphous state, molecular rearrangements mediated by intermolecular secondary relaxation can cause crystal nucleation [7]. A comprehensive understanding of the molecular dynamics in supercooled liquid and glassy phases is required to establish safe storage conditions for amorphous pharmaceuticals [8]. Researchers working in the subject of non-crystalline solids, particularly in the liquid-glass transition, are more interested in the information gained from this research. Moreover, brucine, colchicine, and acemetacin have complex molecular structures whose glass transition study will be of special interest to researchers engaged in the theory of glass formation[2].

Glass formers normally exhibit structural relaxation in the supercooled liquid state ($T>T_g$), (α-process), due to the cooperative motion of molecules and secondary relaxation processes (β-, γ-, δ- etc.) due to the fast local motions of individual or parts of the molecule in the glassy state[9] and is classified into Johari-Goldstein relaxation (β-process) which is intermolecular in nature and intermolecular γ or δ relaxation [10]. JG-relaxation is a universal property of glass-forming liquids that can be linked to primitive relaxation using Ngai's coupling model process [16][17]. JG relaxation, on the other hand, is responsible for the devitrification of amorphous substances [13].

We present a BDS study of brucine, colchicine, and acemetacin in super-cooled liquid and deep glassy states to obtain important information on molecular motions from the glass to the liquid state, as well as the existence of molecular motions that may be responsible for de-vitrification. As compared to other experimental methods for analyzing molecular mobility, such as differential scanning calorimetry (DSC) and NMR spectroscopy [14–17]. BDS is a sensitive and efficient tool [18] for probing molecular dynamics over a broad range of frequencies in super-cooled liquid states and deep glassy states[2]. Paluch's anti-correlation analysis between the width of the structural loss peak at T_g to the dipole moment of the title drugs[19] and the Coupling

model was used to find the nature of the origin of secondary relaxations. The role of hydrogen bonding in the amorphous phase and whether functional groups are preserved in the amorphous state was investigated using IR spectroscopic analysis of the crystalline and amorphous states of brucine, acemetacin, and colchicine. The origin of experimentally observed secondary relaxations was determined theoretically by the quantum computational DFT method using Gaussian software[20].

3.2 Experimental section

The samples selected for study in this chapter are acemetacin, brucine, and colchicine The details of the samples are given in chapter 2. The chemical structure of acemetacin, brucine, and colchicine are shown in figures 3.1,3.2,3.3 respectively.

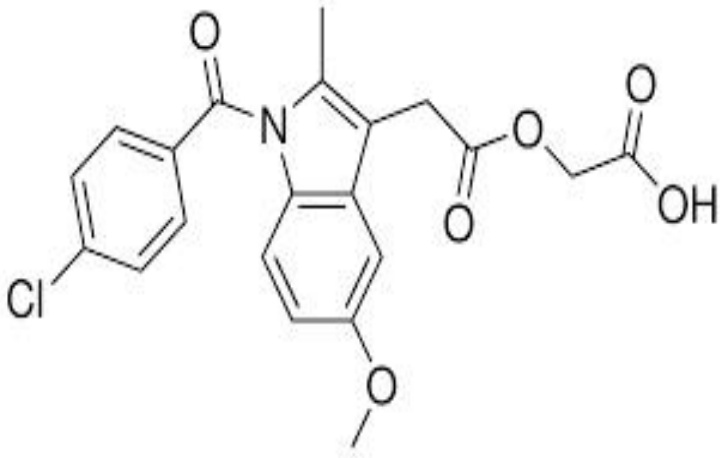

Figure 3.1 Molecular geometry of acemetacin

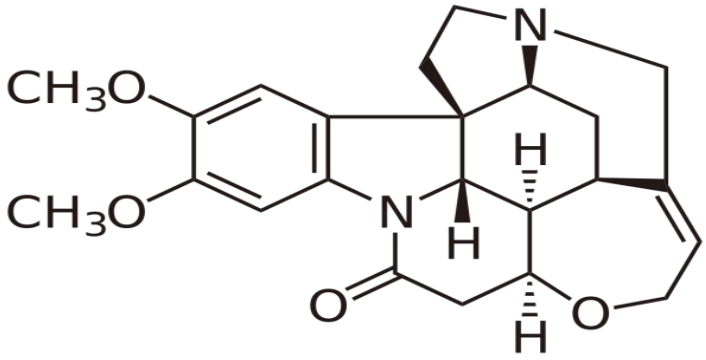

Figure 3.2 Molecular geometry of brucine

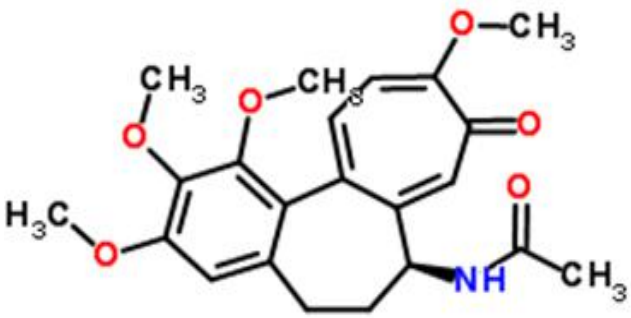

Figure 3.3 Molecular geometry of colchicine

The experimental methods used in this chapter are TGA, DSC, BDS, and FTIR and the computational tools used are DFT using Gaussian-09 [20]**.** The details of the methods are discussed in chapter 2.

3.3 Results and discussion

3.3.1 Thermogravimetric analysis

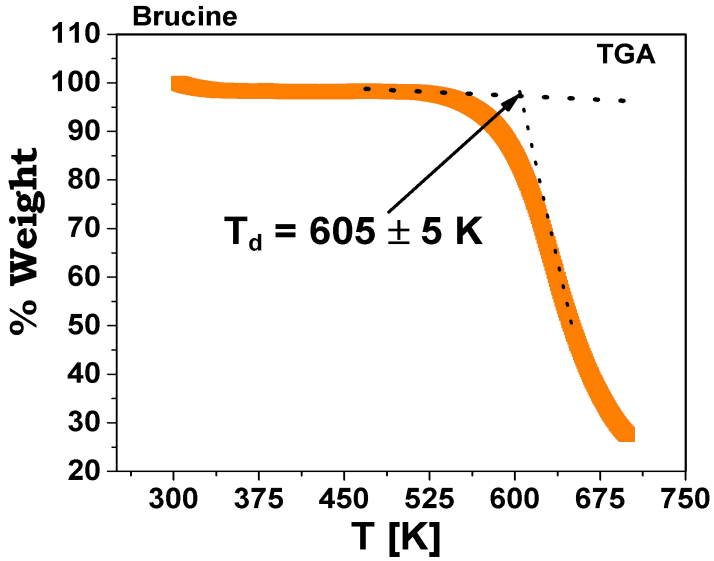

Fig. 3.4 TGA curve of brucine

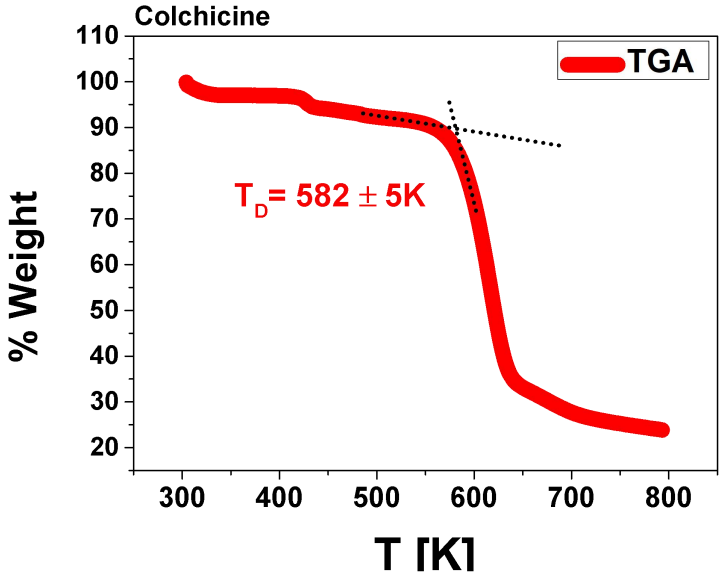

Fig. 3.5 TGA curve of colchicine

Thermogravimetric analysis of brucine and colchicine was done to determine their decomposition temperatures to confirm that they have not decomposed thermally during dielectric measurements. TGA curves of brucine and colchicine are shown in figures 3.4 and 3.5 respectively. The decomposition temperature of brucine was found to be 605K while the decomposition temperature of colchicine was found to be 582K. As the dielectric measurements were taken below these decomposition temperatures for brucine and colchicine, we confirmed that dielectric measurements obtained for brucine and colchicine were that of pure brucine and colchicine.

3.3.2 Differential Scanning Calorimetry

DSC thermograms of brucine, colchicine, and acemetacin showing well-resolved melting, crystallization, and glass transition process are shown in figures 3.6, 3.7, and 3.8 respectively.

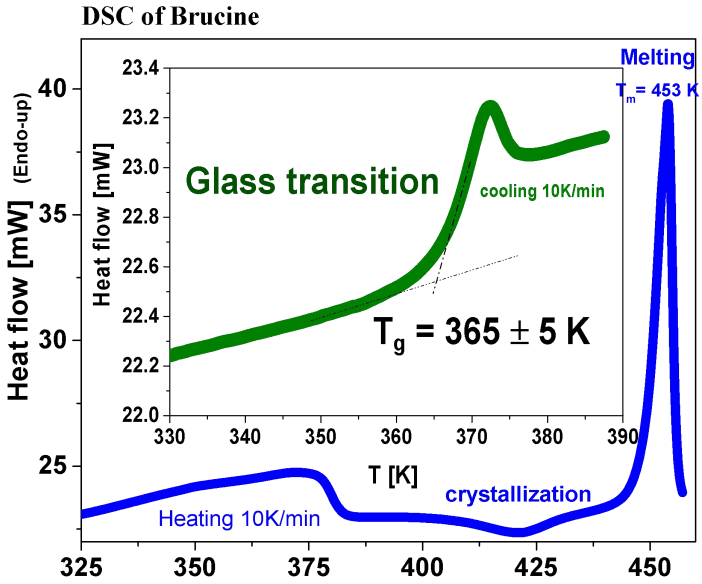

Figure 3.6 DSC curve of brucine. Glass transition is shown in the inset

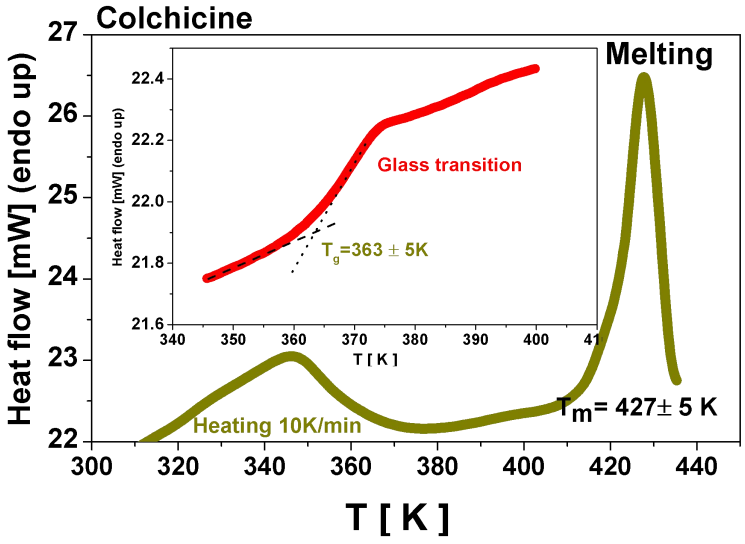

Fig. 3.7 DSC curve of colchicine. Glass transition is shown in the inset

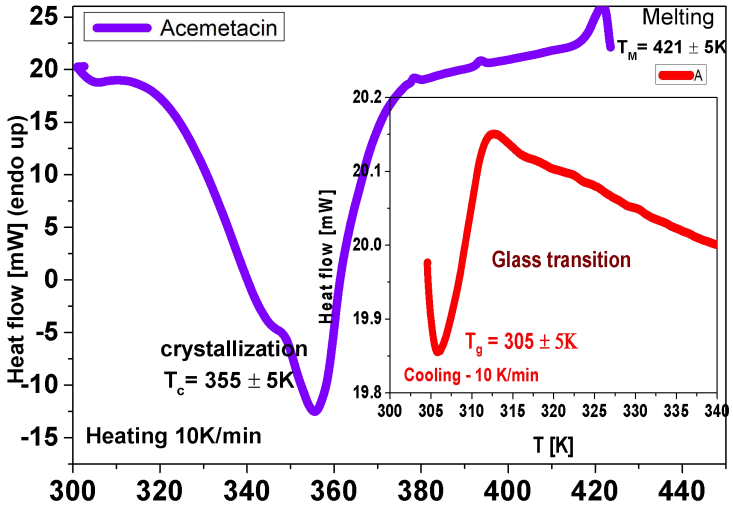

Fig. 3.8 DSC curve of acemetacin. Glass transition is shown in the inset

From the figures 3.6-3.8, the DSC curves show well-resolved melting, crystallization, and glass transition in all title samples, and the corresponding temperatures are shown in Table 3.1. T_g of all title samples is above room temperature which indicates the stability of the amorphous phase at room temperature. T_g for acemetacin is closer to the T_g value reported[21]. The difference between the crystallization temperature and T_g of acemetacin, brucine, and colchicine are approximately 50 K and 57 K and 15 K [22], which is considered as an implication of stability of the amorphous phase, accordingly, amorphous brucine is more stable than colchicine and acemetacin. The temperature value T_g -50K of title samples is above room temperature which enables safe storage at room temperature itself except acemetacin.

Table 3.1 DSC results

Sample	Melting temperature T_m (K)	Glass transition temperature T_g (K)	Crystallization Temperature (K)
Acemetacin	421 ± 5	305 ± 8	355 ± 6
Brucine	453 ± 5	366 ± 8	423.5 ± 6
Colchicine	427 ± 5	363 ± 8	378 ± 6

3.3.3 Broadband dielectric spectroscopy (BDS)

We collected isochronal dielectric permittivity data at three-four test frequencies to obtain preliminary information regarding glass formation and the likelihood of crystallization during cooling, and the response is given in the figures below.

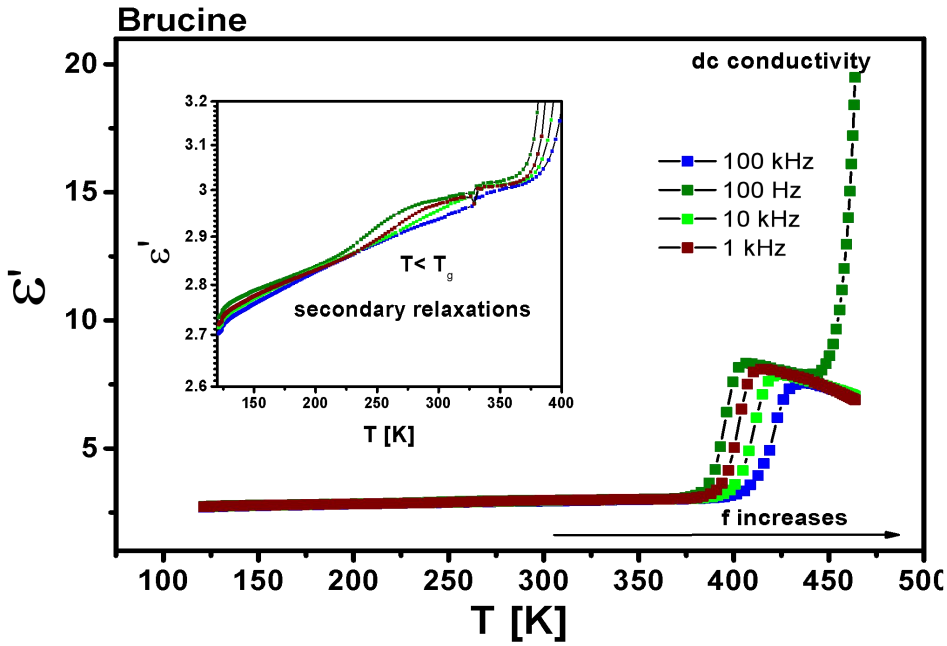

Fig. 3.9 Temperature dependence of dielectric permittivity in brucine on quench cooling the melt brucine

The temperature dependence of real (ε') and imaginary parts (ε") of dielectric permittivity on quench cooling the melt brucine for fixed frequencies f= 10^2 Hz, 10^3 Hz, 10^4 Hz, 10^5 Hz are shown in figures 3.9 and 3.10. A rapid increase in the higher temperature region for 100Hz in figure 3.9 is observed due to dc conductivity in low frequency due to translational motion [23]. The presence of α and secondary relaxations in brucine is confirmed from the bigger dip in permittivity in the higher temperature region and a smaller dip in the lower temperature region. Figure 3.10 presents the dielectric loss variation on cooling showing α and two different secondary relaxations are observed in the brucine as shown in figure 3.10.

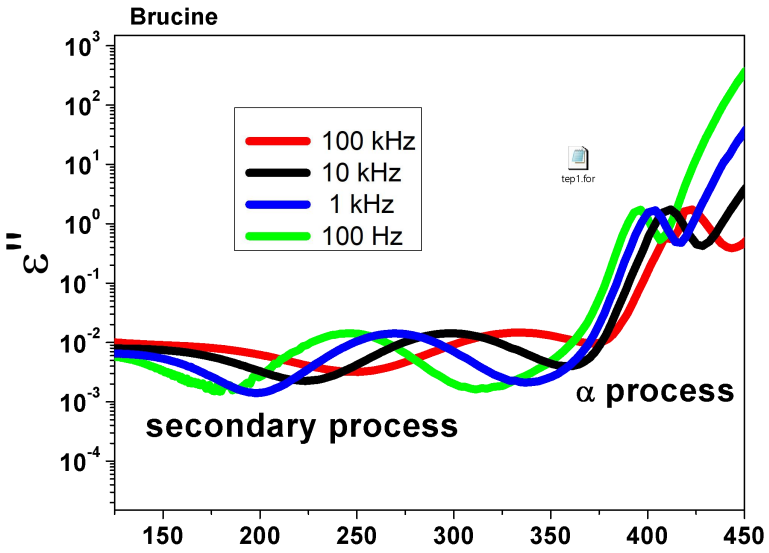

Fig.3.10 Temperature dependence of dielectric loss (ε'') in brucine

3.3.3.1 Dielectric spectra in supercooled liquid state ($T>T_g$)

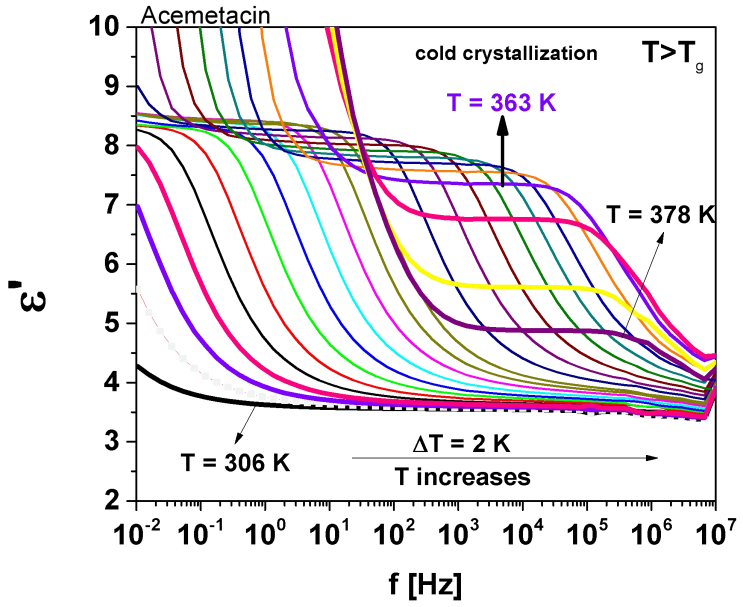

Figure 3.11 Real (ε') part of the complex dielectric permittivity spectrum of acemetacin from 306 K to 383 K ($T > T_g$)

The dielectric measurements were collected from 123.15 K to 441.15 K in brucine and colchicine and up to 378.15 K for acemetacin in a frequency range of 10^{-2} to 10^{7} Hz. The real (ε′) part of the complex dielectric permittivity spectrum of acemetacin for $T > T_g$ is shown in figure 3.11 showing structural relaxation. Similar behaviour is observed in brucine [24] and colchicine (not shown). In figure 3.11, at

363K, the dielectric permittivity ε' begins to decrease with increasing temperature due to cold crystallization which was also observed in colchicine. Due to crystallization, the number of relaxing dipoles decreases, and hence dielectric strength Δε of the α process decreases. Dielectric strength could be defined from the generalized form of Debye theory by Onsager, Fröhlich, and Kirkwood is given by equation 3.1 [25].

$$\Delta\varepsilon = \frac{1}{3\varepsilon_0} g_K F \frac{\mu^2}{k_B T} \frac{N}{V} \tag{3.1}$$

where ε_0 is the dielectric permittivity of vacuum, μ is the mean dipole moment of a moving unit in a vacuum, g_K is the Kirkwood correlation factor, and F is the Onsager factor (equal to 1). The N/V ratio represents the density of dipoles involved in the relaxation process. Therefore, dielectric strength Δε decreases in the same manner as factor N/V, due to the emergence of cold crystallization of acemetacin and colchicine. No such cold crystallization is observed in brucine from the dielectric permittivity spectra and dielectric loss spectra reported [24].

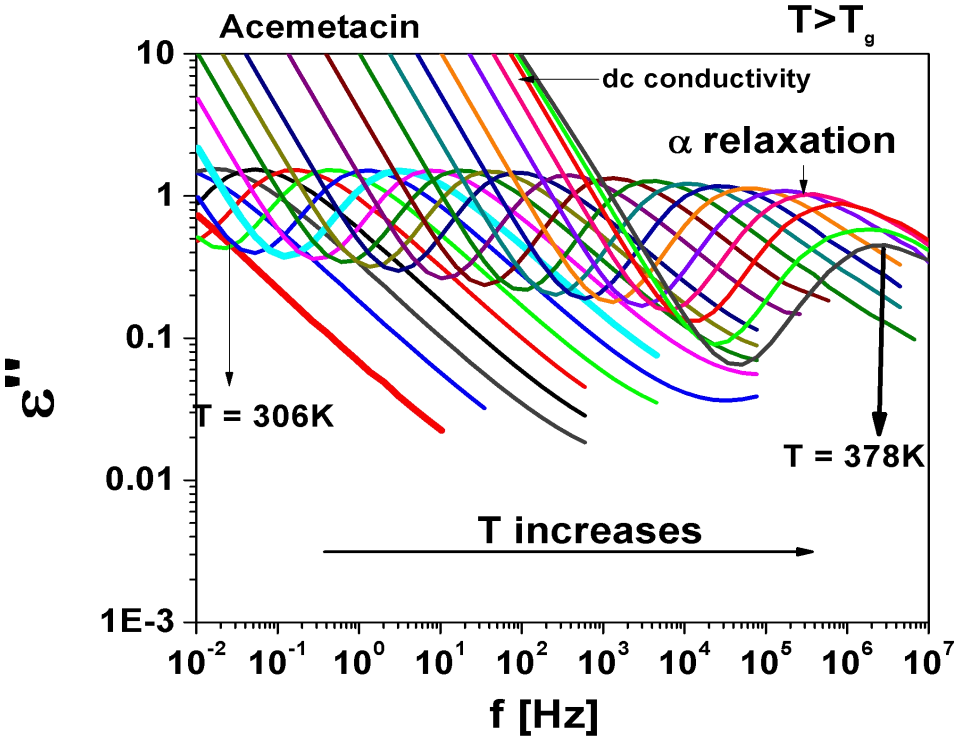

Figure 3.12 Dielectric loss spectra of acemetacin above T_g

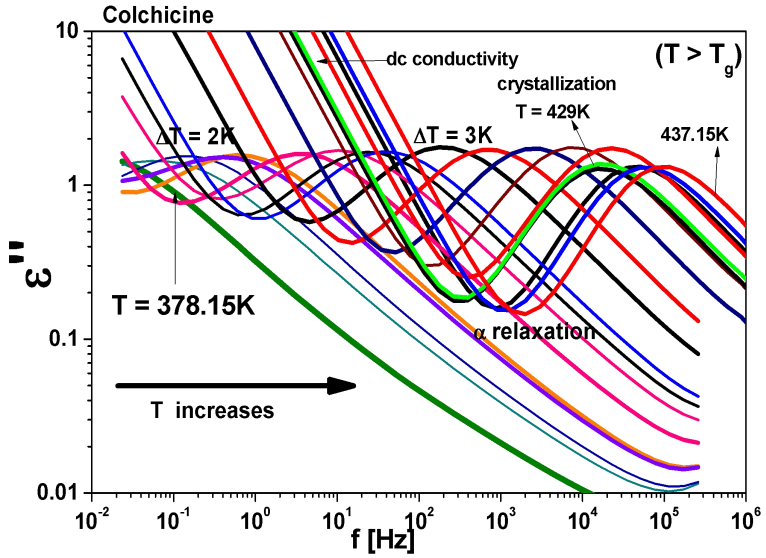

Figure 3.13 Dielectric loss spectra of colchicine above T_g

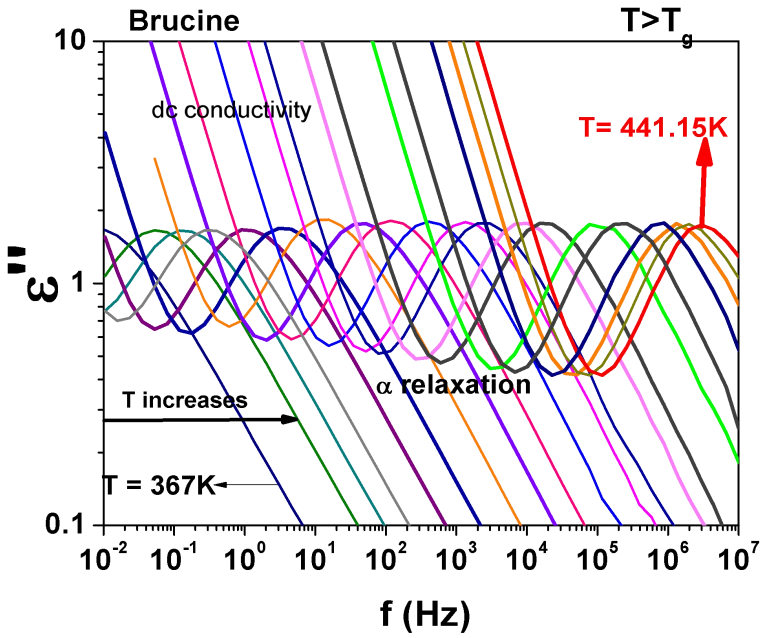

Figure 3.14 Dielectric loss spectra of brucine above T_g

The imaginary part of the complex dielectric spectra of acemetacin, colchicine, and brucine above T_g are shown in figures 3.12,3.13 and 3.14 respectively. Well resolved structural α relaxation is seen in acemetacin and colchicine above Tg, and dc-conductivity is observed in acemetacin and colchicine in the lower frequency region due to translational motion of ions. The dielectric spectra of brucine in a supercooled liquid state also showed well-resolved structural relaxation and dc conductivity. Structural relaxation (α) peaks decline in figures 3.12 and 3.13 while heating from

363.15 K and 429.15 K of acemetacin and colchicine respectively. This is due to crystallization tendency in acemetacin and colchicine in the supercooled liquid state while heating to a temperature high above T_g and such tendency is not observed in brucine. The peak frequency of the dielectric loss curve shifts towards the higher frequency as temperature increases as the increased thermal energy of the molecules decreases the mean relaxation time.

3.3.3.2 Glassy state ($T < T_g$)

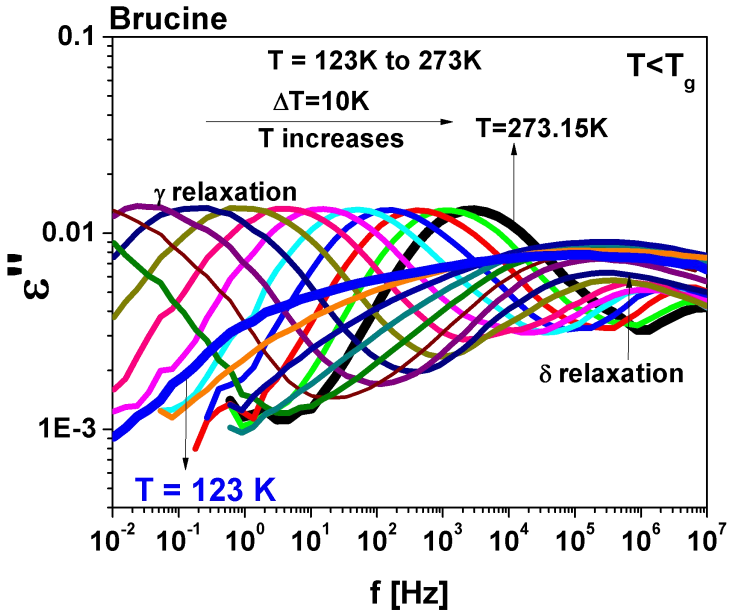

Figure 3.15 Dielectric loss spectrum of brucine below T_g (T=123K to 273K)

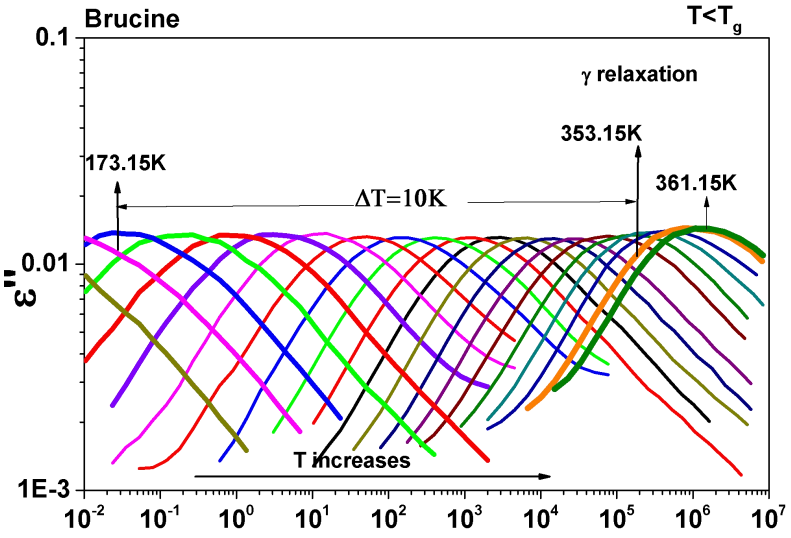

Figure 3.16 Dielectric loss spectrum of brucine below T_g (173K to 361K)

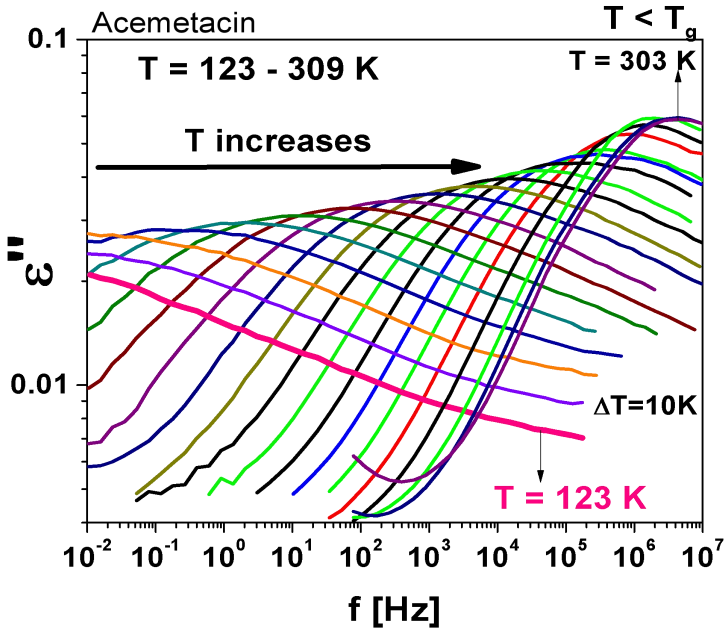

Figure 3.17 Dielectric loss spectrum of acemetacin below T_g

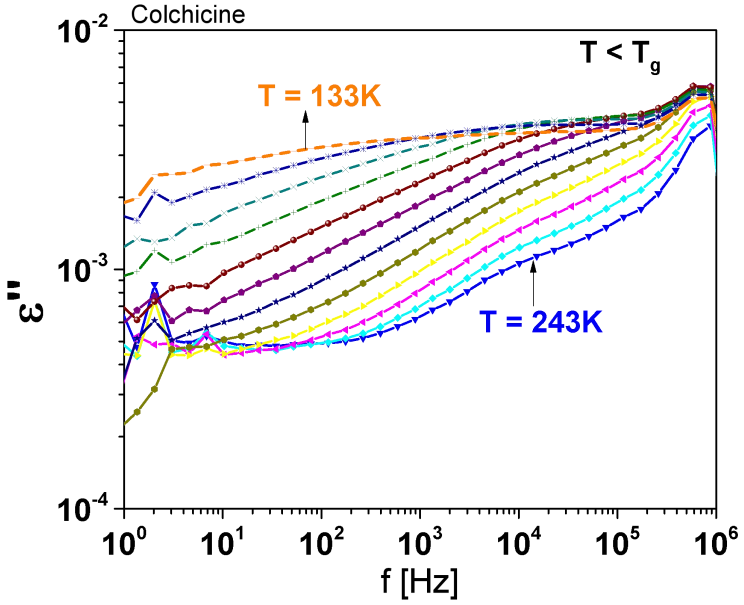

Figure 3.18 Dielectric loss spectrum of colchicine below T_g (133K to 243K)

Figures 3.17 and 3.18 presents the dielectric loss spectra of acemetacin and colchicine respectively in the glassy state showing well resolved secondary relaxation. The dielectric loss increases with an increase in temperature and shifts towards a higher frequency region on an increase in temperature due to an increase in thermal energy. A secondary γ relaxation with single activation energy could be observed in acemetacin and colchicine. The relaxation time of all types of relaxations in the title samples was

fitted by the Havriliak-Negami equation and the fit parameters like relaxation time were determined. Details of the HN equation are given in chapter 2. Brucine and colchicine are alkaloids, whereas acemetacin is a non-alkaloid, but brucine exhibits two different intramolecular secondary relaxations, whereas colchicine and acemetacin exhibit only one, and acemetacin exhibit an increase in the width of the structural relaxation spectra with temperature, whereas brucine and colchicine exhibit the opposite trend, which may aid in the yet unknown.

3.3.3.4 Temperature dependence of relaxation time

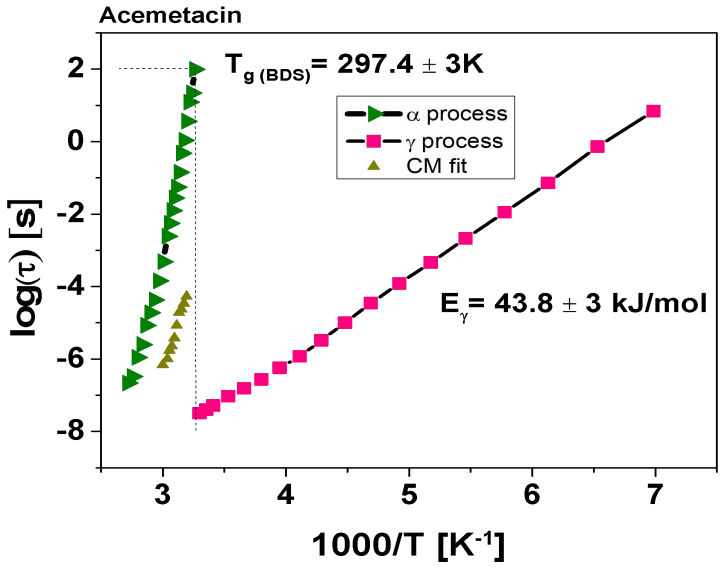

Figure 3.19 Relaxation map of acemetacin. Coupling model predictions are also shown

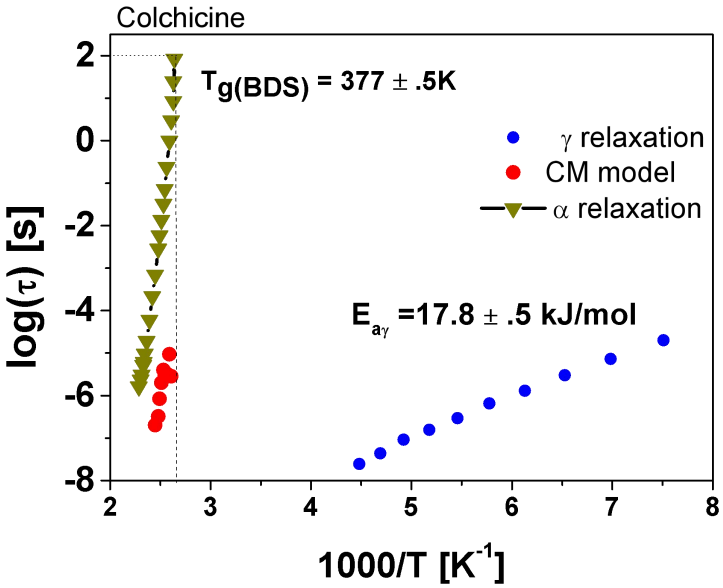

Figure 3.20 Relaxation map of colchicine. Coupling model predictions are also shown

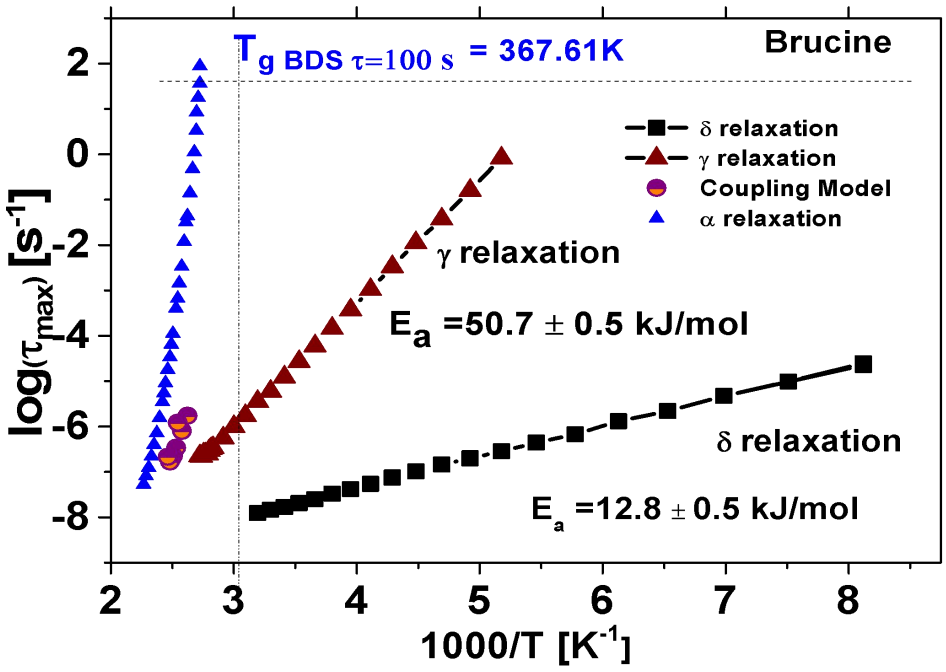

Figure 3.21 Relaxation map of brucine. Coupling model predictions are also shown

The temperature dependence of structural and secondary relaxation times will help us to determine the significant parameters that help to characterize the glassy state of the system. Relaxation map (Arrhenius diagram) showing temperature dependence (1000/T) of molecular relaxation time (log τ) of primary and secondary relaxations of acemetacin, colchicine, and brucine are presented in Figure 3.19, 3.20, and 3.21 respectively. The activation energies of secondary relaxations and primitive relaxation times τ_0 of the coupling model for $T > T_g$ are also shown for all the API. T_g is also determined from the Arrhenius graph, which is considered as the temperature at which the α relaxation time τ_α=100 s. For acemetacin, T_g found is equal to 306.3K which is close to the reported value reported[21]. Similarly, the T_g obtained for brucine and colchicine were also determined and is in good agreement with the T_g value obtained by DSC and VFT fits. Glass transition temperature T_g of acemetacin, brucine, and colchicine were found to behave the room temperature which suggests that the global molecular mobility in the glassy state of the title compounds will be negligible at ambient storage conditions and hence ensuring the stability of amorphous APIs of the title compounds.

The activation energy of secondary relaxation in all title compounds was calculated by the Arrhenius equation given in equation 3.2 and presented in Table 3.2,

$$\tau(T) = \tau_{\infty} \exp\left(\frac{E_a}{RT}\right) \quad (3.2)$$

The activation energies of the γ relaxation are found to be $E_{a\gamma}$ = 43.08 kJ/mol, 50.72 kJ/mol and E_a =17.83 kJ/mol for acemetacin, brucine and colchicine respectively. The δ relaxation observed in the deep glassy state of the brucine has an activation energy of 12.8 kJ/mol. If the activation-energy barrier for secondary relaxation processes is higher (typically, E_a > 50 kJ/mol), then it is due to intermolecular motion, whereas low values (E_a < 50 kJ/mol) could be linked to intermolecular motions [26]. It is reported that the secondary relaxation with a large activation energy ($E_{a\beta}$=80 kJ/mol) was identified as intermolecular JG β process whereas those secondary relaxations with smaller values of activation energies ($E_{a,\gamma}$=51 kJ/mol and $E_{a,\delta}$=21 kJ/mol) were identified as intermolecular γ and δ processes in amorphous Celecoxib [27]. The activation energies of the observed secondary relaxations in acemetacin, brucine, and colchicine suggest the intermolecular nature of the secondary process and are presented in table 3.2.

Table 3.2 Activation energies of secondary relaxations

Samples	$E_{a\gamma}$ (kJ/mol)	$E_{a\delta}$ (kJ/mol)
Acemetacin	43.8 ± 0.5	-
Brucine	50.7 ± 0.5	12.8 ± 0.5
Colchicine	17.8 ± 0.5	-

3.3.3.5 Fragility

The α relaxation times show a curved temperature dependence (non-Arrhenius behaviour) for all the title compounds while the secondary relaxation times in all the title compounds follow linear temperature dependence (Arrhenius behaviour) when plotted as a function of 1000/T. Out of the three title compounds, brucine only exhibited two non-JG secondary relaxations γ and δ with different activation energies in a glassy state. The activation energies of secondary relaxation calculated using the Arrhenius equation are shown in Table 3.2. The Tg values of acemetacin, brucine

reported [3] and colchicine are well above the room temperature, which enables simpler storage conditions for keeping them at 50 K below Tg. The nonlinear temperature dependence of the α process was fitted by the Vogel-Fulcher-Tamann (VFT) equation (Eq.3.3) [70, 24, 65].

$$\tau_{\alpha} = \tau_{\infty} \exp\left(\frac{DT_0}{T - T_0}\right) \tag{3.3}$$

where T is the absolute temperature, D is the strength parameter and T_0 is the VFT temperature (ideal glass transition temperature) at which all important molecular motion stops and relaxation time becomes infinity. At the glass transition temperature T_g, a system falls outs of equilibrium due to the increased viscosity and increasingly restricted molecularmobility[28]. From VFT fit, T_g of acemetacin, brucine, and colchicine was determined and was found to be closer to the values of T_g obtained from the DSC experiment. The VFT fit parameters determined for the title compounds are shown in Table 3.3.

Table 3.3 VFT Fit Parameters

Sample	Glass Transition Temperature T_g (K)	Fragility m	Strength Parameter D	log(τ_{VF})	Vogel Temperature T_0 (K)
Acemetacin	306 ± 1 K	88.5 ± 5	10.3 ± 0.21	15.8 ± 0.20	244.9 ± 1.32
Brucine	364 ± 5 K	90.3 ± 5	9.93 ± 0.18	16.0 ± 0.20	294.7 ± 0.5
Colchicine	374 ± 5 K	69.9 ± 5	28.3 ± 0.38	21.8 ± 0.20	246.8 ± 1.3

The strength parameter D is a measure of fragility where the most fragile glass formers have a value of around 2 while the strongest glasses are on the order of 100. The strength parameter (D) and Vogel temperature T0 obtained from VFT fits for acemetacin are 10.3 and 244.9 K respectively. Brucine has a strength parameter closer to that of acemetacin while the strength parameter of colchicine is higher than that of acemetacin and brucine. Thus, colchicine is found to be a stronger glass former than that of brucine and acemetacin. The ideal glass transition temperature (Vogel temperature) of acemetacin and colchicine is closer to 244 K while that of brucine is 294.7 K which can be achieved under normal conditions.

From VFT fits, the values of T_g obtained for acemetacin, brucine and colchicine are in good agreement with the value of T_g obtained by DSC (Table 3.1). Paluch *et. al.* reported the T_g values of several glass formers, but the T_g of brucine and colchicine was found to be higher than any of the T_g values reported[19]. The fragility of glass formers is considered as a possible criterion to predict their stability and crystallization rates. The steepness index (fragility) m [29] was calculated from the temperature dependences of the structural relaxation times.

$$\mathbf{m} = \frac{\mathbf{d}\,\mathbf{log}\,(\boldsymbol{\tau_\alpha})}{\mathbf{d}(\frac{\mathbf{T_g}}{\mathbf{T}})}\Big|_{\mathbf{T=T_g}} \tag{3.5}$$

The value of fragility index m can be obtained from the VFT parameters from equation 3.6,

$$\mathbf{m} = \mathbf{D}\,\frac{\mathbf{T_o}}{\mathbf{T_g}}\left(\mathbf{1} - \frac{\mathbf{T_0}}{\mathbf{T_g}}\right)^{\mathbf{-2}}\mathbf{log_e} \tag{3.6}$$

The value of fragility (m) ranges between 16 and 200 for a typical glass former,[30] where small values (m < 40) of the fragility parameter indicate Arrhenius-like temperature dependence, where $\log\tau_\alpha(T)$ is linear in the T_g/T range. When the dependence of $\log \tau_\alpha(T)$ deviates strongly from the Arrhenius behaviour (linear), then it is a fragile glass former. Kunal *et al.*[31] highlighted that the packing efficiency of the amorphous chain in the glassy state and chain flexibility are the main parameters influencing the fragility index. The steepness index or fragility parameter (m) of acemetacin, brucine, and colchicine were determined to be 88.5, 90.3, and 69.9 from VFT fit classifying them as intermediate fragile glass formers. Brucine and acemetacin have closer fragility and they can be considered as compounds having structural stability slightly lesser than that of verapamil hydrochloride (m=88)[32] and ketoprofen (m=86.5) [17]. Colchicine is found to be a stronger glass former than acemetacin and brucine due to the lower value of fragility. Colchicine can be considered as a glass former of stability comparable to that of Cimetidine [5]. The values of Tm/Tg, T_g-T_0 suggest that the amorphous form of the title compounds can be stored safely in ambient conditions[23][6]. The extend of deviation from the Arrhenius nature near the glass transition is reflected at the slope in the Angel plot ($\log(\tau) - T_g/T$ plot) which is equal to the fragility m[29].

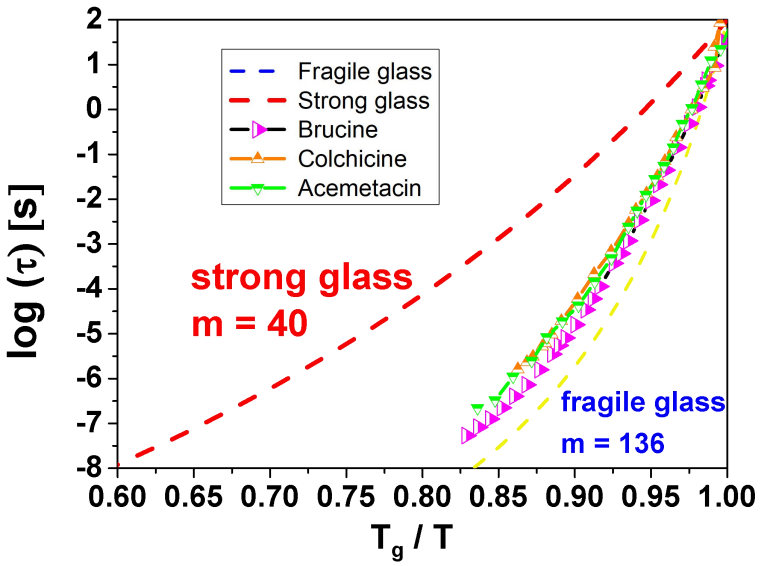

Figure 3.22 Angel plot of acemetacin, colchicine and brucine

Figure 3.22 shows Angel's plot of the supercooled state of acemetacin, brucine, and colchicine. All the samples are showing above medium fragility. Intermediate values of isobaric fragility indicate that the glass-former should be structurally less stable than a strong one, due to considerable changes in molecular mobility near the glass transition, since their frustrations against crystallization are weaker.

3.3.3.6 Coupling model

According to Ngai's Coupling model, the relaxation time of JG secondary relaxation (τ_{JG}) and that of primitive relaxation (τ_0) are correlated. The CM predicts a correlation of relaxation time of JG secondary process $J\tau_{JG}$ (T) from α relaxation times. The primitive relaxation time τ_0 calculated from the equation (3.8), corresponds to the relaxation times of the hidden secondary process [11][19].

$$\tau_{JG}(T) = \tau_0(T) = (t_c)^n \ (\tau_\alpha(T))^{1-n} \qquad (3.1)$$

where t_c is equal to 2 ps for molecular glass formers and ($n = 1-\beta_{KWW}$) is the coupling parameter. The nature of the origin of a secondary relaxation, whether is it a JG relaxation is particularly relevant to the MD of amorphous pharmaceuticals[26] as the intermolecular JG β-relaxation can be the precursor of α relaxation.

The primitive relaxation time calculated for arbitrary temperatures above T_g for acemetacin, brucine, and colchicine do not correspond to the observed molecular

relaxation times of the secondary relaxation which suggests that the observed secondary relaxations in the title compounds are not Johari-Goldstein β relaxation, rather intramolecular in nature. The primitive relaxation frequency ($f_0=1/2\pi\tau_0$) calculated for acemetacin was f_0=4.05×103 Hz for T=323.15 K which is around four decades of frequency away from the α relaxation peak and is in the range of frequencies where the excess wing (JG relaxation) is expected. A similar trend is observed for brucine and colchicine where the f_0 value is in the range of excess wing. Thus, the excess wing is observed in acemetacin, brucine, and colchicine, and to resolve excess wing high-pressure experiments need to be done. The well-resolved secondary relaxations experimentally observed in all the title compounds are non-JG secondary relaxations and are labeled as γ and δ relaxations like Glibenclamide[32,33]. Since the intramolecular process is less sensitive to pressure than the intermolecular process one, α- peak and excess wing (EW) can be separated by high pressure or physical aging [34].

3.3.3.7 Kohlraush-William-Watts (KWW) fit

The details of the KWW fit are given in section 2.2.4 in chapter 2. Above T_g, β_{KWW} are determined for few temperatures and found that the experimental data of acemetacin, brucine, and colchicine fitted well to the KWW function and are shown in Fig. 3.23.

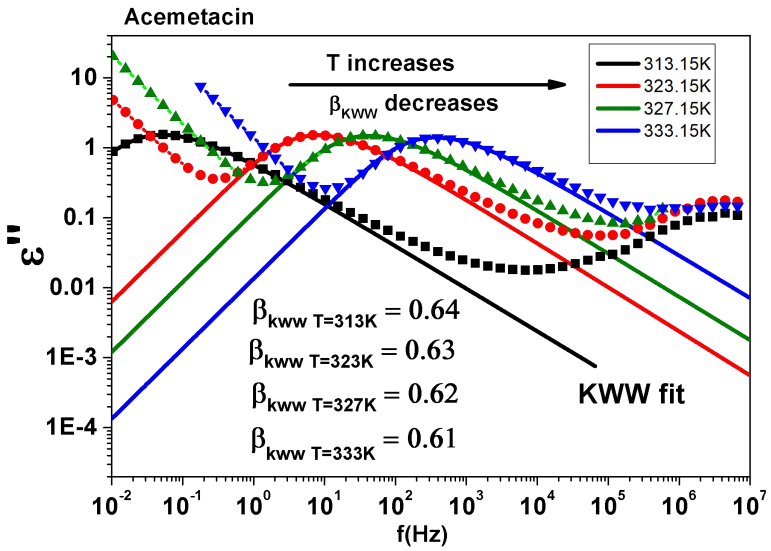

Figure 3.23 KWW fit of acemetacin

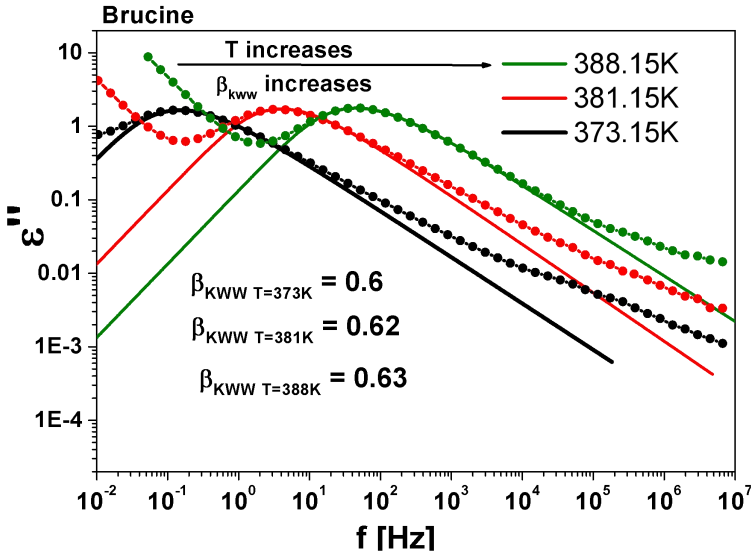

Figure 3.24 KWW fit of brucine

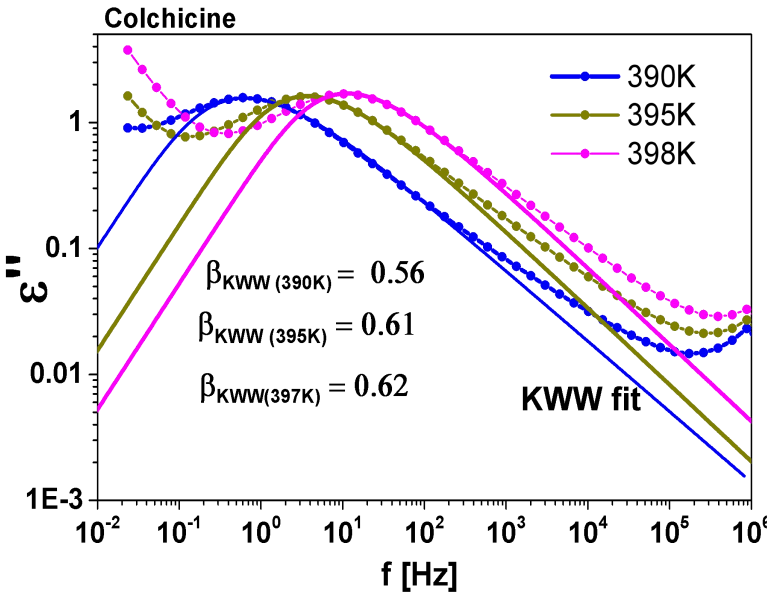

Figure 3.25 KWW fit of colchicine

Fig. 3.23, 3.24, and 3.25. shows the KWW fits for acemetacin, brucine, and colchicine respectively for arbitrary temperatures above T_g. The solid lines represent KWW fit and dotted solid curves represent experimental data. From the KWW fit, for acemetacin T=313.15 K, the stretching parameter β_{KWW}=0.64 and is found to decrease to 0.61 at T=333.15 K suggests that acemetacin is characterized by an above medium degree of non-exponentiality (dielectric loss spectrum is asymmetric and broader than a classical Debye relaxation (β_{KWW}=1) and an above-average distribution of α- relaxation times[35]. Another paradoxical feature observed in supercooled acemetacin is the

decrease of β_{KWW} with an increase of temperature which represents the increase in instability of the amorphous phase with an increase in temperature. The stability of amorphous acemetacin can be compared with that of Triethylacetyl citrate and salol (β_{KWW}=0.64) [19]. In Fig. 3.24. the KWW fit of brucine at T=373.15 K is shown and found that β_{KWW} value increases from 0.6 at 373 K to 0.73 at 406.15 K. The value of β_{KWW} is found to increase with the increase of temperature in brucine which suggests that the width of the α peaks become narrower with temperature (also decrease in distribution of structural relaxation times), amorphous brucine has intermediate stability against crystallization, which shows the tendency of amorphous brucine to resist against recrystallization above T_g which is also evident in the dielectric loss spectra showing no tendency of crystallization. The stability of amorphous brucine is comparable to that of β- adenosine (β_{KWW}=0.6) [46]. The KWW fit of colchicine at 390.15 K is also shown in Fig. 3.24 and the value of β_{KWW} determined is 0.56 which is smaller than that of acemetacin and brucine which suggests that glassy state of colchicine is lesser resistant to crystallization, α relaxation curves in colchicine are characterized by a medium degree of non-exponentiality and are broader than that of acemetacin and brucine. Therefore, from the KWW fits of all the title samples above T_g, we found that colchicine has more tendency to recrystallize from the comparatively lower value of β_{KWW} than that of acemetacin and brucine. From Fig. 3.16, the experimental data is found to deviate from the KWW at higher frequencies due to the emergence of an excess wing which was postulated by the Ngai process [11,19] and confirmed experimentally by other scientists [36]. The excess wing is observed when the high-frequency flank of a secondary relaxation process got covered by the dominant α relaxation is the reason for this. This intermolecular secondary relaxation namely Johari−Goldstein (JG-β) relaxation,[12,37] has been considered as a potential precursor of cooperative structural relaxations.

3.3.3.8 Temperature dependence of β_{KWW}

Figure 3.17 shows the variation of asymmetric stretching parameter β_{KWW} with temperature for acemetacin, brucine, and colchicine. For both brucine and colchicine, β_{KWW} increases with the temperature above T_g in the temperature range 371K to 406K and 390K to 424K for brucine and colchicine respectively. For colchicine, β_{KWW} reaches a value of 0.71 at 409K and remains constant while for brucine, β_{KWW} reaches a

value of 0.73 at 406K. Thus, brucine can be considered more stable than colchicine due to the higher value of β_{KWW} at 406K. For colchicine, a steep increase in β_{KWW} is observed with temperature compared to brucine which suggests a drastic reduction in the distribution of structural relaxation times in colchicine when compared to brucine. For acemetacin, from Fig. 3.26, the distribution of structural relaxation time increases with temperature and hence the dielectric loss spectra become more and more non-exponential in this range of temperature.

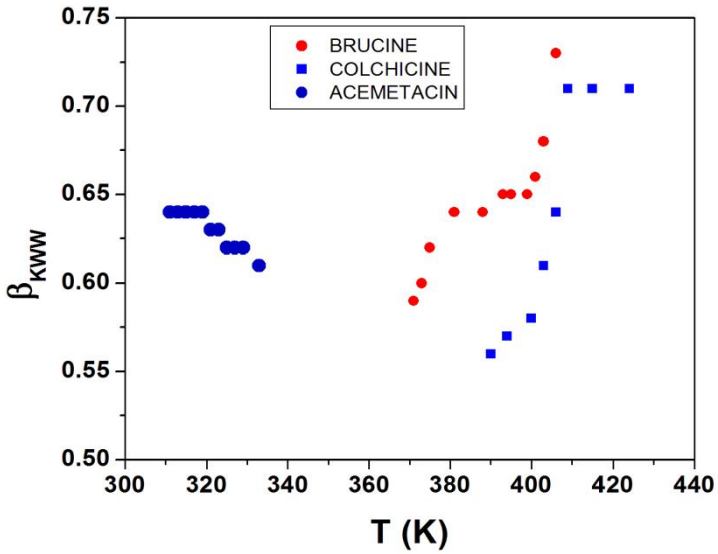

Figure 3.26 Variation of β_{KWW} with temperature for acemetacin, brucine and colchicine

A visualization of the temperature dependence of β_{KWW} is done by master plot analysis after normalizing the peak heights uniformly to one. This is done to ascertain the active role of temperature in the shape of the dielectric loss spectra that would have resulted in different relaxation times depending on the temperature. It is based on the horizontal shifting of the spectra taken at various temperatures to superimpose them onto a reference spectrum following frequency-temperature superposition rules. The arbitrarily selected spectra above T_g are shifted horizontally so that their low-frequency side superimposes with the high-frequency side of our reference ones. Figure 3.27, 3.28, and 3.29 presents the master plots of acemetacin, brucine, and colchicine respectively. As expected from figure 3.26 (β_{KWW}-T graph), the dielectric loss curve becomes more and narrower (slope increases) with an increase in temperature for brucine and colchicine while an opposite trend is shown for acemetacin. Thus, non-

exponentiality decreases with temperature for brucine and colchicine while it increases for acemetacin.

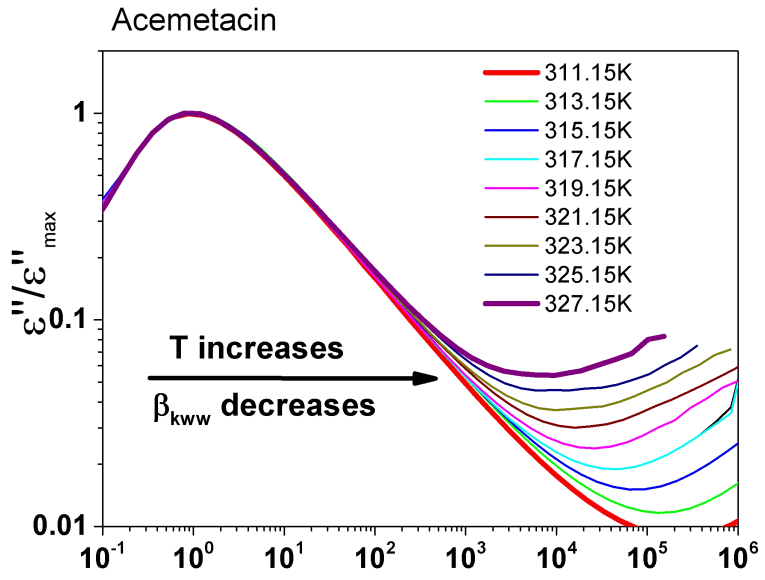

Figure 3.27 Master plot of acemetacin for T = 311K to 327K with reference to T=311K

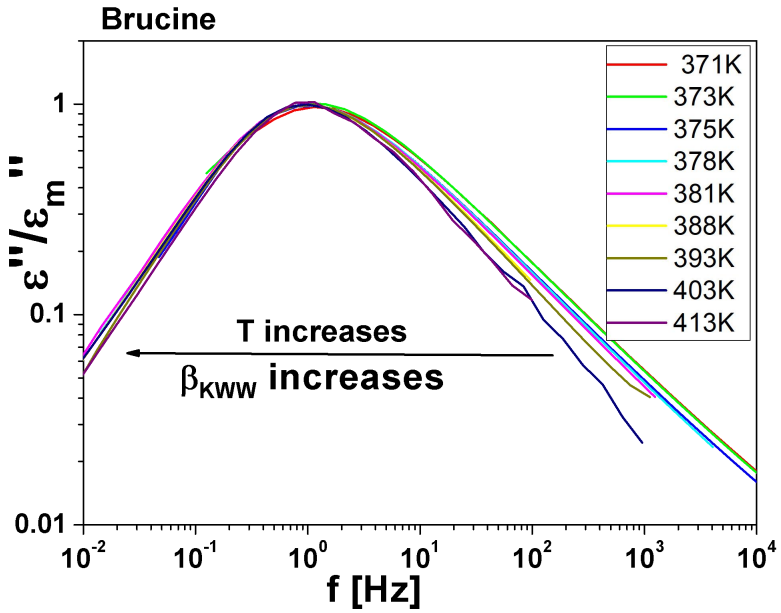

Figure 3.28 Master plot of brucine for T = 371K to 413K with reference at T=371K

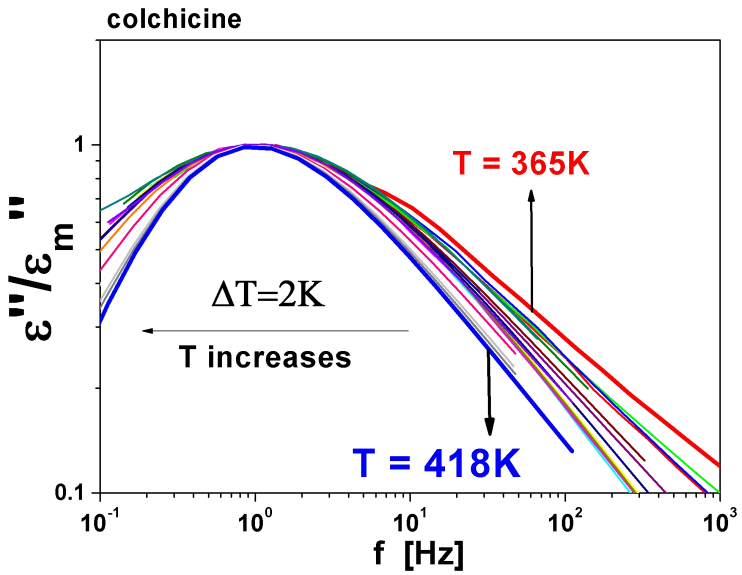

Figure 3.29 Master plot of colchicine for T = 365K to 418K with reference at T=365K

3.3.3.9 Paluch's anticorrelation

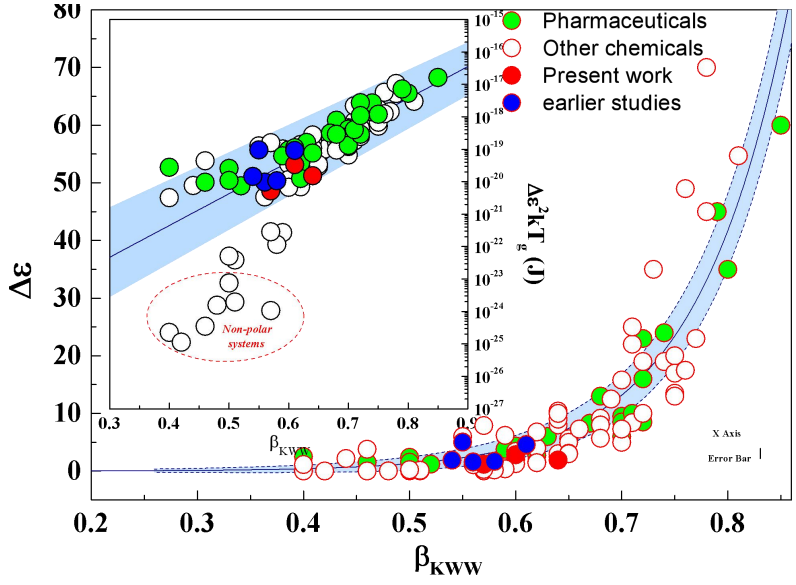

Figure 3.30. Dielectric strength Δϵ (T_g) as a function of the fractional exponent β_{KWW} in the Kohlrausch-Williams-Watts's function. The inset presents kT_g $(\Delta\epsilon(T_g))^2$ against β_{KWW}. The title compounds are found to be within the spread of Paluch's figure.

Paluch *et al.* have found that the asymmetric stretching parameter β_{KWW} of the α-loss peak at or near the glass transition temperature T_g (width of the dielectric loss spectrum) is strongly anti-correlated with the dielectric strength of the relaxation at that temperature (polarity of the molecule) in several glass formers. According to Paluch, the resultant potential more harmonic due to the contribution from the dipole-dipole

interaction potential $V_{dd}(r) = -Dr^{-6}$ to the attractive part of the intermolecular potential, where D is a characteristic constant given by $D \propto \mu^4/kT_g$. The data of the title compounds are within the spread of figure 3.30.

3.3.4 Origin of secondary relaxation: DFT approach

Density Functional Theory (DFT) is a popular computational quantum mechanical modelling method to investigate the properties of a many-electron system by using the functional, spatially dependent electron density. Starting with the optimized structure, the dihedral angle was modified in a constant phase of 10° over a 360° range, allowing for precise sampling. The remainder of the molecule was optimized at the frozen value of the corresponding angle (i.e. relaxed scan procedure) and the energ was calculated.

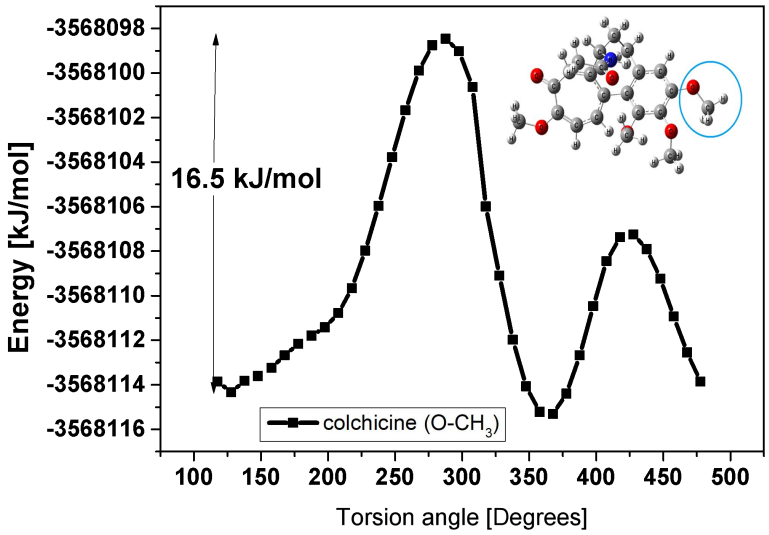

Figure 3.31 Dihedral scan energy diagram of colchicine showing the potential barriers on the the rotation of OCH_3 group

From figure 3.31, the potential energy barrier corresponding to the rotation of the the OCH_3 group in colchicine corresponding to the experimentally observed secondary relaxation with approximately the same activation energy. The rotation of the $NHCOCH_3$ group in colchicine yielded potential energy barriers with the the energy of 71kJ/mol which is not the origin of secondary relaxation.

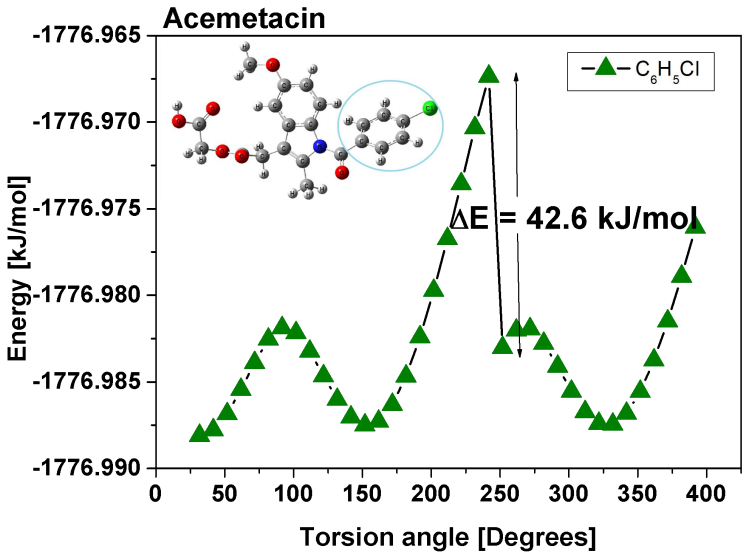

Figure 3.32 Dihedral scan energy diagram of acemetacin showing the potential barriers on the rotation of C_6H_5Cl group

The rotation of the CH_3 group shows that the CH_3 group doesn't originate the observed secondary relaxation. Since there are no other rotatable dihedrals in the molecule, in order to identify the origin of secondary relaxation in brucine high-pressure experiments may be needed.

3.3.5 Vibrational Spectroscopy

The presence and nature of the hydrogen bonding in the crystalline and amorphous states of the title compounds acemetacin, brucine, and colchicine were studied and compared by IR spectroscopy and to analyze the chemical changes in the structure of the title compounds on amorphization. Hydrogen bonding can occur if a proton donor group (X–H) and a proton acceptor (Y) group are present in a molecule and if the s orbital of the proton can effectively overlap with the p or pi orbital of the acceptor. Since the bond strength of the donor and acceptor groups are strongly influenced by hydrogen bond formation and the OH group is more sensitive, it is easy to study the molecular interaction using vibrational spectroscopic data. Common changes include redshift in absorption band, band broadening, and band intensification[39]. Hydrogen bonding changes the force constant of vibration of both groups as a result the X–H stretching band moves to lower frequencies. The optimized structure and Fourier Transform Infrared Spectroscopy (FTIR) spectra of acemetacin,

brucine, and colchicine were obtained using the theoretical DFT method with B3LYP/6-31g level of basis set using Gaussian 09[20,38].

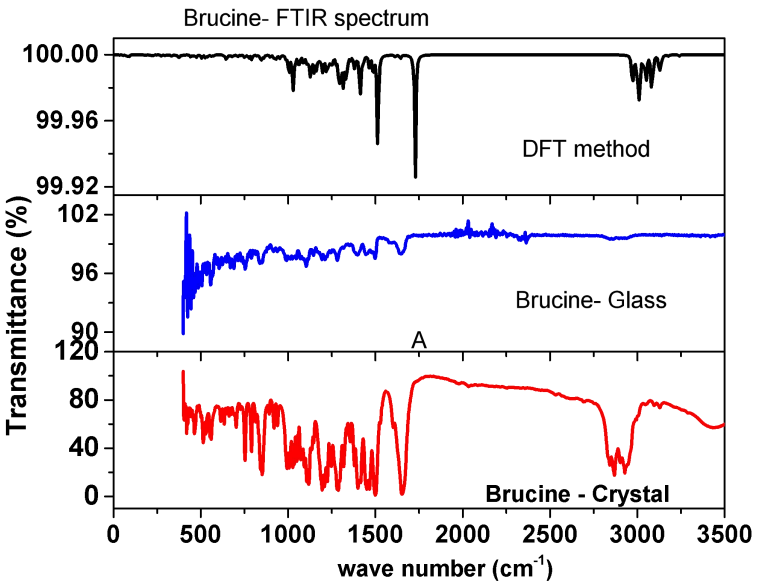

Figure 3.33 FTIR spectrum of brucine (crystal, glass, and DFT)

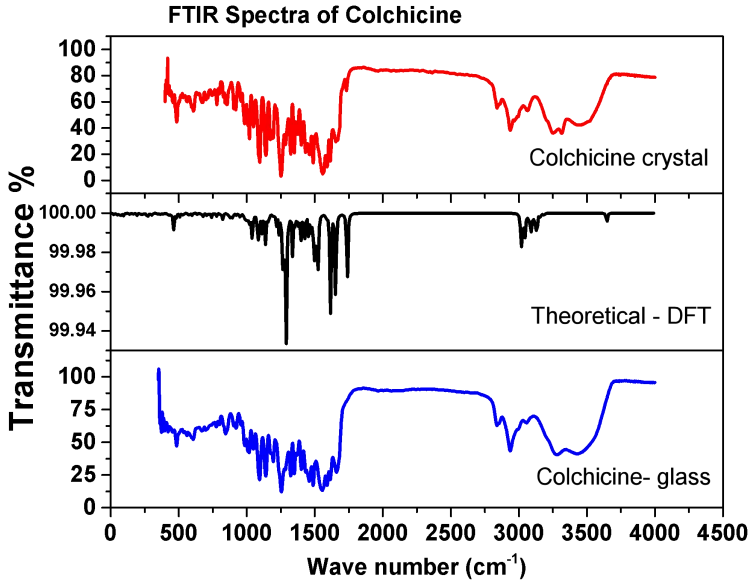

Figure 3.34 FTIR spectrum of colchicine (crystal, glass, and DFT)

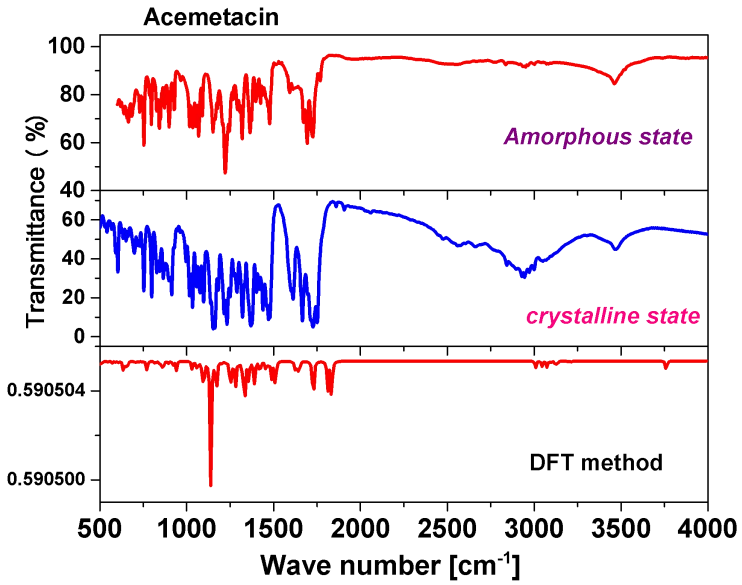

Figure 3.35 FTIR spectra of acemetacin in crystaline and glassy phases along with spectrum obtained by DFT)

The FTIR spectra of brucine, colchicine, and acemetacin in the crystalline and glassy states theoretical FTIR spectrum by DFT method are shown in figures 3.33, 3.34, and 3.35 respectively. The peaks in FTIR spectra of the crystalline state of the title compounds are in good agreement with that of FTIR spectra obtained by the DFT method thus the optimized molecular structure of the title compounds obtained by DFT was verified. The IR spectrum of crystalline brucine shows a C=O stretching mode at 1665 cm^{-1} and amorphous C=O stretching vibration at 1650 cm^{-1}. The corresponding DFT values of C=O stretching modes are 1670 cm^{-1} for brucine. The carbonyl peak position shifts to a new value due to the formation of hydrogen bonding as reported in the literature[40]. The formation of the hydrogen bond is supported by the broad nature of most of the bands in the IR spectrum of the amorphous state of the brucine molecule (bands at 3135, 2939, 1584, 1502, 1441, 1398, 1281, and 851 cm^{-1}) and similar properties are reported in the literature for ibuprofen [41] and ketoprofen [42]. Also, the IR bands in the 2000-2700 cm^{-1} region of the amorphous brucine and support the hydrogen bonding in the system which is absent in the crystalline brucine IR spectrum. The IR spectrum of crystalline Colchicine shows C=O stretching modes at 1725, 1618 cm^{-1} and amorphous C=O stretching vibrations at 1701, 1613 cm^{-1}. The corresponding DFT values of C=O stretching modes are 1670 cm^{-1} for brucine and 1716, 1620 cm^{-1} for colchicine. The carbonyl peak position shifts to a new value due to the formation of hydrogen bonding as reported in the literature[39,43]. The NH stretching mode of the

amorphous colchicine molecule shows a large deviation from 3455 cm^{-1} to 3258 cm^{-1} in the IR spectrum, which reveals the strong hydrogen bond in the colchicine amorphous molecule. The DFT calculations give this NH mode at 3507 cm-1. The formation of the hydrogen bond is supported by the broad nature of most of the bands in the IR spectrum of the amorphous state of the brucine molecule (bands at 3135, 2939, 1584, 1502, 1441, 1398, 1281 and 851 cm^{-1}) and amorphous state colchicine molecule (3258, 2952, 1701, 1613, 1539, 1248, 1137, 1084, 1047, 1011, 958, 918 cm^{-1}) and similar properties are reported in literature for ibuprofen and for ketoprofen. Also, the IR bands in the 2000-2700 cm^{-1} region of the amorphous brucine and colchicine molecules and their large broadening supports the hydrogen bonding in the system which is absent in crystalline brucine IR spectrum [44]. The FTIR spectra of acemetacin were in good agreement with the theoretical values. It was fascinating to note that all the vibrational peaks of acemetacin crystalline were retained in its glass counterpart. In FTIR of acemetacin, the peaks at 1727 cm^{-1} and 1694 cm^{-1} in the glassy state corresponding to C=O vibration were shifted to 1730 cm^{-1} and 1755 cm^{-1} in crystalline acemetacin. This is due to hydrogen bonding and the intensity of the vibrational peaks were reduced on amorphization of acemetacin. Hence the strong intermolecular hydrogen bonding in crystalline phase and expected weakening in amorphous phase is observed for all the title compounds. This is the general observation for most of the amorphous pharmaceuticals though there are notable exceptions. At the same time opposite to the expected character of narrowing the peaks with decrease in crystallinity in quenched sample, an increase in broadness is observed. The same case has been reported for many pharmaceuticals and is due to the broader distribution of hydrogen bond lengths in the disordered amorphous phase [45]. The identity of chemical structure of crystalline and amorphous phase of the title compounds and presence of hydrogen bonding is verified by Fourier Transform Infrared spectroscopy (FTIR).

3.4 Conclusions

In this chapter, the molecular dynamics in the super-cooled liquid and glassy states of three significant API's acemetacin, brucine and colchicine were studied using broadband dielectric relaxation spectroscopy. Brucine and colchicine are anti-cancerous alkaloids derived from plants, while acemetacin is a synthetic drug and is commonly used as an analgesic. From the Differential scanning calorimetric analysis of the title

compounds, acemetacin, brucine, and colchicine were found to be good glass formers with T_g higher than room temperature for all of them. T_g of plant-derived brucine and colchicine was found to be much higher than that of synthetic acemetacin. For safe storage of amorphous brucine and colchicine, the storage temperatures needed for them (T_g-50K) are still above room temperature which enables hassle-free safe storage, while amorphous acemetacin needs to be stored in a refrigerator to avoid crystallization. Broadband Dielectric relaxation spectroscopic measurements revealed structural α relaxation process above T_g in the supercooled liquid state (associated with dynamic glass transition phenomenon) and intramolecular secondary relaxation γ (associated with localized molecular motions) below T_g in the glassy state in all the title compounds, and in addition to it, brucine alone showed another secondary relaxation δ in the deep glassy state. The T_g values determined from the dielectric data from VFT fits and from the Arrhenius graph corresponding to τ=100s are in good agreement with the T_g value determined from DSC. Crystallization tendency was observed in acemetacin and colchicine from the dielectric data while heating at around 70K above the respective T_g of them, while no crystallization tendency was observed in brucine while heating in the supercooled liquid state. From VFT fits of the temperature dependences of α relaxation times, it was found that all the title compounds possess intermediate fragility out of which colchicine is less fragile than brucine and acemetacin. The temperature dependence of secondary relaxation time in all the title compounds followed Arrhenius temperature dependence. The activation energy of secondary relaxation (γ) in colchicine is lesser than that of brucine and acemetacin which suggests a lighter molecular sub-group responsible for γ relaxation. The asymmetrical stretching parameter β_{KWW} determined from KWW fits just above T_g for all the title compounds was found to be lowest for colchicine and highest for acemetacin which suggests considering glassy colchicine as more stable against recrystallization in ambient storage conditions. The dielectric loss peaks above T_g for all the title compounds are intermediately nonexponential and have a medium distribution of α relaxation times (β_{KWW}~0.56-0.64). β_{KWW} is found to increase with temperature for brucine and colchicine which indicates the stability of their amorphous phase while β_{KWW} is found to decrease with temperature for acemetacin which is also evident from the master plot analysis. Ngai's Coupling model was applied to all the title

compounds and found that the primitive relaxation times of Coupling model prediction were not in agreement with the observed secondary relaxation times and thus we concluded that the observed secondary relaxations in all the title compounds were not intermolecular JG-β relaxation. The primitive relaxation frequency calculated for α peak above T_g corresponds to a frequency where the excess wing is expected and there were signals of the presence of excess wing in the experimental α relaxation curves. Paluch's anti-correlation was found to obey all the title compounds like other Vander Waal glass formers. Thus, the difference between T_g and the onset temperature for crystallization, T_c, which is around 40 K for brucine and acemetacin is sufficiently large to avoid recrystallization of amorphous acemetacin, brucine, and colchicine for more than 1 year of storage under ambient conditions. In conclusion, the relatively high value of T_g of the title compounds indicates the possibility of preparing amorphous forms of acemetacin, brucine, and colchicine under standard conditions. The theoretical FTIR spectra of all the title compounds were in good agreement with the experimental FTIR spectra and thus we confirm the identity of the samples used for DSC and BDS experiments. FTIR analysis in the crystalline and glassy states reveals the presence of hydrogen bonding in all the title compounds. This study serves as a reference for the comparative dielectric relaxation study between plant-derived and synthetic pharmaceuticals.

References

[1] H.D. Williams, N.L. Trevaskis, S.A. Charman, R.M. Shanker, W.N. Charman, C.W. Pouton, C.J.H. Porter, Strategies to Address Low Drug Solubility in Discovery and Development, Pharmacol. Rev. 65 (2013) 315 LP – 499. https://doi.org/10.1124/pr.112.005660.

[2] M. Sahra, M.S. Thayyil, A.K. Bansal, K.L. Ngai, M.K. Sulaiman, G. Shete, K.P. Safna Hussan, Dielectric spectroscopic studies of three important active pharmaceutical ingredients - clofoctol, droperidol and probucol, J. Non Cryst. Solids. 505 (2019) 28–36. https://doi.org/10.1016/j.jnoncrysol.2018.10.046.

[3] Y. Sun, L. Zhu, T. Wu, T. Cai, E.M. Gunn, L. Yu, Stability of amorphous pharmaceutical solids: crystal growth mechanisms and effect of polymer additives., AAPS J. 14 (2012) 380–388. https://doi.org/10.1208/s12248-012-

9345-6.

[4] S. Yoshioka, Y. Aso, Correlations between Molecular Mobility and Chemical Stability During Storage of Amorphous Pharmaceuticals, J. Pharm. Sci. 96 (2007) 960–981. https://doi.org/https://doi.org/10.1002/jps.20926.

[5] R. Capen, D. Christopher, P. Forenzo, C. Ireland, O. Liu, S. Lyapustina, J. O'Neill, N. Patterson, M. Quinlan, D. Sandell, J. Schwenke, W. Stroup, T. Tougas, On the shelf life of pharmaceutical products., AAPS PharmSciTech. 13 (2012) 911–918. https://doi.org/10.1208/s12249-012-9815-2.

[6] S.L. Shamblin, B.C. Hancock, M.J. Pikal, Coupling between chemical reactivity and structural relaxation in pharmaceutical glasses, Pharm. Res. 23 (2006) 2254–2268. https://doi.org/10.1007/s11095-006-9080-8.

[7] T. Hikima, M. Hanaya, M. Oguni, β-Molecular Rearrangement Process, But Not an α-Process, as Governing the Homogeneous Crystal-Nucleation Rate in a Supercooled Liquid, Bull. Chem. Soc. Jpn. 69 (1996) 1863–1868. https://doi.org/10.1246/bcsj.69.1863.

[8] L. Chen, T. Okuda, X.-Y. Lu, H.-K. Chan, Amorphous powders for inhalation drug delivery., Adv. Drug Deliv. Rev. 100 (2016) 102–115. https://doi.org/10.1016/j.addr.2016.01.002.

[9] S. Capaccioli, M.S. Thayyil, K.L. Ngai, Critical issues of current research on the dynamics leading to glass trasition, J. Phys. Chem. B. 112 (2008) 16035–16049. https://doi.org/10.1021/jp8057433.

[10] M. Goldstein, The past, present, and future of the Johari-Goldstein relaxation, J. Non. Cryst. Solids. 357 (2011) 249–250. https://doi.org/10.1016/j.jnoncrysol.2010.05.105.

[11] K.L. Ngai, An extended coupling model description of the evolution of dynamics with time in supercooled liquids and ionic conductors, J. Phys. Condens. Matter. 15 (2003) S1107–S1125. https://doi.org/10.1088/0953-8984/15/11/332.

[12] K.L. Ngai, M. Paluch, Classification of secondary relaxation in glass-formers based on dynamic properties, J. Chem. Phys. 120 (2004) 857–873.

https://doi.org/10.1063/1.1630295.

[13] G. Power, J.K. Vij, Johari-Goldstein relaxation and crystallization of sorbitol to ordered and disordered phases, J. Chem. Phys. 120 (2004) 5455–5462. https://doi.org/10.1063/1.1648015.

[14] K.P. Safna Hussan, M. Shahin, Deshpande, Jinitha, K. Vijisha, Rajan, N. K.L, Synthesis and molecular dynamics of double active pharmaceutical ingredient-benzalkonium ibuprofenate, J. Mol. Liq. 223 (2016).

[15] S.H. Safna, M.S. Thayyil, S.K. Deshpande, J. T.V, J. Kolte, Development of ion conducting ionic liquid-based gel polymer electrolyte membrane PMMA/BMPyr.TFSI - With improved electrical, optical, thermal and structural properties, Solid State Ionics. 310 (2017) 166–175. https://doi.org/10.1016/j.ssi.2017.08.012.

[16] S.H. KP, M.S. Thayyil, M. Binesh, S.K. Deshpande, V.K. Rajan, Molecular dynamics in amorphous pharmaceutically important protic ionic liquid–benzalkonium chloride, J. Mol. Liq. 251 (2018) 487–491.

[17] U. Sailaja, M. Shahin Thayyil, N.S. Krishna Kumar, G. Govindaraj, Molecular dynamics in liquid and glassy states of non-steroidal anti-inflammatory drug: Ketoprofen, Eur. J. Pharm. Sci. 49 (2013) 333–340. https://doi.org/10.1016/j.ejps.2013.03.017.

[18] K.P. Safna Hussan, M.S. Thayyil, T. V. Jinitha, J. Kolte, Development of an ionogel membrane PVA/[EMIM] [SCN] with enhanced thermal stability and ionic conductivity for electrochemical application, J. Mol. Liq. 274 (2019) 402–413. https://doi.org/10.1016/j.molliq.2018.10.128.

[19] M. Paluch, J. Knapik, Z. Wojnarowska, A. Grzybowski, K.L. Ngai, Universal Behaviour of Dielectric Responses of Glass Formers: Role of Dipole-Dipole Interactions, Phys. Rev. Lett. 116 (2016) 1–6. https://doi.org/10.1103/PhysRevLett. 116.025702.

[20] M.J. Frisch, G.W. Trucks, H.B. Schlegel, G.E. Scuseria, M.A. Robb, J.R. Cheeseman, G. Scalmani, V. Barone, B. Mennucci, G.A. et. . Petersson, Gaussian 09, Gaussian, Inc. Wallingford, CT,.

[21] A. Alhalaweh, A. Alzghoul, D. Mahlin, C.A.S. Bergström, Physical stability of drugs after storage above and below the glass transition temperature:

Relationship to glass-forming ability, Int. J. Pharm. 495 (2015) 312–317. https://doi.org/https://doi.org/10.1016/j.ijpharm.2015.08.101.

[22] B. Schammé, M. Mignot, N. Couvrat, V. Tognetti, L. Joubert, V. Dupray, L. Delbreilh, E. Dargent, G. Coquerel, Molecular Relaxations in Supercooled Liquid and Glassy States of Amorphous Quinidine: Dielectric Spectroscopy and Density Functional Theory Approaches, J. Phys. Chem. B. 120 (2016) 7579–7592. https://doi.org/10.1021/acs.jpcb.6b04242.

[23] L. Carpentier, R. Decressain, S. Desprez, M. Descamps, Dynamics of the amorphous and crystalline α-, β-phases of indomethacin, J. Phys. Chem. B. 110 (2006) 457–464. https://doi.org/10.1021/jp053545u.

[24] A. Afzal, M.S. Thayyil, M.K. Sulaiman, A.R. Kulkarni, Dielectric relaxation studies in super-cooled liquid and glassy phases of anti-cancerous alkaloid: Brucine, Indian J. Phys. 92 (2018) 565–573. https://doi.org/10.1007/s12648-017-1139-3.

[25] F. Kremer, A. Schönhals Broadband Dielectric Spectroscopy, Eds.; Springer: (2003).

[26] K. Adrjanowicz, K. Kaminski, P. Wlodarczyk, K. Grzybowska, M. Tarnacka, D. Zakowiecki, G. Garbacz, M. Paluch, S. Jurga, Molecular Dynamics of the Supercooled Pharmaceutical Agent Posaconazole Studied via Differential Scanning Calorimetry and Dielectric and Mechanical Spectroscopies, Mol. Pharm. 10 (2013) 3934–3945. https://doi.org/10.1021/mp4003915.

[27] K. Grzybowska, M. Paluch, P. Wlodarczyk, A. Grzybowski, K. Kaminski, L. Hawelek, D. Zakowiecki, A. Kasprzycka, I. Jankowska-Sumara, Enhancement of Amorphous Celecoxib Stability by Mixing It with Octaacetylmaltose: The Molecular Dynamics Study, Mol. Pharm. . 9 (2012) 894−904.

[28] B.C. Hancock, S.L. Shamblin, Molecular mobility of amorphous pharmaceuticals determined using differential scanning calorimetry, Thermochim. Acta. 380 (2001) 95–107. https://doi.org/10.1016/S0040-6031(01)00663-3.

[29] C. A. Angell, Relaxation in liquids, polymers and plastic crystals - strong/fragile patterns and problems, J. Non. Cryst. Solids. 131 (1991) 13–31.

[30] R. Böhmer, K.L. Ngai, C.A. Angell, D.J. Plazek, Nonexponential relaxations in strong and fragile glass formers, J. Chem. Phys. 99 (1993) 4201–4209. https://doi.org/10.1063/1.466117.

[31] K. Kunal, C.G. Robertson, S. Pawlus, S.F. Hahn, A.P. Sokolov, Role of chemical structure in fragility of polymers: A qualitative picture, Macromolecules. 41 (2008) 7232–7238. https://doi.org/10.1021/ma801155c.

[32] D. Psimadas, P. Georgoulias, V. Valotassiou, G. Loudos, Molecular Nanomedicine Towards Cancer :, J. Pharm. Sci. 101 (2012) 2271–2280. https://doi.org/10.1002/jps.

[33] Z. Wojnarowska, K. Adrjanowicz, K. Kaminski, L. Hawelek, M. Paluch, Effect of pressure on tautomers' equilibrium in supercooled glibenclamide drug: Analysis of fragility behaviour, J. Phys. Chem. B. 114 (2010) 14815–14820. https://doi.org/10.1021/jp104444q.

[34] R. Casalini, C.M. Roland, Pressure Evolution of the Excess Wing in a Type-B Glass Former, Phys. Rev. Lett. 91 (2003) 1–4. https://doi.org/10.1103/PhysRevLett.91.015702.

[35] A.C. Rodrigues, M.T. Viciosa, F. Danède, F. Affouard, N.T. Correia, Molecular Mobility of Amorphous S-Flurbiprofen: A Dielectric Relaxation Spectroscopy Approach, Mol. Pharm. 11 (2014) 112–130. https://doi.org/10.1021/mp4002188.

[36] K. Kessairi, S. Capaccioli, D. Prevosto, M. Lucchesi, S. Sharifi, P.A. Rolla, Interdependence of primary and Johari-Goldstein secondary relaxations in glass-forming systems, J. Phys. Chem. B. 112 (2008) 4470–4473. https://doi.org/10.1021/jp800764w.

[37] C.P. Johari, M. Goidstein, Viscous liquids and the glass transition. II. Secondary relaxations in glasses of rigid molecules, J. Chem. Phys. 53 (1970) 2372–2388. https://doi.org/10.1063/1.1674335.

[38] M.J. Frisch, G.W. Trucks, H.B. Schlegel, G.E. Scuseria, M.A. Robb, J.R. Cheeseman, G. Scalmani, V. Barone, B. Mennucci, G.A. *et.al.* Petersson, Gaussian 09, Gaussian, Inc. Wallingford,CT, .

[39] M. Amalanathan, I. Hubert Joe, I. Kostova, Density functional theory calculation and vibrational spectral analysis of 4-hydroxy-3-(3-oxo-1-phenylbutyl)-2H-1-benzopyran-2-one., J. Raman Spectrosc. 9 (2010) 1076–1084.

[40] X.C. Tang, M.J. Pikal, LS. Taylor, Spectroscopic investigations of hydrogen bond patterns in crystalline and amorphous phases in dihydropyridine calcium channel blockers, Pharm. Res, 19 477–483.

[41] AR. Bras, JP. Noronha, AMM.Antunesn, MM. Cardoso, A. Schonhals, F.Affourd, M.Dionisio, NT.Correia, Molecular motions in amorphous ibuprofen as studied by dielectric spectroscopy, J. Phys. Chem., 112 (2008) 11087–11099.

[42] U. Sailaja, M. Shahin Thayyil, N.S. Krishna Kumar, G. Govindaraj, Molecular dynamics in liquid and glassy states of non-steroidal anti-inflammatory drug: Ketoprofen, Eur. J. Pharm. Sci. 49 (2013) 333–340, https://doi.org/ 10.1016/j.ejps.2013.03.017.

[43] M. PJ, H. Kono, LS. Taylor, A comparison of the physical stability of amorphous felodipine and nifidipine systems, Pharm. Res., 23 2306–2316.

[44] D. Philip, A. John, CY. Panicker, HT. Varghese, FT-Raman, FT-IR and surface enhanced Raman scattering spectra of sodium salicylate, Spectrochim. Acta. 57 (2001) 1561–1566.

[45] T. Mihaylov, N. Trendafilova, I. Georgieva, I. Kostova, Coordination properties of warfarin towards Pr(III) predicted from DFT and FT-IR studies. , Chem. Phys. 1–3 (2010) 37–45.

CHAPTER 4

THERMAL AND DIELECTRIC STUDIES IN SUPERCOOLED AND GLASSY STATES OF BEZAFIBRATE, FENOFIBRATE AND BINARY MIXTURE OF FENOFIBRATE

Reproduced in part with the permission of **Aboothahir Afzal** *et.al* from *the* following publication.

1. Molecular Dynamics in the Supercooled Liquid and Glassy States of Bezafibrate and binary mixture of Fenofibrate, **Aboothahir Afzal**, P.A. Sivaramakrishnan; Sailaja Urpayil; Simone Capaccioli, Mohamed Shahin Thayyil, Journal of Non-Crystalline Solids, 550, (2020), 120407. DOI: https://doi.org/10.1016/j.jnoncr ysol.2020.120407.

4.1 Introduction

Overcoming low water solubility and permeability are the two Herculean tasks an active pharmaceutical ingredient (API) for oral delivery had to overcome for getting efficient absorption to have the optimal therapeutic application[1,2]. Despite various strategies and intelligent protocols to enhance the bioavailability, a good number API's fail to fulfill this test mainly due to poor water solubility according to the biopharmaceutics classification system (BCS) [3,4] and hence an improvement of drug solubility is one of the prominent aspects of drug development process [3,5]. The severity of the situation can be read from the fact that about 40% of drugs wait for market approval and 90% of molecules in the drug discovery pipeline are poorly water-soluble[6–8]. Realizing the situation, different solubility enhancement tactics are already in practice on modifying the API's physical and chemical routes without losing their potency. Among these, amorphous formulation of poorly soluble drugs and their stabilization has become a promising approach [9], which can provide significant improvements in the solubility to attain enhanced bioavailability vis-à-vis their crystallized counterparts when administered orally[10]. However, all the accomplished benefits from the metastable state for promoting solubility via excess entropy, enthalpy, and free energy of the amorphous state are prone to their reversion to the crystalline state due to their thermodynamic instability of the former state. The transition can happen as quick as within a few minutes after their preparation to as long as few months during storage, which raises serious questions on their industrial viability [11]. The molecular mobility, the inherent property needed to retain the system in amorphous state and accounts its life expectancy can also initiate crystallization [12], since it opens an avenue for neighbouring molecules to align on to a single lattice array. So this topic has been a focus of study during the last couple of decades for both pharmaceutical scientists and the chemists alike [13]. One intuitive approach to finding a safer temperature zone where crystallization tendencies are least and the amorphous state is retained was by assessing the temperature where the intermolecular relaxation is expected to disappear. Here, the upper-temperature limit for safer storage has been estimated roughly by subtracting 50K from the glass transition temperature (T_g) by judging the hypothetical Kauzmann temperature T_K, where the intermolecular mobility is believed to cease[14]. Experimentally, molecular mobility in the glassy and super-

cooled liquid states of amorphous drugs was estimated by different experimental techniques viz. differential scanning calorimetry (enthalpy relaxation)[15], NMR spectroscopy experiments (spin−lattice relaxation)[16], broadband dielectric spectroscopy or BDS (dipolar relaxation)[17] by estimating the associate time within the different molecular processes. Among these, BDS hailed to be the best in terms of its ease, high sensitivity, and accessible broad dynamic range for monitoring the dynamics by ac impedance measurement and giving quantitative picture on charge transport and rotational fluctuations of molecular dipoles[18–20]. On further investigating the dynamics by varying temperature and/or elevating pressures across T_g, a wealth of information can be explored.

Above T_g, a noticeable structural or α-relaxation originating from cooperative reorientation motions of the drug molecules is seen similar to a typical glass forming system, which moves to higher frequencies on elevating the temperature. Temperatures below T_g, the α-relaxation become slower and goes beyond experimental timescales, while fast local motions originating from inter or intra-molecular processes would be more active within our frequency window, designated as β, γ, δ relaxations. Often the intermolecular secondary relaxations are not visible in the dielectric measurements of most of the samples. Considering its fundamental importance ever since the classic discovery by two pioneering scientists, Johari and Goldstein, researchers have pursued it by conducting dielectric experiments at elevated pressure or as a probe in an apolar host of higher T_g for its detection. Moreover, the comprehensive information gained from the studies can connect to many crucial links for resolving the still unresolved glass transition theory as well as for promoting progress in allied subjects like polymers, metallic glasses, colloids, ionic liquids, plastic crystals etc [21,22].

Bezafibrate and fenofibrate belong to the fibrate class of drugs and are used to treat hypercholesterolemia and hypertriglyceridemia [23,24]. Bezafibrate is also used to treat heart problems [25] such as myocardial infarction in patients suffering from metabolic syndrome[26–28] and used to reduce blood cholesterol levels[29]. The water solubility of bezafibrate is reported to be 0.00155mg/mL at 37^{o}C [30,31] and fenofibrate is virtually insoluble in water [32,33]. Both bezafibrate and fenofibrate belong to class II drugs in the biopharmaceutical classification system (BCS) [34] and are characterized by low solubility and high permeability. Such drugs are not

adequately dissolved in the gastrointestinal fluid, as a result, it is not absorbed in bloodstream adequately, and hence the drug absorbed is inadequate to stimulate the receptors to produce the desired therapeutic effect. One solution is to increase its dose; which usually results in local toxicity, and side effects and is not favorable. The appropriate solution is to employ a suitable solubility enhancement procedure for such drugs, where amorphization is one such technique [35]. As both of these fibrate drugs have similar medical [36,37], it is interesting for a pharmaceutical scientist to identify the amorphous form out of these two drugs having better stability.

To characterize the molecular mobility of amorphous bezafibrate and fenofibrate, we carry out the broadband dielectric spectroscopy (BDS) of neat bezafibrate and compared it with the latter [38]. The experiments from frozen glassy state to vibrant molten state were done to explore the role of parameters describing the complex molecular dynamics and the describing parameters such as glass transition temperature (T_g), the temperature dependence of α-relaxation times (τ_α), the width of structural dispersion and its role on the occurrence of Johari-Goldstein (JG) relaxation, fragility index (m), the apparent activation energy of secondary processes, conductivity relaxation and rotational-translational coupling in the glassy state. Using the current study as a model, the ultimate aim is to explore the benefits of this analysis to study complex drug formulations. The information thus obtained can be used to understand the crystallization behaviour in drug systems and enable us to design stable drugs and to design storage conditions. On noting that most of the pharmaceuticals have narrow α- dispersion which limits the visibility of JG relaxation as a separate process in the dielectric window. To resolve the conundrum and suggest ways to suppress crystallization tendencies during storage, we have further explored the dielectric spectroscopy of binary system of fenofibrate, having lower molecular weight among fibrate drugs as the probe in a test apolar host (polystyrene 800). Recently it was widely accepted that the physical stability of amorphous pharmaceuticals can be improved by mixing them with polymers[39]. The role of polymers in enhancing the physical stability of amorphous pharmaceuticals was reported in the literature[40]. It was reported that the crystal growth rate was reduced by 100 fold in the presence of 1% w/w of the suitable polymer [41].

The molecular dynamics in the glassy state and hence the activation energy of the observed secondary γ relaxation of glass formers could be determined by the experimental methods like BDS, but no experimental technique is available until now to give sufficient information that can help to identify the relevant part of the corresponding molecule whose motion originates the observed intramolecular secondary relaxation in its glassy system. Therefore, our experimental investigations of bezafibrate and fenofibrate[38] using BDS were complemented with quantum computational DFT calculations. Accordingly, the origin of the observed secondary relaxations in fenofibrate and bezafibrate was identified theoretically by DFT/6-311g(d,p) level of theory from calculated energy barriers and dipole moments when appropriate selected flexible molecular end groups are relaxing.

Chemically, both these title fibrate drugs have molecular structures which differ only by their attached groups on the main skeleton, i.e., amide and carboxylic acid in bezafibrate, while keto and esters in fenofibrate. Glassy dynamics studies of complex structures similar to this study have contributed significantly to researchers engaged in the theory of glass transition problem[21,22] and also helped to explore diverse glass-forming systems like amorphous pharmaceuticals, biopolymers, metallic glasses, colloids, ionic liquids, plastic crystals, etc. The findings of this study are of much significance for the researchers engaged in glassy systems as the title drugs have complex molecular structures belonging to different classes of organic compounds.

4.2 Experimental section

Bezafibrate, fenofibrate, and polystyrene $(C_8H_8)_n$ or PS800 were the samples selected for study and were purchased from Sigma Aldrich and were used as received without further purification. A binary system of 10% by weight fenofibrate in PS800 was prepared using weighing balance and the sample was kept at 75^{o}C in dry N_2 gas purge for about 24 hours with slow stirring to ensure uniform mixing. The chemical structures of the three systems are given in figures 4.1, 4.2, and 4.3.

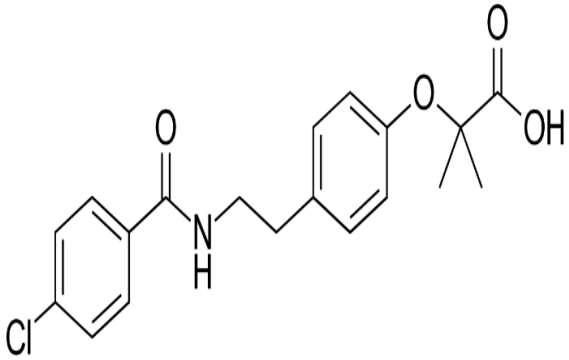

Figure 4.1 Chemical structure of bezafibrate

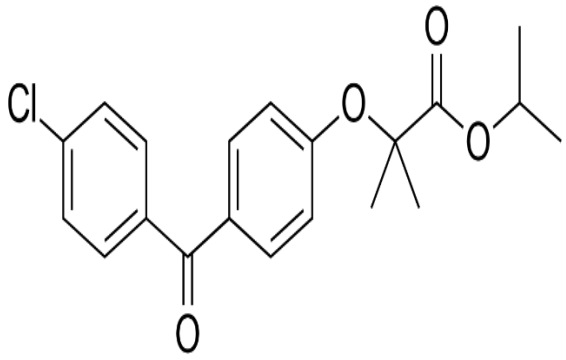

Figure 4.2 Molecular geometry of fenofibrate

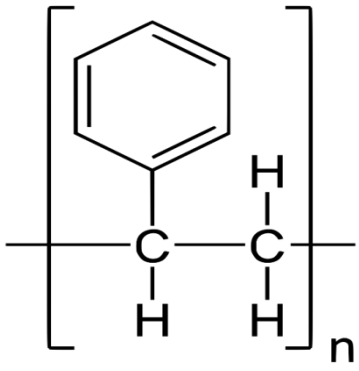

Figure 4.3 Molecular geometry of polystyrene

The experimental methods used in this chapter are TGA, DSC, BDS, FTIR, and FT-Raman and the computational tools used are DFT using Gaussian-09 [42]**.** The details of the methods are discussed in chapter 2. The powdered sample was initially heated in the dielectric cell to a few degrees above its melting temperature by slightly elevating one side of the upper electrode to remove any engulfed air bubbles between the electrodes, and fast cooled to a deep glassy state (~ 120 K) by ensuring a smooth

transit to the deep glassy state by recording isochronal response at few frequencies. Isothermal dielectric data were recorded by stabilizing the sample at a set temperature for about 600 s[17].

4.3 Results and discussion

4.3.1 Thermogravimetric analysis

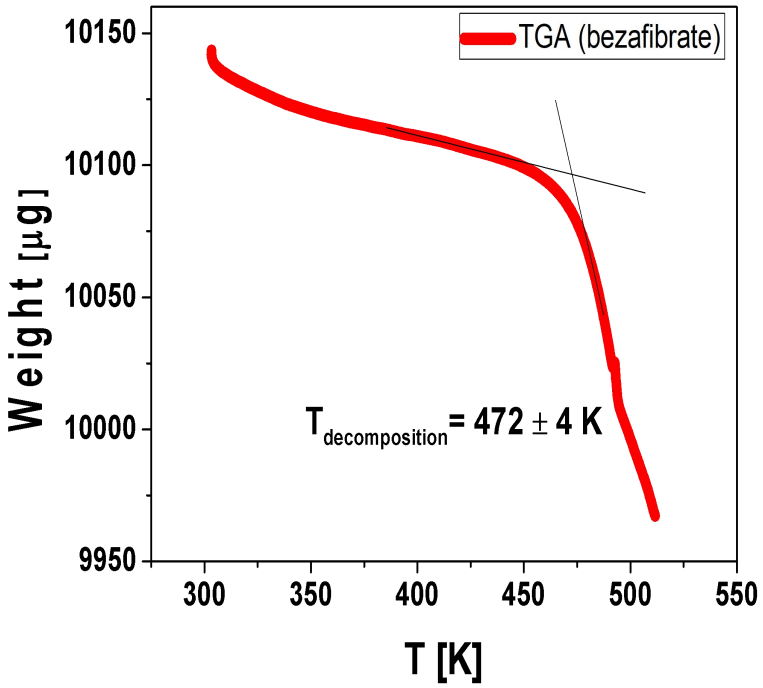

Figure 4.4 TGA curve of bezafibrate

The TGA curve of bezafibrate is shown in figure 4.4. The sample undergoes a decline in weight from 450K due to thermal degradation and the temperature of decomposition is taken as the onset of the thermal decomposition process and is taken as 472K which is above the melting temperature and therefore the dielectric measurements obtained are that of pure bezafibrate.

4.3.2 Differential Scanning Calorimetry

The DSC curve of bezafibrate is shown in Fig. 4.5. Thermogram obtained while heating the crystalline bezafibrate from room temperature to a few degrees above its melting temperature and subsequent cooling and reheating the sample are shown. Melting point (T_m) is evaluated as the onset of the melting endotherm as 460.4 K, which is very close to the value already reported in the PubChem database[43]. The

DSC thermogram of bezafibrate is shown in figure 4.5 showing well-resolved melting and glass transition. The melting temperature was found to be 460K for bezafibrate. From the DSC data in the vicinity of the glass transition, T_g of bezafibrate was determined as the onset of endotherm to be 301 ± 5K. The glass transition temperature (T_g) of bezafibrate was determined to be 301K during the subsequent heating of the supercooled melt sample.

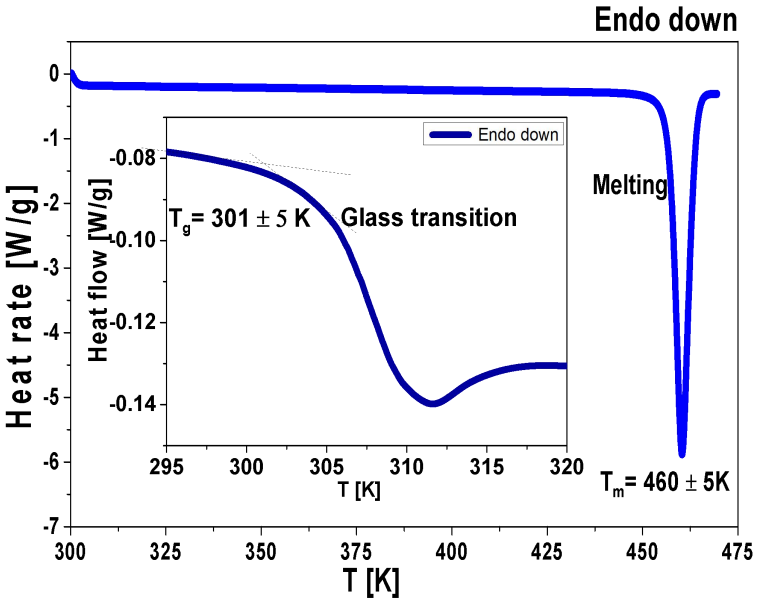

Figure 4.5. DSC curve of bezafibrate. Glass transition is shown in the inset

The T_g of fenofibrate was already reported from our laboratory to be 254.15 K. The stability of an amorphous system increases with the increase of its T_g [44]. According to Kauzman [45] and Turnbull[46], the ratio T_g/T_m can give insights into the glass-forming ability of a material, and a good glass former shows a value greater than 2/3. The ratio gave a value of 0.675 for bezafibrate and 0.72 for fenofibrate, and accordingly, fenofibrate is a better glass former among the two[47,48].

4.3.3 Broadband dielectric spectroscopy

In the present study, we focused our attention on pure bezafibrate to compare with fenofibrate previously explored from our laboratory[38] and further on the binary mixture of fenofibrate with a stable apolar glass former to explore the dielectric relaxations in its supercooled liquid and glassy states in permittivity representation to characterize the significant parameters associated with the glass transition phenomena and to address ways to suppress instability of amorphous phase. To get preliminary

information about the glass formation and the chances of crystallization during cooling, we have acquired isochronal permittivity data at three-four test frequencies of bezafibrate and the response has been shown as the temperature dependence of real and imaginary parts of complex dielectric constant in the figures 4.6 and 4.7 respectively. A smooth passage towards the amorphous phase is evident from the gradual increase of the real part of dielectric permittivity followed by a sharp decrease across the glass transition region without any indications of crystallization typical to most glass formers [49]. Further, the presence of a clear secondary relaxation in bezafibrate is noticed from the real and imaginary parts of permittivity given in figures 4.6 and 4.7.

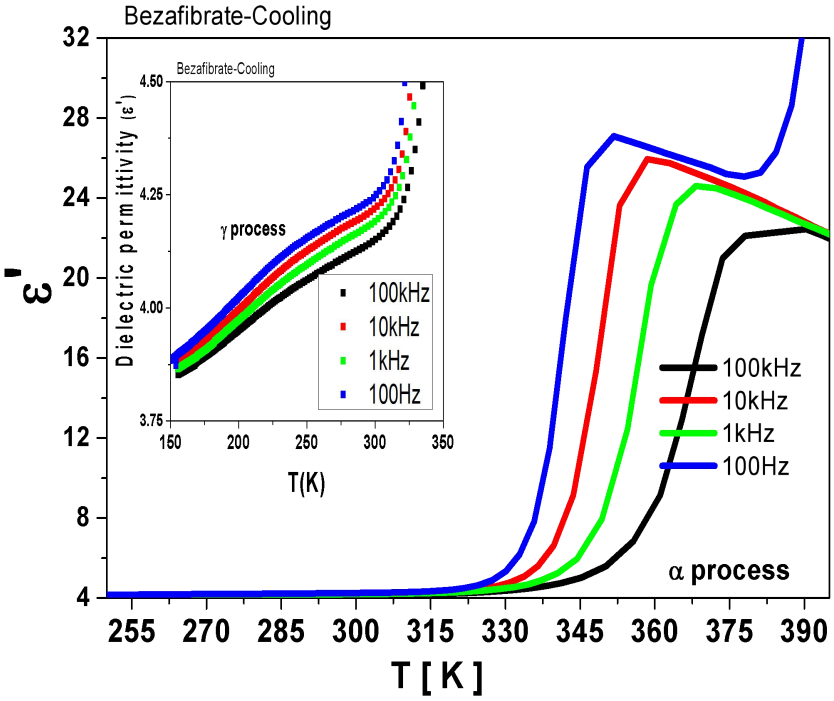

Figure 4.6. ε' vs. T in bezafibrate on quench cooling

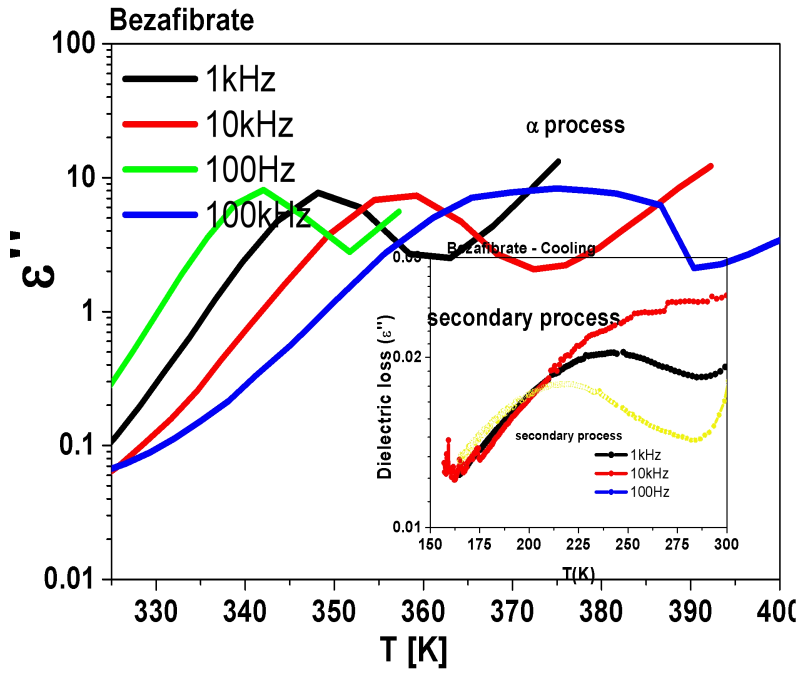

Figure 4.7 ε'' vs. T in bezafibrate on quench cooling

4.3.3.1 Supercooled liquid state (T > T_g)

To get details about the temperature dependence of dielectric properties and other parameters related to glass transition phenomena, we have collected isothermal dielectric data of bezafibrate during heating, covering the temperature ranges of both below and above T_g. The real part of the complex dielectric spectra (ε′) of the bezafibrate and PS800-fenofibrate mixture in the supercooled liquid state are shown in Fig. 4.8 and Fig. 4.9 respectively. Spectra of pure fenofibrate were reported by U. Sailaja *et al.* [38]. The permittivity response shows signatures typical to most molecular glass formers, where the spectra have higher and lower saturation values ε_0 and ε_{inf} at lower and higher frequencies respectively, whose difference is the dielectric strength (ε_0 - ε_{inf} = $\Delta\varepsilon$), and a fast and smooth switchover across a characteristic relaxation frequency. The relaxation frequency moves to higher frequencies on an increase of temperature, while the dielectric strength varies inversely to the absolute temperature in the supercooled region. In the case of pure bezafibrate, a sharp increase from the ε_0 value at higher temperatures is due to the low-frequency side is due to the dc conductivity originating from the hopping of ions present in the molecule. A very low value of dielectric strength in PS800-fenofibrate is due to the relatively very low

mole-fraction of polar molecules present in the binary and it generally maps almost linearly with the mole-fraction in the binary systems.

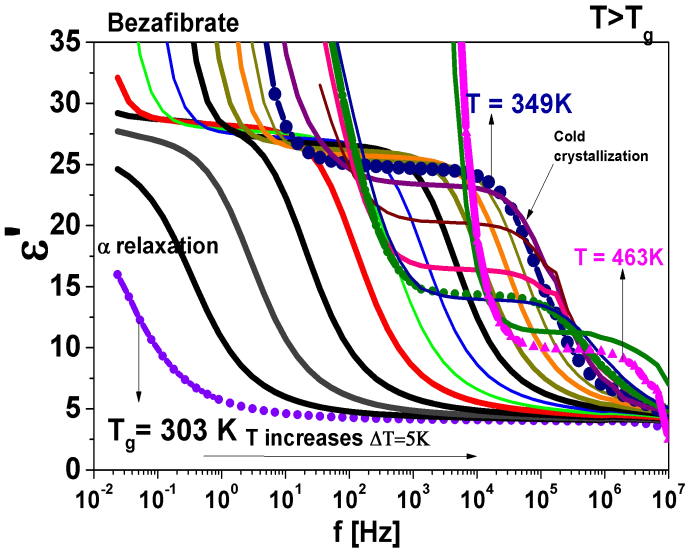

Figure 4.8 Real part of complex dielectric permittivity spectra above T_g of bezafibrate from 303 K to 463K

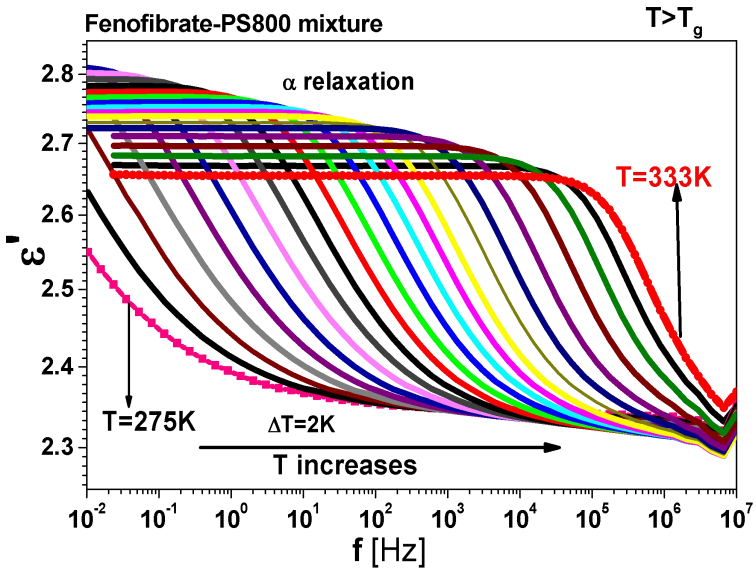

Figure 4.9 Real part of dielectric permittivity spectra above T_g of PS800-fenofibrate mixture from 275 K to 333 K

The dielectric loss spectra above T_g of bezafibrate is shown in Fig.4.10 Increase of dielectric loss at the low-frequency region is observed, which is due to dc conductivity attributed to translation and diffusion of charges, while on the high-frequency side, the increase is due to residual secondary relaxations present at those frequency regions.

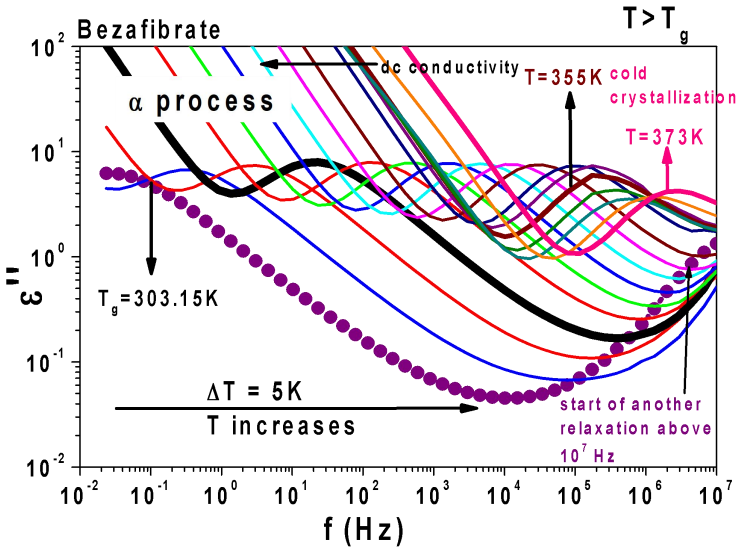

Figure 4.10 Dielectric loss spectra of bezafibrate in the supercooled liquid state showing α relaxations

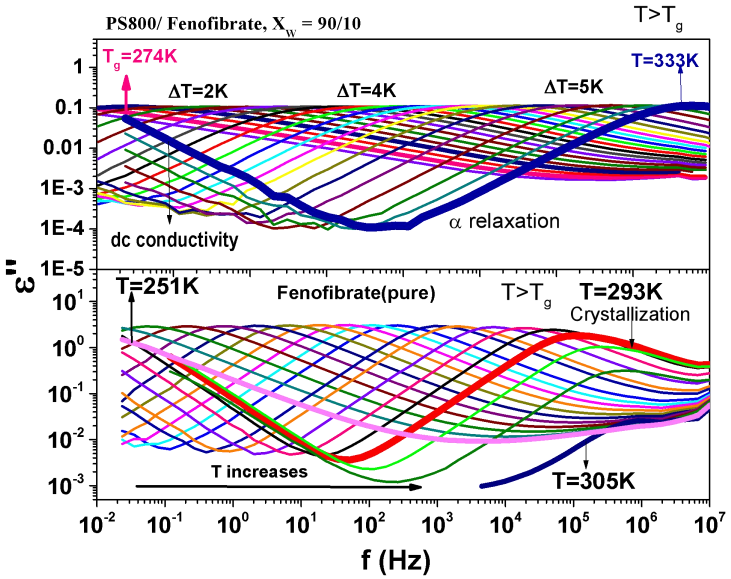

Figure 4.11. Dielectric loss spectra of the fenofibrate-PS mixture (T=274K to 333K) and pure fenofibrate (below) (274K to 305 K) in the supercooled liquid state

The dielectric loss spectra above T_g of pure [38] and binary mixture of fenofibrate are shown in Fig.4.11. Typical of other glass-forming systems, the loss spectra of both bezafibrate and fenofibrate-PS mixture have a characteristic peak and monotonous decrease on either of the peak loss frequency. Structural (α) relaxation observed is well resolved in both bezafibrate and fenofibrate PS800 mixture, which move to higher frequencies on the increase of temperature and whose kinetic freezing results in glass transition phenomena. From T=355 K onwards in bezafibrate, dielectric

loss shows a much-decreasing tendency beyond 1/T behaviour due to crystallization, while the same trend had been reported in fenofibrate from T=289 K onwards [38].

No tendency of crystallization is observed in the PS800-fenofibrate mixture, as it is obvious that due to higher concentration of the PS800. One of the most exciting modifications in the dynamics of the drug molecule by the addition of excipient is on its α-relaxation time, which can shift either longer or shorter times depending on the composition of the mixture and the host Tg. Here, the molecular mobility of fenofibrate is reduced by mixing with a higher Tg host, and hence the crystallization tendency is blocked. Origin of dielectric strengths and its dynamics of a probe molecule in an excipient as explored through dielectric spectroscopy is of great interest for not only deciding the stable storage temperature of an amorphous pharmaceutical but also from the academic perspective. This can critically be examined by choosing a polar drug molecule, here fenofibrate, as a guest in a stable apolar host PS800, where the dielectric spectroscopy can selectively probe the rotational dynamics of the polar molecules alone[50]. Beyond the discussion on the component dynamics in binary mixtures, an important left-out aspect was the fundamental role played by a secondary relaxation, which has properties either mimicking or correlated with that of the α-relaxation, which would be discussed in the coming sections [51]. The imaginary part of the dielectric modulus spectrum of bezafibrate in a glassy state is shown in fig. 4.13, where the observed α-relaxation in dielectric loss spectra and conductivity relaxation in bezafibrate is shown. On comparing the dielectric loss spectra of the three title compounds, the residual secondary relaxation which was observed in the higher frequency region in bezafibrate was not observed in the binary mixture of the fenofibrate-PS mixture.

4.3.3.2 Glassy state ($T < T_g$)

Figures 4.12 (a) and (b) present the imaginary part of dielectric permittivity spectra of bezafibrate in the glassy state from T=128 K to 213 K and T= 223 K to 298 K respectively showing the presence of secondary relaxation. In Fig. 4.12, from T=128 K to 193 K the secondary relaxation is well resolved and complete whereas from T = 193K onwards another relaxation towards higher frequency region is seen and the dielectric loss peaks in the higher temperature region from T = 223K to T = 283K is shown in figure 4.12.

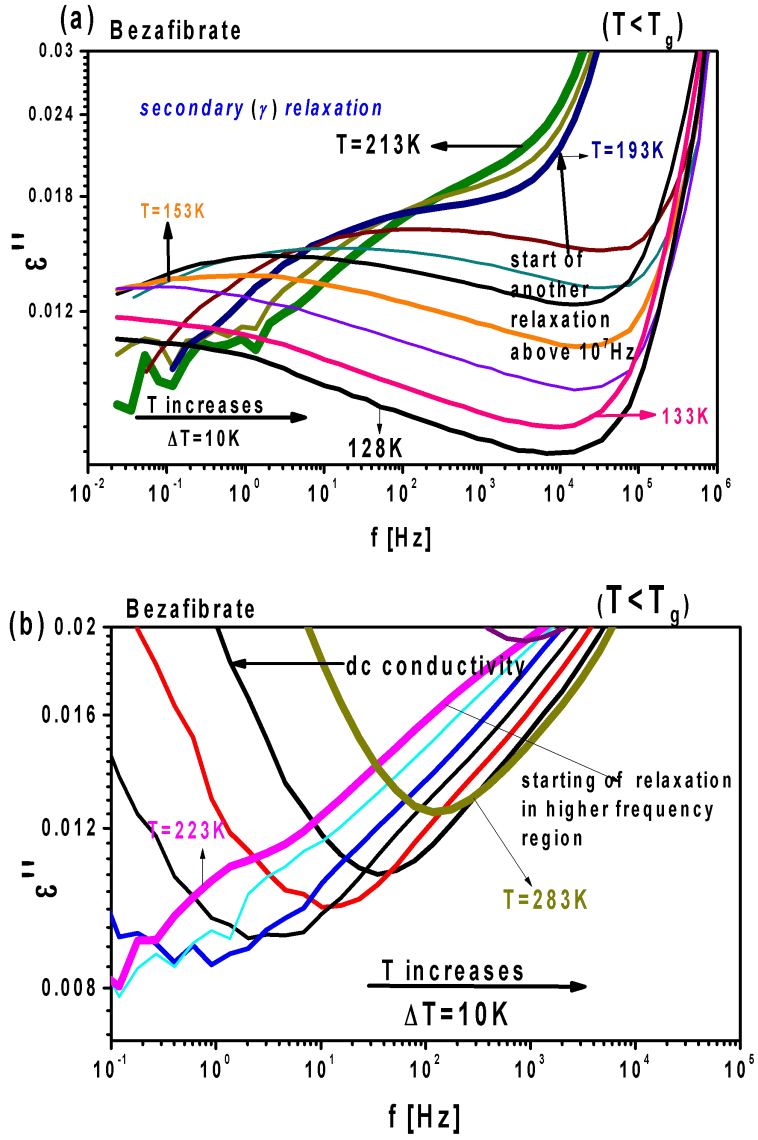

Figure 4.12 Imaginary part of the dielectric permittivity spectra below T_g of bezafibrate a) T = 128 K to 213K, b) T = 223K to 298K

The imaginary part of the complex modulus spectra in the glassy states of bezafibrate is shown in Fig. 4.13 which also shows the same secondary process observed in the dielectric loss spectrum.

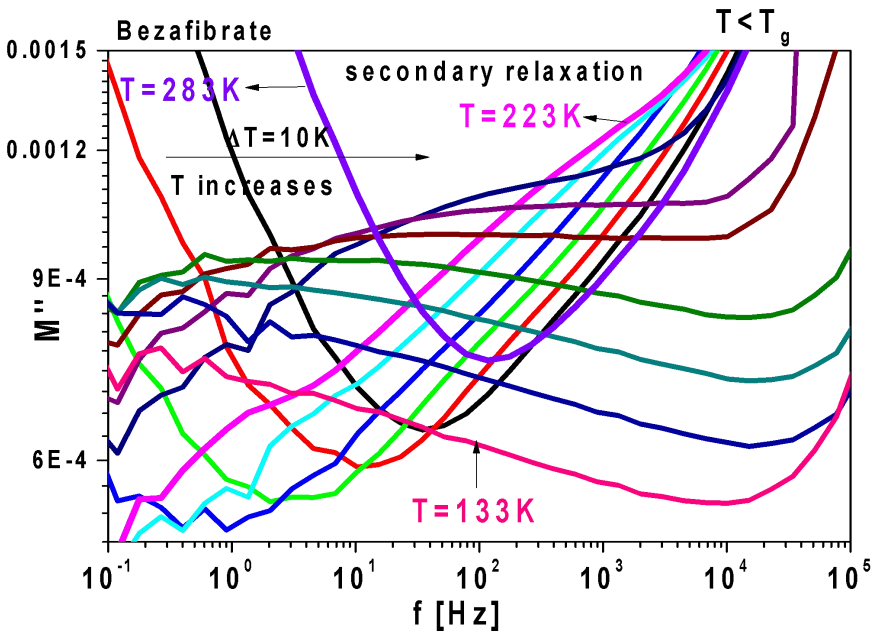

Figure 4.13 Imaginary part of the dielectric modulus spectrum of bezafibrate below T_g

Figures 4.14 a and 4.14 b present the imaginary part of dielectric permittivity and modulus spectra respectively of fenofibrate [38]. The analysis of the measurements in the modulus formalism help to study conductivity relaxations if present in the samples. In bezafibrate, the secondary relaxations are well resolved in the temperature range 133K to 213K, but from 233K, the secondary relaxations are found to be unresolved and conductivity becomes dominant. In the low-frequency region, a rapid increase in dielectric loss which is due to dc conductivity is present in bezafibrate from 253K another relaxation process at a higher frequency out of our experimental window is also observed, as a rapid rise in the dielectric loss after the excess wing, and conducting high-frequency experiments may help to understand the nature of relaxations occurring in the higher frequency region in the glassy state.

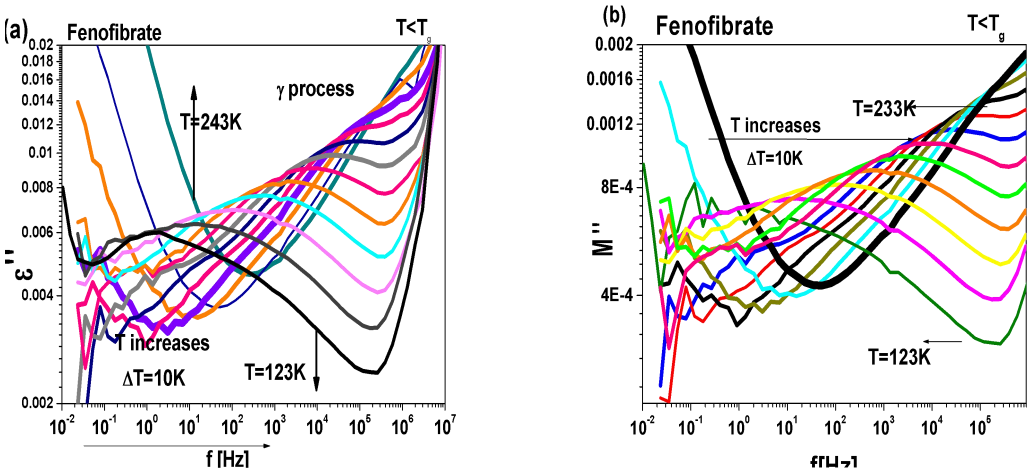

Figure 4.14 Imaginary part of complex dielectric spectra of fenofibrate below T_g in a) permittivity representation b) modulus representation

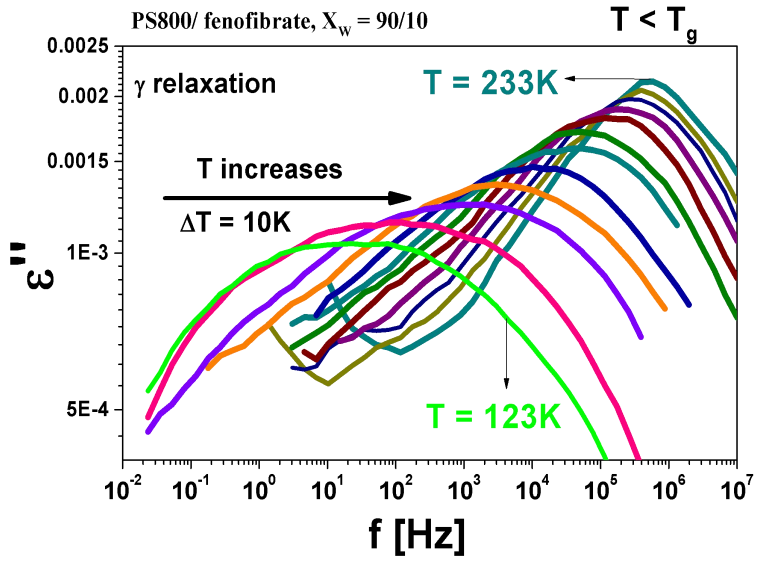

Figure 4.15 Dielectric loss spectra of fenofibrate-PS (T=123K to 233K) in the glassy state

The dielectric loss spectra of the fenofibrate-PS mixture in glassy state below T_g is shown in figure 4.15. A secondary relaxation of intramolecular nature was reported to be observed in fenofibrate from our laboratory [38]. Johari-Goldstein β relaxation is considered universally present in all glass formers and is the precursor of structural α relaxation which is a property of a typical glass former. But this JG β relaxation was not observed in many glass formers including pharmaceuticals including in fenofibrate. If the relaxation time (τβ) of the expected JG-β lies between that of the observed α and γ relaxations, the JG-β is obscured by α and γ-relaxations in the dielectric spectra. Such hidden JG-β relaxation is normally resolved by preparing a mixture of the glass former with a substance having high T_g [50]. The nature of the observed secondary relaxation

in the fenofibrate-PS mixture is found to non-JG (intramolecular) and the expected Johari-Goldstein β relaxation could not be resolved even after mixing fenofibrate with polystyrene 800. This suggests that mixing of polymer PS800 with fenofibrate is not sufficient to resolve the universal JG-β relaxation in glassy fenofibrate, as a polymer of much higher T_g than that of PS800 is needed for resolving JG-β relaxation in fenofibrate.

4.3.3.3 Relaxation map (Temperature dependence of relaxation time)

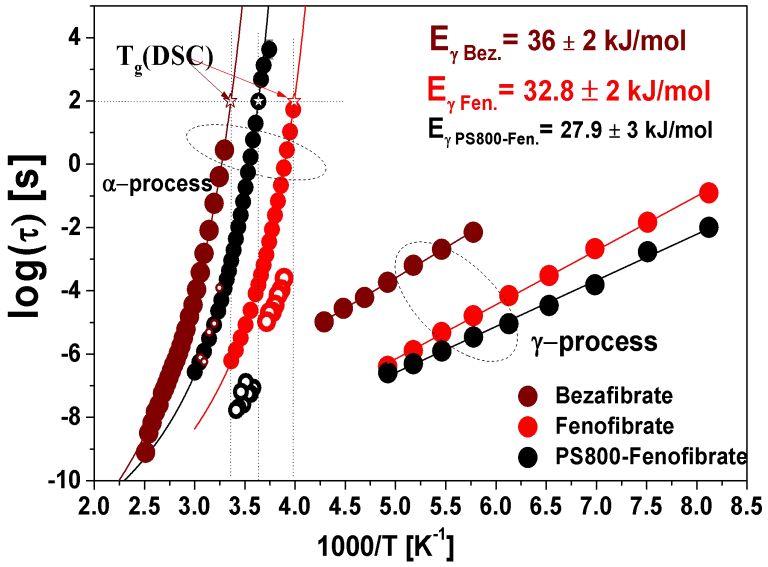

Figure 4.16. Relaxation map of bezafibrate, fenofibrate, and PS - fenofibrate mixture

The characteristic relaxation times at different temperatures in the supercooled liquid and glassy states of bezafibrate and fenofibrate-PS mixture were determined from the HN fits of the corresponding dielectric loss spectra. Relaxation map of bezafibrate, fenofibrate (by permission [38]), and fenofibrate-polystyrene mixture are shown in figure 4.16 for comparison. The values of T_g and activation energies of secondary relaxations determined are shown in figure 4.16. Open colored circles represent primitive relaxation times τ_0 of the coupling model above T_g. From Fig. 4.16, the temperature dependence of structural relaxation times in bezafibrate and fenofibrate-PS shows almost a similar fashion to that in fenofibrate but shifted to higher temperatures in fenofibrate-PS mixture and bezafibrate than pure fenofibrate. On the other hand, the temperature dependence of secondary relaxation times in bezafibrate and PS-fenofibrate shows almost similar fashion to that in fenofibrate but shifted to lower temperatures in the fenofibrate-PS mixture and higher temperatures in

bezafibrate than pure fenofibrate. The structural relaxation times show non-linear temperature dependence while that of secondary relaxation shows linear dependence in Fig. 4.16. T_g is determined from the relaxation map as the temperature at which the τ = 100s and is found to be 300.57K for bezafibrate and 274.7K for fenofibrate-PS mixture. The value of Tg of bezafibrate determined from the BDS method is closer to the value obtained by the DSC method.

The stability of an amorphous pharmaceutical is generally assessed from the gap between its T_g and storage temperature. It is reported that storing an amorphous drug 50K below T_g ensures its physical stability during its shelf life [49], as thermal energy available at such temperatures would be not enough to create molecular mobility and hence can avoid recrystallization. The T_g value of bezafibrate is around 50K more than fenofibrate, which suggests amorphous bezafibrate could be more stable than amorphous fenofibrate under similar ambient storage conditions. The non-linear temperature dependence of structural relaxation times of bezafibrate and fenofibrate-PS mixture was fitted by the Vogel-Fulcher-Tamann (VFT) equation [52–54].

$$\tau_{\alpha} = \tau_{\infty} \exp\left(\frac{DT_0}{T - T_0}\right) \tag{4.4}$$

where T is the absolute temperature, D is the strength parameter and T_0 is the ideal glass transition temperature at which all important molecular motion stops and relaxation time becomes infinity [55]. From the VFT fit parameters shown in Table 4.1, T_g of bezafibrate and fenofibrate-PS mixture was found to be 306.9K and 275.1K respectively. From the strength parameter values (D) in table 1, amorphous bezafibrate is stronger than amorphous fenofibrate and fenofibrate-PS. The value of T_0 determined is 233K for bezafibrate which is also greater than that of fenofibrate and fenofibrate-PS mixture. The value of T_g–T_o for bezafibrate is higher than both the other samples which point to better stability.

The activation energy of secondary relaxation was calculated by the Arrhenius equation (equation 4.5) and presented in table 4.1,

$$\tau(T) = \tau_{\infty} \exp\left(\frac{E_a}{RT}\right) \tag{4.5}$$

The activation energy of the γ process ($E_{a\gamma}$) in bezafibrate is 36.57 kJ/mol which is comparatively larger than that in fenofibrate and fenofibrate-PS mixture. The decrease in the

value of Eaγ in the fenofibrate-PS mixture is attributed to the presence of the high Tg solvent PS800. Similar behaviour is shown by some glass formers reported in the literature[56]. The origin of the secondary process in fenofibrate and bezafibrate was identified by coupling model predictions and further substantiated theoretically by DFT calculations and is discussed in the later section of this chapter.

Table 4.1

VFT Fit Parameters of bezafibrate, fenofibrate, and fenofibrate-PS mixture

Sample	T_g(K)	m	D	log τ_{VF}	T_0(K)	$E_{a\gamma}$ (kJ/mol)
Bezafibrate	306.9 ± 5	79.6 ± .5	10.9	-14.4	233.1	36.57± .5
Fenofibrate	250.5 ± 5	94.02 ±.5	7.04	-13.52	209.3	32.67± .5
Fenofibrate-PS	275.1 ± 5	93.3 ±.5	7.01	-12.6	229.7	24.53± .5

4.3.3.4 Fragility

The fragility or the steepness index (m) [57] was calculated from the temperature dependences of the structural relaxation times from equation 4.6 and is a significant parameter of stability of glass formers.

$$\mathbf{m} = \frac{\mathbf{d}\log(\tau_\alpha)}{\mathbf{d}(\frac{T_g}{T})}\Big|_{T=T_g} \tag{4.6}$$

The value of fragility (m) ranges between 16 and 200 for a typical glass former, [58] where small values (m < 40) of the fragility parameter indicate Arrhenius-like temperature dependence, where log (τ_α) is linear in the T_g/T range. When the dependence of log τ_α(T) deviates strongly from the Arrhenius behaviour (linear), then it is a fragile glass former. Classification of glasses based on fragility was significantly considered as it is an important parameter [59]. The fragility of the bezafibrate and fenofibrate-PS mixture was found to be 79.6 and 93.3 respectively and belongs to intermediate fragile glass formers.

The deviation of molecular mobility from the Arrhenius nature at T_g is determined from the Angel plot (log (τ) –T_g/T plot) whose value of the slope at T=T_g is equal to the fragility (m)[68] and is shown in figure 4.17. It is interesting to note that

the addition of PS800 slows down the dynamics of fenofibrate to lower frequency region, the VFT behaviour of the mixture is almost the same in the Angell plot, showing almost the same fragility as that of pure fenofibrate. The solvent PS800 does not affect the changes in the molecular dynamics of the fenofibrate system as it approaches T_g. A binary mixture of fenofibrate-PS has almost the same fragility as that of pure fenofibrate, which is also evident from the slope near T_g in Fig.4.17. The fragility of bezafibrate is higher than both fenofibrate pure and binary mixture, which is evident from VFT fit and Angel's plot, and the fragility of bezafibrate is comparable to that of glibenclamide[60]. Thus, amorphous bezafibrate can be considered to be more physically stronger than glassy fenofibrate and its binary mixture.

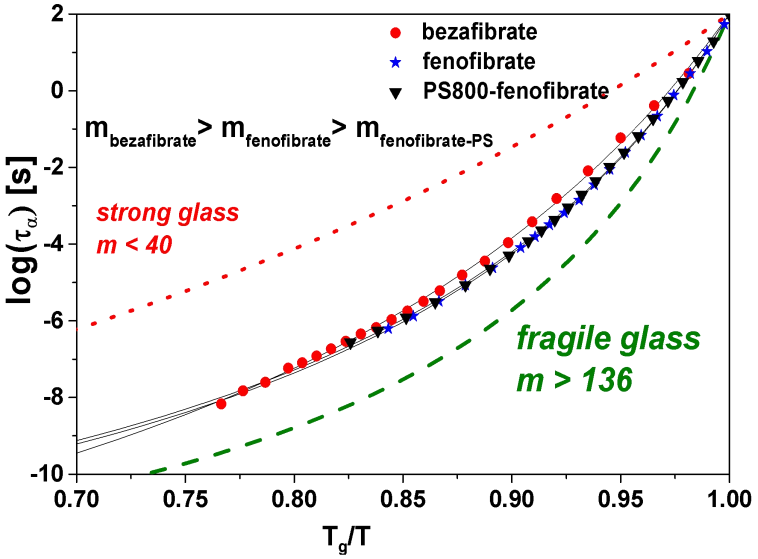

Figure 4.17. Angel's plot of bezafibrate and fenofibrate-PS mixture

4.3.3.5 Kohlraush-William-Watts (KWW) fit

Figure 4.18 shows the spectral shape of the three investigated samples at the vicinity of glass transition temperature by fitting them to KWW function and were compared. The solid lines represent KWW fit and dotted solid curves represent experimental data. The figure also compares the amplitudes of the dielectric loss of the three samples above T_g, where the decrease in the dielectric loss in PS800-fenofibrate is due to a lower concentration of fenofibrate molecules in an apolar host.

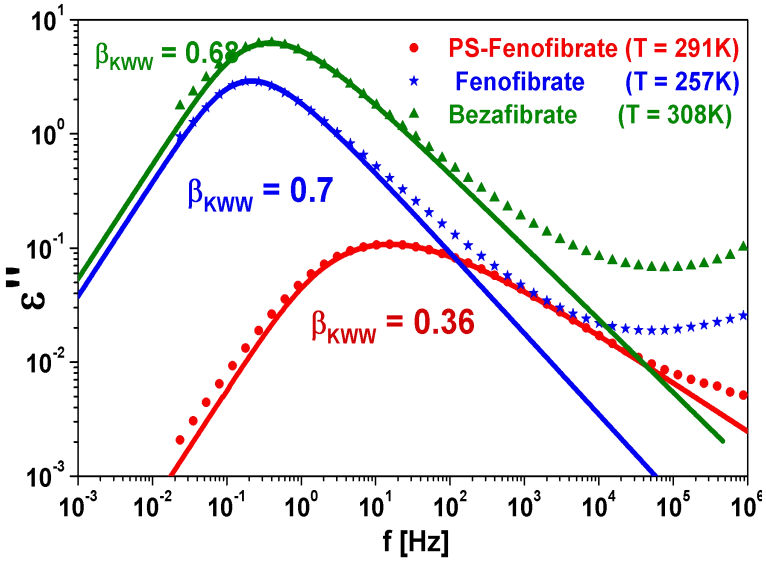

Figure 4.18. KWW fit of bezafibrate, fenofibrate, and fenofibrate-PS mixture after horizontal shifting to superimpose on dielectric loss spectrum of fenofibrate

The dipole moment of bezafibrate is higher than that of fenofibrate. The values of asymmetrical stretching parameter β_{KWW} for bezafibrate, fenofibrate, and PS800-fenofibrate mixture were found to be 0.68, 0.70, and 0.3 respectively, both bezafibrate and fenofibrate have an intermediate distribution of relaxation times, whereas PS800-fenofibrate have a much lower value of β_{KWW} compared to bezafibrate and fenofibrate which indicates that the distribution of structural relaxation times of PS800 is much more than that of pure fenofibrate. The addition of the polymer PS800 has increased the width of the dielectric loss peak and increased the distribution of structural relaxation times manifold and hence reduced the stability as it is far away from the Debye relaxation where β_{KWW} equal 1 [61]. The β_{KWW} value of bezafibrate is closer to that of fenofibrate, which implies bezafibrate has an intermediate distribution of molecular relaxation time and stability like fenofibrate. The β_{KWW} value of the fenofibrate-PS mixture is much lower than that of both fenofibrate and bezafibrate, which suggests that the stability of the fenofibrate-PS mixture is very much lesser than that of fenofibrate and bezafibrate. From the obtained values β_{KWW}, the half-width of the structural relaxation peaks of bezafibrate and fenofibrate are intermediately narrow.

The parameter, β_{KWW} slightly increases with temperature in all three samples. Comparing the spectral width of neat systems and binary, PS800-fenofibrate has a much broader spectral width with a lower value of β_{KWW} is resulted from the

concentration fluctuations of the host and the probe from the mixture and further supplemented by mobility variation of different monomeric units of the PS800. Therefore, from the KWW fits of all the title samples above T_g, we found that PS800-fenofibrate has more tendency to recrystallize from the comparatively lower value of β_{KWW}. From Fig. 4.18, the experimental data is found to deviate from the KWW at higher frequencies due to the presence of another relaxation out of our experimental window or excess wing [60,62] and confirmed experimentally by other scientists [63]. The excess wing is observed when the high-frequency flank of a secondary relaxation process got covered by the dominant α relaxation is the reason for this. This intermolecular secondary relaxation namely Johari−Goldstein (JG-β) relaxation,[64,65] has been considered as a potential precursor of cooperative structural relaxations and needs high-pressure experiments to resolve them.

4.3.3.6 Temperature dependence of β_{KWW}

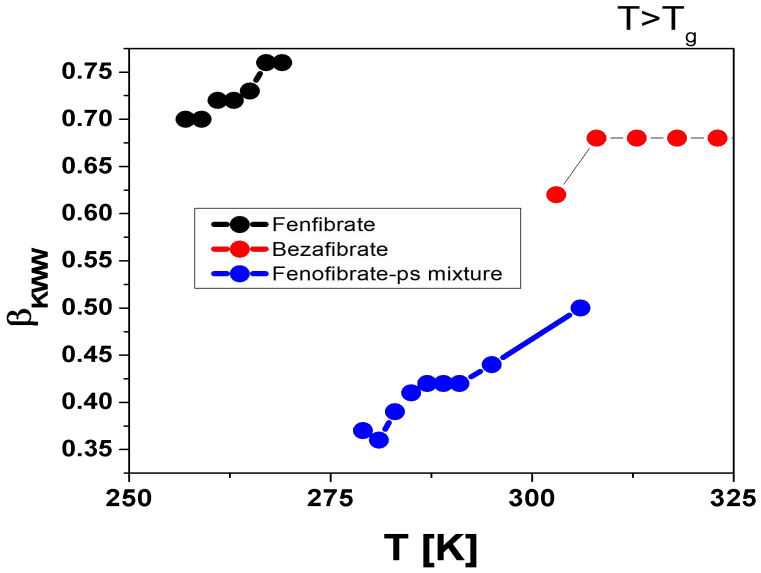

Fig 4.19 Variation of asymmetric stretching parameter β_{KWW} determined from KWW fits above T_g for bezafibrate, fenofibrate, and PS-fenofibrate mixture

Furthermore, on exploring a pharmaceutical system, the distribution of relaxation times and the representative parameter β_{KWW} is a decisive factor in predicting its life expectancy. Thus, a narrow distribution of the structural relaxation (high value of β_{KWW}) indicates a less tendency towards a crystallization. A larger distribution, on the other hand, initiate faster localized molecular motions, leading to a greater inclination towards crystal nucleation and its growth. Thus, the ability of an amorphous

pharmaceutical to crystallize might be correlated to the asymmetric distribution of relaxation time (i.e., β_{KWW}) and as the value deviates from the classic Debye behaviour, the stability of the amorphous API would decrease[66,67]. To give the reader an idea about the spectral shape and its temperature variation, we have presented the master plot by superimposing all the spectra together and normalizing them to peak loss frequency. Figures 4.19 and 4.20 show the master plot of dielectric loss spectra above T_g of bezafibrate and PS800-fenofibrate respectively. The β_{KWW} value of bezafibrate then increases to 0.68 at 308K and remains constant till 327K.

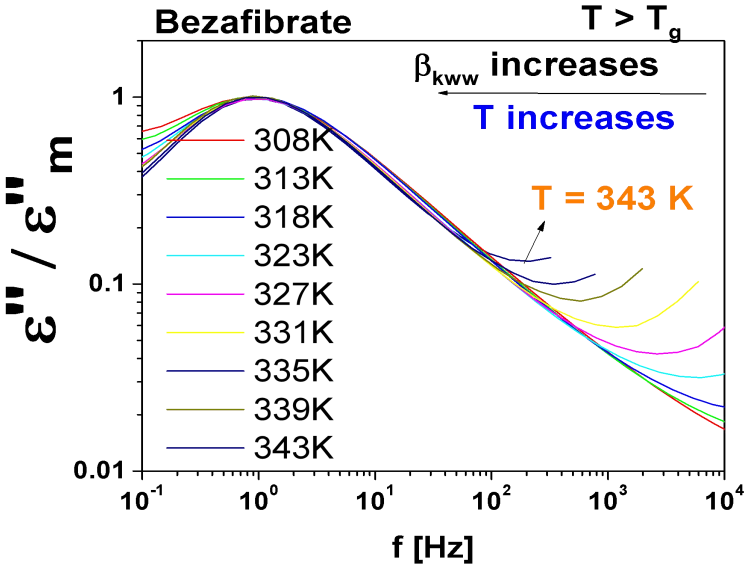

Figure 4.20 Master plot of bezafibrate from 308K to 343K. T=308K is taken as reference

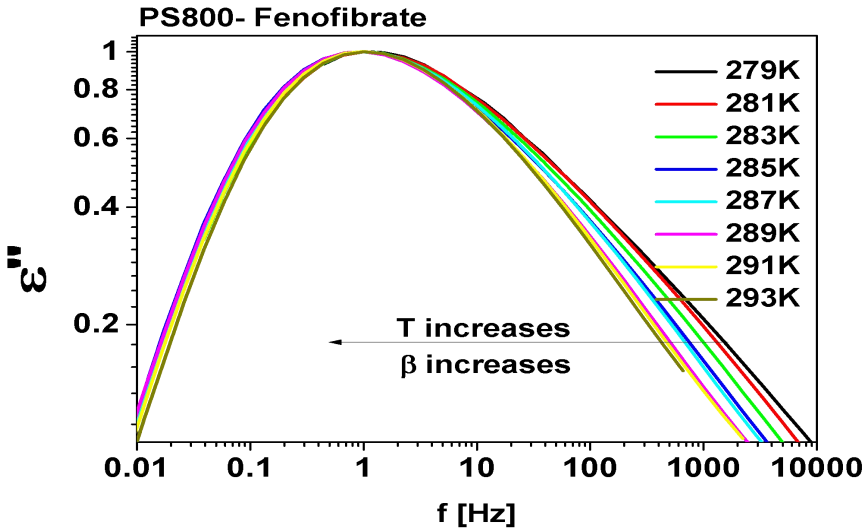

Figure 4.21 Master plot of PS800-fenofibrate from 279K to 293K. T=279K is taken as reference

According to Shamblin *et al.*,[68] the tendency of amorphous pharmaceuticals to crystallize may be correlated to the asymmetric distribution of relaxation time. Thus, the stability of amorphous APIs would decrease as the value of β_{KWW} decreases and vice versa. β_{KWW} of bezafibrate, fenofibrate, and fenofibrate-PS mixture shows an increasing trend with an increase of temperature. The bezafibrate and fenofibrate have similar stability of the amorphous phase as the value of β_{KWW} are approximately equal and it increases with an increase in temperature. The β_{KWW} of the fenofibrate-PS mixture also increases with temperature but the value is very much lower which corresponds to lesser stability comparative to pure fenofibrate and bezafibrate.

4.3.3.7 Nature of secondary relaxation: Extended coupling model

The nature of secondary relaxation observed was verified by Ngai's coupling model[69]. According to the Coupling model, there exists a correlation between the expected Johari-Goldstein intermolecular relaxation time and primitive relaxation time defined by the following equation 8,

$$\boldsymbol{\tau_{JG}(T) \cong \tau_0\,(T) = (t_c)^n\,(\tau_\alpha(T))^{1-n}} \tag{4.7}$$

where t_c is the cross over time that represents the crossover from independent to cooperative motions and equal to 2ps for molecular glass formers and ($n=1-\beta_{KWW}$) is the coupling parameter. The nature of the origin of a secondary relaxation, whether is it a JG relaxation is particularly relevant to the MD of amorphous pharmaceuticals [70] as the intermolecular JG β-relaxation can be a precursor of α relaxation. Resolved secondary relaxation of fenofibrate is of non-JG origin from coupling model predictions[38]. The same trend is repeated in the fenofibrate-PS800 host as well since the position of occurrence in the Arrhenius diagram is almost matching within the vicinity of one decade, though they are not matching similar to other intramolecular systems like phthalates[71], where exact overleap is seen over the entire frequency range [72]. Interestingly, the gamma peaks of fenofibrate are slightly higher at lower temperatures (123 K- 163 K) and eventually matches with that of pure fenofibrate at higher temperature (203 K – 214 K). This conundrum raises a larger uncertainty in the evaluation of activation energy of the γ-process. It had been reported that JG relaxation peaks in different hosts including in its amorphous phase can vary [56] though in many systems where it is independent of the host environment. On critically examining the

PS800-fenofibrate binary system, this can further happen due to the occurrence of the JG process which is sandwiched between intense α- and the resolved γ-processes. This misleads the evaluation of resolved γ-loss peaks to lower frequency side since JG β-relaxation times would always be higher than γ-times, and the occurrence of JG β-process at lower frequency side broadens peak to lower frequency side. We hope that this can be further resolved by exploring fenofibrate in apolar hosts of much higher T_g than PS800.

The primitive relaxation time τ_0 was calculated using the Coupling model from the equation (4.7) for a few arbitrary temperatures above T_g for bezafibrate, fenofibrate, and fenofibrate-PS mixture. The calculated values of τ_0 for some temperatures above T_g for all title compounds are plotted as open circles in the Arrhenius diagram shown in figure 4.16, it is clear that the primitive relaxation times do not correspond to the molecular relaxation times of the observed secondary relaxation which suggests that the observed secondary relaxations in bezafibrate and fenofibrate-PS mixture are not Johari-Goldstein α relaxation like that in fenofibrate, rather they may arise from local molecular motions i.e., intramolecular. Even though we expected to resolve the Johari-Goldstein β relaxation in fenofibrate by using a test excipient polystyrene, but it could not resolve the universally present JG β process in fenofibrate, but it is expected that some other excipient with much higher T_g and experimenting with elevated pressure can resolve the hidden JG β process. The JG β process in diethyl phthalate was resolved by Shahin et.al by mixing it with oligo-styrene at elevated pressure[73].

4.3.3.8 Paluch's anti-correlation

Paluch reported that the width of the dielectric loss curve near T_g is anti-correlated to the dielectric strength ($\Delta\varepsilon$)[60], in other words, the asymmetric stretching parameter β_{kww} which is a function of the width of the dielectric loss curve at or near the glass transition temperature T_g is strongly anti-correlated to the dielectric strength. The reason is that the resultant potential at a molecular dipole becomes more harmonic due to the contribution from the dipole-dipole interaction potential $V_{dd}(r) = -Dr^{-6}$ to the attractive part of the intermolecular potential, where D is a characteristic constant given by $D \propto \mu^4/kT_g$. Paluch's plot is shown in figure 4.22 including the samples studied. Fenofibrate, bezafibrate, and fenofibrate-PS are within the spread of the data of all

glass formers ever studied by BDS and hence all the three fibrate drugs are found to obey this anticorrelation.

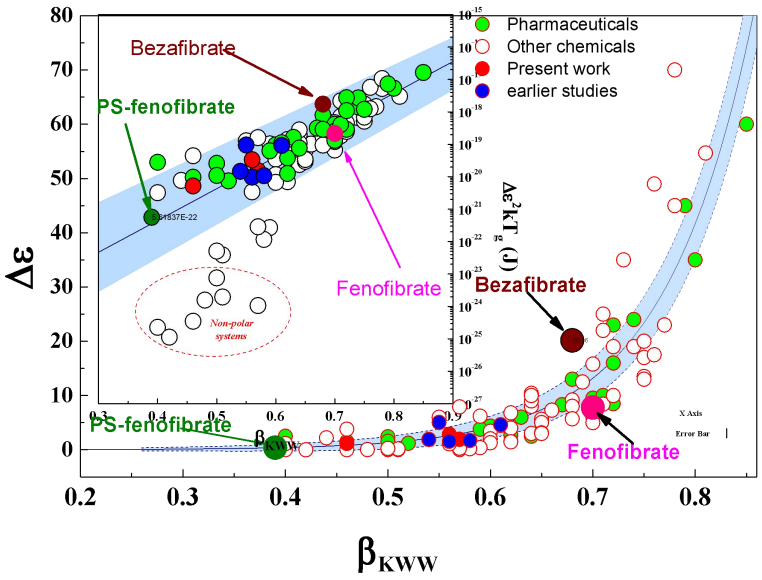

Figure 4.22 Dielectric strength Δϵ (T_g) versus asymmetric stretching parameter β_{KWW}. The inset presents $kT(\Delta\epsilon)^2$ against β_{KWW}.

4.3.4 Origin of secondary relaxation: DFT approach

Schamme *et al.* reported the successful identification of the relevant part of the quinidine molecule which originates the observed secondary relaxation by the quantum computational method using DFT[74]. We have done a similar approach for identifying the origin of the secondary relaxation in title compounds. For this purpose, the initial three-dimensional structure of bezafibrate and fenofibrate were obtained from the PubChem database [45,75] and optimized at 6-311/g(d,p) level of theory. A dihedral angle was randomly selected in the title molecules by using redundant coordinates in Gauss view software and then this dihedral was scanned continuously through 360o by constant step of 10o, at the frozen value of the angles set, the rest of the molecule was optimized, and simultaneously the energy and dipole moment of the molecule were calculated by DFT method at B3LYP/6-311/g(d,p) level of theory in gas phase using mod redundant coordinates. In order to identify the associated local motion in fenofibrate and bezafibrate molecules by DFT method the relaxed dihedral scan to rotate a particular flexible side group of the corresponding molecules were performed on several possible dihedral angles by computer simulation method using mod

redundant coordinates using the interface Gauss view 05[76] and calculated by using Gaussian 09 package[42].

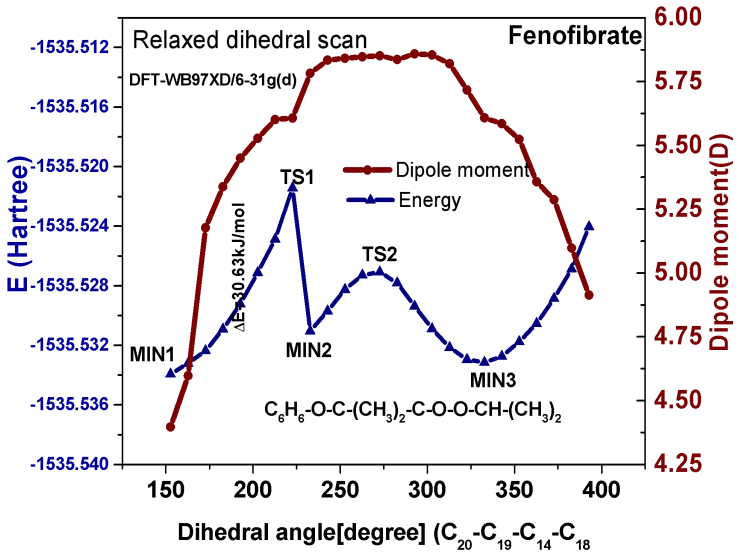

Figure 4.23 Energy (ΔE) and dipole moment scan diagram during rotation of the $C_6H_4O(CH_3)COO(CH_3)_2$ group in fenofibrate

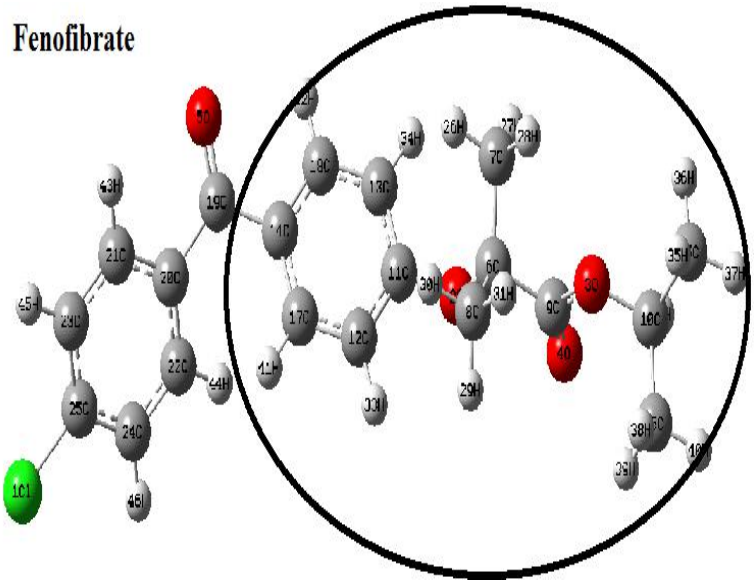

Figure 4.24 DFT optimized structure of fenofibrate showing the subgroup originating the secondary relaxation shown in the circle ($C_6H_4O(CH_3)COO(CH_3)_2$)

Sailaja *et al.* [38] reported the activation energy of secondary relaxation in fenofibrate is 32.67kJ/mol. The energy scan graph of fenofibrate related to the rotation of the $(C_6H_4O(CH_3)COO(CH_3)_2$ group presented in Fig. 4.23 shows that there are potential barriers at different torsional angles of dihedral which are three MIN and three TS. The associated molecular sub-group which is the origin of secondary relaxation in

fenofibrate is shown in figure 4.24. The variation of dipole moment as a function of dihedral angle is also shown in Fig. 4.23, from which the dihedral scan energy corresponds to dipole moment on the barriers, similarly observed in quinidine[74]. The rotation of the selected group led to the conformational interconversions specified by energy minima (MIN1.) and transition state (TS1). The energy difference corresponding to different potential energy barriers of the transition states are matched with the observed activation energy of secondary relaxation in fenofibrate. But only the energy barrier corresponding to the rotation of the $(C_6H_4O(CH_3)COO(CH_3)_2$ obtained from the DFT method is 30.6 kJ/mol corresponding to dihedral angle values between 150 and 225 degrees result in the intermediate states MIN1/TS1 in fenofibrate whose energy difference is closer to the value of the experimental activation energy of the secondary relaxation. The calculated and observed activation energies in fenofibrate may be due to the fact that calculations are done on an individual molecule. Therefore, the observed secondary relaxation in fenofibrate is due to the rotation of the $(C_6H_4O(CH_3)$ $COO(CH_3)_2$ of the fenofibrate molecule associated to the dihedral angle associated with C_{18}-C_{14}-C_{19}-C_{20} atoms.

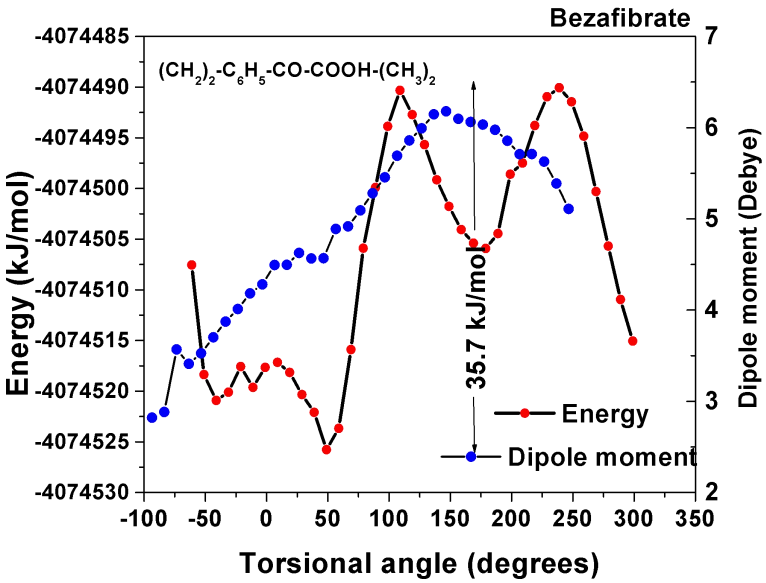

Figure 4.25 Energy scan diagram on the dihedral scan of $(CH_2)_2$)-C_6H_5-CO-COOH-$(CH_3)_2$) of bezafibrate

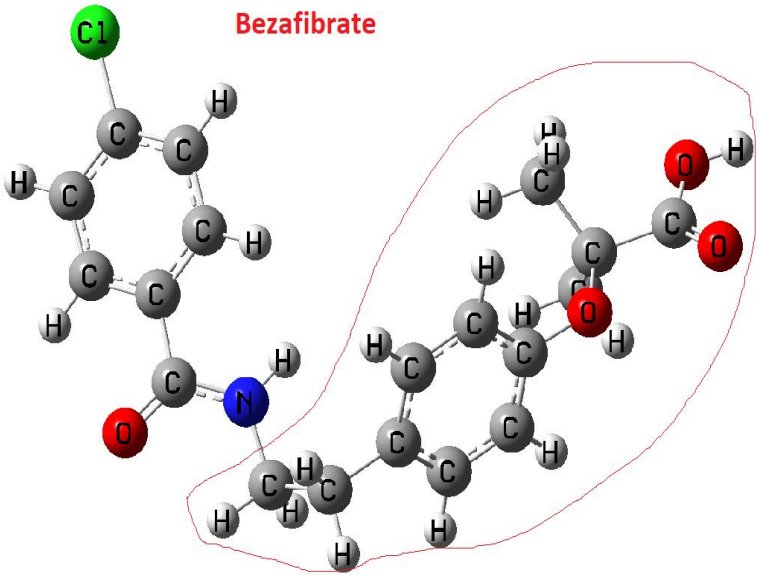

Figure 4.26. DFT optimized structure of bezafibrate showing the subgroup originating the secondary relaxation shown in the circle the $(CH_2)_2$)-C_6H_5-CO-COOH-$(CH_3)_2$) of bezafibrate

The same procedure was applied to different dihedral angles in bezafibrate to identify the origin of secondary relaxation in bezafibrate. The rotation of the group $(CH_2)_2$)-C_6H_5-CO-COOH-$(CH_3)_2$) in bezafibrate associated with the dihedral angle N_5-C_{10}-C_8-C_9 and the using obtained corresponding energy barriers the energy calculated as 35.73 kJ/mol and the corresponding energy (ΔE) scan diagram is shown in Fig. 4.25 and the relevant subgroup that originates the observed secondary relaxation in bezafibrate is shown in Fig.4.26. To confirm the obtained dihedral scan results, we have conducted the scan on different subgroups and obtained values of activation energies different from the experimentally observed activation energy of secondary relaxation (not shown).

4.3.5 Vibrational Spectroscopy

The IR and Raman spectra with their relative intensities in the crystalline and amorphous phase along with theoretically calculated spectra are shown in figures 4.27 and 4.28 respectively.

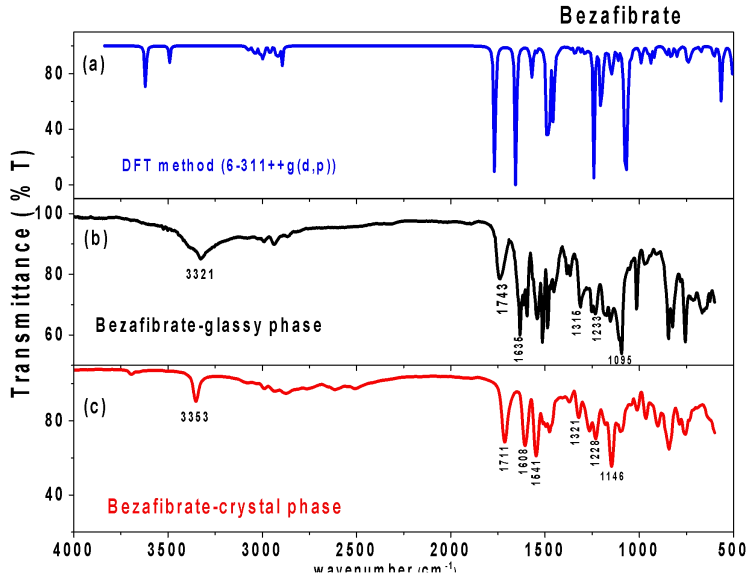

Figure 4.27 FTIR Spectra of bezafibrate by
a) DFT method, b) in the glassy state, c) in the crystal phase

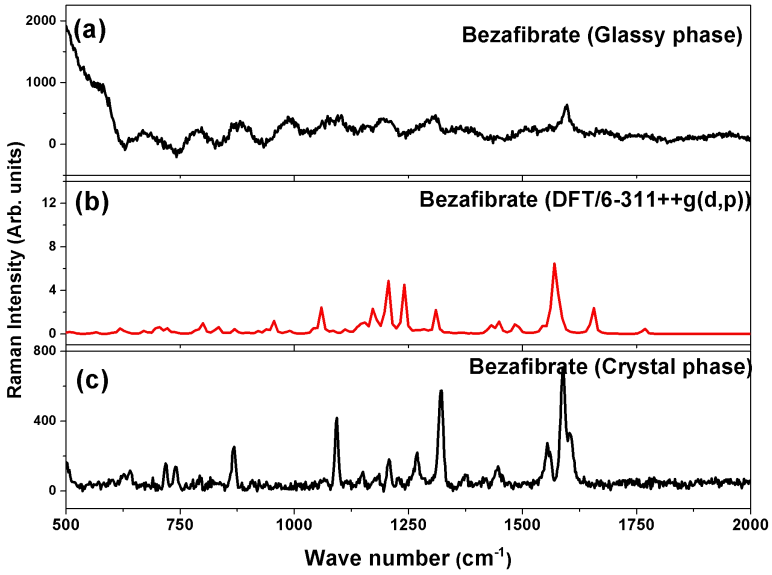

Figure 4.28 FT-Raman Spectra of bezafibrate in
(a) glassy state, (b) by DFT method, (c) in the crystal phase

The FTIR spectra of bezafibrate in the crystalline and glassy states along with that obtained by the DFT method are shown in Fig. 4.27. The FT-Raman spectra of bezafibrate in the crystalline and glassy phases along with the theoretical obtained spectrum are shown in figure 4.28. The FTIR spectrum of crystalline bezafibrate has all characteristic peaks of a stable form. Raman scattering is sensitive to the degree of crystallinity in a sample. In a typical Raman spectrum of a crystalline substance, the peaks will be sharper and intense, on the other hand for an amorphous substance, the

Raman peaks will be broader and less intense. FTIR and Raman spectra obtained by theoretical and experimental methods of bezafibrate are in good agreement. The FTIR spectra obtained are in good agreement with the reported values in the literature[77]. A strong intermolecular hydrogen bonding (O-H N) is formed between the amide N-H and the C-O of the carboxylic group and observed as a peak at 3358 cm^{-1} in crystalline bezafibrate, and is shifted to 3325 cm^{-1} in its glassy state (broadened). Between 3345 cm^{-1} and 1711 $cm^{-1,}$ several peaks of low intensity are observed which shows the presence of hydrogen bonding in the glassy state. to 1596,1307 and 1193 cm^{-1} in the glassy phase and all the peaks in the glassy state are broadened which indicates the amorphous nature of the sample. The shifts are due to hydrogen bonding present in the glassy state of bezafibrate which is also observed in the FTIR spectra and also observed in some pharmaceuticals. IR and Raman bands in the glassy states are weaker and broader, similar behaviour was observed in fenofibrate, which was due to hydrogen bonding in the amorphous state [38,78].

4.4 Conclusions

We have done a comprehensive investigation to study the molecular dynamics of two solubility limited active pharmaceutical ingredients bezafibrate and fenofibrate, and the binary mixture of fenofibrate in polystyrene 800 from their deep glassy state to the melting by broadband dielectric spectroscopy (BDS), and other supporting thermal, spectroscopic measurements along with computational studies using density functional theory (DFT) calculations. The effort was done to get more insights into their glass transition phenomena and to suggest ways to suppress their crystallization tendencies for augmenting the amorphous shelf-life. The presence of hydrogen bonding in the amorphous phase was analyzed by vibrational spectroscopy and the thermal stability of amorphous bezafibrate was studied by differential scanning calorimetry (DSC). The T_g of bezafibrate was found to be 302.5 K which is much higher than that of fenofibrate. The BDS revealed a structural (α) and single secondary γ-relaxation in all the three samples, where α-relaxation followed a VFT temperature dependence while γ-process showed a thermally activated behaviour. On further plotting the temperature dependence normalized to the T_g, fragility index was found to be 73 for bezafibrate, 94 for fenofibrate, and 93.3 for PS800- fenofibrate mixture identifying these systems to be intermediate fragile. Sub-T_g relaxation showed activation energy of 36.5 kJ/mol. For

neat bezafibrate, of 27.9 kJ/mol. for fenofibrate, in its binary mixture with PS800, slightly lesser than its value of 32.6 kJ/mol. in its pure form. α-relaxation showed slightly broader spectral width β_{KWW} = 0.68 for bezafibrate, 0.7 for fenofibrate, and 0.36 for PS800-fenofibrate mixture. PS800-fenofibrate has a much broader spectral width as expected from concentration fluctuations from the binary mixing and further supplemented by mobility variation of different polystyrene monomers. On plugging these values in the coupling model predictions, the observed secondary relaxations in all the investigated systems were found to have an intramolecular (non-JG) origin. Mixing of polymer PS800 is not sufficient to resolve the universal JG-β relaxation, as a polymer of much higher T_g is needed for resolving JG-β relaxation in fenofibrate. All three samples follow Paluch's anticorrelation between the width of dielectric loss curves and the dielectric strength at T_g. The origin of the secondary relaxation, i.e., the relevant part of the molecule whose local motion originates the observed secondary relaxation was identified theoretically by the DFT method with B3LYP/6–311 g (d, p) level of theory for fenofibrate and bezafibrate. On comparing the vibrational spectra of crystalline and amorphous phases of bezafibrate, the presence of hydrogen bonding in the amorphous phase of the title drugs is confirmed. Overall, the data present a lot of insights on the dynamics of amorphous pharmaceuticals.

References

[1] R. Peng, J. Huang, L. He, L. Zhao, C. Wang, W. Wei, T. Xia, Y. Mao, Y. Wen, L. Wang, J. Yang, Polymer/lipid interplay in altering in vitro supersaturation and plasma concentration of a model poorly soluble drug, Eur. J. Pharm. Sci. 146 (2020). https://doi.org/10.1016/j.ejps.2020.105262.

[2] A. Afzal, M.S. Thayyil, P.A. Sivaramakrishnan, S. Urpayil, S. Capaccioli, Molecular dynamics in the supercooled liquid and glassy states of bezafibrate and binary mixture of fenofibrate, J. Non. Cryst. Solids. 550 (2020) 120407. https://doi.org/10.1016/j.jnoncrysol.2020.120407.

[3] Y. Kawabata, K. Wada, M. Nakatani, S. Yamada, S. Onoue, Formulation design for poorly water-soluble drugs based on biopharmaceutics classification system: Basic approaches and practical applications, Int. J. Pharm. 420 (2011) 1–10. https://doi.org/10.1016/j.ijpharm.2011.08.032.

[4] G.L. Amidon, H. Lennernäs, V.P. Shah, J.R. Crison, A Theoretical Basis for a Biopharmaceutic Drug Classification: The Correlation of in Vitro Drug Product Dissolution and in Vivo Bioavailability, Pharm. Res. 12 (1995) 413–420. https://doi.org/10.1023/A:1016212804288.

[5] S. Gupta, R. Kesarla, A. Omri, Formulation Strategies to Improve the Bioavailability of Poorly Absorbed Drugs with Special Emphasis on Self-Emulsifying Systems, ISRN Pharm. 2013 (2013). https://doi.org/10.1155/2013/848043.

[6] S. Kalepu, V. Nekkanti, Insoluble drug delivery strategies: Review of recent advances and business prospects, Acta Pharm. Sin. B. 5 (2015) 442–453. https://doi.org/10.1016/j.apsb.2015.07.003.

[7] K.T. Savjani, A.K. Gajjar, J.K. Savjani, Drug Solubility: Importance and Enhancement Techniques, ISRN Pharm. 2012 (2012) 1–10. https://doi.org/10.5402/ 2012/195727.

[8] K.P. Safna Hussan, M. Shahin, Deshpande, Jinitha, K. Vijisha, Rajan, N. K.L, Synthesis and molecular dynamics of double active pharmaceutical ingredient-benzalkonium ibuprofenate, J. Mol. Liq. 223 (2016).

[9] A. Schittny, J. Huwyler, M. Puchkov, Mechanisms of increased bioavailability through amorphous solid dispersions: a review, Drug Deliv. 27 (2020) 110–127. https://doi.org/10.1080/10717544.2019.1704940.

[10] A. Karagianni, K. Kachrimanis, I. Nikolakakis, Co-Amorphous Solid Dispersions for Solubility and Absorption Improvement of Drugs: Composition, Preparation, Characterization and Formulations for Oral Delivery, Pharmaceutics. 10 (2018) 98. https://doi.org/10.3390/pharmaceutics10030098.

[11] K. Kawakami, Crystallization Tendency of Pharmaceutical Glasses: Relevance to Compound Properties, Impact of Formulation Process, and Implications for Design of Amorphous Solid Dispersions, Pharmaceutics. 11 (2019) 202. https://doi.org/10.3390/pharmaceutics11050202.

[12] B. Karolewicz, A. Górniak, D.M. Marciniak, I. Mucha, Molecular Mobility and Stability Studies of Amorphous Imatinib Mesylate, Pharmaceutics. 11 (2019) 304. https://doi.org/10.3390/pharmaceutics11070304.

[13] A. Newman, J.E. Hastedt, M. Yazdanian, New directions in pharmaceutical amorphous materials and amorphous solid dispersions, a tribute to Professor George Zografi – Proceedings of the June 2016 Land O'Lakes Conference, AAPS Open. 3 (2017). https://doi.org/10.1186/s41120-017-0017-6.

[14] H. Tanaka, Relation between Thermodynamics and Kinetics of Glass-Forming Liquids, Phys. Rev. Lett. 90 (2003). https://doi.org/10.1103/physrevlett.90.055701.

[15] A. Newman, G. Zografi, Commentary: Considerations in the Measurement of Glass Transition Temperatures of Pharmaceutical Amorphous Solids, AAPS PharmSciTech. 21 (2020). https://doi.org/10.1208/s12249-019-1562-1.

[16] G.R. Thuduppathy, R. Blake Hill, Applications of NMR Spin Relaxation Methods for Measuring Biological Motions, Methods Enzymol. (2004) 243–264. https://doi.org/10.1016/s0076-6879(04)84015-1.

[17] A. Afzal, M. Shahin Thayyil, P.A. Sivaramakrishnan, M.K. Sulaiman, K.P. Safna Hussan, C. Yohannan Panicker, K.L. Ngai, Dielectric spectroscopic studies in supercooled liquid and glassy states of Acemetacin, Brucine and Colchicine, J. Non. Cryst. Solids. 508 (2019) 33–45. https://doi.org/10.1016/j.jnoncrysol.2019.01.008.

[18] K.P.S. Hussan, K.P. Safna Hussan, M.S. Thayyil, A. Poulose, K.L. Ngai, Glassy Dynamics and Translational–Rotational Coupling of an Ionically Conducting Pharmaceutical Salt-Sodium Ibuprofen, J. Phys. Chem. B. 123 (2019) 7764–7770. https://doi.org/10.1021/acs.jpcb.9b06478.

[19] T. K.K., M.S. Thayyil, T. Rosalin, K.K. Elyas, T. Dipin, P.K. Sahu, N.S. Krishna Kumar, V.C. Saheer, M. Messali, T. Ben Hadda, Thermal and spectroscopic investigations on three phosphonium based ionic liquids for industrial and biological applications, J. Mol. Liq. 307 (2020) 112960. https://doi.org/https://doi.org/10.1016/j.molliq.2020.112960.

[20] A. Afzal, M. Shahin Thayyil, M.K. Sulaiman, A.R. Kulkarni, Dielectric relaxation studies in super-cooled liquid and glassy phases of anti-cancerous alkaloid: Brucine, Indian J. Phys. 92 (2018) 565–573. https://doi.org/10.1007/s12648-017-1139-3.

[21] M. Sahra, M.S. Thayyil, A.K. Bansal, K.L. Ngai, M.K. Sulaiman, G. Shete, K.P. Safna Hussan, Dielectric spectroscopic studies of three important active pharmaceutical ingredients - clofoctol, droperidol and probucol, J. Non Cryst. Solids. 505 (2019) 28–36. https://doi.org/10.1016/j.jnoncrysol.2018.10.046.

[22] K.P. Safna Hussan, M.S. Thayyil, S.K. Deshpande, T. V. Jinitha, K. Manoj, K.L. Ngai, Molecular dynamics, physical and thermal stability of neat amorphous amlodipine besylate and in binary mixture, Eur. J. Pharm. Sci. 119 (2018) 268–278. https://doi.org/10.1016/j.ejps.2018.04.030.

[23] G.M. Keating, Fenofibrate: A review of its lipid-modifying effects in dyslipidemia and its vascular effects in type 2 diabetes mellitus, Am. J. Cardiovasc. Drugs. 11 (2011) 227–247. https://doi.org/10.2165/11207690-000000000-00000.

[24] A. Tenenbaum, M. Motro, E.Z. Fisman, Dual and pan-peroxisome proliferator-activated receptors (PPAR) co-agonism: The bezafibrate lessons, Cardiovasc. Diabetol. 4 (2005) 1–5. https://doi.org/10.1186/1475-2840-4-14.

[25] Secondary prevention by raising HDL cholesterol and reducing triglycerides in patients with coronary artery disease., Circulation. 102 (2000) 21–27. https://doi.org/10.1161/01.cir.102.1.21.

[26] J.K. Aronson, Bezafibrate, Side Effects of Drugs Annual, n.d.

[27] N.R. Rose, I.R.B.T.-T.A.D. (Sixth E. Mackay, eds., Front-matter, in: Academic Press, 2020: pp. i–iii. https://doi.org/https://doi.org/10.1016/B978-0-12-812102-3.00073-7.

[28] N.S. Ghonem, J.L. Boyer, Fibrates as adjuvant therapy for chronic cholestatic liver disease: Its time has come, Hepatology. 57 (2013) 1691–1693. https://doi.org/10.1002/hep.26155.

[29] L.Z. Benet, The role of BCS (biopharmaceutics classification system) and BDDCS (biopharmaceutics drug disposition classification system) in drug development., J. Pharm. Sci. 102 (2013) 34–42. https://doi.org/10.1002/jps.23359.

[30] D.S. Wishart, Y.D. Feunang, A.C. Guo, E.J. Lo, A. Marcu, J.R. Grant, T. Sajed, D. Johnson, C. Li, Z. Sayeeda, N. Assempour, I. Iynkkaran, Y. Liu, A. Maciejewski, N. Gale, A. Wilson, L. Chin, R. Cummings, D. Le, A. Pon, C. Knox, M. Wilson, DrugBank 5.0: a major update to the DrugBank database for 2018., Nucleic Acids Res. 46 (2018) D1074–D1082. https://doi.org/10.1093/nar/gkx1037.

[31] R. Sun, C. Shen, S. Shafique, O. Mustapha, T. Hussain, I.U. Khan, Y. Mehmood, K. Anwer, Y. Shahzad, A.M. Yousaf, Electrosprayed polymeric nanospheres for enhanced solubility, dissolution rate, oral bioavailability and antihyperlipidemic activity of bezafibrate, Int. J. Nanomedicine. 15 (2020) 705–715. https://doi.org/10.2147/IJN.S235146.

[32] S.D. Bhise, Effect of Hydroxypropyl β- Cyclodextrin Inclusion Complexation on Solubility of Fenofibrate, Int. J. 2 (2011) 596–604.

[33] S. Ming-Thau, Y. Ching-Min, T.D. Sokoloski, Characterization and dissolution of fenofibrate solid dispersion systems, Int. J. Pharm. 103 (1994) 137–146. https://doi.org/https://doi.org/10.1016/0378-5173(94)90094-9.

[34] M.A. de Oliveira, G.D. da Silva, M.S.T. Campos, Chemical degradation kinetics of fibrates: Bezafibrate, ciprofibrate and fenofibrate, Brazilian J. Pharm. Sci. 52 (2016) 545–553. https://doi.org/10.1590/s1984-82502016000300019.

[35] C.W. Pouton, Formulation of poorly water-soluble drugs for oral administration: Physicochemical and physiological issues and the lipid formulation classification system, Eur. J. Pharm. Sci. 29 (2006) 278–287. https://doi.org/10.1016/j.ejps.2006.04.016.

[36] J.H. Burn, Medical Pharmacology, 1961. https://doi.org/10.1136/bmj.2.5260.1131.

[37] Y. Le, J.F. Chen, M. Pu, Electronic structure and UV spectrum of fenofibrate in solutions, Int. J. Pharm. 358 (2008) 214–218. https://doi.org/10.1016/j.ijpharm.2008.03.033.

[38] U. Sailaja, M.S. Thayyil, N.S.K. Kumar, G. Govindaraj, Molecular dynamics of amorphous pharmaceutical fenofibrate studied by broadband dielectric

spectroscopy., J. Pharm. Anal. 6 (2016) 165–170. https://doi.org/10.1016/j.jpha.2014.09.003.

[39] X. Lin, Y. Hu, L. Liu, L. Su, N. Li, J. Yu, B. Tang, Z. Yang, Physical Stability of Amorphous Solid Dispersions: a Physicochemical Perspective with Thermodynamic, Kinetic and Environmental Aspects., Pharm. Res. 35 (2018) 125. https://doi.org/10.1007/s11095-018-2408-3.

[40] K. Kothari, V. Ragoonanan, R. Suryanarayanan, The Role of Drug–Polymer Hydrogen Bonding Interactions on the Molecular Mobility and Physical Stability of Nifedipine Solid Dispersions, Mol. Pharm. 12 (2015) 162–170. https://doi.org/10.1021/mp5005146.

[41] H. Ishida, T. Wu, L. Yu, Sudden rise of crystal growth rate of nifedipine near Tg without and with polyvinylpyrrolidone, J. Pharm. Sci. 96 (2007) 1131–1138. https://doi.org/10.1002/jps.20925.

[42] M.J. Frisch, G.W. Trucks, H.B. Schlegel, G.E. Scuseria, M.A. Robb, J.R. Cheeseman, G. Scalmani, V. Barone, B. Mennucci, G.A. et. . Petersson, Gaussian 09, Gaussian, Inc. Wallingford, CT, .

[43] National Centre for Biotechnology Information (2021). PubChem Compound Summary for CID 39042, Bezafibrate. Retrieved June 1, 2021 from https://pubchem.ncbi.nlm.nih.gov/compound/Bezafibrate.

[44] L. Chen, T. Okuda, X.-Y. Lu, H.-K. Chan, Amorphous powders for inhalation drug delivery., Adv. Drug Deliv. Rev. 100 (2016) 102–115. https://doi.org/10.1016/j.addr.2016.01.002.

[45] W. Kauzmann, The Nature of the Glassy State and the Behaviour of Liquids at Low Temperatures., Chem. Rev. 43 (1948) 219–256. https://doi.org/10.1021/cr60135a002.

[46] D. Turnbull, Under what conditions can a glass be formed?, Contemp. Phys. 10 (1969) 473–488. https://doi.org/10.1080/00107516908204405.

[47] L. Carpentier, R. Decressain, S. Desprez, Dynamics of the Amorphous and Crystalline α-, γ-Phases of Indomethacin, J. Phys. Chem. B. 110 (2006) 457–464. https://doi.org/10.1021/jp053545u.

[48] B.C. Hancock, G. Zografi, Characteristics and Significance of the Amorphous State in Pharmaceutical Systems, J. Pharm. Sci. 86 (1997) 1–12. https://doi.org/10.1021/js9601896.

[49] A. Afzal, M.K. Sulaiman, Dielectric Relaxation studies in super-cooled liquid and glassy phases of Anticancerous Alkaloid: Brucine, Indian J. Phys. 92 (2017) 565–573. https://doi.org/https://doi.org/10.1007/s12648-017-1139-3.

[50] M.S. Thayyil, S. Capaccioli, D. Prevosto, K.L. Ngai, Is the Johari-Goldstein β-relaxation universal?, Philos. Mag. 88 (2008) 4007–4013. https://doi.org/10.1080/ 14786430802270082.

[51] M. Shahin Thayyil, S. Capaccioli, P.A. Rolla, K.L. Ngai, The component dynamics of miscible binary mixtures of glass formers: New features, Philos. Mag. 88 (2008) 4047–4055. https://doi.org/10.1080/14786430802562140.

[52] H. Vogel, The Law of the Relation between the Viscosity of Liquids and the Temperature, Phys. Z., 22. (1921).

[53] G.S. Fulcher, ANALYSIS OF RECENT MEASUREMENTS OF THE VISCOSITY OF GLASSES, J. Am. Ceram. Soc. 8 (1925) 339–355. https://doi.org/https://doi.org/10.1111/j.1151-2916.1925.tb16731.x.

[54] G. Tammann, W. Hesse, The Dependence of Viscosity upon the Temperature of Supercooled Liquids., Z. Anorg. Allg. Chem. 156, . (1926) 245−257.

[55] B.C. Hancock, S.L. Shamblin, Molecular mobility of amorphous pharmaceuticals determined using differential scanning calorimetry, Thermochim. Acta. 380 (2001) 95–107. https://doi.org/10.1016/S0040-6031(01)00663-3.

[56] M. Shahin, S.S.N. Murthy, Sub-T g relaxations due to dipolar solutes in nonpolar glass-forming solvents, J. Chem. Phys. 122 (2005) 14507.

[57] C.A. Angell, Relaxation in liquids, polymers and plastic crystals—strong/fragile patterns and problems, J. Non. Cryst. Solids. 131 (1991) 13–31.

[58] R. Böhmer, K.L. Ngai, C.A. Angell, D.J. Plazek, Nonexponential relaxations in strong and fragile glass formers, J. Chem. Phys. 99 (1993) 4201–4209. https://doi.org/10.1063/1.466117.

[59] K. Kunal, C.G. Robertson, S. Pawlus, S.F. Hahn, A.P. Sokolov, Role of chemical structure in fragility of polymers: A qualitative picture, Macromolecules. 41 (2008) 7232–7238. https://doi.org/10.1021/ma801155c.

[60] M. Paluch, J. Knapik, Z. Wojnarowska, A. Grzybowski, K.L. Ngai, Universal Behaviour of Dielectric Responses of Glass Formers: Role of Dipole-Dipole Interactions, Phys. Rev. Lett. 116 (2016) 1–6. https://doi.org/10.1103/ Phys Rev Lett. 116.025702.

[61] A.C. Rodrigues, M.T. Viciosa, F. Danède, F. Affouard, N.T. Correia, Molecular Mobility of Amorphous S-Flurbiprofen: A Dielectric Relaxation Spectroscopy Approach, Mol. Pharm. 11 (2014) 112–130. https://doi.org/10.1021/ mp4002188.

[62] K.L. Ngai, An extended coupling model description of the evolution of dynamics with time in supercooled liquids and ionic conductors, J. Phys. Condens. Matter. 15 (2003) S1107–S1125. https://doi.org/10.1088/0953-8984/15/11/332.

[63] K. Kessairi, S. Capaccioli, D. Prevosto, M. Lucchesi, S. Sharifi, P.A. Rolla, Interdependence of primary and Johari-Goldstein secondary relaxations in glass-forming systems, J. Phys. Chem. B. 112 (2008) 4470–4473. https://doi.org/10.1021/jp800764w.

[64] C.P. Johari, M. Goidstein, Viscous liquids and the glass transition. II. Secondary relaxations in glasses of rigid molecules, J. Chem. Phys. 53 (1970) 2372–2388. https://doi.org/10.1063/1.1674335.

[65] K.L. Ngai, M. Paluch, Classification of secondary relaxation in glass-formers based on dynamic properties, J. Chem. Phys. 120 (2004) 857–873. https://doi.org/10.1063/1.1630295.

[66] S.L. Shamblin, B.C. Hancock, Y. Dupuis, M.J. Pikal, Interpretation of relaxation time constants for amorphous pharmaceutical systems, J. Pharm. Sci. 89 (2000).

[67] B. Schammé, M. Mignot, N. Couvrat, V. Tognetti, L. Joubert, V. Dupray, L. Delbreilh, E. Dargent, G. Coquerel, Molecular Relaxations in Supercooled Liquid and Glassy States of Amorphous Quinidine: Dielectric Spectroscopy and

Density Functional Theory Approaches, J. Phys. Chem. B. 120 (2016) 7579–7592. https://doi.org/10.1021/acs.jpcb.6b04242.

[68] S. Shamblin, B. Hancock, Y. Dupuis, M. Pikal, Interpretation of relaxation time constants for amorphous pharmaceutical system, J. Pharm. Sci. 89 (2000) 417–427.

[69] K.L. Ngai, Relation between some secondary relaxations and the α relaxations in glass-forming materials according to the coupling model, J. Chem. Phys. 109 (1998) 6982–6994. https://doi.org/10.1063/1.477334.

[70] K. Adrjanowicz, K. Kaminski, M. Paluch, P. Wlodarczyk, K. Grzybowska, Z. Wojnarowska, L. Hawelek, W. Sawicki, P. Lepek, R. Lunio, Dielectric relaxation studies and dissolution behaviour of amorphous verapamil hydrochloride, J. Pharm. Sci. 99 (2010) 828–839.

[71] M. Sekula, S. Pawlus, S. Hensel-Bielowka, J. Ziolo, M. Paluch, C.M. Roland, Structural and secondary relaxations in supercooled di-n-butyl phthalate and diisobutyl phthalate at elevated pressure, J. Phys. Chem. B. 108 (2004) 4997–5003.

[72] S. Capaccioli, M.S. Thayyil, K.L. Ngai, Critical issues of current research on the dynamics leading to glass transition, J. Phys. Chem. B. 112 (2008) 16035–16049. https://doi.org/10.1021/jp8057433.

[73] M.S. Thayyil, K.L. Ngai, D. Prevosto, S. Capaccioli, Revealing the rich dynamics of glass-forming systems by modification of composition and change of thermodynamic conditions, J. Non. Cryst. Solids. 407 (2015) 98–105.

[74] B. Schammé, M. Mignot, N. Couvrat, V. Tognetti, L. Joubert, V. Dupray, L. Delbreilh, E. Dargent, G. Coquerel, Molecular relaxations in supercooled liquid and glassy states of amorphous quinidine: dielectric spectroscopy and density functional theory approaches, J. Phys. Chem. B. 120 (2016) 7579–7592.

[75] J.K. Aronson, Side Effects of Drugs Annual: A world-wide yearly survey of new data and trends in adverse drug reactions, Elsevier, 2003.

[76] Dennington, R., Keith, T. and Millam, J. (2009) Gauss View, Version 5. Semichem Inc., Shawnee Mission

[77] N.K. Chithra, C. James, Quantum chemical computations including intermolecular interactions, natural bond orbital analysis and scaled quantum mechanical force field calculations on bezafibrate—A cholesterol drug for HIV infected, Vib. Spectrosc. 59 (2012) 9–17. https://doi.org/https://doi.org/10.1016/j.vibspec.2012.01.001.

[78] X.C. Tang, M.J. Pikal, L.S. Taylor, The effect of temperature on hydrogen bonding in crystalline and amorphous phases in dihydropyrine calcium channel blockers, Pharm. Res. 19 (2002) 484–490. https://doi.org/10.1023/A:1015199713635.

CHAPTER 5

MOLECULAR DYNAMICS IN THE SUPERCOOLED LIQUID AND GLASSY STATES OF ACETOHEXAMIDE

5.1. Introduction

Glass formation and transformation dynamics are currently regarded as a major unsolved issue in condensed matter physics and physical chemistry[1]. In the last few decades, experimental and theoretical efforts have made some progress, but a solution to the problem remains elusive. The fact that there are many glass-formers with widely varying chemical compositions and physical structures, resulting in a broad range of thermodynamic and dynamic properties to consider, adds to the problem's complexity. Ionic liquids, amorphous pharmaceuticals, and biomolecules, on the other hand, benefit from these complex properties. The study discussed in this paper is an example of how convergence between basic science and research into the applications of glass-formers drives new material research. The molecular dynamics of glass-forming materials that show not only the structural relaxation responsible for glass transition and viscous flow but also the ionic conductivity relaxation are of interest to researchers. The properties of the two forms of relaxation are actually of concern to the two study groups. If a connection between the two relaxations can be found, it will greatly enhance our understanding of the dynamics. The work presented in this paper is the molecular dynamics of an amorphous drug which shows ionic conductivity relaxation in addition to the normally observed structural relaxation, such research outcomes will enrich our knowledge of the glass transition phenomenon. Molecular dynamics of glass-forming materials showing ionic conductivity relaxation and dipolar relaxation are of special interest as the interaction between the two relaxations would greatly improve the fundamental understanding of dynamics. With this in mind, we studied an ionically conducting glass-former, acetohexamide, which is also pharmaceutical for the treatment of diabetes.

Despite the numerous benefits of amorphous pharmaceuticals, recrystallization of amorphous pharmaceuticals during storage is a significant challenge for the pharmaceutical industry. This research will aid in the identification of the factors that control devitrification in amorphous piroxicam, providing valuable information to the pharmaceutical research community. The molecular motion responsible for secondary relaxation is one of the governing factors for recrystallization in many amorphous pharmaceuticals, even though the molecular relaxations responsible for crystallization differ from case to case. As a result, it's critical to comprehend both secondary dipolar

and conductivity relaxations, as well as their relationship to structural relaxations. The electric modulus is a better representation of conductivity relaxation data, particularly in glass-formers where dc conductivity masks structural relaxation.[2]. For the study of samples with high conductivity and electrode polarization contributions, modulus representation of the dielectric data is preferable to permittivity representation. The modulus method for measuring orientational polarization and ionic conductivity is conceptually simple[3].

In this work, we aim to get a better understanding of the molecular and ionic dynamics of acetohexamide from different experimental methods like differential scanning calorimetry (DSC) and broadband dielectric spectroscopy (BDS) in the glassy and the supercooled liquid states. The measurements enable us to characterize the significant parameters the decide the glass-forming abilities and dynamic properties (such as fragility and nonexponentiality) of the primary α-relaxation and the secondary dipolar and conductivity relaxations, as well as the relation between the structural relaxation and ionic conductivity relaxation in their properties. Computational calculations were also carried out to gain a better understanding of the relaxation processes in acetohexamide. The outcome of this work will benefit the research community engaged in the field of conductivity relaxation and glass transition theory as novel findings are encountered in this study.

Acetohexamide is a low water-soluble, sulphonylurea drug mainly used to treat diabetes with hypoglycaemic activity[4]. We have studied the molecular dynamics of acetohexamide in its supercooled liquid and glassy states by broadband dielectric spectroscopy. The molecular and ionic mobility in acetohexamide in its supercooled liquid and glassy states was characterized and significant parameters that determine the physicochemical stability of amorphous acetohexamide in ambient storage conditions were characterized. This study is of interest to pharmaceutical research and as well to researchers engaged in the theory of glass transition. In many pharmaceuticals, molecular mobility associated with the Johari-Goldstein β relaxation is found to be responsible for the recrystallization tendency[5], therefore the study of secondary dipolar and conductivity relaxations below glass transition temperature (T_g) is of important information for the researchers. Experimental methods such as BDS may be used to calculate the activation energy of observed secondary relaxations in glass

formers, but no such tool exists to date that can help classify the relevant part of the molecule whose motion causes the observed secondary relaxation in its glassy state. Quantum computational calculations were also done in the theoretical framework of density functional theory (DFT) calculations to identify the origin of the experimentally observed secondary relaxations.

5.2 Experimental section

5.2.1 Materials

Acetohexamide, a white crystalline powder shape and a molecular weight of 324.4 g/mol was purchased from Sigma Aldrich with 99.8% purity. It is chemically known as1-(4-acetyl phenyl) sulfonyl-3-cyclohexylurea with molecular formula $C_{15}H_{20}N_2O_4S$. It was used without further purification. The chemical structure of acetohexamide is shown in figure 5.1. Acetohexamide belongs to the organic group of alkyl-phenyl ketones. These are aromatic compounds containing a ketone substituted by one alkyl group, and a phenyl group.

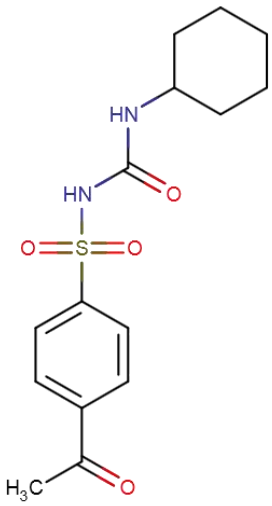

Figure 5.1 Molecular geometry of acetohexamide

5.2.2 Methods

5.2.2.1 Density functional theory

The optimized molecular geometry of Acetohexamide was obtained using DFT using the Gaussian 09 package with Gauss View 05 [6–8] as the visualization package. The initial geometry was obtained from the PubChem database and optimized with the B3LYP/6-311++G (d, p) level of theory. The origin of local molecular motions below

T_g was identified by quantum computational simulations of the side chain rotation in acetohexamide molecule by relaxed dihedral scan corresponding to different molecular subgroups[9]. FTIR and FT-Raman spectra of acetohexamide were obtained by the B3LYP/6-311++G (d, p) level of theory.

5.2.2.2 Differential scanning calorimetry (DSC)

To find the crystallization and glass transition temperature of acetohexamide, a DSC experiment was performed using a TA Instrument Trios V4.3.0.38388 DSC system in the range of 303 K to 495 K with a heating rate of 20 K/ min. The sample 20mg is taken in an aluminum sample pan and is heated to melting temperature and then quench cooled and then reheated again to melting temperature.

5.2.2.3 Broadband dielectric spectroscopy (BDS)

Isobaric measurements of the dielectric permittivity $\varepsilon^*(\omega) = \varepsilon'(\omega) - i\varepsilon''(\omega)$ were carried out using the Alpha analyzer (Novo-Control Technologies) over a frequency range from 10^{-2} to 10^7 Hz at ambient pressure. Each of the tested samples was placed between two stainless steel electrodes (Cylindrical shape, diameter 30 mm, gap 0.2 mm) and mounted on a cryostat maintained under dry nitrogen gas flow. Two poly Tetra Fluoro Ethylene strips were placed on the lower side of the crystalline sample. These strips prevent direct contact between the upper and lower electrodes when the sample is in the molten state and ensured constant thickness of the molten sample throughout the experiment. The temperature was controlled by QuatroSystem using a Nitrogen gas cryostat, with stability better than 0.1 K. Dielectric measurements were performed after its vitrification by heating the samples to the temperature of T_m+5K, and held for 10 minutes, then quench cooling the melt of the samples at 10K/min to 123.15K. The sample showed no sign of crystallization while cooling from the melting temperature. The dielectric measurements were taken from 123.15K to a few degrees below melting temperature in different steps of increase in temperature. A fresh amorphous sample is prepared by quench cooling each time and the BDS instrument is calibrated by an empty cell. The dielectric data is fitted with winfit software provided by Novocontrol technologies.

5.3 Results and discussions

5.3.1 Optimized geometry and molecular electrostatic potential surface

The initial structure of acetohexamide was optimized using Gaussian09 with the DFT level of theory in the B3LYP/6311-G++ level. For decades, scientists have recognized the importance of electrostatic calculations in understanding and predicting molecular properties [10–12]. The ability of molecular electrostatics to predict a molecule's chemical reactivity and ability to shape certain forms of interactions is well-known. Electrostatic potential (ESP) surfaces are a common way of visualizing the electrostatic existence of molecules[13]. Molecular ESP surfaces are created by moving a unit charge probe across the molecule's surface in a systematic manner. The probe's ESP energy is measured at each surface point, and the molecular surface is colored accordingly. The optimized molecular structure with its molecular electrostatic potential surface (MEP) is shown in figure 5.2. A maximum positive region located around the NH group. At the same time, the most negative electrostatic potential area is situated around the C=O group and the second most negative region is present around the S=O group. The rest of the atoms (except few) have zero potential. According to this study, the NH and C=O groups are the most preferred area for an electrophilic and a nucleophilic attack, respectively. The colour code of MEP diagram lies in between -0.0733 au (dark red) and 0.0733 au (dark blue) for Acetohexamide. From the figure 5.2, it is clear that the acetohexamide molecule is polar in nature and has two separated electropositive and electronegative regions.

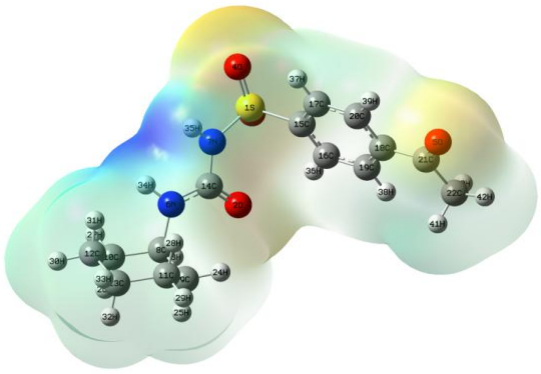

Figure 5.2 Molecular Electrostatic Potential Surface of Acetohexamide. Optimized molecular geometry of acetohexamide along with molecular electrostatic potential surface showing electron density. The red colour indicates the electronegative area while the blue colour indicates the electropositive region

5.3.2 Differential scanning calorimetry (DSC)

DSC thermogram of acetohexamide is shown in figure 5.3 which shows well-resolved melting, crystallization, and glass transition process. The melting temperature of acetohexamide was found to be 463K which is close to the reported value and the value of T_g was found to be 313K which is higher than the room temperature. The crystallization temperature of acetohexamide was found to be 400K and hence the difference between T_g and T_c is 83K which suggests that amorphous acetohexamide will be stable under optimum storage conditions. The melting temperature of acetohexamide was found to be 462K which is close to the reported value and the value of T_g was found to be 313K which is higher than the room temperature. The crystallization temperature of acetohexamide was found to be 401K and hence the difference between T_g and T_c is 88K which suggests that amorphous acetohexamide will be stable under optimum storage conditions. The temperature gap between T_g and T_c of a glass-forming system varies inversely with the crystallization tendency hence hints about the stability of the amorphous phase[14]. According to Kauzman [15] and Turnbull[16], the ratio T_g/T_m can give lights to the glass-forming ability of the material, and good glass former shows a value greater than 2/3. The ratio, which gave a value of 0.675 for acetohexamide which hints at the good glass-forming ability of acetohexamide.

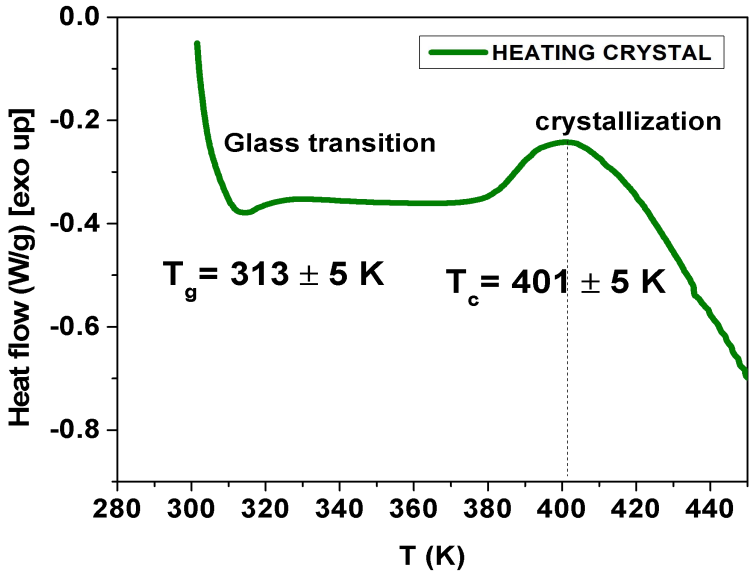

Figure 5.3.a DSC thermogram of acetohexamide on the heating crystal to melting temperature

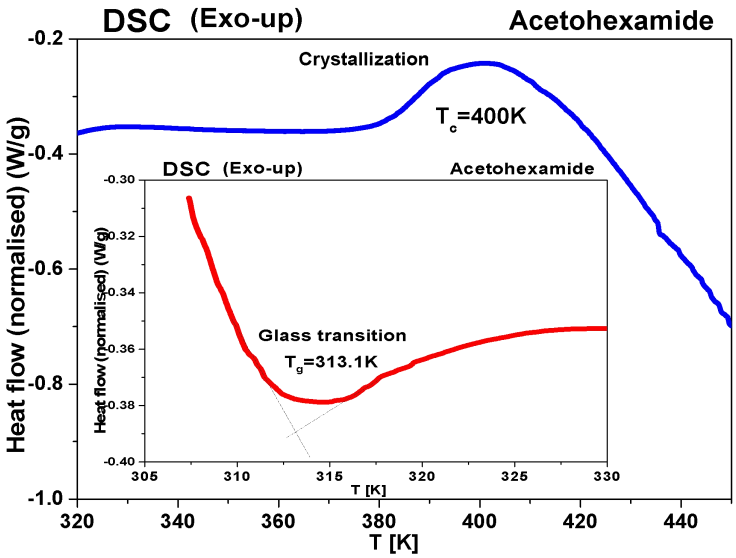

Figure 5.3.b DSC thermogram of acetohexamide showing glass transition and crystallization process

5.3.3 Broadband dielectric spectroscopy (BDS)

The molecular mobility of acetohexamide in the glassy and supercooled liquid states were crucial to characterize the molecular dynamics. The isothermal dielectric measurements of acetohexamide at ambient pressure were taken from the deep glassy state (133K) to temperatures near the melting point (473 K) in a wide frequency range from 10^{-2} to 10^{7} Hz.

5.3.3.1 Quench cooling

The temperature dependence of dielectric loss curves of acetohexamide during quench cooling of the melted sample is shown in Fig. 5.4. From figure 5.4 we can see that above T_g, there is a rapid increase in the dielectric loss which is due to dc conductivity, whereas below T_g dc conductivity contribution is not observed which is evident from the presence of secondary relaxation in figure 5.4.

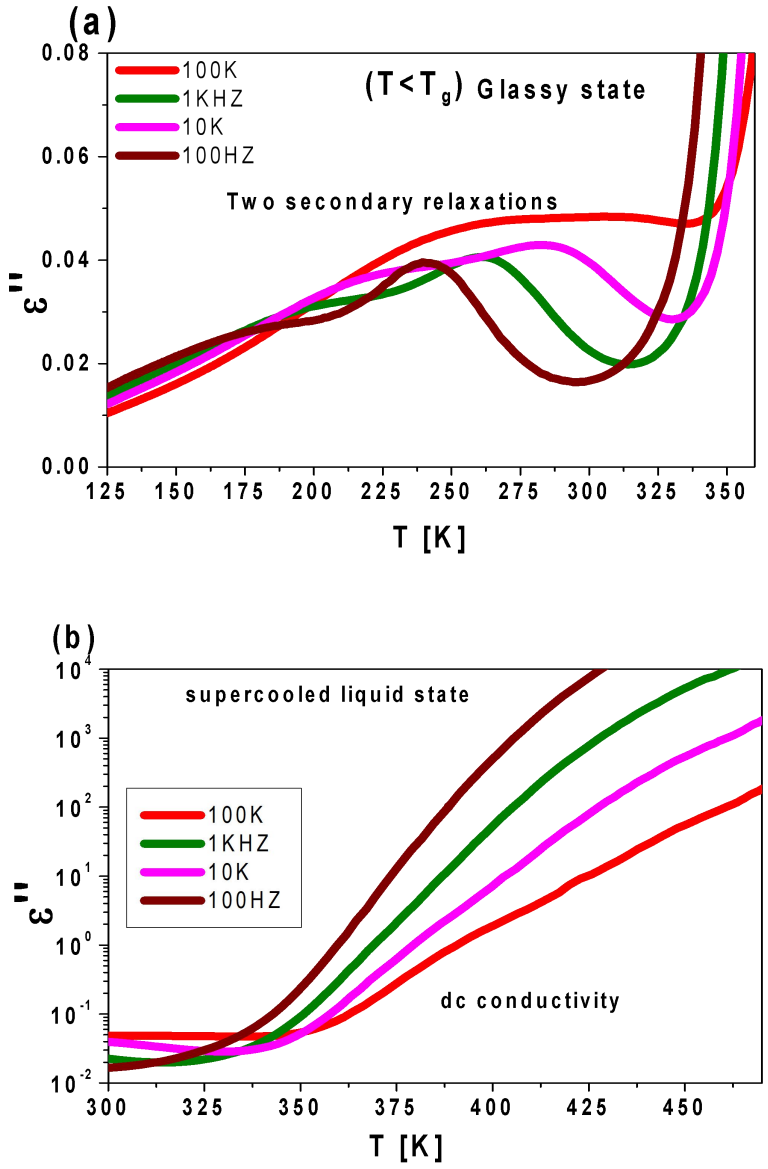

Figure 5.4 (a) Temperature dependence of dielectric loss of acetohexamide on quench cooling the melt to glassy state 5.4. (b) in the supercooled liquid state

To resolve the structural relaxations, we shall use dielectric modulus formalism. The temperature dependence of the real and imaginary parts of dielectric modulus is shown in figure 5.5 and figure 5.6 respectively. The peak shifts to higher temperatures with an increase in frequency. Therefore, to characterize the molecular dynamics of acetohexamide in supercooled and glassy states, modulus representation is used above T_g and dielectric permittivity representation is used below T_g. Two types of secondary relaxations in the lower temperature region and structural relaxation in the higher temperature are observed in acetohexamide as seen from figure 5.6.

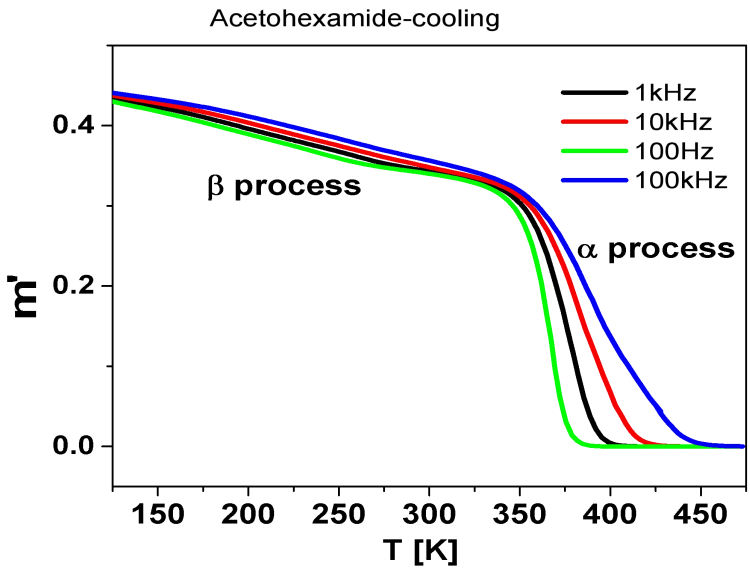

Figure 5.5 Temperature dependence of real part of modulus M' in acetohexamide

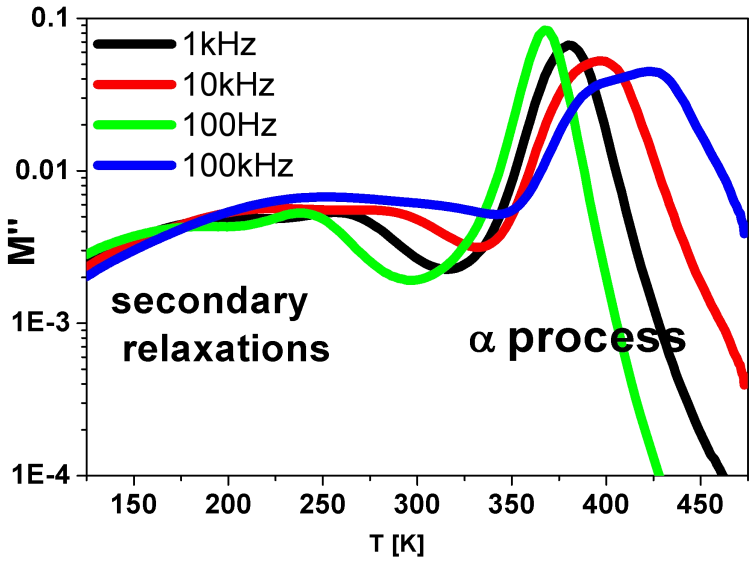

Figure 5.6 Temperature dependence of imaginary part of modulus M'' in acetohexamide

5.3.3.2 Supercooled liquid state ($T > T_g$)

Figures 5.7 and 5.8 present the real and imaginary parts of the complex dielectric spectra for acetohexamide obtained on heating the sample from the glassy state to the supercooled liquid state at atmospheric pressure from 343K to 468K with an increment of 2K; for sake of clarity, we have chosen to only show steps of 4K).

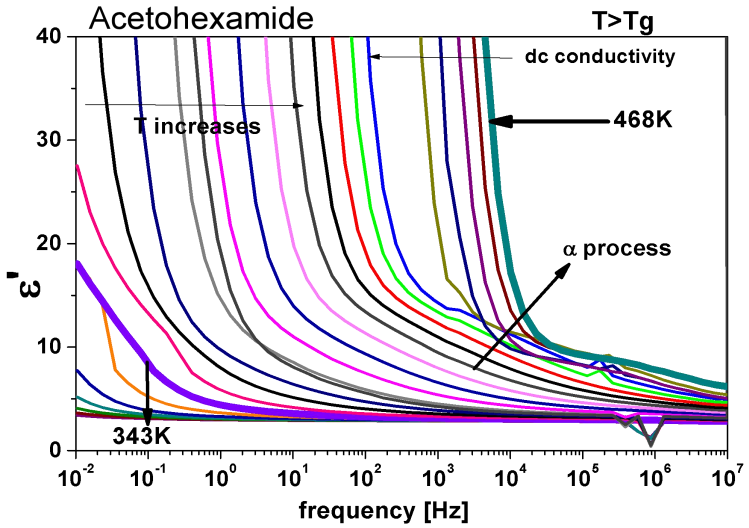

Figure 5.7 Dielectric permittivity spectrum (ε' vs f) of acetohexamide (T>T_g)

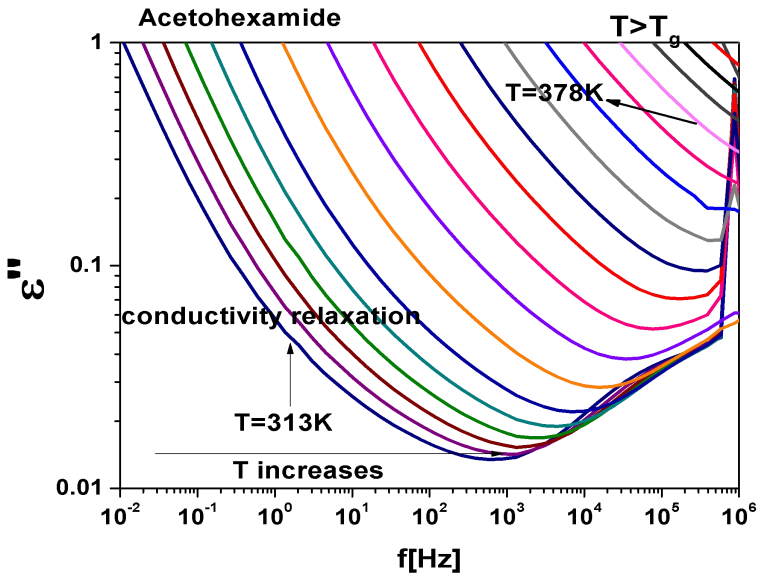

Figure 5.8 Imaginary part of the complex dielectric spectrum (ε'' vs. f) for acetohexamide (T > T_g)

It was found that the spectra for all temperatures above T_g were dominated by conductivity relaxation due to dc conductivity in acetohexamide, making the structural relaxation in the dielectric permittivity formalism unresolved. Even though the dielectric measurements can be represented by different frequency-dependent complex quantities like the permittivity, and the electric modulus, all of them are equivalent. In such situations, the electric modulus is a more appropriate representation of the conductivity relaxation data particularly in glass-formers where the structural relaxation is masked by dc conductivity [17,18].

From figures 5.7 and 5.8, the dc-conductivity relaxation which is due to the translation of ions is present above T_g and it dominates the dipolar structural relaxation. In such situations, the electric modulus is a more appropriate representation of the conductivity relaxation data particularly in glass-formers where the structural relaxation is masked by dc conductivity. Modulus representation of the dielectric data instead of permittivity representation is suitable for the analysis of samples having high conductivity and electrode polarization contributions. Modulus is a conceptually straightforward method for measuring orientational polarization and ionic conductivity. Below T_g, as the structural relaxation by dielectric representation is well resolved, the measured complex dielectric permittivity data is fitted to the Havriliak-Negami equation while above T_g, the measured dielectric modulus data measured is fitted with the Havriliak-Negami function as given below and from the fit parameters we obtained the molecular relaxation time and α-conductivity relaxation time.

$$\boldsymbol{M^*(\omega) = M'(\omega) + iM''(\omega) = \frac{1}{\varepsilon^*(\omega)} = M_\alpha + \frac{\Delta M}{(1 + (-i(\omega\tau_{\sigma\alpha})^{-1})^\alpha)^\beta}} \quad (5.1)$$

The real and imaginary parts of the dielectric modulus spectra are shown in figures 5.9 and 5.10 respectively showing α-conductivity relaxation in the supercooled liquid state. On increase in temperature the conductivity loss peaks shift towards higher frequencies due to the increased thermal energy. The presence of conductivity relaxation in the supercooled liquid state is due to the motion of the positive and negative parts of the molecule due to thermal energy and on the application of the electric field as it is clear from the MEP diagram that there are electropositive and electronegative regions in the molecular surface. The description of modulus M* and permittivity ε* are different. When ε* represents the relaxation of the electric displacement vector D at the constant electric field, while, the modulus represents the relaxation of the electric field E at constant displacement vector D. Hence, while dielectric modulus represents the real relaxation process, susceptibility represents the dielectric retardation process.

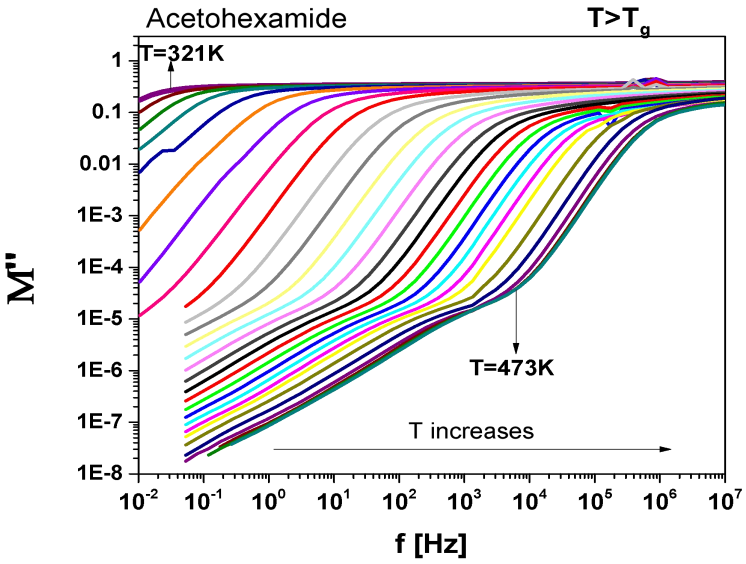

Figure 5.9 Real part of complex dielectric modulus spectrum for acetohexamide in the supercooled liquid state (T>T_g)

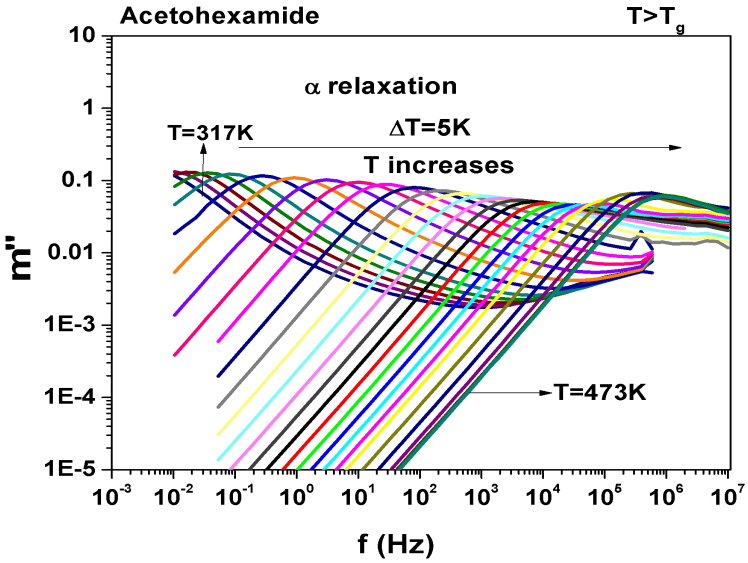

Figure 5.10 Imaginary part of complex dielectric modulus spectrum for acetohexamide in the supercooled liquid state (T>T_g)

5.3.3.3 Glassy state (T < T_g)

The real part of the complex dielectric constant spectra of acetohexamide in the glassy state (T<T_g) is shown in figure 5.11 showing a small change in dielectric permittivity which corresponds to the secondary relaxation. The imaginary part of the complex dielectric spectra of acetohexamide in the deep glassy state from 133K to 213K is shown in figure 5.12 which shows the dielectric data on heating from 133K in steps of 10K. Two resolved secondary relaxations labeled as γ and δ are observed in acetohexamide in the glassy state in the temperature range 133K to 213K as shown in

figures 5.12 and 5.13 which was also observed in the cooling curves shown in figure 5.6. To check the nature and correlation between conductivity relaxation and dipolar relaxation in the glassy state, in other words, to check the presence of translational rotational coupling, the imaginary part of the dielectric modulus spectra from 133K to 203K is shown in figure 5.13.

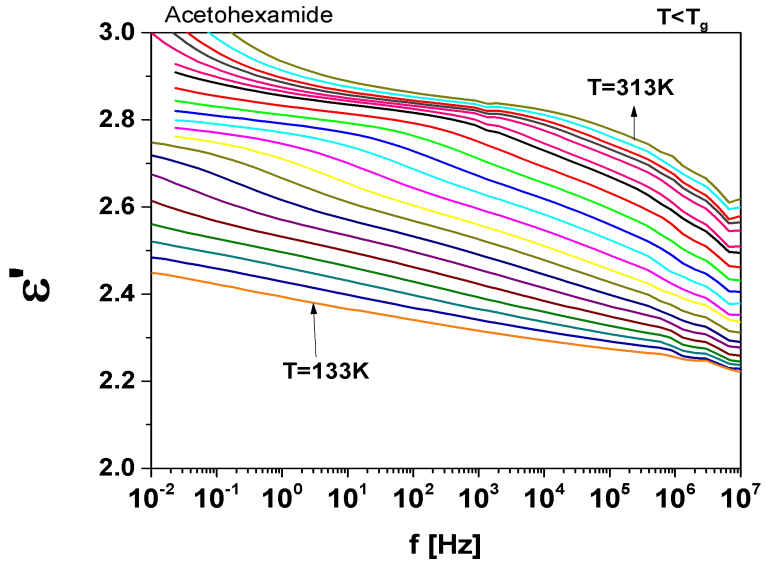

Figure 5.11 Dielectric permittivity spectra (ε' vs. f) of acetohexamide (T<T_g)

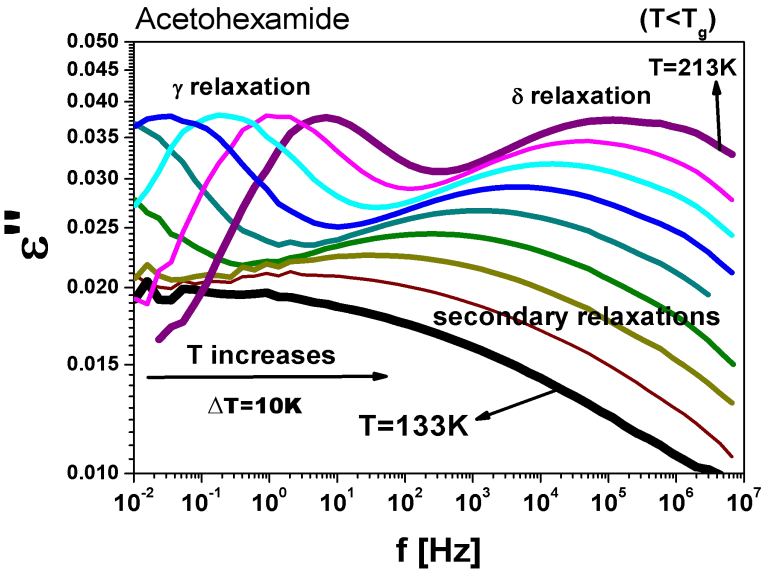

Figure 5.12 Dielectric loss spectra (ε'' vs. f) of acetohexamide in the glassy state (T<T_g)

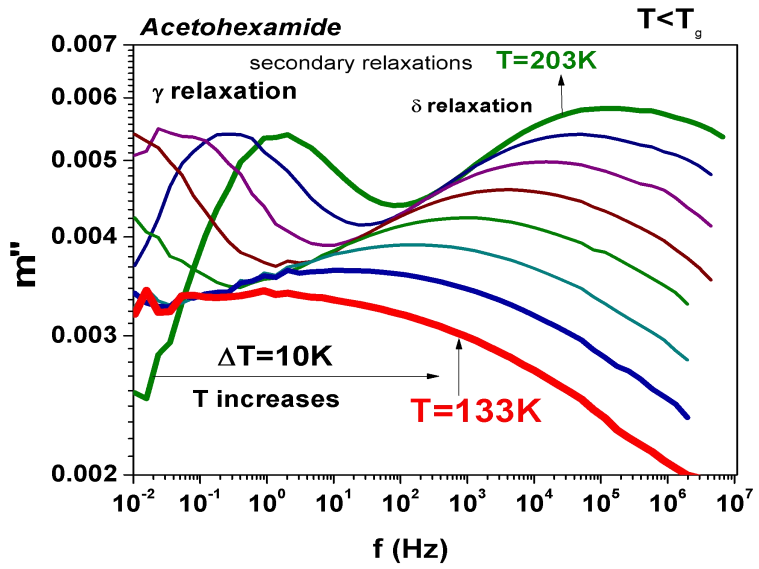

Figure 5.13 Imaginary part of the dielectric modulus spectra of acetohexamide in the glassy state

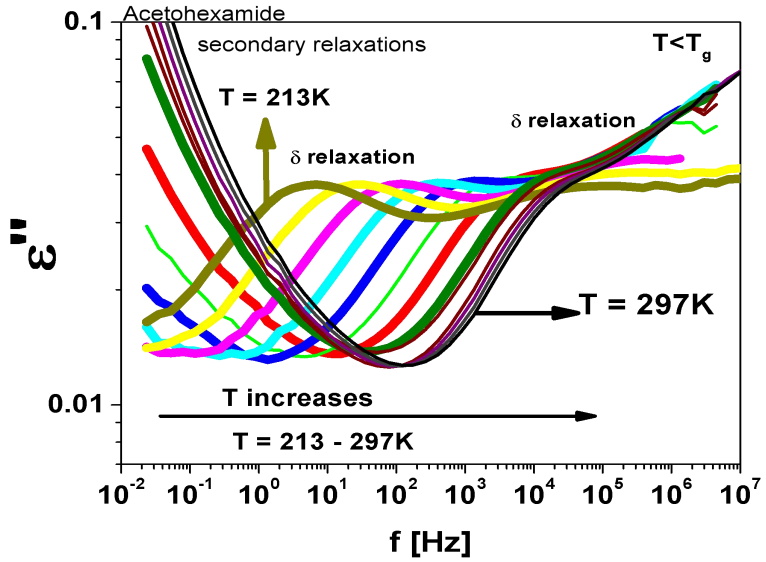

Figure 5.14. Dielectric loss spectra of acetohexamide in the deep glassy state from 213 K to 297 K

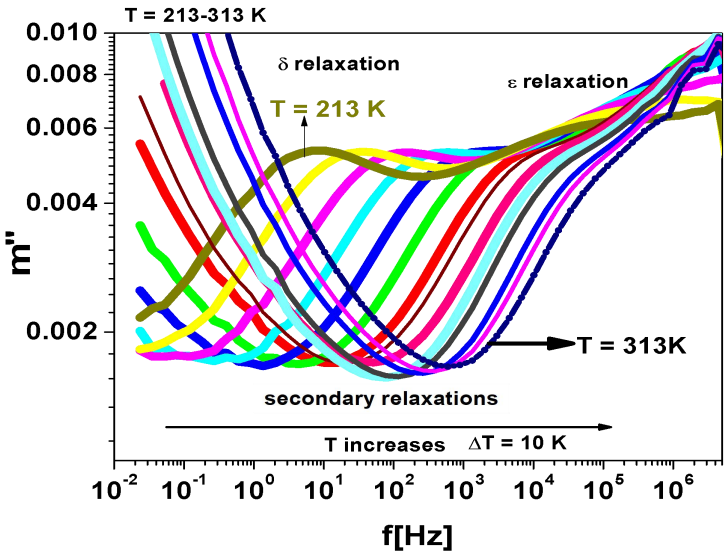

Figure 5.15 Imaginary part of the dielectric modulus spectra of acetohexamide in the deep glassy state from 213 K to 313 K

The dielectric loss spectra of acetohexamide in the glassy state in the temperature range from 213 to 297K on heating is shown in figure 5.14 and the imaginary part of the modulus spectrum in the same temperature range is shown in figure 5.15 shows the presence of two secondary relaxations labeled δ and ε. The secondary relaxation labeled ε goes out of the experimental window.

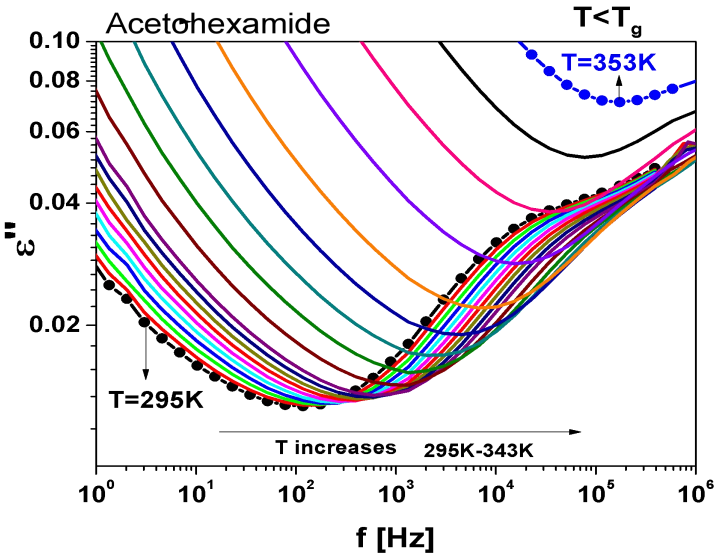

Figure 5.16 Imaginary part of the complex dielectric constant of acetohexamide in the from 295K to 353K

The imaginary part of the complex dielectric constant and dielectric modulus of acetohexamide from 295K to 353K is shown in figures 5.16 and 5.17 respectively. The structural relaxation is observed in the modulus spectra whereas due to conductivity the relaxation is masked in the dielectric permittivity spectrum. From this figure, it is clear that the secondary relaxation is observed in both the spectra, whereas the relaxation is observed only in modulus spectra above T_g and also the frequency of the secondary relaxation is the same in the permittivity and modulus representation which is due to a translational rotational coupling which is observed in some other pharmaceuticals also. To characterize the nonexponential character of the conductivity relaxation, the M''(f) loss peaks were fitted using the one-sided Fourier transform of the Kohlrausch–Williams–Watts (KWW)[19,20]. Only one well-resolved secondary relaxation is observed below the glass transition temperature, which is detected either as a dipolar rotation in dielectric susceptibility or as an ion conductivity relaxation in the electric modulus. Interestingly, the secondary dipolar and conductivity relaxation times calculated in both scenarios superimpose perfectly, as is seen in Fig. 5.15 5.16 and 5.17. These properties suggest the presence of a strong translation–rotation coupling of the molecules, leading to equivalent secondary conductivity and dipolar relaxation times. The latter can be considered as the Johari–Goldstein (JG) β relaxation relating to the dipolar structural α-relaxation, which is supposed to be a universal feature of glass-forming systems of all kinds [21]. While the secondary conductivity relaxation is the precursor of the conductivity a-relaxation, an analogue of the relation of the JG b-relaxation to the structural a-relaxation has been found before in an ionic liquid. The fitting parameters of the VFT and the value of T_g obtained from BDS, as well as from DSC, have already been reported by Safna *et al.*[22]. Here, we focus more on the origin of the secondary relaxation found in AMB, and so the fitting parameters of the Arrhenius equations are tabulated in Table 5.1. In passing, it is worth pointing out that the translation–rotation coupling has been found before from the fact that the same a-conductivity relaxation and a-dipolar relaxation have the same relaxation time and frequency dispersion in two ionic liquids, which was studied using light scattering and dielectric spectroscopy by Pabst *et al.*[23].

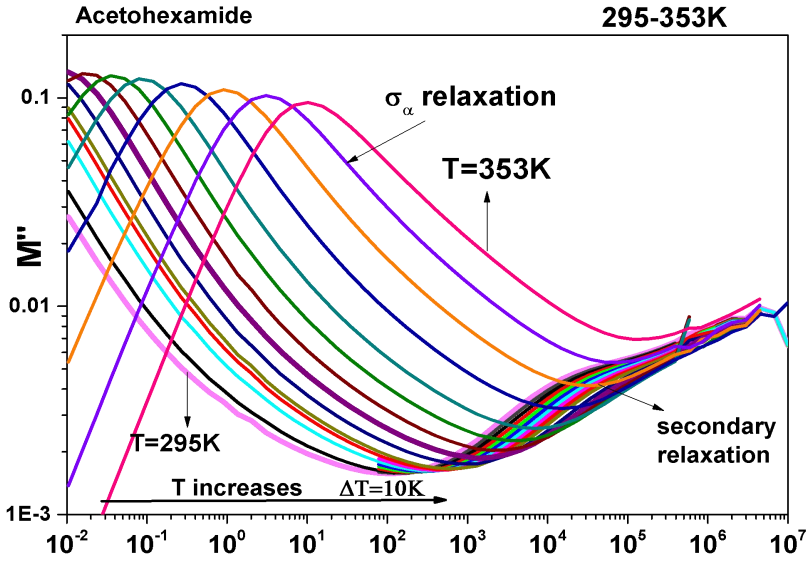

Figure 5.17 Imaginary part of the dielectric modulus spectra of acetohexamide in the from 295K to 353K

5.3.3.4 Temperature dependence of relaxation time

The measured dielectric modulus data measured is fitted with the Havriliak-Negami function as given below and from the fit parameters we obtained the molecular relaxation time and α-conductivity relaxation time. To identify the nature of the origin of secondary relaxation whether it is dipolar rotation in dielectric susceptibility or as an ion conductivity relaxation in the electric modulus, the relaxation times deduced from fitting the dielectric loss curves and imaginary part of modulus were compared and the temperature dependence of the molecular relaxation times are plotted in relaxation map shown in figure 5.18.

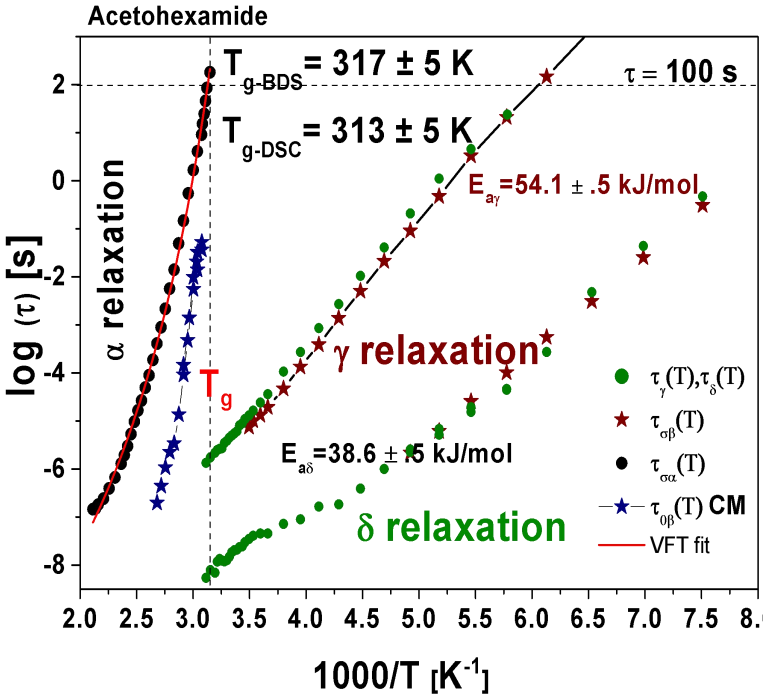

Figure 5.18. Relaxation map (Arrhenius diagram) of acetohexamide showing temperature dependence of structural and conductivity relaxations below and above T_g. The relaxation time below T_g from dielectric and modulus formalism are represented by green dots and brown stars.

The measured dielectric data is fitted to the Havriliak -Negami equation and the parameters corresponding to the dipolar and conductivity relaxations are determined. The temperature dependence of the molecular relaxation time below and above T_g was represented in the relaxation map (Arrhenius diagram) when plotted as a function of 1000/T. T_g is also determined from the Arrhenius graph, is considered as the temperature at which the α relaxation time τ_α = 100 s and obtained as 320K and is closer to the value of T_g obtained by the DSC experiment. The α conductivity relaxation times followed a curved temperature dependence and the secondary relaxation times follow linear temperature dependence. The activation energy of secondary relaxation was calculated by the Arrhenius equation

$$\tau(T) = \tau_\infty \exp\left(\frac{E_a}{RT}\right) \qquad (5.2)$$

From figures 5.13-5.17, even though three secondary relaxations are observed, only two secondary relaxations are well resolved and observed in acetohexamide in the glassy state, which is also evident from the imaginary part of the dielectric permittivity and modulus spectra. The temperature dependency of the secondary relaxation times

are fitted with the Arrhenius equation (equation 5.2) and obtained the values of the activation energy of the secondary relaxations and are shown in table 5.1.

5.3.3.5 Fragility

Liquid fragility is a term that has been commonly used in the glass community to identify the behaviour of glass-forming liquids, with a specific emphasis on the possibility of correlating fragility with the material's chemical structure. Angell[24] popularized the idea to explain variations in a liquid's ability to vitrify, and it is based on his belief that strong liquids must have stable structures (local to intermediate-range order) and properties that do not change drastically when transitioning from a liquid to a glassy state. For fragile liquids, on the other hand, such structures would be brittle, and the property changes from liquid to glass would be more noticeable. Fragile liquids are expected to have large configurational heat capacities as a result of their configurational entropy changing rapidly with temperature, while strong liquids are expected to have limited configurational heat capacities as a result of their different temperature dependencies of structure. Regardless, the fragile liquid glass former should exhibit strongly non-Arrhenius behaviour in the Angell plot, while the solid-liquid glass former should exhibit nearly Arrhenius-type behaviour when traversing the glass transition temperature, which is commonly described as 10^{12} Pas in terms of viscosity.

The Vogel–Tammann–Fulcher (VTF) equation is used to describe the non-Arrhenius version of fragility. The temperature dependence of structural relaxation (σ_α) process was fitted by the Vogel-Fulcher-Tamann (VFT) equation (5.3).

$$\tau(T) = \tau_0 \exp\left(\frac{B}{T - T_0}\right) = \tau_0 \exp\left(\frac{DT_0}{T - T_0}\right) \qquad (5.3)$$

where T is absolute temperature, D is the strength parameter and T_0 is the Vogel temperature and are positive constants. The VFT fit parameters of acetohexamide are shown in table 5.1 like some reported drugs.

Table 5.1 VFT parameters of acetohexamide

T_g(K)	Fragility m	Strength Parameter D	log τ_{VF}	T_0(K)	E_a (kJ/mol)
320 ±2	51.1±.5	13.14	-11.67	229.17	56.2 43.7

The value of T_g obtained by VFT fit is approximately closer to the value of T_g obtained by DSC. Since the value of T_g is higher than room temperature, and the difference between Tg and crystallization temperature is 80K, it suggests that the amorphous acetohexamide will be stable in the ambient storage conditions. The strength parameter D and fragility values of acetohexamide correspond to intermediate fragility.

The most famous depiction of the dynamic fragility of glass-forming liquids is the Angell plot. The increase in the relaxation timescale of supercooled liquids is notable not only for a large number of decades involved but also for the temperature dependence. Figure 5.19 shows the logarithm of relaxation time as a function of T_g/T in acetohexamide. It comes in handy when it comes to classifying supercooled liquids. Depending on its position in the Angell plot, a liquid is labeled as strong or fragile. Strong glass-formers and an Arrhenius behaviour are represented by straight lines. In this case, the plot can be used to derive effective activation energy, implying a relatively simple relaxation mechanism involving the breaking of a chemical bond locally. The energy barrier to activate this process then dominates the typical relaxation time, resulting in an Arrhenius behaviour. This category includes window glasses.

Normally, the Angell plot shows the data as the logarithm of the zero shear rate viscosity versus T_g /T in a reduced Arrhenius plot. Although Angell was not the first to create such a plot, he was the first to use it extensively and to suggest that dynamic fragility and thermodynamic fragility could be related. As a result, the Angell plot has become a common way to depict the viscosity's temperature dependence. Furthermore, the nonexponentiality of the structural relaxation function, the chemical structure of polymers, structural recovery in the glassy state, and vibrational motions have all been linked to dynamic fragility.

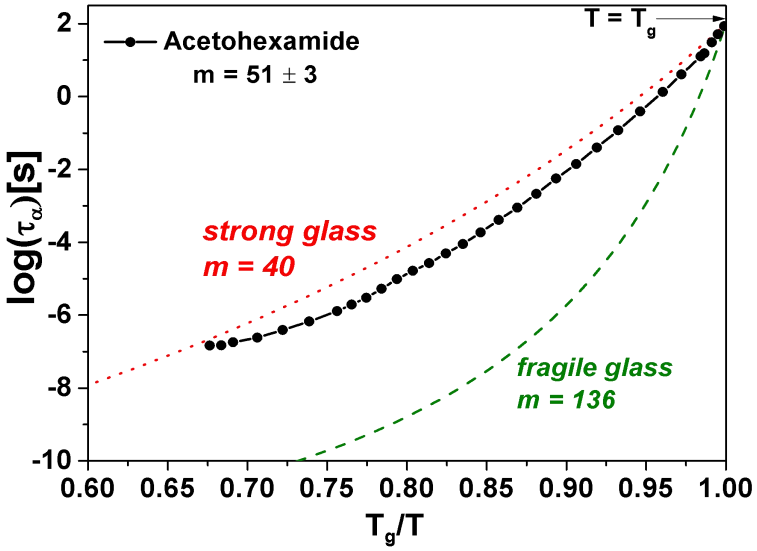

Figure 5.19 Angell's plot for acetohexamide. For strong glasses, a nearly straight line shown in red dot lines is obtained and for fragile glass formers a curve shown as green dot lines are obtained

5.3.3.6 Nature of secondary relaxation: Coupling model

Two well-resolved secondary relaxations were observed in the glassy state of acetohexamide having activation energies 56 and 43kJ/mol. The relaxation time of the secondary relaxations observed in the glassy state of acetohexamide in the modulus representation and the dielectric permittivity representation matches perfectly and is evident from figure 5.18. This type of behaviour was reported in some glass formers [1,25] and was found to be the presence of coupling between the translation and rotation of the molecules resulting in equivalent conductivity and dipolar relaxation times. The conductivity and dipolar relaxation simultaneously observed in the glassy state of acetohexamide gives an idea about the nature of the conductivity α relaxation. The secondary conductivity relaxation is the precursor of the observed conductivity α relaxation like Johari-Goldstein β relaxation is the precursor of structural α relaxation[26].

However, the possibility of an intramolecular secondary relaxation due to the presence of a dihedral side chain with amine groups cannot be excluded. To resolve the issue and confirm the presence of the secondary conductivity relaxation, we used the Coupling Model (CM). Originally, the CM was applied to secondary relaxations having properties strongly connected to the structural a-relaxation. The existence and universal presence of this kind of secondary relaxation called the Johari–Goldstein (JG)

b-relaxation, was suggested by its analogy to the primitive relaxation of the CM, which started in a paper in 1998[27], and has since been extensively developed[28–31].

To confirm the presence of the secondary conductivity relaxation and to find the origin of the observed dipolar secondary relaxation, i.e. whether it is JG type or non-JG type coupling model [32,33] has been applied. The coupling model accounts for the intermolecular coupling effects like the many-body dynamics and dynamic heterogeneity considering other contributions in mind as caging effect and configurational entropy. The coupling model describes the existence of a crossover time t_c, at times shorter than this t_c, (2 ps for molecular liquids) the molecules relax independently and have a normalized correlation function of exponential form.

$$\boldsymbol{\phi(t) = \exp\left(-\frac{t}{t_0}\right) \quad t < t_c} \tag{5.4}$$

The primitive relaxation time is given by the equation according to the Coupling model is

$$\boldsymbol{\tau_{JG}(T) \approx \tau_0(T) = (t_c)^{\,n}\,(\tau_\alpha(T))^{1-n}} \tag{5.5}$$

where t_c is equal to 2ps for molecular glass formers and ($n=1-\beta_{KWW}$) is the coupling parameter. Although similar, the JG b-relaxation and the primitive relaxation are not identical processes, and hence their relaxation times, $\tau_{JG}(T)$ and $\tau_0(T)$, are not necessarily equal. Only approximate correspondence between their orders of magnitude can be expected or predicted, Thus $\tau_{JG}(T)$ calculated using the CM equation provides an order of magnitude estimate of $\tau_{JG}(T)$ to compare with its experimental value.

The nature of the origin of a secondary relaxation, whether is it a JG relaxation is particularly relevant to the MD of amorphous pharmaceuticals as the intermolecular JG β-relaxation can be the precursor of α relaxation. As the Coupling Model applies to all interacting systems showing relaxations the conductivity relaxation is not excluded from the CM fit. For conductivity relaxations, the CM equation is written as

$$\boldsymbol{\tau_{\sigma\alpha} = (t_c^{\,-n_\sigma}\tau_{\sigma 0})1 - n\sigma^{1-n_\sigma}} \tag{5.6}$$

where tc ≈1 ps for most ionic conductors. Using this equation we calculated the values of $\tau_{\sigma 0}(T)$ and plotted them in the relaxation map in figure 5.18. From figure 5.18 we found that the calculated conductivity primitive relaxation time of acetohexamide does

not correspond to the temperature dependence of experimentally observed secondary relaxation and therefore the observed secondary relaxation is not Johari-Goldstein type β relaxation rather it originates from local molecular motion. The temperature dependence of the secondary relaxation time below T_g obtained on fitting the dielectric loss spectrum and dielectric modulus spectrum coincides in the relaxation map and hence we confirm the presence of translational rotational coupling in acetohexamide. But the dielectric loss peaks above T_g due to structural α relaxation are masked by the conductivity contribution the molecular relaxation time corresponding to structural α relaxation could not be determined. The CM equation is generally applicable to relaxation and diffusion in all interacting systems, including not only structural relaxation but also ion conductivity relaxation because the molecules or ions are densely populated and interacting in both cases. For this reason, the CM also has long since been applied successfully to the ion conductivity relaxation of crystalline, glassy, and molten ionic conductors[17,33–35]. There is also the CM equation relating the conductivity relaxation time $\tau_{\sigma\alpha}(T)$ to the conductivity primitive relaxation time $\tau_{\sigma 0}(T)$, which is given by equation 5.6.

5.3.3.7 Translational-rotational coupling

We have determined the relaxation time of conductivity secondary relaxation $\tau_{\sigma\beta}(T)$ of acetohexamide at temperatures below Tg from the electric modulus data in Fig. 5.13, 5.14 and 5.15 and the temperature dependence of it is shown in the relaxation map shown in Fig. 5.18. The temperature dependence of primitive relaxation times ($\tau_{\sigma 0}(T)$) calculated from the experimental values of $\tau_{\sigma\alpha}(T)$ above T_g using the CM equation and the line is the fit to the temperature dependence of $\tau_{\sigma 0}(T)$ are also shown in Fig.5.18. By extrapolating the $\tau_{\sigma\beta}(T)$ and $\tau_{\sigma 0}(T)$ both towards T_g, shown in Fig. 5.18, there is an approximate agreement between $\tau_{\sigma 0}(T_g)$ and $\tau_{\sigma\beta}(T_g)$ and thus confirmed that the conductivity β-relaxation present is in accord with the CM prediction as like in other ionic conductors.

We concluded that there is translation–rotation coupling based on the strong agreement of secondary conductivity relaxation and secondary dipolar relaxation times shown in Fig. 5.18. This can be verified in theory by comparing the values of (T) with the structural relaxation times (T). Unfortunately, this is not possible since the acetohexamide dielectric loss peaks are obscured by the dc-conductivity that results

from ion hopping, as shown in Fig. 5.8. We may have to conduct tests at high pressure to accomplish this. This supports the identification of this secondary relaxation as the conductivity-relaxation of acetohexamide, which acts as a precursor to the conductivity-relaxation, as previously stated for other ionic conducting pharmaceuticals, such as procainamide HCl, [28,36] lidocaine HCl,[37] procaine HCl[17], chlorpromazine HCl[34] and an ionic liquid[22].

5.3.3.8 Kohlraush-William-Watts (KWW) fit

The Kohlraush-William-Watts (KWW) function[19,38] describes the non-exponential behaviour of dielectric relaxation and more details of it are given in chapter 1. Kohlrausch-Williams-Watts's function is given by

$$\boldsymbol{\phi(t) = \exp\left(-\frac{t}{\tau_{\sigma\alpha}}\right)^{\beta_{KWW}}} \qquad (5.7)$$

Where $\phi(t)$ is the relaxation function, $\tau_{\sigma\alpha}$ is the conductivity relaxation time and β_{KWW} is the stretched exponential parameter and is related to the distribution of molecular relaxation times and is a relevant criterion in predicting the safe shelf life of amorphous pharmaceuticals.

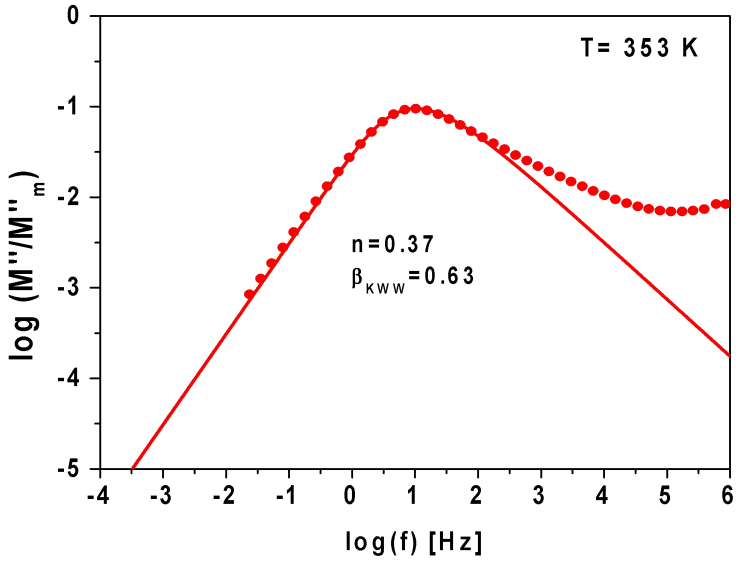

Figure 5.20 KWW fit of acetohexamide at 353K showing the measure of nonexponentiality and the presence of excess wing

From figure 5.20, the value of the fractional exponent of the KWW function at 353K is found to be 0.6. Since the β_{KWW} value is also a measure of the distribution of relaxation time, acetohexamide has an above intermediate distribution of conductivity

relaxation times. The primitive relaxation frequency f_0 of the coupling model was obtained to be 1.34 x 10^3Hz which falls in the region in the higher frequency side of the peak where the excess wing is expected.

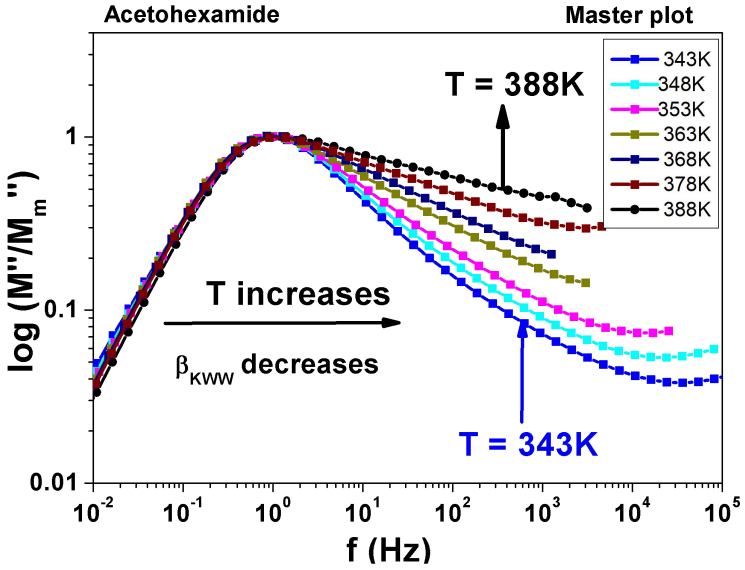

Figure 5.21 Master plot of acetohexamide above the T_g (343K to 388K)

A visualization of the temperature dependence of conductivity loss peaks is done by master plot analysis after normalizing the peak heights uniformly to unity and is shown in figure 5.21. It is based on the horizontal shifting of the spectra taken at various temperatures above T_g to superimpose them onto a spectrum at 343K following frequency-temperature superposition rules. The full width at half maximum of the conductivity loss peak is found to increase with an increase in temperature in acetohexamide as seen in figure 5.21. Furthermore, it has been demonstrated that the KWW parameter, which describes the distribution of molecular motions, can be used to predict the life expectancy of amorphous pharmaceuticals. A narrow structural relaxation distribution, i.e., high KWW values, would indicate a low proclivity for amorphous API to crystallize. A larger distribution of -relaxation times, on the other hand, could indicate faster localized molecular motions, leading to a greater tendency toward crystal nucleation[39]. We used the one-sided Fourier transform of the Kohlrausch-Williams-Watts (KWW) function[38] to check the importance of this parameter in our scheme. The stretching parameter KWW decreases from 0.71 at 343K to 0.56 at 373K over the temperature range studied. In the supercooled liquid state of acetohexamide, the distribution of relaxation times is asymmetric and far broader than

in a classical Debye-type process (β_{KWW} =1). From the analysis of the master plot (Figure 5.21), a reliable complementary visualization of stretching parameter β_{KWW} was conducted. This special procedure enables to ascertain whether temperature plays an active role in the shape of the structural relaxation that would have resulted with different relaxation times depending on the temperature. With β_{KWW} equal to 0.7 for acetohexamide, temperature has influence on the shape of the conductivity relaxation and observed that the asymmetric stretching parameter decreases with increasing in temperature which corresponds to more instability of the amorphous phase. Furthermore, experimental data deviates from the KWW pattern at higher frequencies, as can be seen.

5.3.4 Origin of secondary relaxation : DFT approach

While dielectric measurements could be used to determine the activation energy of the relaxation, no proof of the relevant part of the molecular moieties involved in the transition could be inferred directly. Indeed, the root of secondary relaxations has remained a mystery, with no clear answer available until now. Secondary relaxations may occur as a result of complex intramolecular changes involving multiple moieties or as a result of a JG process, but this is not the case here. In recent years, there has been an increase in interest in theoretical conformational calculations or MD simulations to decipher the physical structure of the transition at the atomic level, which is often combined with experimental studies [40,41]. In line with this synergetic approach, more knowledge is sought to reveal the origin of secondary processes by using measured energy barriers and dipole moments when suitable versatile end groups relax. Using DFT calculations, Schamme et al.[9] published an effective identification pathway for identifying the specific part of a molecule that manifests the observed secondary relaxation. They tested a technique by using dihedral scans to map the molecule's energy and dipole moment as a function of torsional angles. Exploration of the potential energy surface (PES) associated with the rotation of a flexible side group leads to conformational interconversions through various feasible minima (MIN) and transition states (TS). A one-to-one correspondence can be found when plotting molecular dipole moment as a function of torsional dihedral angle. Among various combinations of MINs and TS, the energy can be related to a shift in the dipole moment. Using mod-redundant coordinates in Gaussview software[6,8], a

dihedral angle was randomly selected and scanned continuously through 360° by a constant step of 10°. The remainder of the molecule was optimized while the energy and dipole moment were measured at a frozen value of the angles set. The relaxed dihedral scans on several possible dihedral angles corresponding to versatile side groups matching with the experimentally observed activation energy using Gaussian 09[6] package are used to classify the related local motion in a molecule. The energy scan graph of acetohexamide related to the rotation of the $NH{=}O\text{-}NH\text{-}SO_2\text{-}C_6H_{12}$ group is presented in Fig. 5.22. The associated molecular subgroup, which causes the observed secondary relaxation in acetohexamide, is shown circled in Fig. 5.23. The rotation of the selected group led to the conformational interconversions specified by energy minima (MIN1.) and transition state (TS1). The energy difference corresponding to different potential energy barriers of the transition states are matched with the observed activation energy of secondary relaxation in fenofibrate. The potential energy scan diagram showing the variation of potential energy with a torsional angle corresponding to the rotation of the $NH{=}O\text{-}NH\text{-}SO_2\text{-}C_6H_{12}$ group obtained from the DFT method is shown in figure 5.22. Two potential barriers corresponding to two minima and maxima are obtained. Two secondary relaxations are observed experimentally in acetohexamide below T_g, with activation energies 54.1kJ/mol and 34.1kJ/mol. These values of activation energies of secondary relaxation experimentally observed in acetohexamide matches with the theoretically obtained values corresponding to dihedral scan and hence the potential barrier obtained between MIN1 and MAX1 and MIN1 and MAX1 are 34kJ/mol and 54kJ.mol on the rotation of the selected side group between 0 and 100 degrees for potential energy barrier 1 and between 150^o and 300^o for potential energy barrier 2. These values are closer to the value of the experimental activation energy of the secondary relaxation.

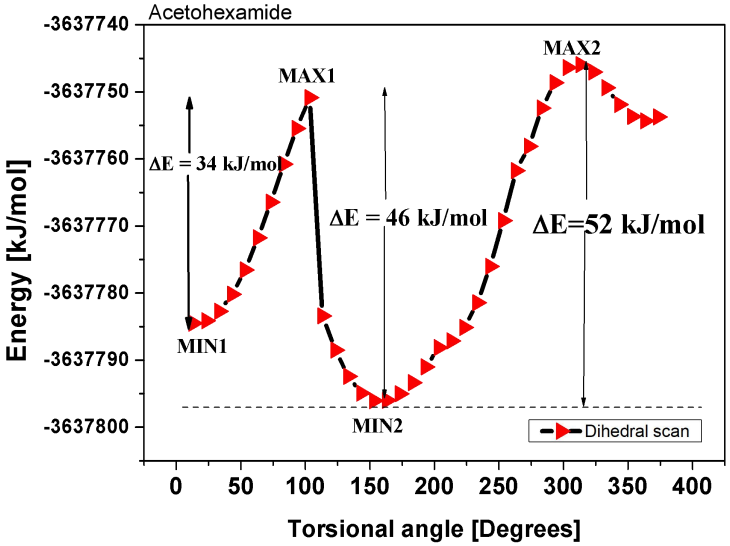

Figure 5.22 Potential energy scan graph of acetohexamide

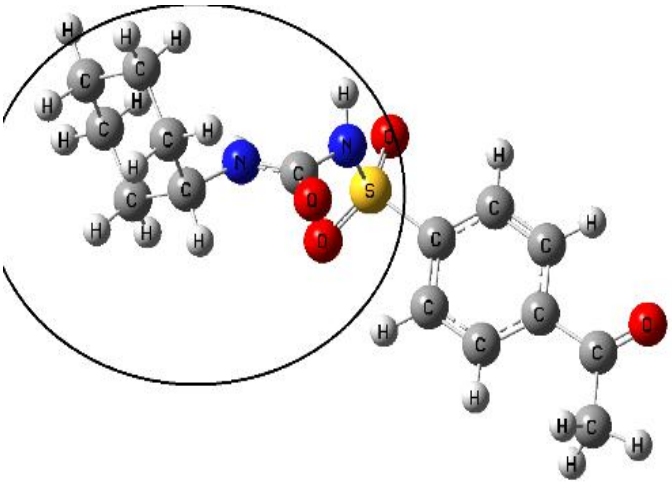

Figure 5.23 Optimized geometry of acetohexamide. The rotated molecular subgroup is shown in the circle

5.3.5 Vibrational Spectroscopy

FTIR and FT-Raman spectra of crystalline and amorphous acetohexamide are shown in figures 5.24 and 5.25. The identity of the sample is confirmed by comparing the vibrational spectrum obtained by the DFT method with the experimental spectrum. Since the bond strength of the donor and acceptor groups are strongly influenced by hydrogen bond formation and the OH group is more sensitive, it is easy to study the molecular interaction using vibrational spectroscopic data. Common changes include redshift in absorption band, band broadening, and band intensification. From the FTIR spectrum shown in figure 5.24, shifting and broadening of peaks are observed in the

amorphous phase of acetohexamide when compared to the crystalline acetohexamide. Hence the strong intermolecular hydrogen bonding in the crystalline phase and expected weakening in the amorphous phase is observed for acetohexamide. This is the general observation for most of the amorphous pharmaceuticals though there are notable exceptions. At the same time opposite to the expected character of narrowing the peaks with the decrease in crystallinity in the quenched sample, an increase in broadness is observed. The same case has been reported for many pharmaceuticals and is due to the broader distribution of hydrogen bond lengths in the disordered amorphous phase.

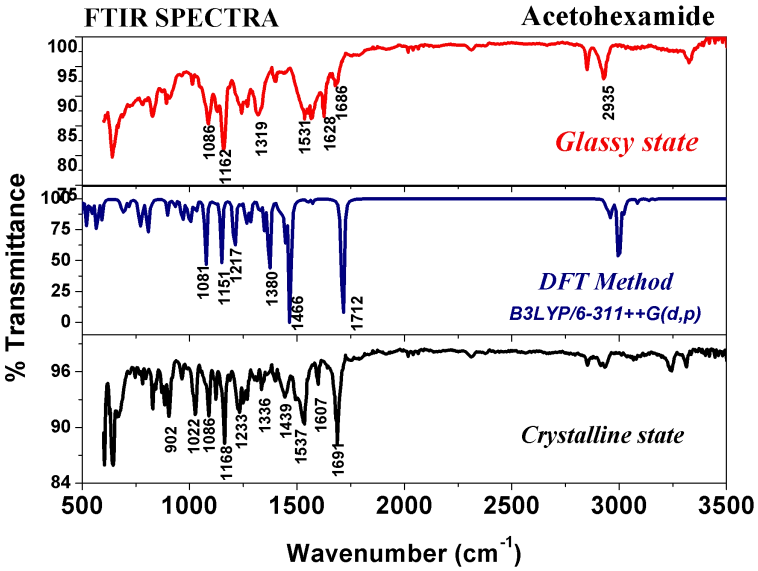

Figure 5.24 FTIR spectra of acetohexamide

From the FT-Raman spectrum of acetohexamide shown in figure 5.25, there is a good agreement between the peak in the crystalline phase and amorphous phase and with the peaks obtained from the DFT method.

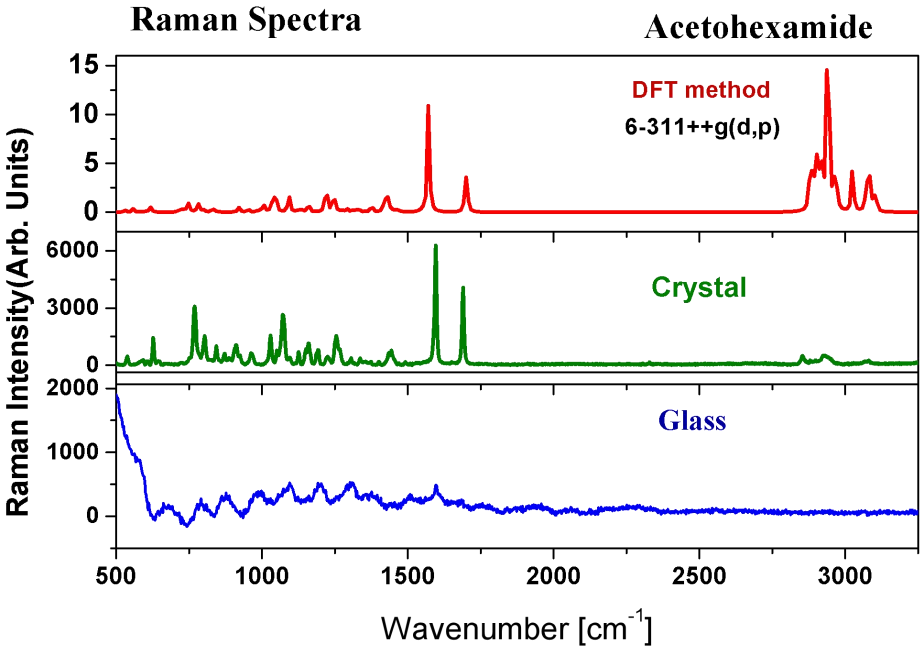

Figure 5.25 Raman spectra of acetohexamide

5.4 Conclusions

In this chapter, the molecular dynamics of the acetohexamide in supercooled liquid and glassy states were analyzed by experimental methods such as DSC, BDS, and vibrational spectroscopy. Acetohexamide is found to be a good glass-former and is also an ionic conductor. A well-resolved conductivity relaxation and two well-resolved secondary conductivity relaxations were observed in the modulus formalism and two well-resolved secondary dipolar relaxations are observed below T_g in acetohexamide. No well-resolved α relaxation in dielectric formalism was observed above T_g as it is masked by dc conductivity. The molecular and ionic dynamics in acetohexamide were studied by both the conductivity and structural relaxations. Physical stability or recrystallization of the amorphous phase is an important concern in the application of amorphous pharmaceuticals. The value of T_g obtained for acetohexamide is 320K which is higher than room temperature hints at the stability of the amorphous acetohexamide. From the study of the conductivity relaxation and the analysis of the data using electric modulus representation above and below T_g, we have observed and characterized the conductivity σ_α relaxation responsible for dc conductivity in the liquid state above T_g, and a conductivity σ_β relaxation in the glassy state. In the glassy state, the observed conductivity σ_β relaxation and having its relaxation time $\tau_{\sigma\beta}$ has a non-trivial relation to $\tau_{\alpha\sigma}$ similar to τ_0 as per coupling model, there is an evidence of the

evolution of the ionic dynamics from the primitive relaxation time and terminating in the many-ion α relaxation on approaching T_g. Therefore, the conductivity α-relaxation may originate from the intermolecular JG-relaxation which highlights the importance of considering the relationship between the structural and conductivity relaxations. Incidentally, when the same bds data of acetohexamide is analyzed in the dielectric permittivity formalism, a secondary dipolar relaxation with the same relaxation time and activation energy as the conductivity relaxations in the glassy state which is due to the presence of coupling between translational and rotational motion in the glassy acetohexamide. Translation–rotation coupling of acetohexamide possibly explains the dual conductivity and dipolar nature of the secondary relaxation. We conducted computer simulation studies of an acetohexamide molecule, integrating all possible sidechain rotations about different dihedral angles, to not rule out the possibility of intramolecular secondary relaxation. As a result, the secondary dipolar relaxation likely observed is due to sidechain rotation. Despite this possibility, the dipolar JG mechanism, which requires the motion of the entire acetohexamide molecule rather than a side group, cannot be the source of the observed secondary dipolar relaxation. Moreover, by DFT methods, we found that the two values of energy at a different range of torsion angles of the potential energy barriers obtained by the dihedral scan rotation of $(CH_2)_6$-NH group in acetohexamide corresponds to the experimentally observed two activation energy values of the two secondary dipolar relaxations. From this incident, the observed secondary dipolar relaxation is found to be intramolecular and we have identified the particular molecular sub-group responsible for the secondary relaxation. We can again confirm by investigating the pressure dependence of the secondary dipolar relaxation. If its relaxation time is pressure-sensitive, then the possibility of it being the side-chain rotation can be eliminated. In that case, due to the translation–rotation coupling, the secondary dipolar relaxation must be the Johari–Goldstein b-relaxation of the structural a-relaxation.

References

[1] K. P. Safna Hussan, M.S. Thayyil, S.K. Deshpande, Jinitha. T. V, Manoj. K, K.L. Ngai, Molecular dynamics and the translational–rotational coupling of an ionically conducting glass-former: amlodipine besylate, RSC Adv. 8 (2018) 20630–20636. https://doi.org/10.1039/C8RA01544A.

[2] A. Telfah, M.M. Abdul-Gader Jafar, I. Jum'h, M.J.A. Ahmad, J. Lambert, R. Hergenröder, Identification of relaxation processes in pure polyethylene oxide (PEO) films by the dielectric permittivity and electric modulus formalisms, Polym. Adv. Technol. 29 (2018) 1974–1987. https://doi.org/https://doi.org/10.1002/pat.4306.

[3] D.L. Sidebottom, B. Roling, K. Funke, Ionic conduction in solids: Comparing conductivity and modulus representations with regard to scaling properties, Phys. Rev. B. 63 (2000) 24301. https://doi.org/10.1103/PhysRevB.63.024301.

[4] B.L. Furman, Acetohexamide, in: S.J. Enna, D.B.B.T.T.C.P.R. Bylund (Eds.), Elsevier, New York, 2007: pp. 1–5. https://doi.org/https://doi.org/10.1016/B978-008055232-3.63718-3.

[5] S. Bhattacharya, R. Suryanarayanan, Local Mobility in Amorphous Pharmaceuticals—Characterization and Implications on Stability, J. Pharm. Sci. 98 (2009) 2935–2953. https://doi.org/https://doi.org/10.1002/jps.21728.

[6] M.J. Frisch, G.W. Trucks, H.B. Schlegel, G.E. Scuseria, M. a. Robb, J.R. Cheeseman, G. Scalmani, V. Barone, G. a. Petersson, H. Nakatsuji, X. Li, M. Caricato, a. V. Marenich, J. Bloino, B.G. Janesko, R. Gomperts, B. Mennucci, H.P. Hratchian, J. V. Ortiz, a. F. Izmaylov, J.L. Sonnenberg, Williams, F. Ding, F. Lipparini, F. Egidi, J. Goings, B. Peng, A. Petrone, T. Henderson, D. Ranasinghe, V.G. Zakrzewski, J. Gao, N. Rega, G. Zheng, W. Liang, M. Hada, M. Ehara, K. Toyota, R. Fukuda, J. Hasegawa, M. Ishida, T. Nakajima, Y. Honda, O. Kitao, H. Nakai, T. Vreven, K. Throssell, J. a. Montgomery Jr., J.E. Peralta, F. Ogliaro, M.J. Bearpark, J.J. Heyd, E.N. Brothers, K.N. Kudin, V.N. Staroverov, T. a. Keith, R. Kobayashi, J. Normand, K. Raghavachari, a. P. Rendell, J.C. Burant, S.S. Iyengar, J. Tomasi, M. Cossi, J.M. Millam, M. Klene, C. Adamo, R. Cammi, J.W. Ochterski, R.L. Martin, K. Morokuma, O. Farkas,

J.B. Foresman, D.J. Fox, G16_C01, (2016) Gaussian 16, Revision C.01, Gaussian, Inc., Wallin.

[7] A.D. Becke, Density functional calculations of molecular bond energies, J. Chem. Phys. 84 (1986) 4524–4529. https://doi.org/10.1063/1.450025.

[8] M.J. Frisch, G.W. Trucks, H.B. Schlegel, G.E. Scuseria, M.A. Robb, J.R. Cheeseman, G. Scalmani, V. Barone, B. Mennucci, *et al*. Petersson, Gaussian 09, Gaussian, Inc. Wallingford, CT.

[9] B. Schammé, M. Mignot, N. Couvrat, V. Tognetti, L. Joubert, V. Dupray, L. Delbreilh, E. Dargent, G. Coquerel, Molecular Relaxations in Supercooled Liquid and Glassy States of Amorphous Quinidine: Dielectric Spectroscopy and Density Functional Theory Approaches, J. Phys. Chem. B. 120 (2016) 7579–7592. https://doi.org/10.1021/acs.jpcb.6b04242.

[10] E. Scrocco, J. Tomasi, The electrostatic molecular potential as a tool for the interpretation of molecular properties BT - New Concepts II, in: Springer Berlin Heidelberg, Berlin, Heidelberg, 1973: pp. 95–170.

[11] C. Petrongolo, Quantum Chemical study of isolated and interacting molecules with biological-activity, Gazz. Chim. Ital. 108 (1978) 445–478.

[12] J. Tomasi, R. Bonacorsi, E. Serocco, Molecular SCF calculation for the ground state of some three-membered ring molecules, J. Chem. Phys. 52 (1970) 5270–5284.

[13] P.K. Weiner, R. Langridge, J.M. Blaney, R. Schaefer, P.A. Kollman, Electrostatic potential molecular surfaces, Proc. Natl. Acad. Sci. 79 (1982) 3754–3758.

[14] L. Chen, T. Okuda, X.-Y. Lu, H.-K. Chan, Amorphous powders for inhalation drug delivery., Adv. Drug Deliv. Rev. 100 (2016) 102–115. https://doi.org/10.1016/j.addr.2016.01.002.

[15] W. Kauzmann, The Nature of the Glassy State and the Behaviour of Liquids at Low Temperatures., Chem. Rev. 43 (1948) 219–256. https://doi.org/10.1021/cr60135a002.

[16] D. Turnbull, Under what conditions can a glass be formed?, Contemp. Phys. 10 (1969) 473–488. https://doi.org/10.1080/00107516908204405.

[17] Z. Wojnarowska, A. Swiety-Pospiech, K. Grzybowska, L. Hawelek, M. Paluch, K.L. Ngai, Fundamentals of ionic conductivity relaxation gained from study of procaine hydrochloride and procainamide hydrochloride at ambient and elevated pressure., J. Chem. Phys. 136 (2012) 164507. https://doi.org/10.1063/1.4705274.

[18] F. Kremer, A. Scho nhals, Broadband Dielectric Spectroscopy; Eds.; Springer:

[19] R. Kohlrausch, Theorie des elektrischen Rückstandes in der Leidener Flasche, Ann. Phys. 167 (1854) 56–82. https://doi.org/https://doi.org/10.1002/andp.18541670103.

[20] G. Williams, D.C. Watts, Non-symmetrical dielectric relaxation behaviour arising from a simple empirical decay function, Trans. Faraday Soc. 66 (1970) 80–85. https://doi.org/10.1039/TF9706600080.

[21] M.T. Ottou Abe, N.T. Correia, L.-C. Valdes, J.M.B. Ndjaka, F. Affouard, Local molecular organizations of ibuprofen, flurbiprofen and ketoprofen in the liquid phase: Insights from molecular dynamics simulations, J. Mol. Liq. 205 (2015) 74–77. https://doi.org/https://doi.org/10.1016/j.molliq.2014.08.015.

[22] K. Adrjanowicz, K. Kaminski, M. Paluch, P. Wlodarczyk, K. Grzybowska, Z. Wojnarowska, L. Hawelek, W. Sawicki, P. Lepek, R. Lunio, Dielectric relaxation studies and dissolution behaviour of amorphous verapamil hydrochloride, J. Pharm. Sci. 99 (2010) 828–839.

[23] F. Pabst, J. Gabriel, P. Weigl, T. Blochowicz, Molecular dynamics of supercooled ionic liquids studied by light scattering and dielectric spectroscopy, Chem. Phys. 494 (2017) 103–110.

[24] C. A. Angell, Relaxation in liquids, polymers and plastic crystals - strong/fragile patterns and problems, J. Non. Cryst. Solids. 131 (1991) 13–31.

[25] Z. Wojnarowska, K. Grzybowska, L. Hawelek, A. Swiety-Pospiech, E. Masiewicz, M. Paluch, W. Sawicki, A. Chmielewska, P. Bujak, J. Markowski, Molecular Dynamics Studies on the Water Mixtures of Pharmaceutically Important Ionic Liquid Lidocaine HCl, Mol. Pharm. 9 (2012) 1250–1261. https://doi.org/10.1021/mp2005609.

[26] K. Adrjanowicz, M. Paluch, K. Ngai, Determining the structural relaxation times deep in the glassy state of the pharmaceutical Telmisartan, J. Phys. Condens. Matter. 22 (2010) 125902. https://doi.org/10.1088/0953-8984/22/12/125902.

[27] K.L. Ngai, Relation between some secondary relaxations and the α relaxations in glass-forming materials according to the coupling model, J. Chem. Phys. 109 (1998) 6982–6994. https://doi.org/10.1063/1.477334.

[28] Z. Wojnarowska, K. Kołodziejczyk, K.J. Paluch, L. Tajber, K. Grzybowska, K.L. Ngai, M. Paluch, Decoupling of conductivity relaxation from structural relaxation in protic ionic liquids and general properties, Phys. Chem. Chem. Phys. 15 (2013) 9205–9211.

[29] K.L. Ngai, Short-time and long-time relaxation dynamics of glass-forming substances: a coupling model perspective, J. Phys. Condens. Matter. 12 (2000) 6437–6451. https://doi.org/10.1088/0953-8984/12/29/316.

[30] S. Capaccioli, M. Paluch, D. Prevosto, L.-M. Wang, K.L. Ngai, Many-Body Nature of Relaxation Processes in Glass-Forming Systems, J. Phys. Chem. Lett. 3 (2012) 735–743. https://doi.org/10.1021/jz201634p.

[31] M.S. Thayyil, S. Capaccioli, D. Prevosto, K.L. Ngai, Is the Johari-Goldstein β-relaxation universal?, Philos. Mag. 88 (2008) 4007–4013. https://doi.org/10.1080/ 14786430802270082.

[32] K.L. Ngai, M. Paluch, Classification of secondary relaxation in glass-formers based on dynamic properties, J. Chem. Phys. 120 (2004) 857–873. https://doi.org/10.1063/1.1630295.

[33] K.L. Ngai, An extended coupling model description of the evolution of dynamics with time in supercooled liquids and ionic conductors, J. Phys. Condens. Matter. 15 (2003) S1107–S1125. https://doi.org/10.1088/0953-8984/15/11/332.

[34] S. Hensel-Bielowka, K.L. Ngai, A. Swiety-Pospiech, L. Hawelek, J. Knapik, W. Sawicki, M. Paluch, On the molecular origin of secondary relaxations in amorphous protic ionic conductor chlorpromazine hydrochloride - High

pressure dielectric studies, J. Non. Cryst. Solids. 407 (2015) 81–87. https://doi.org/https://doi.org/10.1016/j.jnoncrysol.2014.08.005.

[35] S.N. Tripathy, Z. Wojnarowska, J. Knapik, H. Shirota, R. Biswas, M. Paluch, Glass transition dynamics and conductivity scaling in ionic deep eutectic solvents: The case of (acetamide + lithium nitrate/sodium thiocyanate) melts, J. Chem. Phys. 142 (2015) 184504. https://doi.org/10.1063/1.4919946.

[36] Z. Wojnarowska, C.M. Roland, A. Swiety-Pospiech, K. Grzybowska, M. Paluch, Anomalous Electrical Conductivity Behaviour at Elevated Pressure in the Protic Ionic Liquid Procainamide Hydrochloride, Phys. Rev. Lett. 108 (2012) 15701. https://doi.org/10.1103/PhysRevLett.108.015701.

[37] A. Swiety-Pospiech, Z. Wojnarowska, S. Hensel-Bielowka, J. Pionteck, M. Paluch, Effect of pressure on decoupling of ionic conductivity from structural relaxation in hydrated protic ionic liquid, lidocaine HCl, J. Chem. Phys. 138 (2013) 204502. https://doi.org/10.1063/1.4807487.

[38] G. Williams, D.C. Watts, Non-symmetrical dielectric relaxation behaviour arising from a simple empirical decay function, Trans. Faraday Soc. 66 (1970) 80–85. https://doi.org/10.1039/TF9706600080.

[39] S L Shamblin, B C Hancock, Y Dupuis, M J, M.J. Pikal, Interpretation of relaxation time constants for amorphous pharmaceutical systems., J.Pharm.Sci. 89(2000) 417–427.

[40] H. Weingärtner, A. Knocks, S. Boresch, P. Höchtl, O. Steinhauser, Dielectric spectroscopy in aqueous solutions of oligosaccharides: Experiment meets simulation, J. Chem. Phys. 115 (2001) 1463–1472. https://doi.org/10.1063/1.1380205.

[41] P. Wlodarczyk, M. Paluch, Z. Wojnarowska, L. Hawelek, K. Kaminski, J. Pilch, Theoretical and experimental studies on the internal mobility of two sulfonylurea agents: Glibenclamide and glimepiride, J. Phys. Condens. Matter. 23 (2011) 425901. https://doi.org/10.1088/0953-8984/23/42/425901.

CHAPTER 6

MOLECULAR DYNAMICS IN THE SUPERCOOLED LIQUID AND GLASSY STATES OF PIROXICAM

6.1 Introduction

The dynamics of glass-forming liquids and glass transformation is currently considered to be a significant unresolved problem in condensed matter physics and physical chemistry[1]. Experimental and theoretical attempts in the past few decades have made some strides but a solution to the problem is still needed. The existence of a variety of glass-formers with widely varying chemical compositions and physical structures, which give rise to diverse thermodynamic and dynamic properties to be reckoned with, adds to the complexity of solving the issue. These diverse properties, on the other hand, are useful in a variety of applications, including ionic liquids, amorphous pharmaceuticals, biomolecules, biopolymers, metallic glasses, colloids, and so on. The study mentioned in this paper is an example of how the synergy between basic research and research into the applications of glass-formers propels further studies of novel materials. The glass-former under investigation is piroxicam, a pharmaceutical showing both dipolar and conductivity relaxations. The research community is interested in the molecular dynamics of glass-forming materials that demonstrate not only the structural relaxation responsible for glass transition and viscous flow but also the ionic conductivity relaxation. The two corresponding research groups are currently interested in the properties of the two types of relaxation. Any relationship between the two relaxations, if discovered, would greatly improve our fundamental understanding of the dynamics.

From the pharmaceutical industry's point of view, despite several advantages from the amorphous pharmaceuticals, an important challenge is the recrystallization of amorphous pharmaceuticals during storage. This study will help to identify the factors that govern devitrification in amorphous piroxicam which provide insights to the pharmaceutical research community. Even though the molecular relaxations responsible for crystallization vary from case to case, the molecular motion responsible for secondary relaxation is one of the governing factors for recrystallization in many amorphous pharmaceuticals. Therefore, understanding both the secondary dipolar and conductivity relaxations and their connection to the structural relaxations are necessary. The electric modulus is a more appropriate representation of the conductivity relaxation data particularly in glass-formers where the structural relaxation is masked by dc conductivity[2]. Modulus representation of the dielectric data instead of permittivity

representation is suitable for the analysis of samples having high conductivity and electrode polarization contributions. Modulus is a conceptually straightforward method for measuring the orientational polarization and ionic conductivity[3].

In this study, a comprehensive analysis of the molecular dynamics of an amorphous drug that exhibits conductivity relaxation as well as structural relaxation is performed which will help us to understand more about the glass transition phenomenon. Any relation between these two relaxations if found in such glass formers would significantly enhance the fundamental understanding of glassy dynamics and is of particular interest to the research community. With this in mind, we investigated piroxicam, an ionically conducting glass-former that is also a pharmaceutical used for the treatment of debilitating inflammatory conditions such as inflammation, musculoskeletal disorders, and dystonia. Piroxicam is a poorly water-soluble drug of the Oxicam class[4]. The water solubility of piroxicam is very low which is reported to be 0.0076mg/ml and is a Class II drug with low solubility and high permeability, according to the biopharmaceutics Drug Classification Scheme [5].

A complete picture of molecular relaxations of the amorphous state using differential scanning calorimetry (DSC) and broadband dielectric spectroscopy (BDS) in the supercooled liquid and glassy states of piroxicam `is discussed in this chapter. These experiments help us to assess the glass-forming ability and dynamic properties of the primary α relaxation and the secondary dipolar and conductivity relaxations, and the interconnection between the molecular rotation and translation. Quantum computational calculations were also done in the theoretical framework of density functional theory (DFT) calculations to complement the experimental results.

6.2 Experimental section

6.2.1 Materials

Piroxicam (crystalline powder) having a molecular weight of 331.34 g/mol, was purchased from Sigma Aldrich with 99.8% purity. Piroxicam is a nonsteroidal anti-inflammatory drug (NSAID) of the oxicam group used to treat osteoarthritis and rheumatoid arthritis. Piroxicam is a Class 2 drug, characterized by low solubility – high permeability, 23 mg/L (at 22°C) melting temperature is 198-200°C. The molecular formula of Piroxicam is $C_{15}H_{13}N_3O_4S$ and molecular weight is 331.346 g/mol. IUPAC

name is given by 4-hydroxy-2-methyl-1,1-dioxo-N-pyridine-2-yl-1λ6,2-benzothiazine-3-carboxamide. The chemical structure of piroxicam is shown in figure 6.1.

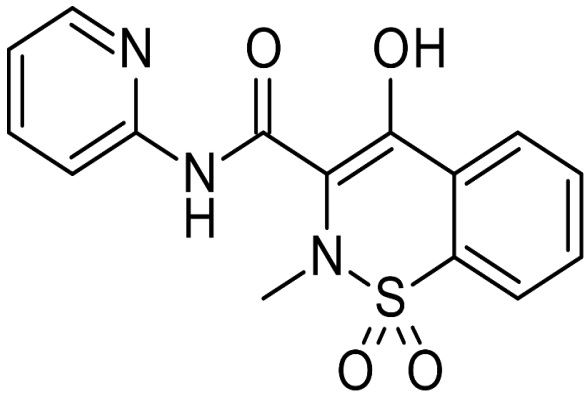

Figure 6.1 Molecular geometry of piroxicam

6.2.2 Methods

6.2.2.1 Differential scanning calorimetry

Differential scanning calorimetric analysis of piroxicam was done using DSC 4000 (PerkinElmer Life and Analytical Sciences, MA) and was calibrated using indium. The sample (5mg) was placed inside the sealed aluminum pan weighing 25 mg and was heated from room temperature to 5K above the melting temperature at the heating rate of 10°C/min. Subsequently, the sample was cooled to room temperature at a cooling rate of 10°C/min. The quench-cooled sample was again heated at the heating rate of 10°C/min.

6.2.2.2 Broadband dielectric spectroscopy

Isobaric measurements of the dielectric permittivity $\varepsilon^*(\omega) = \varepsilon'(\omega) - i\varepsilon''(\omega)$ were carried out using the Alpha analyzer (Novo-Control Technologies) over the frequency range from 1×10^{-2} to 1×10^{7}Hz at ambient pressure. Each of the tested samples was placed between two stainless steel electrodes (Cylindrical shape, diameter 30 mm, gap 0.2 mm) and mounted on a cryostat maintained under dry nitrogen gas flow. Two poly Tetra Fluoro Ethylene strips were placed on the lower side of the crystalline sample. These strips prevent direct contact between the upper and lower electrodes when the sample is in the molten state and ensured constant thickness of the molten sample throughout the experiment. The temperature was controlled by Quatro System using a Nitrogen gas cryostat, with stability better than 0.1 K. Dielectric measurements were performed after its vitrification by heating the samples to the temperature of T_m+5K,

and held for 10 minutes, then quench cooling the melt of the samples at 10K/min to 123.15K. The sample showed no sign of crystallization while cooling from the melting temperature. The dielectric measurements were taken from 123.15K to a few degrees below melting temperature in different steps of increase in temperature. The fresh amorphous sample is prepared by quench cooling each time and the BDS instrument is calibrated by an empty cell. The dielectric data is fitted with winfit software provided by Novocontrol technologies. The temperature scan dielectric measurements during quench cooling the melted sample to 123.15K, helps to understand the presence of various relaxation processes and the extent of dc conductivity in the supercooled liquid and glassy states of the samples. The presence of dielectric relaxation processes is characterized by a peak in the imaginary part of the dielectric constant at a temperature for a given frequency. The structural relaxation causes a larger peak than the secondary relaxation in the dielectric loss and dielectric permittivity graphs in the temperature scan.

6.2.2.3 Density functional theory

The optimized molecular geometry of piroxicam was obtained using DFT using the Gaussian 09 package with GaussView05 as the visualization package[6]. The initial geometry was obtained from the PubChem database[7] and optimized with the B3LYP/6-311++G (d,p) level of theory. The origin of local molecular motions below Tg was identified by quantum computational simulations of the side chain rotation in piroxicam molecule by relaxed dihedral scan corresponding to different molecular subgroups[8]. The experimental FTIR spectrum is also compared with theoretical spectra and verified the optimized structure of piroxicam.

6.2.2.4 FTIR Spectroscopy

Vibrational analysis (50-4000 cm−1) of the title compounds in both crystalline and glassy samples was done using JASCO FTIR 4100 instrument. The samples were pelletized using KBr.

6.3 Results and discussion

6.3.1 Differential scanning calorimetry

DSC thermogram of piroxicam is shown in figure 6.2 showing well-resolved melting, crystallization, and glass transition process. The melting endotherm refers to the part of the DSC curve that deviates from the baseline before returning to it. Melting is a physical process that causes a substance's phase transition from solid to liquid. This happens as the solid's internal energy rises, usually due to the application of heat, which raises the temperature of the material to the melting point. When using DSC, the sample gradually reaches its melting temperature as the temperature rises (T_m). The DSC curve shows an endothermic peak as a result of the melting process. The melting temperature of piroxicam was found to be 474K which is close to the reported value and the value of T_g was found to be 334K which is higher than the room temperature. The crystallization temperature of piroxicam was found to be 401K and hence the difference between T_g and T_c is 88K which suggests that amorphous piroxicam will be stable under optimum storage conditions. The temperature gap between T_g and T_c of a glass-forming system varies inversely with the crystallization tendency hence hints about the stability of the amorphous phase [9,10]. According to Kauzman [10] and Turnbull [11], the ratio T_g/T_m can give lights to the glass-forming ability of material, and good glass former shows a value greater than 2/3. The ratio, which gave a value of 1.41 for piroxicam which hints at the good glass-forming ability of piroxicam[12,13].

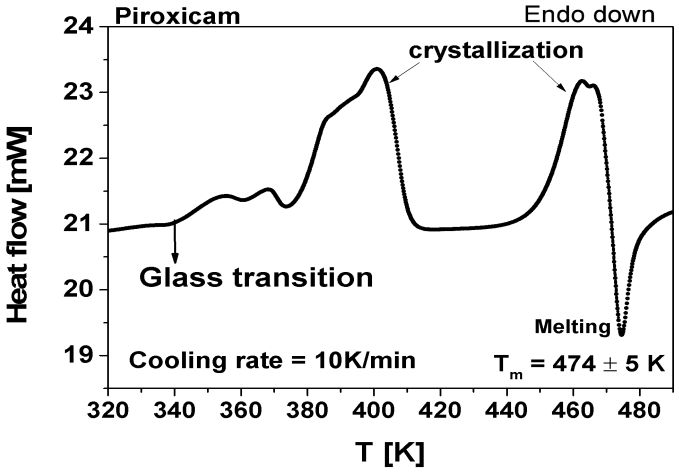

Figure 6.2 DSC curve of piroxicam on cooling showing melting, crystallization and glass transition phenomena

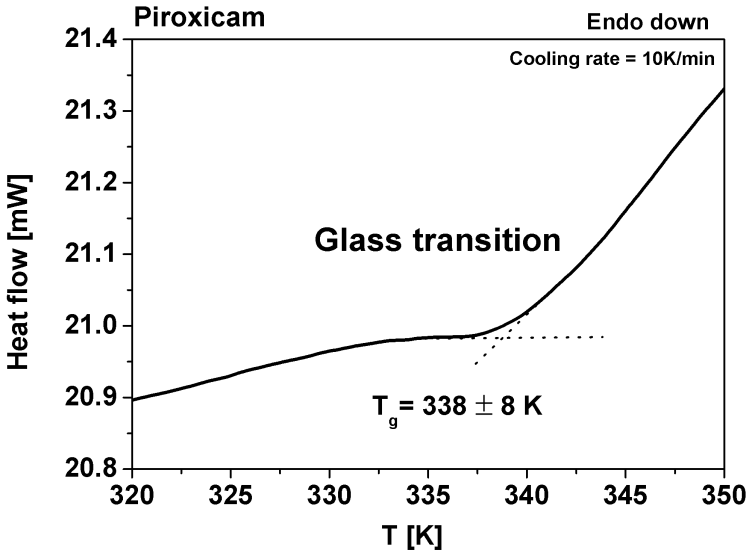

Figure 6.2.b DSC curve of piroxicam on cooling showing melting, crystallization and glass transition phenomena

DSC thermogram shows an endothermic peak corresponding to melting in the range of 473 to 479K, with a sharp peak at 474K. Two crystallization peaks are observed which may be due to polymorphism. Crystallization in piroxicam was found to occur at 400K and 460K. The glass transition phenomenon is seen as an endothermic peak around a temperature of 334K and the glass transition temperature T_g is taken as the onset of the endotherm as 334 ± 10K.

6.3.2 Broadband dielectric spectroscopy

In the present study, we focused our attention on piroxicam to explore the dielectric relaxations in its supercooled liquid and glassy states in permittivity representation to characterize the significant parameters associated with the glass transition phenomena and to address ways to suppress instability of the amorphous phase.

6.3.2.1 Quench cooling

To get preliminary information about the glass formation and the chances of crystallization during quench cooling, we have acquired isochronal permittivity data at three-four test frequencies of piroxicam and the response has been shown in figures 6.3.

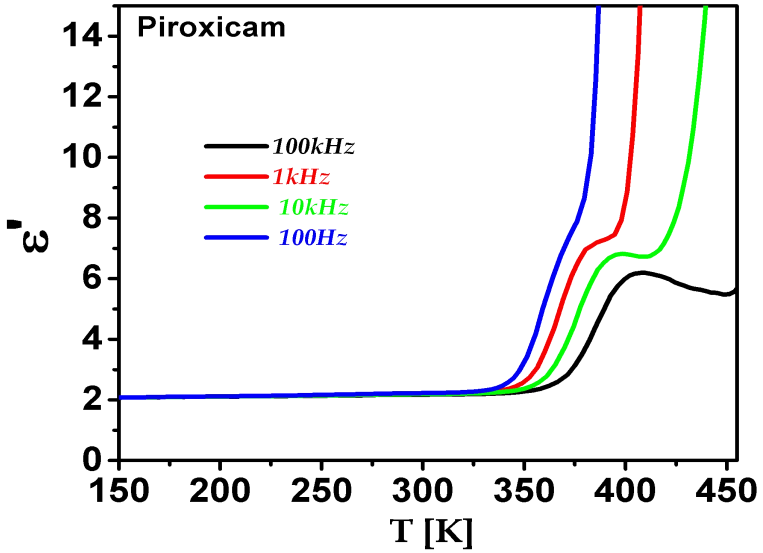

Figure 6.3 Temperature dependence of dielectric permittivity of piroxicam from a deep glassy state to the supercooled liquid state

The temperature dependence of dielectric loss curves of piroxicam during quench cooling the melt is shown in Fig. 6.3 showing a gradual increase of the real part of dielectric permittivity followed by a sharp decrease across the glass transition region without any indications of crystallization is observed denoting glass formation like a typical glass former.

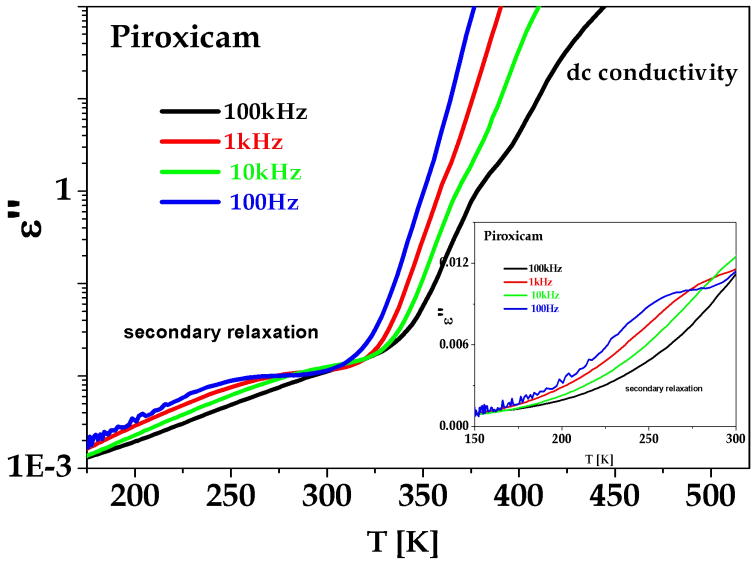

Figure 6.4 Temperature dependence of dielectric loss of piroxicam from deep glassy state to the supercooled liquid state. Secondary relaxation is shown in the inset

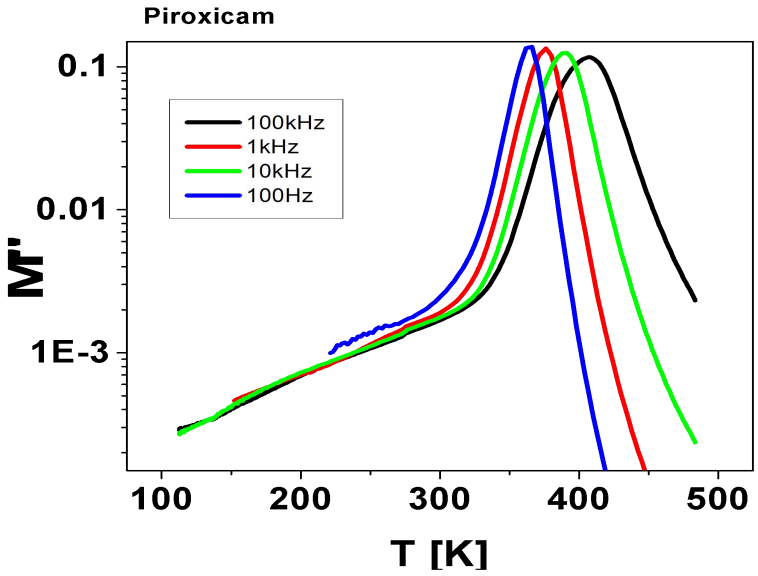

Figure 6.5 Temperature dependence of imaginary part of the dielectric modulus of piroxicam on quench cooling the melt to the glassy state

Further, the presence of a secondary relaxation in piroxicam is seen from the imaginary part of permittivity shown in figure 6.4 in the lower temperature region. There is a rapid increase in the dielectric loss in higher temperature regions due to dc conductivity. Figure 6.5 shows the temperature dependence of the imaginary part of the dielectric modulus where conductivity relaxation is observed in the higher temperature region.

6.3.2.2 Supercooled liquid state

The molecular mobility of piroxicam in the glassy and supercooled liquid states was crucial to characterize the molecular dynamics. The dielectric measurements of piroxicam at ambient pressure were taken from the deep glassy state (133K) to temperatures near the melting point (473 K) in a wide frequency range from 10^{-2} to 10^{7} Hz.

Figure 6.6 present the real part of the complex dielectric spectra for piroxicam obtained on heating the sample from the glassy state to the supercooled liquid state from 328K to 460K in different temperature steps for sake of clarity, which shows that dc conductivity contribution is dominated over structural relaxation which is also seen in figure 6.4.

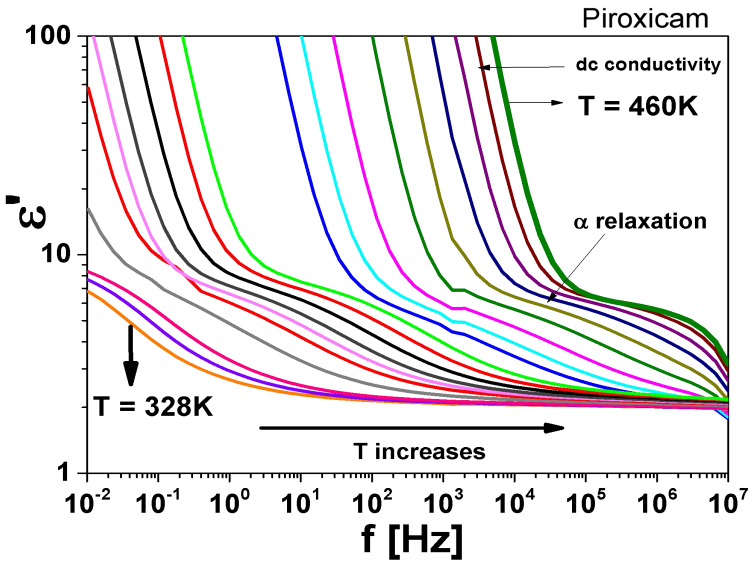

Figure 6.6 Real part of the complex dielectric permittivity spectra of piroxicam below and above T_g

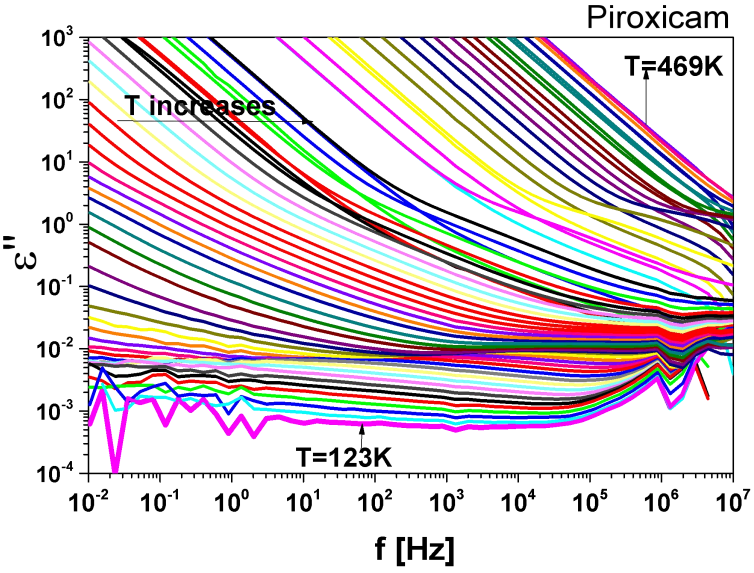

Figure 6.7 Dielectric loss spectra of piroxicam above and below T_g

Figure 6.7 shows the imaginary part of the complex dielectric spectrum from 123K to 469K. The spectra for all temperatures above T_g were dominated by conductivity relaxation making the structural relaxation in the dielectric permittivity formalism unresolved. Even though the dielectric measurements can be represented by different frequency-dependent complex quantities like the permittivity, and the electric modulus, all of them are equivalent. In such situations, the electric modulus is a more appropriate representation of the conductivity relaxation data particularly in glass-formers where the structural relaxation is masked by dc conductivity [14,15]. Complex

dielectric permittivity ε*(f) represents the relaxation of the electric displacement vector D at the constant electric field, while, the modulus M*(f) represents the relaxation of the electric field E at constant displacement vector D.

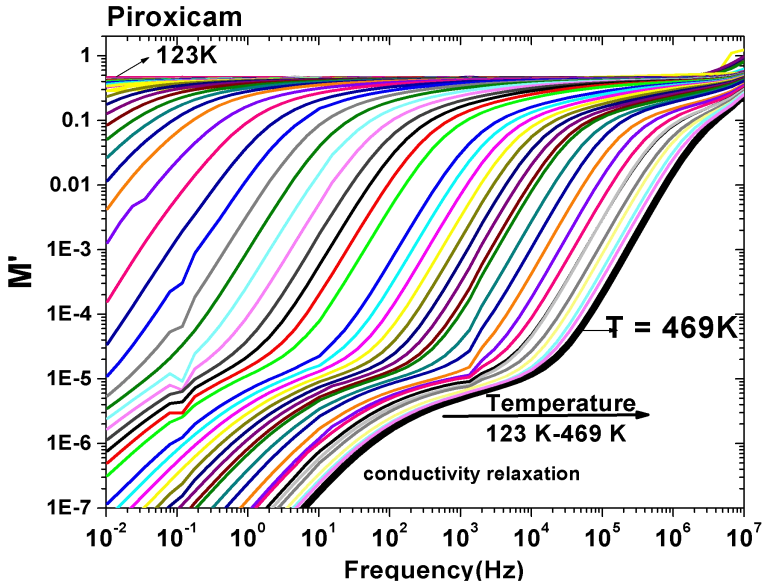

Figure 6.8 Real part of the complex dielectric modulus spectra of piroxicam above T_g

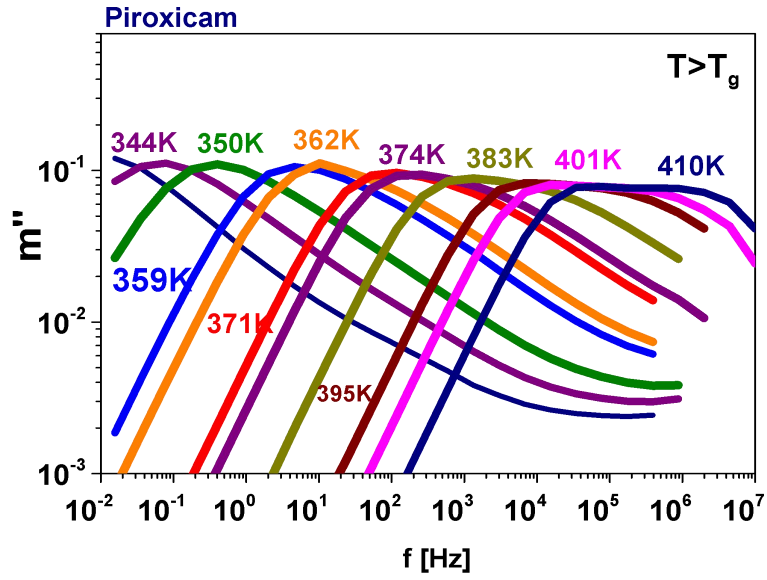

Figure 6.9 Imaginary part of the complex dielectric modulus spectra of piroxicam from 344K to 410K (T> T_g)

Fig 6.8 shows the real part of modulus spectra of piroxicam in the temperature range 123K to 469K showing well resolved primary and secondary conductivity relaxations. As temperature increases, the curves shift to higher frequency regions due to an increase in global mobility.

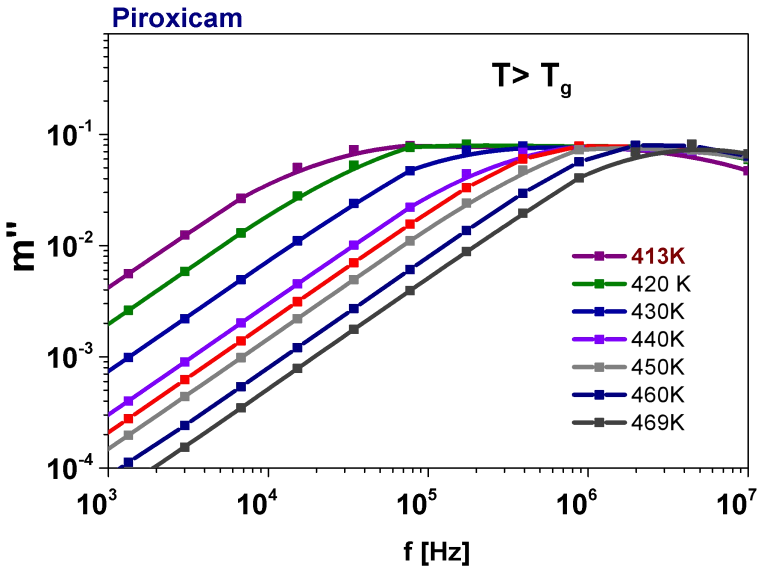

Figure 6.10 Imaginary part of the complex dielectric modulus spectra of piroxicam 413K to 469K (T> T_g)

The imaginary part of the dielectric modulus spectra of piroxicam in the supercooled liquid state is shown in figures 6.9 and 6.10, showing conductivity structural relaxation (σ_α process). The dielectric loss peak shifts to a higher frequency with an increase of temperature as seen in figure 6.8 indicating decreasing time scale of global mobility.

6.3.2.3 Glassy state

The real part of the complex dielectric constant spectra of piroxicam in the glassy state (T < T_g) is shown in figure 6.11 showing a small change in dielectric permittivity which corresponds to the secondary relaxation. As the dielectric strength of secondary relaxation is smaller than that of the α process, the presence of secondary relaxation in piroxicam is confirmed by the small change in dielectric permittivity in figure 6.11 in the temperature range of 123K to 319K.

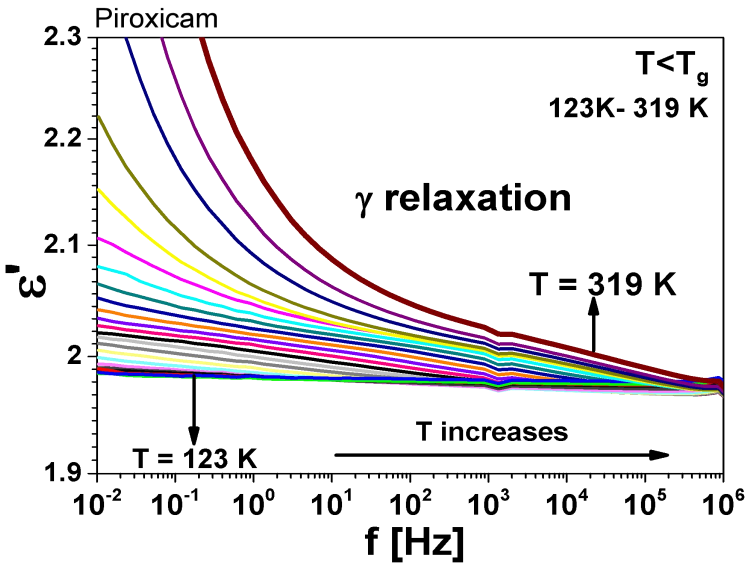

Figure 6.11 Real part of the complex dielectric spectra below T_g in piroxicam

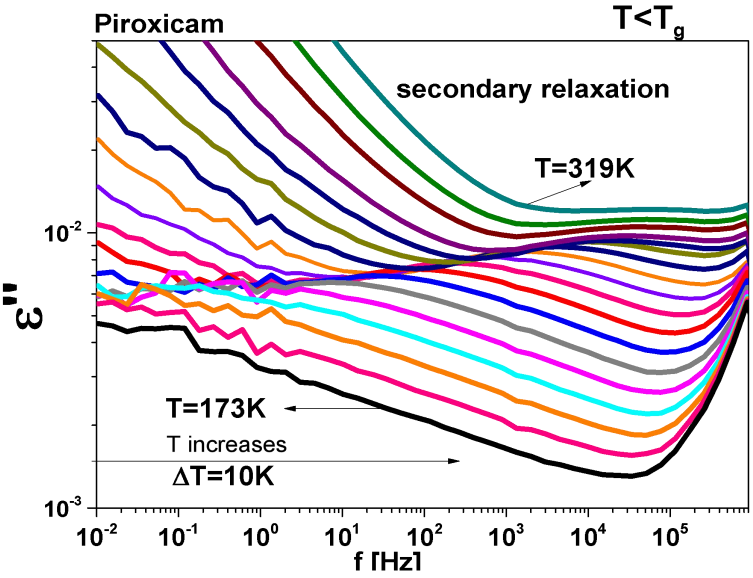

Figure 6.12 Dielectric loss spectra of piroxicam in the glassy state

The dielectric loss spectrum (imaginary part of the complex dielectric permittivity) of piroxicam in the deep glassy state from 173K to 319K is shown in figure 6.12 which shows the dielectric data on heating from 173K in steps of 10K showing resolved secondary relaxation. To find any correlation between conductivity relaxation and dipolar relaxation in the glassy state the imaginary part of the dielectric modulus spectra from 173K to 319K is shown in figure 6.13.

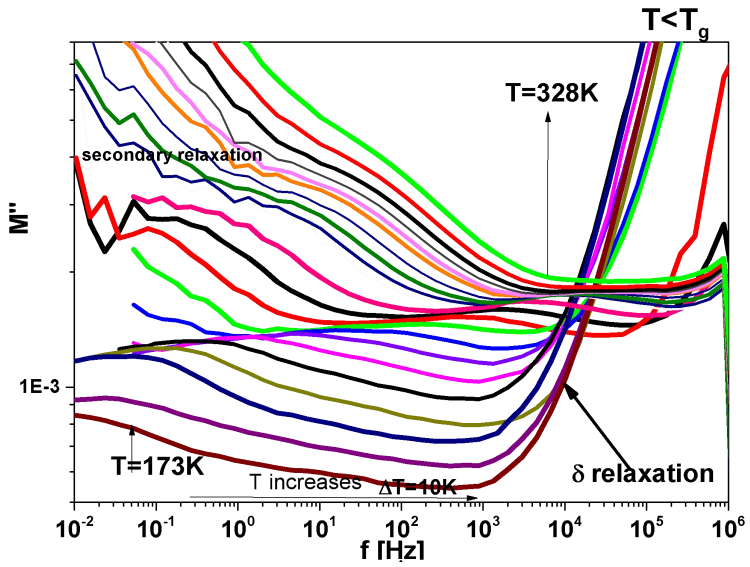

Figure 6.13 Imaginary part of the dielectric modulus spectrum of piroxicam in the glassy state

From figures 6.12 and 6.13, it is interesting to note that for a given frequency, the temperature at which the peak due to secondary relaxation in piroxicam occurs is similar in both the dielectric loss graph and modulus representation. Below T_g, as the structural relaxation by dielectric representation is well resolved, the measured complex dielectric permittivity data is fitted to the Havriliak-Negami equation while above T_g, the measured dielectric modulus data measured is fitted with the Havriliak-Negami function as given below and from the fit parameters we obtained the molecular relaxation time and α-conductivity relaxation time. For the sake of clarity, the results and discussion of BDS are shown in two parts, one in the supercooled liquid state ($T>T_g$) and the second in the glassy state ($T < T_g$).

$$\mathbf{M^*(\omega) = M'(\omega) + iM''(\omega) = \frac{1}{\varepsilon^*(\omega)} = M_\alpha + \frac{\Delta M}{(1 + (-i(\omega\tau_{\sigma\alpha})^{-1})^\alpha)^\beta}} \quad (6.1)$$

From the HN fit parameters, the relaxation times below T_g from the modulus and the dielectric representation were similar. The modulus representation and the dielectric loss representation below T_g shown in Figures 6.11 and 6.12 correspond to the same process, which is due to a translational rotational coupling which is also observed in other glass formers[16,17].

6.3.2.4 Temperature dependence of relaxation time

Relaxation map showing temperature dependence (1000/T) of molecular relaxation time of α and secondary relaxations of piroxicam are shown in figure 6.13. The glass transition temperature of piroxicam (T_g) is calculated from the relaxation map at the temperature at which the α relaxation time τ_α = 100 s and is found to be 329K which is close to the T_g determined by DSC. The α process in the Arrhenius diagram obeys curved or non-Arrhenius temperature dependence which is normally observed in a typical glass former, and the secondary γ process shows Arrhenius behaviour (linear temperature dependence).

The Vogel–Tammann–Fulcher (VTF) equation is used to describe the non-Arrhenius version of fragility. The temperature dependence of structural relaxation (σ_α) process was fitted by the Vogel-Fulcher-Tamann (VFT) equation (6.2).

$$\boldsymbol{\tau(T) = \tau_0 \exp\left(\frac{B}{T - T_0}\right) = \tau_0 \exp\left(\frac{DT_0}{T - T_0}\right)} \qquad (6.2)$$

where T is absolute temperature, D is the strength parameter and T_0 is the Vogel temperature and are positive constants.

From the relaxation map shown in fig 6.13, it is evident that the secondary relaxation process below T_g has Arrhenius type of temperature dependence. So, it is fitted with the Arrhenius equation. Above glass transition temperature the plot is nonlinear and it can be fitted with Vogel- Fulcher-Tamann equation. The temperature dependence of secndary relaxation is fitted with the Arrhenius equation. The activation energy of secondary relaxation was calculated by the Arrhenius equation given by equation 6.3,

$$\boldsymbol{\tau(T) = \tau_\infty \exp\left(\frac{E_a}{RT}\right)} \qquad (6.3)$$

The activation energy of the secondary processes in piroxicam was determined to be as 25 kJ/ mol and 61 kJ/mol. The glass transition temperature from VFT fitting is 327.9K which is in agreement with the DSC result.

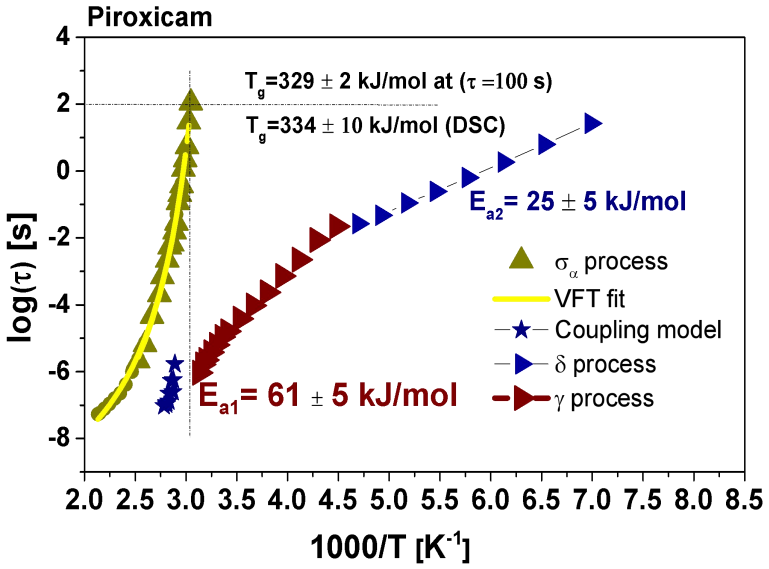

Figure 6.14 Relaxation map of piroxicam

From the VFT fit, the value of T_g is calculated to be 327.9K. The value of T_g is above the room temperature thereby enabling easy safe storage of amorphous state. The VFT fit parameters are shown in Table 6.1.

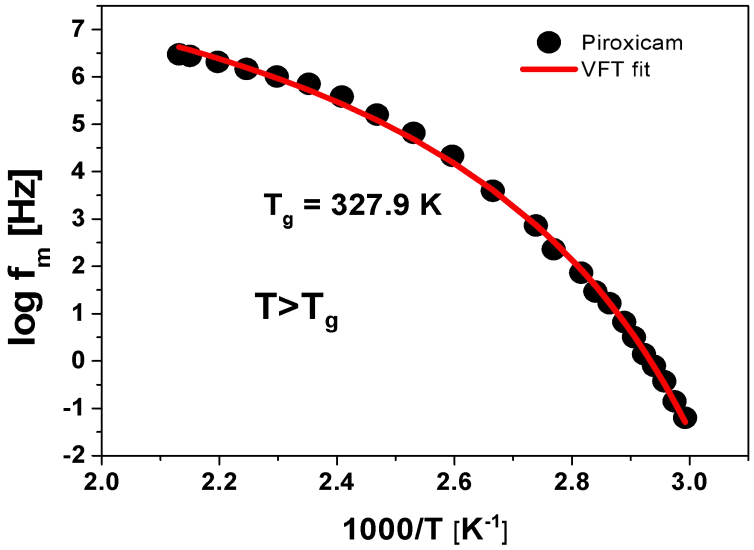

Figure 6.15 VFT fit of relaxation map of piroxicam ($T>T_g$)

Table 6.1 VFT fit parameters of piroxicam

Primitive relaxation frequency f_0	Strength parameter D	Vogel temperature T_0	Glass transition temperature T_g	Fragility m	Activation energy of secondary relaxation E_a
3.46 x 10^9 Hz	4.36	284.3	327.9 K	92.6	61 ± 2 25 ± 2

The value of T_0 was obtained as 284.3 K. The temperature T_0 is often referred to as the Kauzmann temperature T_K, a hypothetical temperature where configurational entropy of supercooled liquid would be equal to the entropy of the crystal and molecular mobility would reduce to the same level as that of the crystal (strictly speaking the molecular mobility is not zero). For most of the glassy systems, it lies between 50 and 70 K, below T_g and it is sufficient to ensure safe storage. The value of T_g obtained by VFT fit is approximately closer to the value of T_g obtained by DSC. Since the value of T_g is higher than room temperature, and the difference between T_g and crystallization temperature is 67K, it suggests that the amorphous piroxicam will be stable in the ambient storage conditions. The strength parameter D and fragility values of piroxicam correspond to intermediate fragility.

6.3.2.5 Fragility

This index represents the temperature sensitivity of the relaxation time of the primary process. It is remarkable that the fragility index is the center of attention and one of the most discussed parameters in current glass transition research. Fragility index is a measure of rapidity with which the ordering happens in the amorphous glassy phase and is disrupted on reheating. It represents the rate at which molecular motion is arrested when the amorphous glassy state is reached. The different $\tau(T, P)$ dependencies of the melt and crystal states can also be discussed in terms of the "fragility plot" [18,19]where the relaxation times are plotted as a function of reduced temperature. This representation for the lower members of the series has shown a systematic dependence of the "steepness index "and thus of the fragility on the length of the alkyl side chain. The "fragility or steepness index" [20] is defined as

$$m = \left. \frac{d(\log \tau_{max})}{d\left(\frac{T_g}{T}\right)} \right| at\ T \approx T_g \tag{6.4}$$

Glass transition temperature T_g is defined as the temperature corresponding to a relaxation time of 100 s and is used here. Strong systems have fragility of less than 40 and fragile systems have fragility greater than 75. Fragile glass formers are physically unstable compared with the strong ones. Fragility "m" in the case of piroxicam was estimated as 92 from VFT fit and hence piroxicam is intermediately fragile glass former[21]. This value is comparable to that found in recent studies of other amorphous pharmaceuticals, such as telmisartan, [22] (m = 87) indomethacin (m = 83)[23], or verapamil hydrochloride (m = 88)[24] . It should be noted that the fragility index (and thus the relaxation time) can be misinterpreted at times [25].

The most famous depiction of the dynamic fragility of glass-forming liquids is the Angell plot. The increase in the relaxation timescale of supercooled liquids is notable not only for a large number of decades involved but also for the temperature dependence. It comes in handy when it comes to classifying supercooled liquids. Depending on its position in the Angell plot, a liquid is labeled as strong or fragile. Strong glass-formers and an Arrhenius behaviour are represented by straight lines. In this case, the plot can be used to derive effective activation energy, implying a relatively simple relaxation mechanism involving the breaking of a chemical bond locally. The energy barrier to activate this process then dominates the typical relaxation time, resulting in an Arrhenius behaviour. This category includes window glasses. When using the slope of the curve in Fig. 6.13 to determine effective activation energy for fragile glass-formers, one discovers that this energy scale increases as the temperature decreases.

Normally, the Angell plot shows the data as the logarithm of the zero-shear rate viscosity versus T_g /T in a reduced Arrhenius plot. Although Angell was not the first to create such a plot, he was the first to use it extensively and to suggest that dynamic fragility and thermodynamic fragility could be related. As a result, the Angell plot has become a common way to depict the viscosity's temperature dependence. Furthermore, the nonexponentiality of the structural relaxation function, the chemical structure of polymers, structural recovery in the glassy state, and vibrational motions have all been

linked to dynamic fragility. The deviation of molecular mobility from the Arrhenius nature at Tg is determined from the Angel plot (log (τ) –Tg/T plot) whose value of the slope at T=Tg is equal to the fragility (m)[68] and is shown in figure 6.16. The fragility of piroxicam falls in the range of fragile glass systems. [26].

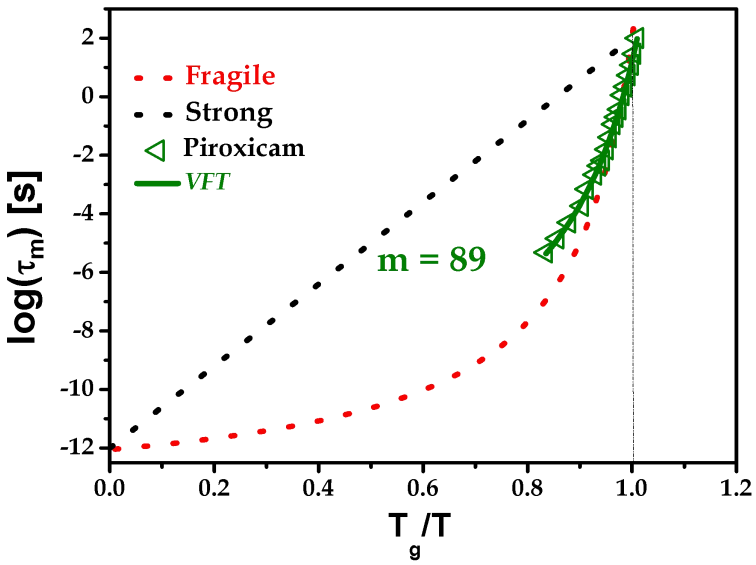

Figure 6.16 Angel plot of piroxicam

6.3.2.6 Kohlraush-William-Watts (KWW) fit

The Kohlraush-William-Watts (KWW) function[27,28] describes the non-exponential behaviour of dielectric relaxation and is used to find the asymmetrical stretching parameter β_{KWW} which measures the asymmetric distribution of relaxation time and its deviation from Debye relaxation (β_{KWW}=1). The breadth of the structural relaxation peak was described using the stretching parameter β_{KWW} ($0 < \beta_{KWW} \leq 1$) which can be determined by fitting the α-peak in the frequency domain by the one-sided Fourier transform of the KWW function. Kohlrausch-Williams-Watts's function is given by

$$\boldsymbol{\phi(t) = \exp\left(-\frac{t}{\tau_{\sigma\alpha}}\right)^{\beta_{KWW}}} \qquad (6.5)$$

Where $\phi(t)$ is the relaxation function, $\tau_{\sigma\alpha}$ is the conductivity relaxation time and β_{KWW} is the stretched exponential parameter and is related to the distribution of molecular relaxation times and is a relevant criterion in predicting the safe shelf life of amorphous pharmaceuticals.

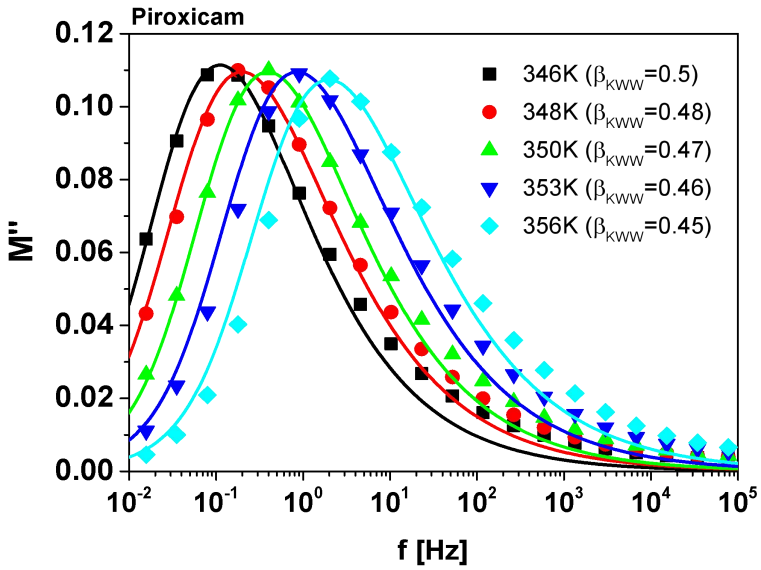

Figure 6.17 KWW fits of piroxicam ($T > T_g$)

From figure 6.17, the value of the fractional exponent of the KWW function at 346K is found to be 0.5. Since the β_{KWW} value is also a measure of the distribution of relaxation time, piroxicam has an above intermediate distribution of conductivity relaxation times. A visualization of the temperature dependence of conductivity loss peaks is done by master plot analysis after normalizing the peak heights uniformly to unity and is shown in figure 6.18. It is based on the horizontal shifting of the spectra taken at various temperatures above T_g to superimpose them onto a spectrum at 346K following frequency temperature superposition rules. The full width at half maximum of the conductivity loss peak is found to increase with the increase in temperature in piroxicam.

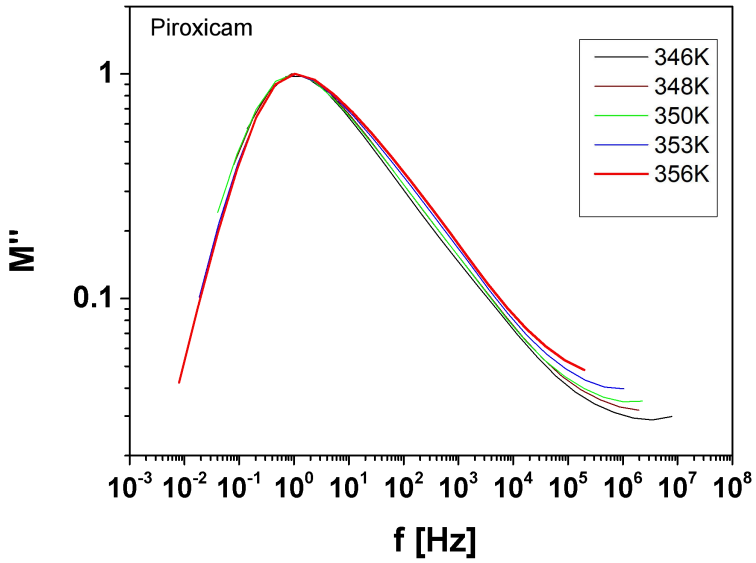

Figure 6.18 Master plot of piroxicam T=346K is taken as origin

A visualization of the temperature dependence of conductivity loss peaks is done by master plot analysis after normalizing the peak heights uniformly to unity and is shown in figure 6.18. It is based on the horizontal shifting of the spectra taken at various temperatures above T_g to superimpose them onto a spectrum at 343K under frequency-temperature superposition rules. The full width at half maximum of the conductivity loss peak is found to increase with the increase in temperature in piroxicam as seen in figure 6.18. Furthermore, it has been demonstrated that the KWW parameter, which describes the distribution of molecular motions, can be used to predict the life expectancy of amorphous pharmaceuticals. A narrow structural relaxation distribution, i.e., high KWW values, would indicate a low proclivity for amorphous API to crystallize. A larger distribution of α -relaxation times, on the other hand, could indicate faster localized molecular motions, leading to a greater tendency toward crystal nucleation[29]. We used the one-sided Fourier transform of the Kohlrausch-Williams-Watts (KWW) function [28] to check the importance of this parameter in our scheme. The stretching parameter KWW decreases from β_{KWW} decreases from 0.5 in 346K to 0.45 in 356K over the temperature range studied. In the supercooled liquid state of piroxicam, the distribution of relaxation times is asymmetric and far broader than in a classical Debye type process (β_{KWW} =1) which suggests the instability nature of amorphous piroxicam.

6.3.2.7 Nature of secondary relaxation : Coupling model

Two well-resolved secondary relaxations were observed in the glassy state of piroxicam having activation energies 61 and 25 kJ/mol. The relaxation time of the secondary relaxations observed in the glassy state of piroxicam in the modulus representation and the dielectric permittivity representation matches perfectly and is evident from figures 6.13. This type of behaviour was reported in some glass formers [1,30] and was found to be the presence of coupling between the translation and rotation of the molecules resulting in equivalent conductivity and dipolar relaxation times. The conductivity and dipolar relaxation simultaneously observed in the glassy state of piroxicam gives an idea about the nature of the conductivity α relaxation. The secondary conductivity relaxation is the precursor of the observed conductivity α relaxation like Johari-Goldstein β relaxation is the precursor of structural α relaxation[31].

However, the possibility of an intramolecular secondary relaxation due to the presence of a dihedral side chain with amine groups cannot be excluded. To resolve the issue and confirm the presence of the secondary conductivity relaxation, we used the Coupling Model (CM). Originally, the CM was applied to secondary relaxations having properties strongly connected to the structural α-relaxation. The existence and universal presence of this kind of secondary relaxation called the Johari–Goldstein (JG) β-relaxation, was suggested by its analogy to the primitive relaxation of the CM, which started in a paper in 1998[32], and has since been extensively developed [33–36].

To confirm the presence of the secondary conductivity relaxation and to find the origin of the observed dipolar secondary relaxation, i.e. whether it is JG type or non-JG type coupling model [37,38] has been applied. The coupling model accounts for the intermolecular coupling effects like the many-body dynamics and dynamic heterogeneity considering other contributions in mind as caging effect and configurational entropy. The coupling model describes the existence of a crossover time t_c, at times shorter than this t_c, (2 ps for molecular liquids) the molecules relax independently and has a normalized correlation function of the exponential form shown in equation 6.6.

$$\phi(t) = \exp\left(-\frac{t}{t_0}\right) \quad t < t_c \tag{6.6}$$

The primitive relaxation time is given by the equation according to Coupling model is given in equation 6.7

$$\tau_{JG}(T) \approx \tau_0(T) = (t_c)^{n} (\tau_\alpha(T))^{1-n} \tag{6.7}$$

where t_c is equal to 2ps for molecular glass formers and ($n = 1- \beta_{KWW}$) is the coupling parameter. Although similar, the JG b-relaxation and the primitive relaxation are not identical processes, and hence their relaxation times, $\tau_{JG}(T)$ and $\tau_0(T)$, are not necessarily equal. Only approximate correspondence between their orders of magnitude can be expected or predicted, thus $\tau_{JG}(T)$ calculated using the CM equation provides an order of magnitude estimate of $\tau_{JG}(T)$ to compare with its experimental value.

The nature of the origin of a secondary relaxation, whether is it a JG relaxation is particularly relevant to the MD of amorphous pharmaceuticals as the intermolecular JG β-relaxation can be the precursor of α relaxation. As the Coupling Model applies to all interacting systems showing relaxations the conductivity relaxation is not excluded from the CM fit. For conductivity relaxations, the CM equation is written as

$$\tau_{\sigma\alpha} = (t_c{}^{-n_\sigma}\tau_{\sigma 0})1 - n\sigma^{1-n_\sigma} \tag{6.8}$$

where tc ≈1 ps for most ionic conductors. Using this equation, we calculated the values of $\tau_{\sigma 0}(T)$ and plotted them in the relaxation map in figure 6.13. From figure 6.13 we found that the calculated conductivity primitive relaxation time of piroxicam does not correspond to the temperature dependence of experimentally observed secondary relaxation and therefore the observed secondary relaxation is not Johari-Goldstein type β relaxation rather it originates from local molecular motion. The temperature dependence of the secondary relaxation time below T_g obtained on fitting the dielectric loss spectrum and dielectric modulus spectrum coincides in the relaxation map and hence we confirm the presence of translational rotational coupling in piroxicam. But the dielectric loss peaks above T_g due to structural α relaxation are masked by the conductivity contribution the molecular relaxation time corresponding to structural α relaxation could not be determined. The CM equation is generally applicable to relaxation and diffusion in all interacting systems, including not only structural relaxation but also ion conductivity relaxation because the molecules or ions are

densely populated and interacting in both cases. For this reason, the CM also has long since been applied successfully to the ion conductivity relaxation of crystalline, glassy, and molten ionic conductors[14,38–40]. There is also the CM equation relating the conductivity relaxation time $\tau_{\sigma\alpha}(T)$ to the conductivity primitive relaxation time $\tau_{\sigma 0}(T)$.

6.3.2.8 Translational-rotational coupling

From HN fits, the relaxation time of conductivity secondary relaxation $\tau_{\sigma\beta}(T)$ of piroxicam at temperatures below T_g from the electric modulus data and also from the dielectric data from dipolar relaxation. The temperature dependence of these two data corresponding to secondary conductivity relaxation and dipolar secondary relaxation are shown in the relaxation map shown in figure 6.13 and these two data superpose on each other. We concluded that there is translation–rotation coupling based on the strong agreement of secondary conductivity relaxation and secondary dipolar relaxation times. This can be verified in theory by comparing the values of $\tau_{\sigma}(T)$ with the structural relaxation times $\tau_{\alpha}(T)$. Unfortunately, this is not possible since the piroxicam dielectric loss peaks are obscured by the dc-conductivity that results from ion hopping. We may have to conduct tests at high pressure to accomplish this. This supports the identification of this secondary relaxation as the conductivity-relaxation of piroxicam, which acts as a precursor to the conductivity-relaxation, as previously stated for other ionic conducting pharmaceuticals, such as procainamide HCl, [33,41] lidocaine HCl,[42] procaine HCl[14], chlorpromazine HCl[39] and an ionic liquid[24].

6.3.3 Origin of secondary relaxation : DFT approach

Though dielectric measurements could be used to calculate the relaxation's activation energy, there was no clear proof of the related molecular moieties involved in the transition. Indeed, until now, the cause of secondary relaxations has remained a mystery, with no definite answer. Secondary relaxations may result from complex intramolecular changes involving multiple moieties or from a JG process, but this is not the case here. As previously stated, dielectric measurements can provide useful information about secondary relaxations occurring below T_g. Though dielectric measurements could be used to calculate the relaxation's activation energy, there was no clear proof of the related molecular moieties involved in the transition. Indeed, until now, the cause of secondary relaxations has remained a mystery, with no definite

answer. Secondary relaxations may result from complex intramolecular changes involving multiple moieties or from a JG process, but this is not the case here. There has been a surge of interest in theoretical conformational calculations to decode the physical structure of the transition at the atomic level in recent years, which is often coupled with experiments[40,41]. More information is sought to expose the origin of secondary processes by using calculated energy barriers and dipole moments when suitable flexible end groups relax, in line with this synergetic approach.

The knowledge about the origin of the secondary processes seems to be crucial in the determination of the optimal temperature condition at which the amorphous form of an API will be stable.it is clear from the result of coupling model fit that the secondary relaxation observed in Piroxicam is non-JG relaxation, it seems that only the motions responsible for this kind of secondary relaxation may induce crystallization process and hence these relaxations cannot trigger the crystallization process. Using DFT calculations, Schamme *et al*.[43] published a successful identification pathway for identifying the particular part of a molecule that manifests the observed secondary relaxation using DFT calculations. They put their technique to the test by using dihedral scans to map the energy and dipole moment of a molecule as a function of torsional angles. Exploration of the potential energy surface (PES) associated with the rotation of a flexible side group leads to conformational interconversions through a variety of MINs and transition states (TS). When plotting molecular dipole moment as a function of torsional dihedral angle, a one-to-one correspondence can be observed. Among various combinations of MINs and TS, the energy can be related to a shift in the dipole moment. Using mod-redundant coordinates in Gauss view software[44,45], a dihedral angle was randomly selected and scanned continuously through 360° by a constant step of 10°. The remainder of the molecule was optimized while the energy and dipole moment were measured at a frozen value of the angles set. The relaxed dihedral scans on several possible dihedral angles corresponding to versatile side groups matching with the experimentally observed activation energy using Gaussian 09[45] package are used to classify the related local motion in a molecule.

The potential energy scan diagram showing the variation of potential energy with a torsional angle corresponding to the rotation of the C_5NH_4NHCO group obtained from the DFT method is shown in Fig. 6.18. The associated molecular subgroup, which

causes the observed secondary relaxation in Piroxicam, is shown circled in Fig. 6.19. The rotation of the selected group led to the conformational interconversions specified by energy minima (MIN1) and transition state (TS1). The energy difference corresponding to different potential energy barriers of the transition states are matched with the observed activation energy of secondary relaxation in piroxicam. Two secondary relaxations are observed experimentally in Piroxicam below T_g, with activation energies 61kJ/mol and 25kJ/mol out of which 61kJ/mol approximately matches the difference between the energy values of the potential barriers between MIN1 and MIN2 which is equal to 60kJ/mol as shown in the figure 6.18. The origin of the secondary relaxation having activation energy of 25kJ/mol cannot be identified as no energy barriers are matching with 25kJ/mol.

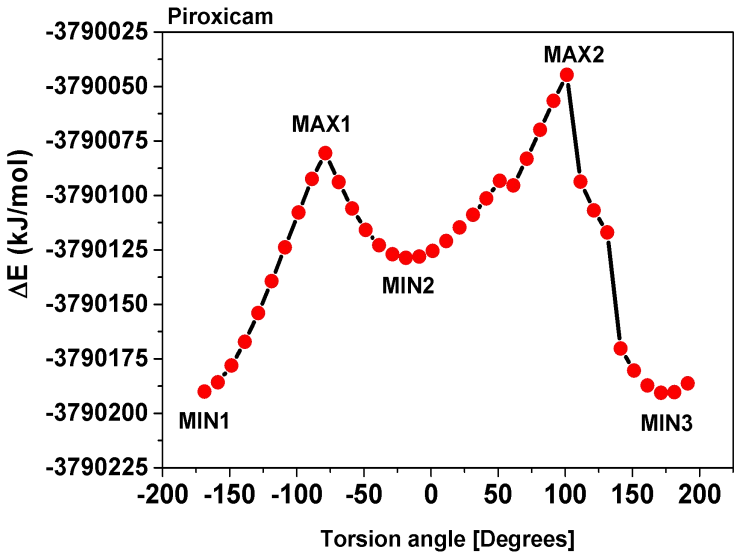

Figure 6.19 Potential energy scan on the rotation of dihedral angle with group C_5NH_4NHCO

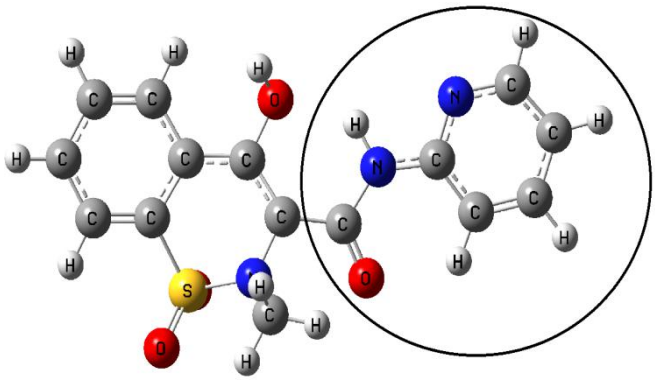

Figure 6.20 Optimized geometry of piroxicam by B3LYP/6311. The encircled part shows the rotating subgroup

6.3.4 FTIR spectroscopy

Figure 6.20 display the FTIR spectra of crystalline and amorphous piroxicam along with the spectrum obtained by the B3LYP/6311 level of theory. The sample's identity is confirmed by comparing the DFT-derived vibrational spectrum to the experimental spectra. Since hydrogen bond formation has a strong influence on the bond strength of the donor and acceptor groups, and the OH group is more sensitive, it is simple to study the molecular interaction using vibrational spectroscopic data. Absorption band redshift, band broadening, and band intensification are all common changes for the FTIR spectrum of the amorphous sample. There is a slight decrease in transmittance in the spectrum of amorphous piroxicam when compared to crystalline sample thereby confirming the amorphous nature of the sample used for dielectric measurements. We have confirmed the identity of the sample from the spectrum of crystalline sample on comparison with the theoretical spectrum.

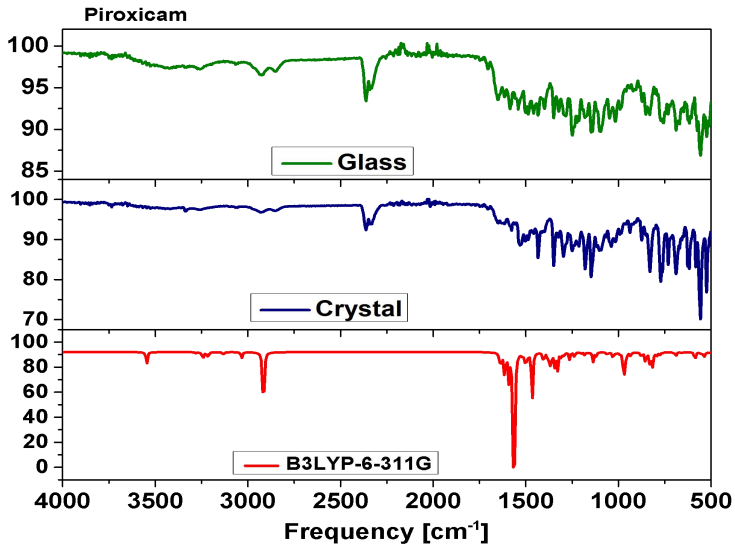

Figure 6.21 FTIR spectra of piroxicam in glassy crystalline phases along with spectrum obtained by DFT method

6.4 Conclusions

In this chapter, the molecular dynamics of the piroxicam in supercooled liquid and glassy states were analyzed by experimental methods such as DSC, BDS, and vibrational spectroscopy. Piroxicam is found to be a good glass-former and is also an ionic conductor. A well-resolved conductivity relaxation and two well-resolved

secondary conductivity relaxations were observed in the imaginary part of the modulus spectrum below T_g, as well as two well-resolved secondary dipolar relaxations are also observed below T_g in piroxicam in the imaginary part of the dielectric permittivity spectrum. The dielectric relaxation is well fitted in the whole temperature range by the Havriliak – Negami function. The non-Arrhenius behaviour of the primary process is fitted with the Vogel-Fulcher –Tammann equation. The primary α relaxation process and secondary β relaxation process are observed. The activation energies of the secondary relaxations in piroxicam are E_γ= 61 kJ/mol and E_β= 25 kJ/mol. Another parameter obtained by VFT fitting is the fragility index or steepness index (m). No well-resolved relaxation in the dielectric loss spectrum was observed above T_g as it is masked by dc conductivity. The molecular and ionic dynamics in piroxicam were studied by both the conductivity and structural relaxations. Physical stability or recrystallization of the amorphous phase is an important concern in the application of amorphous pharmaceuticals. The value of T_g obtained for Piroxicam is 330K which is higher than room temperature hints at the stability of the amorphous Piroxicam. For piroxicam the fragility is 92, the classical value of m is between 50 and 150 for fragile systems. Strong liquids exhibit m values <40 and fragile liquids having an m value >75. There is a continuity of system with intermediate fragility. According to this classification, piroxicam is a fragile glass former. From the study of the conductivity relaxation and the analysis of the data using electric modulus representation above and below T_g, we have observed and characterized the conductivity σ_α relaxation responsible for dc conductivity in the liquid state above T_g, and a conductivity σ_β relaxation in the glassy state. Therefore, the conductivity α-relaxation may originate from the intermolecular JG-relaxation which highlights the importance of considering the relationship between the structural and conductivity relaxations. Incidentally, when the same bds data of piroxicam is analyzed in the dielectric permittivity formalism, a secondary dipolar relaxation with the same relaxation time and activation energy as the conductivity relaxations in the glassy state which is due to the presence of coupling between translational and rotational motion in the glassy piroxicam. Translation–rotation coupling of piroxicam possibly explains the dual conductivity and dipolar nature of the secondary relaxation. We conducted computer simulation studies of a piroxicam molecule, integrating all possible sidechain rotations about different dihedral angles, to not rule out the possibility of intramolecular secondary relaxation. As a result,

the secondary dipolar relaxation likely observed is due to sidechain rotation. Despite this possibility, the dipolar JG mechanism, which requires the motion of the entire piroxicam molecule rather than a side group, cannot be the source of the observed secondary dipolar relaxation.

References

[1] K. P. Safna Hussan, M.S. Thayyil, S.K. Deshpande, Jinitha. T. V, Manoj. K, K.L. Ngai, Molecular dynamics and the translational–rotational coupling of an ionically conducting glass-former: amlodipine besylate, RSC Adv. 8 (2018) 20630–20636. https://doi.org/ 10.1039/C8RA01544A.

[2] A. Telfah, M.M. Abdul-Gader Jafar, I. Jum'h, M.J.A. Ahmad, J. Lambert, R. Hergenröder, Identification of relaxation processes in pure polyethylene oxide (PEO) films by the dielectric permittivity and electric modulus formalisms, Polym. Adv. Technol. 29 (2018) 1974–1987. https://doi.org/https://doi.org/ 10.1002/pat.4306.

[3] D.L. Sidebottom, B. Roling, K. Funke, Ionic conduction in solids: Comparing conductivity and modulus representations with regard to scaling properties, Phys. Rev. B.63(2000) 24301. https://doi.org/10.1103/ PhysRevB.63.024301.

[4] O.R. Sadeq, Piroxicam- Induced Hepatotoxicity, Biomed. J. Sci. & Tech. Res. 2 (2018)2601–2606.

[5] P. Panzade, G. Shendarkar, S. Shaikh, P. Rathi, Pharmaceutical Cocrystal of Piroxicam: Design, Formulation and Evaluation, Adv. Pharm. Bull. 7 (2017) 399–408. https://doi.org/10.15171/apb.2017.048.

[6] M.J. Frisch, G.W. Trucks, H.B. Schlegel, G.E. Scuseria, M.A. Robb, J.R. Cheeseman, G. Scalmani, V. Barone, B. Mennucci, G.A. et. . Petersson, Gaussian 09, Gaussian, Inc. Wallingford,CT,. .

[7] National Center for Biotechnology Information (2021). PubChem Compound Summary for CID 54676228, Piroxicam. Retrieved June 1, 2021 from https://pubchem.ncbi.nlm.nih.gov/compound/Piroxicam..

[8] B. Schammé, M. Mignot, N. Couvrat, V. Tognetti, L. Joubert, V. Dupray, L. Delbreilh, E. Dargent, G. Coquerel, Molecular relaxations in supercooled liquid

and glassy states of amorphous quinidine: dielectric spectroscopy and density functional theory approaches, J. Phys. Chem. B. 120 (2016) 7579–7592.

[9] L. Chen, T. Okuda, X.-Y. Lu, H.-K. Chan, Amorphous powders for inhalation drug delivery., Adv. Drug Deliv. Rev. 100 (2016) 102–115. https://doi.org/10.1016/j.addr.2016.01.002.

[10] W. Kauzmann, The Nature of the Glassy State and the Behaviour of Liquids at Low Temperatures., Chem. Rev. 43 (1948) 219–256. https://doi.org/10.1021/cr60135a002.

[11] D. Turnbull, Under what conditions can a glass be formed?, Contemp. Phys. 10 (1969) 473–488. https://doi.org/10.1080/00107516908204405.

[12] L. Carpentier, R. Decressain, S. Desprez, M. Descamps, Dynamics of the amorphous and crystalline α-, β-phases of indomethacin, J. Phys. Chem. B. 110 (2006) 457–464. https://doi.org/10.1021/jp053545u.

[13] B.C. Hancock, G. Zografi, Characteristics and significance of the amorphous state in pharmaceutical systems, J.Pharm.Sci. 86 (1997) 1–12.

[14] Z. Wojnarowska, A. Swiety-Pospiech, K. Grzybowska, L. Hawelek, M. Paluch, K.L. Ngai, Fundamentals of ionic conductivity relaxation gained from study of procaine hydrochloride and procainamide hydrochloride at ambient and elevated pressure., J. Chem. Phys. 136 (2012) 164507. https://doi.org/10.1063/1.4705274.

[15] F. Kremer, A. Scho nhals, Broadband Dielectric Spectroscopy; Eds.; Springer: , n.d.

[16] K.P. Safna Hussan, M.S. Thayyil, A. Poulose, K.L. Ngai, Glassy Dynamics and Translational–Rotational Coupling of an Ionically Conducting Pharmaceutical Salt-Sodium Ibuprofen, J. Phys. Chem. B. 123 (2019) 7764–7770. https://doi.org/10.1021/acs.jpcb.9b06478.

[17] K.P. Safna Hussan, M.S. Thayyil, S.K. Deshpande, T. V. Jinitha, K. Manoj, K.L. Ngai, Molecular dynamics, physical and thermal stability of neat amorphous amlodipine besylate and in binary mixture, Eur. J. Pharm. Sci. 119 (2018) 268–278. https://doi.org/10.1016/j.ejps.2018.04.030.

[18] N.T. Correia, J.J. Ramos, M. Descamps, G. Collins, Molecular mobility and fragility in indomethacin: a thermally stimulated depolarization current study, Pharm. Res. 18 (2001) 1767–1774. https://doi.org/10.1023/a:1013339017070.

[19] C.A. Angell, Relaxation in liquids, polymers and plastic crystals-strong/fragile patterns and problems, J. Non. Cryst. Solids. 131 (1991) 13–31.

[20] R. Böhmer, K.L. Ngai, C.A. Angell, D.J. Plazek, Nonexponential relaxations in strong and fragile glass formers, J. Chem. Phys. 99 (1993) 4201–4209. https://doi.org/10.1063/1.466117.

[21] K. Graeser, J. Patterson, J. Zeitler, K. Gordon, T. Rades, Correlating thermodynamic and kinetic parameters with amorphous stability, Eur. J. Pharm. Sci. 37 (2009) 492– 498. https://doi.org/10.1016/j.ejps.2009.04.005.

[22] K. Adrjanowicz, Z. Wojnarowska, P. Wlodarczyk, K. Kaminski, M. Paluch, J. Mazgalski, Molecular mobility in liquid and glassy states of Telmisartan (TEL) studied by Broadband Dielectric Spectroscopy, Eur. J. Pharm. Sci. 38 (2009) 395–404. https://doi.org/https://doi.org/10.1016/j.ejps.2009.09.009.

[23] Z. Wojnarowska, K. Adrjanowicz, P. Wlodarczyk, E. Kaminska, K. Kaminski, K. Grzybowska, R. Wrzalik, M. Paluch, K.L. Ngai, Broadband Dielectric Relaxation Study at Ambient and Elevated Pressure of Molecular Dynamics of Pharmaceutical: Indomethacin, J. Phys. Chem. B. 113 (2009) 12536–12545. https://doi.org/10.1021/jp905162r.

[24] K. Adrjanowicz, K. Kaminski, M. Paluch, P. Wlodarczyk, K. Grzybowska, Z. Wojnarowska, L. Hawelek, W. Sawicki, P. Lepek, R. Lunio, Dielectric relaxation studies and dissolution behaviour of amorphous verapamil hydrochloride, J. Pharm. Sci. 99 (2010) 828–839.

[25] G.P. Johari, R. Shanker, on determining the relaxation time of glass and amorphous pharmaceuticals' stability from thermodynamic data, Thermochim. Acta - THERMOCHIM ACTA. 511 (2010) 89–95. https://doi.org/ 10.1016/j.tca.2010.07.029.

[26] M. Paluch, J. Knapik, Z. Wojnarowska, A. Grzybowski, K.L. Ngai, Universal Behaviour of Dielectric Responses of Glass Formers: Role of Dipole-Dipole

Interactions, Phys. Rev. Lett. 116 (2016) 1–6. https://doi.org/10.1103/PhysRevLett.116.025702.

[27] R. Kohlrausch, Theorie des elektrischen Rückstandes in der Leidener Flasche, Ann. Phys. 167 (1854) 56–82. https://doi.org/https://doi.org/10.1002/andp.18541670103.

[28] G. Williams, D.C. Watts, Non-symmetrical dielectric relaxation behaviour arising from a simple empirical decay function, Trans. Faraday Soc. 66 (1970) 80–85. https://doi.org/10.1039/TF9706600080.

[29] Shamblin SL, Hancock BC, Dupuis Y, Pikal MJ. Interpretation of relaxation time constants for amorphous pharmaceutical systems. J Pharm Sci. 2000 Mar;89(3):417-27.

[30] Z. Wojnarowska, K. Grzybowska, L. Hawelek, A. Swiety-Pospiech, E. Masiewicz, M. Paluch, W. Sawicki, A. Chmielewska, P. Bujak, J. Markowski, Molecular Dynamics Studies on the Water Mixtures of Pharmaceutically Important Ionic Liquid Lidocaine HCl, Mol. Pharm. 9 (2012) 1250–1261. https://doi.org/10.1021/mp2005609.

[31] K. Adrjanowicz, M. Paluch, K. Ngai, Determining the structural relaxation times deep in the glassy state of the pharmaceutical Telmisartan, J. Phys. Condens. Matter. 22 (2010) 125902. https://doi.org/10.1088/0953-8984/22/12/125902.

[32] K.L. Ngai, Relation between some secondary relaxations and the α relaxations in glass-forming materials according to the coupling model, J. Chem. Phys. 109 (1998) 6982–6994. https://doi.org/10.1063/1.477334.

[33] Z. Wojnarowska, K. Kołodziejczyk, K.J. Paluch, L. Tajber, K. Grzybowska, K.L. Ngai, M. Paluch, Decoupling of conductivity relaxation from structural relaxation in protic ionic liquids and general properties, Phys. Chem. Chem. Phys. 15 (2013) 9205–9211.

[34] K.L. Ngai, Short-time and long-time relaxation dynamics of glass-forming substances: a coupling model perspective, J. Phys. Condens. Matter. 12 (2000) 6437–6451. https://doi.org/10.1088/0953-8984/12/29/316.

[35] S. Capaccioli, M. Paluch, D. Prevosto, L.-M. Wang, K.L. Ngai, Many-Body Nature of Relaxation Processes in Glass-Forming Systems, J. Phys. Chem. Lett. 3 (2012) 735–743. https://doi.org/10.1021/jz201634p.

[36] M.S. Thayyil, S. Capaccioli, D. Prevosto, K.L. Ngai, Is the Johari-Goldstein β-relaxation universal?, Philos. Mag. 88 (2008) 4007–4013. https://doi.org/10.1080/14786430802270082.

[37] K.L. Ngai, M. Paluch, Classification of secondary relaxation in glass-formers based on dynamic properties, J. Chem. Phys. 120 (2004) 857–873. https://doi.org/10.1063/1.1630295.

[38] K.L. Ngai, An extended coupling model description of the evolution of dynamics with time in supercooled liquids and ionic conductors, J. Phys. Condens. Matter. 15 (2003) S1107–S1125. https://doi.org/10.1088/0953-8984/15/11/332.

[39] S. Hensel-Bielowka, K.L. Ngai, A. Swiety-Pospiech, L. Hawelek, J. Knapik, W. Sawicki, M. Paluch, On the molecular origin of secondary relaxations in amorphous protic ionic conductor chlorpromazine hydrochloride- High pressure dielectric studies, J. Non. Cryst. Solids. 407 (2015) 81–87. https://doi.org/ https://doi.org/10.1016/j.jnoncrysol.2014.08.005.

[40] S.N. Tripathy, Z. Wojnarowska, J. Knapik, H. Shirota, R. Biswas, M. Paluch, Glass transition dynamics and conductivity scaling in ionic deep eutectic solvents: The case of (acetamide + lithium nitrate/sodium thiocyanate) melts, J. Chem. Phys. 142 (2015) 184504. https://doi.org/10.1063/1.4919946.

[41] Z. Wojnarowska, C.M. Roland, A. Swiety-Pospiech, K. Grzybowska, M. Paluch, Anomalous Electrical Conductivity Behaviour at Elevated Pressure in the Protic Ionic Liquid Procainamide Hydrochloride, Phys. Rev. Lett. 108 (2012) 15701. https://doi.org/10.1103/PhysRevLett.108.015701.

[42] A. Swiety-Pospiech, Z. Wojnarowska, S. Hensel-Bielowka, J. Pionteck, M. Paluch, Effect of pressure on decoupling of ionic conductivity from structural relaxation in hydrated protic ionic liquid, lidocaine HCl, J. Chem. Phys. 138 (2013) 204502. https://doi.org/10.1063/1.4807487.

[43] B. Schammé, M. Mignot, N. Couvrat, V. Tognetti, L. Joubert, V. Dupray, L. Delbreilh, E. Dargent, G. Coquerel, Molecular Relaxations in Supercooled Liquid and Glassy States of Amorphous Quinidine: Dielectric Spectroscopy and Density Functional Theory Approaches, J. Phys. Chem. B. 120 (2016) 7579–7592. https://doi.org/10.1021/acs.jpcb.6b04242.

[44] M.J. Frisch, G.W. Trucks, H.B. Schlegel, G.E. Scuseria, M.A. Robb, J.R. Cheeseman, G. Scalmani, V. Barone, B. Mennucci, G.A. *et.al.* Petersson, Gaussian 09, Gaussian, Inc. Wallingford, CT.

[45] M.J. Frisch, G.W. Trucks, H.B. Schlegel, G.E. Scuseria, M. a. Robb, J.R. Cheeseman, G. Scalmani, V. Barone, G. a. Petersson, H. Nakatsuji, X. Li, M. Caricato, a. V. Marenich, J. Bloino, B.G. Janesko, R. Gomperts, B. Mennucci, H.P. Hratchian, J. V. Ortiz, a. F. Izmaylov, J.L. Sonnenberg, Williams, F. Ding, F. Lipparini, F. Egidi, J. Goings, B. Peng, A. Petrone, T. Henderson, D. Ranasinghe, V.G. Zakrzewski, J. Gao, N. Rega, G. Zheng, W. Liang, M. Hada, M. Ehara, K. Toyota, R. Fukuda, J. Hasegawa, M. Ishida, T. Nakajima, Y. Honda, O. Kitao, H. Nakai, T. Vreven, K. Throssell, J. a. Montgomery Jr., J.E. Peralta, F. Ogliaro, M.J. Bearpark, J.J. Heyd, E.N. Brothers, K.N. Kudin, V.N. Staroverov, T. a. Keith, R. Kobayashi, J. Normand, K. Raghavachari, a. P. Rendell, J.C. Burant, S.S. Iyengar, J. Tomasi, M. Cossi, J.M. Millam, M. Klene, C. Adamo, R. Cammi, J.W. Ochterski, R.L. Martin, K. Morokuma, O. Farkas, J.B. Foresman, D.J. Fox, G16_C01, (2016) Gaussian 16, Revision C.01, Gaussian, Inc., Wallin.

CHAPTER 7

VIBRATIONAL SPECTROSCOPY, DFT INVESTIGATIONS AND MOLECULAR DOCKING OF BRUCINE AND COLCHICINE

Reproduced in part with the permission of A Afzal *et.al* from *the* following publication

Anti-Cancerous Brucine and Colchicine: Experimental and Theoretical Characterization **Aboothahir Afzal**,* Mohamed Shahin Thayyil, Mohammad Shariq, Yohannan Sheena Mary, Kaippallil Sundaresan Resmi, Renjith Thomas, Nasarul Islam and Ajithan Jyothi Abinu, Chemistry Select 2018, DOI: https://doi.org/10.1002/ slct.201902698

7.1 Introduction

Brucine is an alkaloid, extracted from the Nux-vomica tree, found abundantly in Asian countries, and is used as a constituent of traditional medicines in Asian countries especially China for many years[1,2]. It is used to treat patients with arthritic and traumatic pain by its anti-inflammatory, analgesic, and anti-rheumatic properties,[3] and is also used for preparing drugs used in Ayurveda and Homeopathy[4]. Surprisingly, Qin *et al*.[5] in 2012 reported that brucine is effective against hepatocellular carcinoma, while Serasanambati *et al.*,[6]in 2014 reported its potential activity against breast cancer, which may revolutionize anticancer treatment. Unfortunately, brucine is toxic above a limited dose (narrow therapeutic window) which puts a limitation to treat cancer. Colchicine, another alkaloid is commonly used for treating gout, [7] pericarditis[8], Bechet's disease, and familial Mediterranean fever [9]and is a tubulin destabilizer first-ever reported with amazing anti-mitotic activity and can treat cancer like chronic leukemia [10], and also can treat cardiovascular problems[11]. Several studies on structural variations in colchicine to increase its therapeutic efficiency were reported[12]. Brucine and colchicine are large chiral molecules, as they can find good applications as chiral resolving agents by enantiomer selective recognition, brucine is used as a chiral selector[13] in fractional distillation to resolve dihydroxy fatty acids[14]. The chiral application potential of natural alkaloids is not explored to the maximum, but researchers have found the possibility of applying optically pure alkaloids as chiral resolving agents[15]. Stereo-chemically related molecules can be used for the separation of acids of opposite configurations by producing diastereomeric salts having different solubility[16] [17]. The chiral properties of brucine and colchicine are determined by Vibrational circular dichroism (VCD) spectroscopy.

The possible electrophilic and nucleophilic attacks on tertiary atoms of the title molecules and hyper molecular interaction were studied by NBO analysis. The distribution of charges in the atoms of the molecule is calculated by natural bonding orbitals (NBO) analysis, which helps to understand the electron density localization, hyperconjugation effects, and intermolecular or intramolecular interaction[15]. Both brucine and colchicine are polar molecules and have a dielectric permittivity value of around 3[18]. Non-linear optical (NLO) properties like electric dipole moment, the

isotropic polarizability, and the first hyperpolarizability can be theoretically calculated by Density Functional Theory (DFT) method for understanding the NLO properties for possible applications in nonlinear optics[15]. Organic solar cells are getting more popular, as organic solar cells with 13% power conversion efficiency were developed[19]. The light-harvesting efficiency (LHE) is defined as the fraction of light intensity absorbed by the solar cell at a certain wavelength to the incident light intensity[20].

Brucine and colchicine are significant to the pharmaceutical industry due to their anti-cancerous effects, but a complete quantum computational characterization of molecular properties is lacking in the literature. This motivated me to perform quantum computational calculations for characterizing structural, vibrational, and electronic properties on brucine and colchicine. In this paper, analysis using IR, Raman, UV-Visible spectroscopy, Vibrational circular dichroism spectral analysis(VCD), natural bonding orbitals (NBO) analysis, Frontier molecular orbitals (FMO), Molecular electrostatic potential surfaces(MEP), LHE analysis by DFT method using Gaussian-09 [21]. Nonlinear optical properties like linear polarizability (α) and first-order hyper-polarizability (β), and the molecular chemical stability due to charge delocalization and hyper-conjugative interactions were also calculated.

Computational molecular docking is a powerful tool for structure-based drug discovery[22]. To understand the anticancer effects of the title compounds, the in-silica molecular docking of brucine and colchicine with cancer target proteins available in the literature was done. Quantum computational techniques proved to be irreplaceable and inexpensive theoretical tools for the characterization of molecules, identification of reactive areas of molecules, spectroscopic analysis and is also used for the characterization and structural confirmations of new or yet to be synthesized molecules [23][24][25][26]. One of the biggest challenges in drug discovery is the screening of compounds to identify a prospective drug which is a long-time consuming process, where docking is proved to be very useful. If we dock several compounds into target receptor structures virtually, only a few numbers of compounds are needed to be experimentally screened. The molecular docking software package Glide in Schrodinger suite [27][28] is found to be very effective for the screening of drugs and is widely used by researchers, especially in the pharmaceutical industry. Quantum

computational calculations of brucine and colchicine were done by DFT method [29] in the ground state using Gaussian-09 with B3LYP/6-311++G(d,p) basis[21] with Gaussview-05 as interface[30]. The molecular structure of brucine and colchicine were optimized at the B3LYP/6-311++ basis set while natural bond orbital analysis (NBO) was done using the NBO program in Gaussian-09[31]. Theoretical calculations on FTIR, FT-Raman, Vibrational Circular Dichroism (VCD) spectra, NLO properties, NBO analysis, and VCD spectra of brucine, colchicine, and its halogen substitutions were performed. The harmonic vibrational frequencies of FTIR and FT-Raman spectra were calculated and scaled by the scaling factor 0.961[12]. The optimized structures of the title compounds were then used in NBO analysis using NBO 3.1 program[13]. UV-Visible spectra by TD-DFT method[14][15]. HOMO-LUMO energy levels and Molecular Electrostatic Potential (MEP) were calculated using Gauss View 5.0. Light Harvesting Efficiency (LHE) of brucine and colchicine and also for its different halogen substitutions were also determined by TD-DFT method using Gaussian-09 for its possible application in organic solar cells.

To do the in-silica analysis for the understanding the anti-cancer effects of brucine and colchicine, molecular docking was carried out using the Schrodinger suite using the Maestro version 18.4 packages such as receptor grid generation, Ligprep, and Glide XP docking. The PDB files of proteins were obtained from RCSB protein bank [32] whose PDBID's are 1JNX[33], 3U9U[34], 5NQR[35], 1BHG[36], 3S7S[37], 4AOW[38], 3U9U[34], 5JM5[35], 5NWH[35] and 5G3N[39]. Each target protein was prepared using the protein preparation wizard in the Maestro 18–4 version[40]. Then, it was pre-processed, and the overlapped residues were removed, optimization and minimization processes were done. The water molecules if any present in the protein structure were removed from the protein structure before the minimization process since they were not suitable for molecular docking[41]. A sitemap can locate the binding sites of proteins whose functionality size and solvent exposure meet the user specification[28]. It also shows the regions in the binding sites which are suitable for ligands hydrogen-bond donors, acceptors, or hydrophobic groups to occupy. The site scores obtained can be used to rank the possible binding sites accurately to eliminate those sites which are not likely to be relevant. The ligand molecules, brucine, and colchicine were prepared using Ligprep, which generates energy minimized molecular

structures in 3D. It eliminates the mistakes in the ligands and applies sophisticated methods to correct the Lewis structures to reduce the computational errors. Optimization using the OPLS3e force field generated the low energy isomer of the ligands. Finally, these ligand molecules in the complex structure were docked with the target proteins. The ligand molecules were docked with the binding sites of each of the corresponding cancer target proteins using the glide grid ligand docking package [42] of the Schrodinger software. Glide accurately finds the exact binding modes for a large set of test cases. Glide does a virtual screening from HTVS to SP to XP, modifying the data at each level such that only fewer compounds need to be studied at a higher accuracy level. The ligands were docked to the active site of cancer targets using Glide Extra precision (XP), which determine the flexibility of ligands. Only those molecules, which are small and active, would receive favourable docking scores with accurate hydrophobic contact with the ligand and protein.

7.2 Experimental section

The materials selected for study in this chapter are brucine and colchicine, purchased in 99% pure form from Sigma Aldrich. The details of brucine and colchicine are given in sections 2.4 and 3.2. The experimental studies performed are FT-IR, FT-Raman, and UV-Visible spectroscopy, and the computational studies are done by the DFT method in the B3LYP/6-311g(d,p) level of theory using Gaussian 09 software. The quantum computational studies performed are confirmational analysis, geometry optimization, vibrational spectroscopy, vibrational circular dichroism, UV-Visible spectroscopy, frontier molecular orbitals, molecular electrostatic potential surfaces, non-linear optical properties, light-harvesting efficiency, and molecular docking.

7.3 Results and discussions

7.3.1 Conformational Analysis

For the conformational analysis of the brucine and colchicine molecules, relaxed potential energy scans [43] [44] were performed by rotation of side groups in brucine and colchicine molecules separately at arbitrarily selected dihedral angles. We obtained the potential energy in the gas phase through relaxed geometry scans by selecting redundant coordinates using the Gaussview-05 interface and Gaussian-09[21][30]. The dihedral angle in the optimized structure was changed continuously by

a constant step of 10^0 in the range of 180^0. At a particular dihedral angle selected, the rest of the molecule was optimized and at this position, energy, as well as molecular dipole moment, was calculated. The PES corresponding to the rotation of the CH_3 group proved that conformational interconversions through stationary points are shown in Figures 7.1 and 7.2. The molecular dipole moment as a function of the torsional dihedral angle is also studied which in turn is linked to change in energy.

The first scan was performed on the brucine between the dihedrals C_{27}-O_4-C_{29}-H_{55} in the intervals of 10 degrees for 180 degrees using B3LYP/6-311++G (d, p). The second scan in the brucine molecule was done with the dihedral C_{26}-O_3-C_{28}-H_{51}. The variation of potential energy and dipole moment with dihedral angle are shown in figures 7.1 and 7.2 respectively. It is found that there are three global maxima and four global minima in the potential energy surface for both the conformers. The conformational stabilization energy is determined to be 1.3544 kcal/mol. The global minima are observed in the dihedrals of -180, -6, +60, and +180 degrees, and the maxima are in the dihedrals of -120, 0, and +120 degrees. Similarly, the relaxed dihedral scan was performed on colchicine for dihedral angle H_{41}-C_{25}-C_{22}-N_7 and obtained three global minima in the same range of rotation angles.

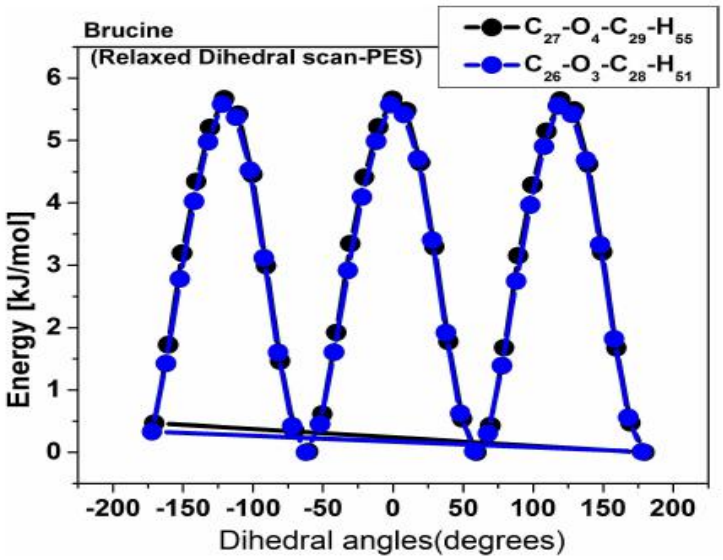

Figure 7.1 Graph showing the variation of potential energy with rotation of dihedral angle for the relaxed scan of two selected dihedrals of brucine

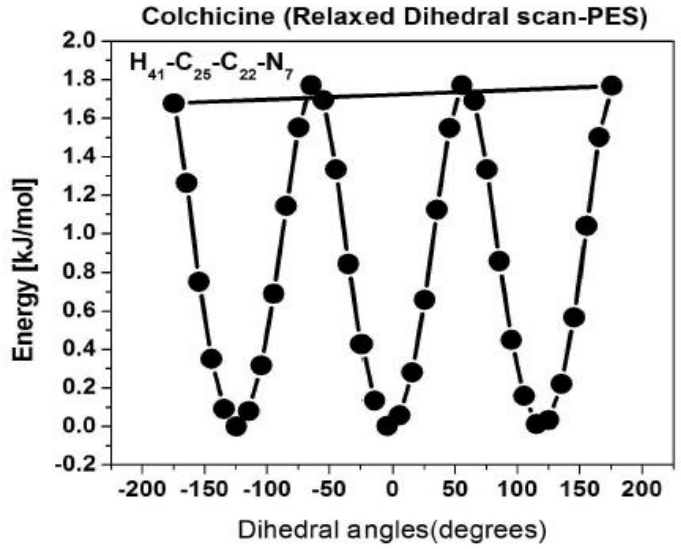

Figure 7.2 Graph showing the variation of potential energy with rotation of dihedral angle for the relaxed scan of a selected dihedral of colchicine

7.3.2 Geometry optimization

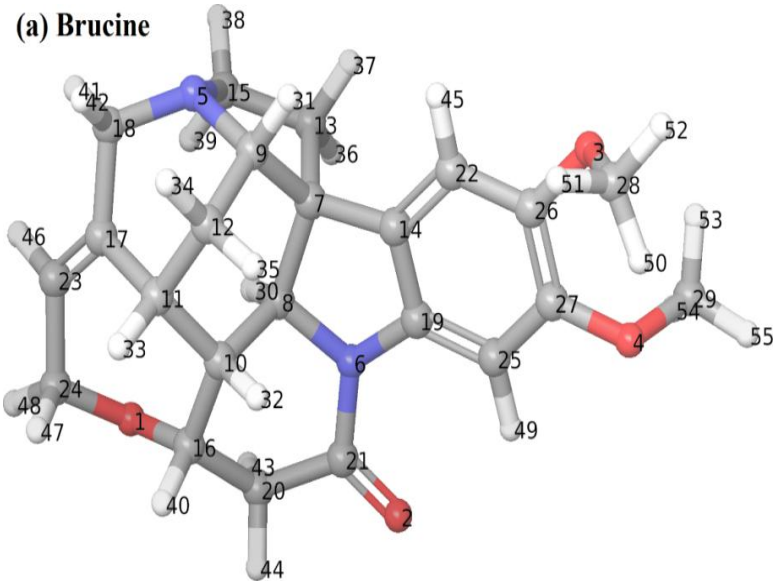

Figure 7.3 Optimized geometry of brucine obtained by B3LYP/6-311++G(d,p) method

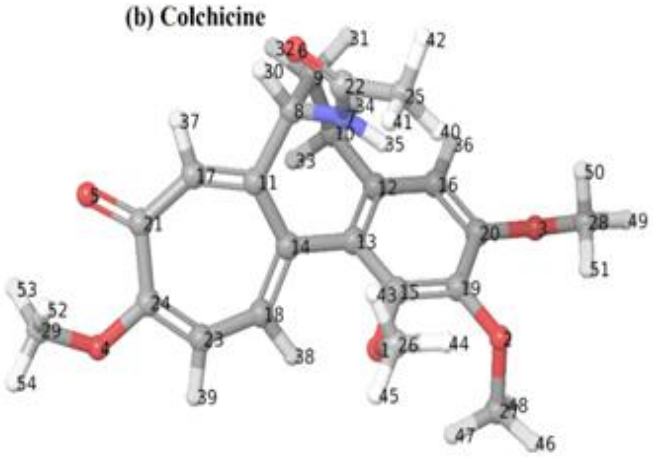

Figure 7.4 optimized geometry of colchicine obtained by B3LYP/6-311++G (d, p) method

The equilibrium molecular geometries of brucine and colchicine were obtained by the B3LYP/6-311++G (d, p) method is shown in Figures 7.3 and 7.4 respectively. Bond length values (theoretical and experimental) of colchicine are shown in table 7.1. The optimized parameters of colchicine are in good agreement with the experimental data.

Table 7. 1 Structural parameters of colchicine optimized by B3LYP/6-311++G (d, p)

Bond	Bond length (Å)		Bond	Bond angle (degree)	
	Theoretical	Experimental		Theoretical	Experimental
O_1-C_{15}	1.3753	1.38	C_{15}-O_1-C_{26}	115.4795	116
O_1-C_{26}	1.4358	1.4	C_{19}-O_2-C_{27}	114.5555	
O_2-C_{19}	1.3746	1.385	C_{20}-O_3-C_{28}	116.5231	116.5
O_2-C_{27}	1.4381	1.42	C_{24}-O_4-C_{29}	122.0724	119.5
O_3-C_{20}	1.3703	1.365	C_8-N_7-C_{22}	122.0581	
O_3-C_{28}	1.4355	1.445	C_8-N_7-H_{35}	119.1324	
O_4-C_{24}	1.3476		C_{22}-N_7-H_{35}	118.7839	
O_4-C_{29}	1.4425	1.42	N_7-C_8-C_9	112.4517	
C_{21}-O_5	1.2357	1.26	N_7-C_8-C_{11}	113.5122	113.5
C_{22}-O_6	1.2212	1.22	N_7-C_8-H_{30}	103.5083	
C_8-N_7	1.4628	1.465	C_9-C_8-C_{11}	111.8636	110
N_7-C_{22}	1.3694	1.33	C_9-C_8-H_{30}	107.82	

N_7-H_{35}	1.007		C_{11}-C_8-H_{30}	107.0233	
C_8-C_9	1.5494	1.55	C_8-C_9-C_{10}	114.7267	
C_8-C_{11}	1.5393	1.53	C_8-C_9-H_{31}	107.75	
C_8-H_{30}	1.0884		C_8-C_9-H_{32}	108.3134	
C_9-C_{10}	1.542	1.525	C_{10}-C_9-H_{31}	110.3485	
C_9-H_{31}	1.0943		C_{10}-C_9-H_{32}	108.4925	
C_9-H_{32}	1.0941		H_{31}-C_9-H_{32}	106.9171	
C_{12}-C_{10}	1.5098	1.5	C_9-C_{10}-C_{12}	112.609	
C_{10}-H_{33}	1.0946		C_9-C_{10}-H_{33}	108.9554	
C_{10}-H_{34}	1.0925		C_9-C_{10}-H_{34}	109.2413	
C_{11}-C_{14}	1.4421	1.465	C_{12}-C_{10}-H_{33}	109.2549	
C_{11}-C_{17}	1.3715	1.375	C_{12}-C_{10}-H_{34}	109.9195	
C_{12}-C_{13}	1.4125	1.395	H_{33}-C_{10}-H_{34}	106.6808	
C_{16}-C_{12}	1.3935	1.335	C_8-C_{11}-C_{14}	118.9748	117.5
C_{13}-C_{14}	1.4995	1.475	C_8-C_{11}-C_{17}	113.9129	113.5
C_{13}-C_{15}	1.4099	1.435	C_{14}-C_{11}-C_{17}	127.0369	128
C_{18}-C_{14}	1.3795	1.35	C_{10}-C_{12}-C_{13}	119.5213	119.5
C_{15}-C_{19}	1.4048	1.405	C_{10}-C_{12}-C_{16}	120.3055	
C_{20}-C_{16}	1.3935	1.395	C_{13}-C_{12}-C_{16}	120.1417	
C_{16}-H_{36}	1.0842		C_{12}-C_{13}-C_{14}	120.6336	
C_{17}-C_{21}	1.4556	1.455	C_{12}-C_{13}-C_{15}	118.0748	118.5
C_{17}-H_{37}	1.0866		C_{14}-C_{13}-C_{15}	121.2808	122.5
C_{23}-C_{18}	1.4109	1.395	C_{11}-C_{14}-C_{13}	119.7152	
C_{18}-H_{38}	1.0827		C_{11}-C_{14}-C_{18}	124.0598	123
C_{19}-C_{20}	1.4005	1.405	C_{13}-C_{14}-C_{18}	116.2244	
C_{21}-C_{24}	1.477	1.475	O_1-C_{15}-C_{13}	120.6064	119.5
C_{22}-C_{25}	1.5193	1.49	O_1-C_{15}-C_{19}	117.9794	
C_{23}-C_{24}	1.3739	1.379	C_{13}-C_{15}-C_{19}	121.3524	
C_{23}-H_{39}	1.0862		C_{12}-C_{16}-C_{20}	121.5396	121.5
C_{25}-H_{40}	1.092		C_{12}-C_{16}-H_{36}	120.4336	
C_{25}-H_{41}	1.0917		C_{20}-C_{16}-H_{36}	118.0162	
C_{25}-H_{42}	1.0921		C_{11}-C_{17}-C_{21}	134.9745	135
C_{26}-H_{43}	1.0944		C_{11}-C_{17}-H_{37}	115.8336	
C_{26}-H_{44}	1.0927		C_{21}-C_{17}-H_{37}	108.9737	
C_{26}-H_{45}	1.0894		C_{14}-C_{18}-C_{23}	131.9261	132.5

C_{27}-H_{46}	1.0895		C_{14}-C_{18}-H_{38}	115.025	
C_{27}-H_{47}	1.0928		C_{23}-C_{18}-H_{38}	112.99	
C_{27}-H_{48}	1.0939		O_2-C_{19}-C_{15}	120.1209	119.5
C_{28}-H_{49}	1.0893		O_2-C_{19}-C_{20}	120.1899	
C_{28}-H_{40}	1.0955		C_{15}-C_{19}-C_{20}	119.6778	120
C_{28}-H_{51}	1.0912		O_3-C_{20}-C_{16}	118.8053	118.5
C_{29}-H_{52}	1.092		O_3-C_{20}-C_{19}	121.8623	122.5
C_{29}-H_{53}	1.0866		C_{16}-C_{20}-C_{19}	119.2059	
C_{29}-H_{54}	1.0893		O_5-C_{21}-C_{17}	119.3217	
			O_5-C_{21}-C_{24}	119.9998	120
			C_{17}-C_{21}-C_{24}	120.6387	
			O_6-C_{22}-N_7	123.0857	
			O_6-C_{22}-C_{25}	121.5572	
			N_7-C_{22}-C_{25}	115.3556	
			C_{18}-C_{23}-C_{24}	131.6341	130
			C_{18}-C_{23}-H_{39}	115.0139	
			C_{24}-C_{23}-H_{39}	113.3454	
			O_4-C_{24}-C_{21}	119.9387	118
			O_4-C_{24}-C_{23}	114.2895	110
			C_{21}-C_{24}-C_{23}	125.339	128

Dihedral	**Angle (°) Theoretical**
C_{26}-O_1-C_{15}-C_{13}	-103.8572
C_{26}-O_1-C_{15}-C_{19}	78.9639
C_{15}-O_1-C_{26}-H_{43}	63.3324
C_{15}-O_1-C_{26}-H_{44}	-59.2438
C_{15}-O_1-C_{26}-H_{45}	-178.3183
C_{27}-O_2-C_{19}-C_{15}	82.183
C_{27}-O_2-C_{19}-C_{20}	-99.0469
C_{19}-O_2-C_{27}-H_{46}	179.5724
C_{19}-O_2-C_{27}-H_{47}	-61.4302
C_{19}-O_2-C_{27}-H_{48}	60.7883
C_{28}-O_3-C_{20}-C_{16}	116.7071
C_{28}-O_3-C_{20}-C_{19}	-67.4166
C_{20}-O_3-C_{28}-H_{49}	-179.5134
C_{20}-O_3-C_{28}-H_{50}	-61.394
C_{20}-O_3-C_{28}-H_{51}	61.014

C_{29}-O_4-C_{24}-C_{21}	-30.4452
C_{29}-O_4-C_{24}-C_{23}	156.7068
C_{24}-O_4-C_{29}-H_{52}	-44.6399
C_{24}-O_4-C_{29}-H_{53}	77.3117
C_{24}-O_4-C_{29}-H_{54}	-162.5513
C_{22}-N_7-C_8-C_9	128.1803
C_{22}-N_7-C_8-C_{11}	-103.5617
C_{22}-N_7-C_8-H_{30}	12.0881
H_{35}-N_7-C_8-C_9	-49.9568
H_{35}-N_7-C_8-H_{11}	78.3012
H_{35}-N_7-C_8-H_{30}	-166.049
C_8-N_7-C_{22}-O_6	1.6083
C_8-N_7-C_{22}-C_{25}	-177.9381
H_{35}-N_7-C_{22}-O_6	179.7517
H_{35}-N_7-C_{22}-C_{25}	0.2052
N_7-C_8-C_9-C_{10}	89.2384
N_7-C_8-C_9-H_{31}	-34.0859
N_7-C_8-C_9-H_{32}	-149.4127
C_{11}-C_8-C_9-C_{10}	-39.8803
C_{11}-C_8-C_9-H_{31}	-163.2046
C_{11}-C_8-C_9-H_{32}	81.4686
H_{30}-C_8-C_9-C_{10}	-157.2889
H_{30}-C_8-C_9-H_{31}	79.3868
H_{30}-C_8-C_9-H_{32}	-35.94
N_7-C_8-C_{11}-C_{14}	-56.3395
N_7-C_8-C_{11}-C_{17}	126.5979
C_9-C_8-C_{11}-C_{14}	72.2206
C_9-C_8-C_{11}-C_{17}	-104.8421
H_{30}-C_8-C_{11}-C_{14}	-169.8936
H_{30}-C_8-C_{11}-C_{17}	13.0437
C_8-C_9-C_{10}-C_{12}	-45.8576
C_8-C_9-C_{10}-H_{33}	75.524
C_8-C_9-C_{10}-H_{34}	-168.2868
H_{31}-C_9-C_{10}-C_{12}	76.0648
H_{31}-C_9-C_{10}-H_{33}	-162.5535
H_{31}-C_9-C_{10}-H_{34}	-46.3644
H_{32}-C_9-C_{10}-H_{12}	-167.1085
H_{32}-C_9-C_{10}-H_{33}	-45.7269
H_{32}-C_9-C_{10}-H_{34}	70.4623

C_9-C_{10}-C_{12}-C_{13}	70.8992
C_9-C_{10}-C_{12}-C_{16}	-107.0593
H_{33}-C_{10}-C_{12}-C_{13}	-50.3118
H_{33}-C_{10}-C_{12}-C_{16}	131.7297
H_{34}-C_{10}-C_{12}-C_{13}	-167.0542
H_{34}-C_{10}-C_{12}- C_{16}	14.9874
C_8-C_{11}-C_{14}-C_{13}	-3.722
C_8-C_{11}-C_{14}-C_{18}	176.573
C_{17}-C_{11}-C_{14}-C_{13}	172.9137
C_{17}-C_{11}-C_{14}-C_{18}	-6.7913
C_8-C_{11}-C_{17}-C_{21}	173.0421
C_8-C_{11}-C_{17}-H_{37}	-0.8625
C_{14}-C_{11}-C_{17}-C_{21}	-3.7385

7.3.3 Vibrational spectroscopy

The FT-IR and FT-Raman spectra (both theoretical and experimental) of brucine and colchicine are presented in figures 7.5 to 7.8.

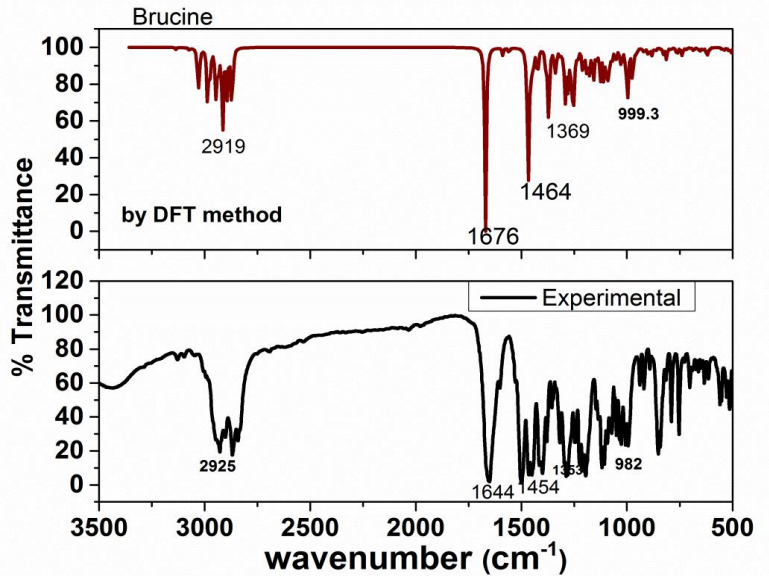

Figure 7.5 FTIR spectra of brucine. Theoretical spectrum is also shown

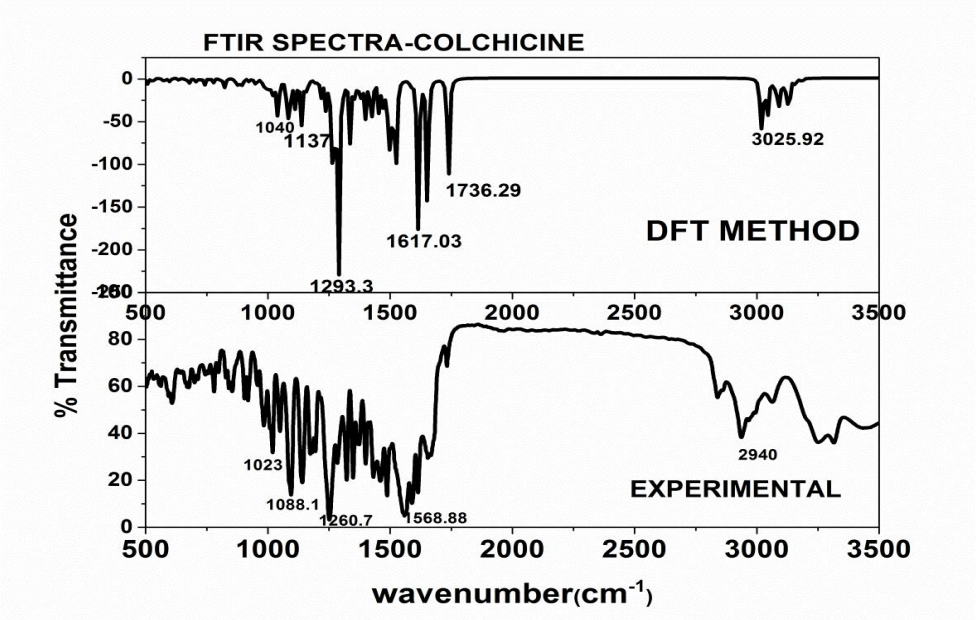

Figure 7.6 FTIR spectra of colchicine. Theoretical spectrum is also shown

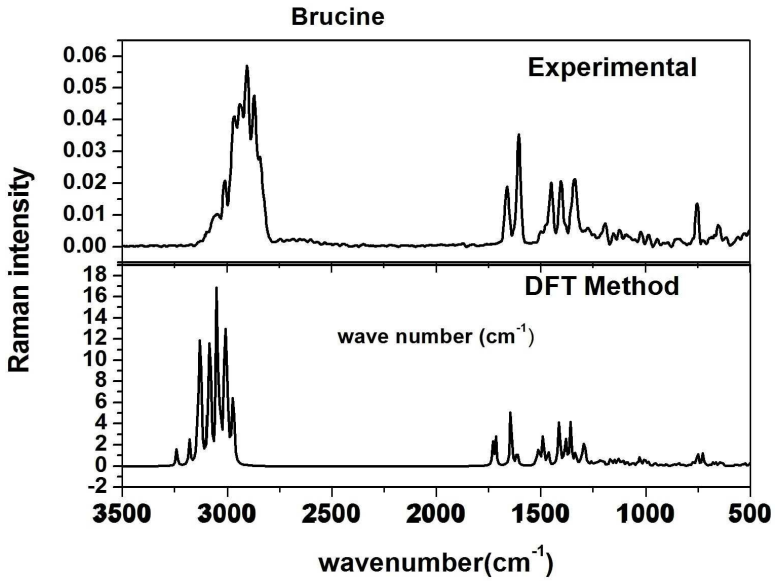

Figure 7.7 FT-Raman spectra of brucine Theoretical spectrum is also shown

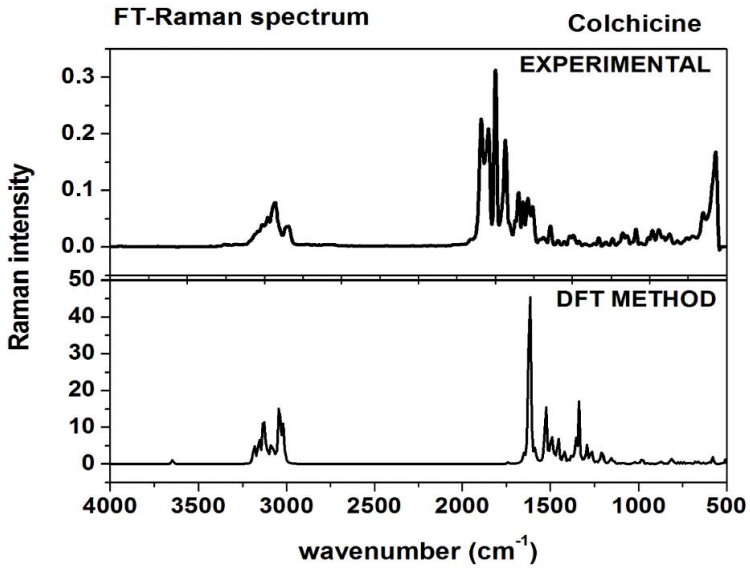

Figure 7.8 FT-Raman spectra of colchicine Theoretical spectrum is also shown

The assignments of skeletal vibrational modes and functional group vibrations in the mid-IR region are given in Tables 7.2 and 7.3. The carbonyl stretching C=O vibrations appear at 1665 cm^{-1} (IR), 1670 cm^{-1}(DFT) for brucine and 1723, 1618 (IR), 1716, 1620 cm^{-1} (DFT) for colchicine while C=C stretching modes were assigned at 1660 (Raman), 1658 (DFT) for brucine and at 1584, 1560, 1488 (IR), 1590 (Raman), 1583, 1572, 1489 (DFT) for colchicine. The C-O modes were seen in the range 1250–1020 cm^{-1}(IR), and at 1250, 1193 cm^{-1}(Raman) for brucine and at 1086, 1050, 921 (IR), 1098, 1060, 926 (Raman) for colchicine[44]. Most of the ring modes are also in agreement with theoretically predicted wavenumbers. To have a full understanding of the spectral and chiro-optic properties of these nonlinear oligo cyclic systems, we performed a detailed analysis of absorption behaviour and vibrational circular dichroism exhibited by these biologically active molecules.

Table 7.2 FTIR and FT-Raman peak positions of brucine

Sl. No	B3LYP/6-311G (d, p)			Experimental		Assignments
	Wavenumber (cm^{-1})	IR intensity	Raman activity	Crystal	Glassy	
1	33	1.1	0.21			
2	45	0.3	0.71			
3	51	2.12	0.39			
4	67	4.4	2.27			
5	80	2.99	0.71			
6	86	0.27	1.15			
7	103	0.21	0.88			
8	119	0.6	1.05			
9	146	0.33	0.9			
10	155	0.27	0.1			
11	166	0.93	1.19			
12	179	2.9	0.53			
13	195	0.75	4.16			
14	211	3.52	2.77			
15	221	1.89	5.01			
16	239	0.89	1.71			
17	263	3.75	0.92			
18	265	1.06	1.76			
19	286	3.3	1.2			
20	300	1.15	2.91			
21	320	6.02	3.36			
22	322	0.45	0.47			
23	345	1.53	1.47			
24	360	13.22	2.62			
25	364	0.37	4.09			
26	375	2.07	0.68			
27	395	0.55	1.67	402	408	

28	423	1.76	0.34	423		
29	428	6.76	1.4	430		
30	439	3.96	1.93	438		
31	455	10.73	1.29	456	458	
32	478	0.74	5.72	467	466	
33	486	11.15	0.85	485	486	
34	506	11.56	3.96	503	505	
35	519	5.48	1.78	517	521	
36	538	4.36	1.68			
37	546	1.31	1.03		542	
38	550	3.2	1.35	552	559	
39	609	3.8	5.78		605	
40	620	12.54	3.65	618	623	δ_{rings}
41	626	5.47	1.76	630		δ_{rings}
42	641	3.4	4.64		646	
43	653	5.64	3.48	649		δ_{rings}
44	662	3.33	1.13	661	669	δ_{rings}
45	684	7.65	1.47	685	689	$\gamma_{C=O}$
46	698	1.51	14.28	695		γ_{CC} of phenyl ring
47	718	4.33	14.81	722	712	γ_{CC} of phenyl ring
48	738	9.31	13.3		733	
49	741	8.88	3.94		744	
50	763	16.48	1.18	758	775	δ_{CH2}
51	792	3.42	2.19	791	790	δ_{CH}
52	810	2.59	2.01		802	
53	813	22.38	4.14	815	816	δ_{CH2}
54	829	12.47	3.08	830		δ_{CH2}
55	840	1	1.38	842	839	γ_{CH}, δ_{CH2}
56	861	4.02	0.46	857	851b	γ_{CH}
57	869	2.74	2.84		873	
58	883	16.52	0.39		888	
59	897	6.54	1.96	895		δ_{CH2}

60	900	9.35	0.36			
61	919	9.54	3.3	920	914	δ_{CH2}
62	926	2.41	3.56			
63	953	9.56	5.46	947		δ_{CH2}
64	965	4.13	1.99			
65	968	18.66	4.15			
66	975	51.78	7.71			
67	988	4.58	2.66		984	
68	998	104.08	10.76	996		υ_{CO}
69	1000	7.62	3			
70	1006	21.29	4.2	1007	1006	δ_{CH}
71	1026	30.56	4.2	1026	1025	υ_{CO}, δ_{CH2}
72	1032	15.01	2.6	1033		υ_{CO}
73	1051	13.29	4.3	1049	1047	δ_{CO}, δ_{CH2}
74	1055	15.17	2.95	1056		υ_{CO}, δ_{CH}
75	1070	15.03	5.62	1072	1070	δ_{CH2}
76	1075	10.16	2.19			
77	1083	23.6	4.67	1081		υ_{CN}, δ_{CH2}
78	1092	44.86	5.52	1092		υ_{CN}
79	1095	34.65	6.59			
80	1109	64.25	10.58	1108	1105	υ_{CN}
81	1124	54.15	6.02	1121	1118	δ_{CH2}
82	1130	10.84	8.45	1131		δ_{CH3}
83	1132	0.06	1.28			
84	1142	19.02	0.7	1144	1147	υ_{CO}
85	1157	45.41	0.54			
86	1162	26.19	8.16			
87	1171	2.98	5.32			
88	1178	42.44	6.91			
89	1186	9.98	2.73			
90	1189	35.5	3.01			
91	1193	11.02	3.39	1194	1193	υ_{CO}
92	1203	13.22	1.68			

93	1210	38.87	3.38	1209	1209	δ_{CH2}, υ_{CN}
94	1219	2.43	6.19			
95	1234	18.05	1.8	1228		δ_{CH}, δ_{CH2}
96	1243	13.32	4.43		1243	
97	1254	121.15	49.18	1250		υ_{CN}, δ_{CH2}
98	1260	47.91	6.54			
99	1266	19.8	11.96			
100	1277	38.6	1.56	1278		δ_{CH2}
101	1278	30.58	1.07	1278	1281b	δ_{CH2}
102	1283	10.78	1.97			
103	1291	80.92	3.74	1290		υ_{CC} of Phenyl ring, υ_{CN}
104	1294	22.76	15.78	1295		δ_{CH}
105	1301	19.1	2.85			
106	1314	5.67	33.95		1315	
107	1317	1.75	2.52			
108	1318	6.56	29.36	1318		δ_{CH2}
109	1337	42.07	34.11	1335		δ_{CH2}
110	1340	10.33	15.29			
111	1346	7.97	4.49			
112	1349	1.16	7.33	1350	1347	δ_{CH2}
113	1365	20.76	5.11	1362		δ_{CH}, δ_{CH2}
114	1369	45.85	33.76			
115	1374	105.04	61.6	1376		υ_{CN}, δ_{CH}
116	1384	37.83	0.43		1398b	
117	1423	55.61	20.29	1419		δ_{CH3}
118	1427	4.35	8.08			
119	1442	23.24	10	1444	1441b	δ_{CH3}
120	1449	5.92	13.91	1450		δ_{CH2}
121	1450	12.3	13.65			
122	1451	13.74	11.01			
123	1451	11.24	13.28			

124	1453	3.83	9.29			
125	1466	215.65	22.51	1466		υ_{CC} of Phenyl ring, δ_{CH3}
126	1467	6.58	2.02			
127	1471	95.5	12.79			
128	1480	7.72	7.56			
129	1484	0.39	7.79	1490	1502b	δ_{CH2}
130	1559	9.53	30.74	1535		υ_{CC} of phenyl ring
131	1588	13.88	124.59		1584b	
132	1658	10.04	47.43			
133	1670	384.37	38.75	1665	1650b	$\upsilon_{C=O}$
134	2866	37.46	38.67			
135	2868	6.98	23.96			
136	2873	83.31	138.31	2871		υ_{CH2}
137	2884	9.33	18.47			
138	2893	55.14	163.13			
139	2896	45.32	60.2			
140	2913	33.17	88.37	2909		υ_{CH2}
141	2914	80.31	117.28			
142	2917	64.38	165.98			
143	2933	34.39	128.62	2930	2939b	υ_{CH2}
144	2942	2.49	105.8			
145	2944	54.79	139.59			
146	2947	43.35	230	2947		υ_{CH2}
147	2950	16.83	52.09			
148	2973	46.23	65.45			
149	2980	14.57	108.37			
150	2984	23.67	33.23			
151	2986	34.07	66.43			
152	2988	20.1	46.2			
153	2988	33.71	156.68	2990		υ_{CH2}
154	3020	10.58	108.38	3015		υ_{CH2}

155	3028	29.86	162.64			
156	3029	32.18	165.11			
157	3033	31.67	190.32	3041		υ_{CH}
158	3073	5.39	62.27	3100		υ_{CH}
159	3136	3.77	46.66	3133	3135b	υ_{CH}

b-broad: υ-stretching; δ in-plane deformation; γ-out-of-plane deformation

Table 7.3 FTIR and FT-Raman peak positions of colchicine

Sl. no.	B3LYP/6-31G*			Crystal	amorphous	Assignments
		IR intensity	Raman activity			
1	20	3.15	3.56			
2	28	0.6	1.44			
3	34	0.72	2.49			
4	36	1.88	1.08			
5	43	2.28	0.58			
6	49	3.99	1.5			
7	57	5.41	0.7			
8	67	0.47	0.32			
9	69	7.71	3.73			
10	75	3.33	1.39			
11	88	5.92	1.64			
12	90	1.75	1.42			
13	105	0.44	1.91			
14	133	4.53	9.73			
15	137	1.39	3.38			
16	150	1.15	0.79			
17	155	0.67	1.9			
18	163	0.6	1.56			
19	165	0.21	0.42			
20	168	1.21	0.92			
21	187	5.42	0.86			
22	211	2.7	1.42			
23	222	3.17	1.96			
24	231	2.75	0.46			
25	239	1.11	0.7			

26	258	8.46	1.87			
27	266	10.29	1.47			
28	287	6.2	0.79			
29	297	7.51	0.22			
30	330	1.52	1.52			
31	337	2.8	0.82			
32	350	1.31	3.96			
33	355	5.6	1.02			
34	372	2.93	2.44			
35	381	0.55	0.67			
36	402	2.58	4.07	405		
37	414	7.34	26.22	414		
38	424	34.02	0.16	424		
39	430	30.92	1.49	432	436	
40	445	9.93	3.01	442	448	
41	465	12.14	5.79	463	470	
42	490	13.69	15.98	488	484	
43	511	12.64	5.71	512	508	
44	550	5.69	3.25			
45	560	3.47	24.81	562	568	δ_{rings}
46	575	5.37	3.87			
47	578	3.31	5.39			
48	610	2.36	1.54	609	606	γ_{NH}, $\gamma_{C=O}$
49	614	1.55	5.28			
50	634	1.41	10.95	635	637	γ_{rings}
51	653	15.77	12.32			
52	680	9.53	2.22	678	667	γ_{rings}
53	689	6.55	7.01			
54	712	13.25	3.68	713	709	γ_{rings}
55	726	3.98	6.48			
56	744	6.39	11.88	744	745	δ_{rings}
57	757	7.01	4.35	756	762	δ_{rings}
58	779	5.45	4.58	781	777	δ_{rings}
59	789	17.51	31.63			
60	837	8.8	11.96	832	823	δ_{CH2}
61	844	13.54	6.89	842	843	γ_{CH}

62	858	8.83	4.03	856		γ_{CH}
63	862	16.56	1.46			
64	894	7.3	1.35			
65	920	6.31	2.57	918	918b	υ_{CO}
66	926	14.01	7.46			
67	941	0.26	7.92			
68	950	2.64	26.48			
69	962	16.74	4.08	960	958b	υ_{CO}, δ_{CH3}
70	975	30.41	3.77	978	986	υ_{CO}
71	992	40.31	7.95			
72	1001	30.28	7.23			
73	1015	91.88	3.1	1012	1011b	υ_{CO}
74	1025	5.58	0.61	1022		δ_{CH3}
75	1049	88.27	3.36	1049	1047b	υ_{CC}
76	1062	73.63	5.38			
77	1074	7.04	1.48			
78	1083	82.23	3.6	1085	1084b	υ_{CN}
79	1105	92.37	6.62	1099		υ_{CO}, δ_{CH2}
80	1125	33.55	15.69			
81	1126	12.31	15.4			
82	1133	0.13	4.31			
83	1135	5.56	12.66			
84	1136	5.61	5.84	1140	1137b	δ_{CH3}
85	1160	10.2	5.3			
86	1168	6.84	50.75			
87	1173	1.77	17.19	1174	1172	δ_{CH3}
88	1175	0.27	14.15			
89	1185	39.4	20.34	1184	1190	δ_{CH3}
90	1202	61.46	15.4	1198	1190	δ_{CH}, δ_{CH2}
91	1216	7.16	6.79	1215	1221	δ_{CH2}, δ_{NH}
92	1227	152.94	40.55			
93	1234	17.09	38.39			
94	1245	92.56	55.23	1249	1248b	υ_{C-C}
95	1258	5.1	57.58			
96	1264	556.68	6.56			
97	1277	45.87	16.33	1280	1280	δ_{CH2}

98	1303	107.34	185.19			
99	1314	59.46	122.66	1318	1323	δ_{CH}
100	1329	18.67	39.06			
101	1340	64.95	49.52			
102	1354	56.74	14.01	1352	1348	δ_{CH}
103	1371	40.29	8.32	1371	1370	δ_{CH3}
104	1381	57.02	76.86			
105	1389	85.57	24.49			
106	1416	62.02	68.48	1414		υ_{C-C}
107	1419	37.9	75.33			
108	1440	14.52	20.48	1435	1429	δ_{CH3}
109	1441	6.39	27.21			
110	1444	5.37	7.9			
111	1445	4.77	8.08			
112	1449	9.74	25.24			
113	1454	44.42	74.02			
114	1455	31.43	45.57			
115	1458	24.44	13.76			
116	1459	10.5	12	1460	1456	δ_{CH3}
117	1460	0.6	42.85	1460	1456	δ_{CH3}
118	1463	53.03	11.3			
119	1463	11.71	36.55			
120	1466	13.96	24.87			
121	1474	8.57	7.33			
122	1476	34.4	19.63			
123	1481	242.37	18.42			
124	1484	18.01	22.48			
125	1489	22.9	379.9	1489	1482	$\upsilon_{C=C}$
126	1539	14.78	60.45	1528	1539b	υ_{C-C}
127	1572	216.76	477.01	1560		$\upsilon_{C=C}$
128	1576	45.98	788.1			
129	1583	14.88	38.13	1585	1584	$\upsilon_{C=C}$
130	1620	374.92	16.01	1618	1613b	$\upsilon_{C=O}$
131	1716	241.21	7.06	1725	1701b	$\upsilon_{C=O}$
132	2920	71.39	88.92			
133	2925	44.77	72.57			
134	2929	55.16	98.5			

135	2933	22.1	41.5			
136	2937	25.94	167.69	2937	2935	υ_{CH2}
137	2944	7.67	120.45			
138	2956	83.37	231.4	2960	2952b	υ_{CH3}
139	2971	22.38	94.67			
140	2984	30.94	79.46			
141	2995	28.7	27.77	2995	2984	υ_{CH3}
142	2998	21.62	37.3			
143	3001	36.07	79.98			
144	3010	7.41	27.2			
145	3015	16.13	69.56			
146	3021	7.82	60.11			
147	3029	35.8	145.36			
148	3033	30.93	138.98			
149	3036	21.23	83.55			
150	3039	23.38	149.27			
151	3054	3.23	63.56			
152	3055	11.907	99.57	3060	3053	υ_{CH}
153	3073	7.43	72.21			
154	3080	6.62	115.4			
155	3089	5.38	68.7			
156	3507	35.52	41.72	3455	3258b	υ_{NH}

7.3.4 Vibrational circular dichroism (VCD)

Vibrational circular dichroism (VCD) is an extension of circular dichroism spectroscopy into the IR and near-infrared region used to identify the absolute configuration and solution phase conformations[45] [46][47]. The VCD spectra of brucine and colchicine are shown in figure 7.9. The C-C stretching modes of the aromatic rings, C-H and C=O stretching modes at stereogenic centers generate VCD signals, and these are efficient identifiers of configuration identification of molecules, and also for optical purity and solution conformations that are primarily applied to alkaloid like organic systems[48]. Chiral molecules show differential absorption of left versus right circularly polarized IR radiation by a molecular vibrational transition depends on the product of the electric dipole transition moment onto the magnetic dipole transition moment. All (3N-6) vibrational modes of a chiral molecule (N being

the number of atoms in the molecule) can give rise to circular dichroism. For biologically significant molecules, VCD analysis can help in finding selective applications of the bio-active enantiomers in the pharmaceutical industry and understanding their biochemical interactions[49][50]. Brucine has two enantiomeric forms, and their calculated VCD spectra contain some important information about their chirality characteristics.

The CH_2 stretching modes of brucine show right polarization at 3004, 2950, 2940, 2895 cm^{-1}while modes at 3025, 2974, 2925cm^{-1} in the VCD spectra show left polarization. The VCD bands at 1380, 1357, 1317, 1273, 1075, 1025 $cm^{-1}$and 1447, 1346, 1301, 1244, 1222 cm^{-1} due to CH_2 and CH_3 groups are configuration markers showing right polarization and left polarization respectively for brucine. For brucine, the carbonyl stretching mode showing left polarization at 1678 cm^{-1}. For brucine, CO stretching modes at 1149 cm^{-1} show left polarization. For halogen-substituted brucine, the carbonyl stretching mode shows left polarization at 1669 (chlorine), 1667 (bromine), and 1668cm^{-1} (fluorine). The VCD bands in the range 11400–1100 cm^{-1} correspond to CH_2 andCH_3 groups are good markers of the configuration showing right polarization and left polarization for halogen-substituted brucine. The CH_2 stretching modes of colchicine (Fig.7.9) showing right polarization at 2973, 2931cm^{-1} while modes at 3095, 2939cm^{-1} in the VCD spectra showing left polarization. VCD spectral bands at 1595, 1527, 1493cm^{-1} corresponding to C=C stretching and 1466, 1432, 1370, 1269, 1224cm^{-1} corresponding to CH_2 and CH_3 groups are good markers of the configuration showing right polarization and left polarization respectively for colchicine. For colchicine, the carbonyl stretching mode shows the right polarization at 1629cm^{-1} and CO stretching modes of 1004cm^{-1} show left polarization. The VCD spectral bands in the range 11400–1100cm^{-1} from CH_2, and CH_3 groups are good markers of a configuration having right polarization and left polarization respectively for the halogen-substituted colchicine.

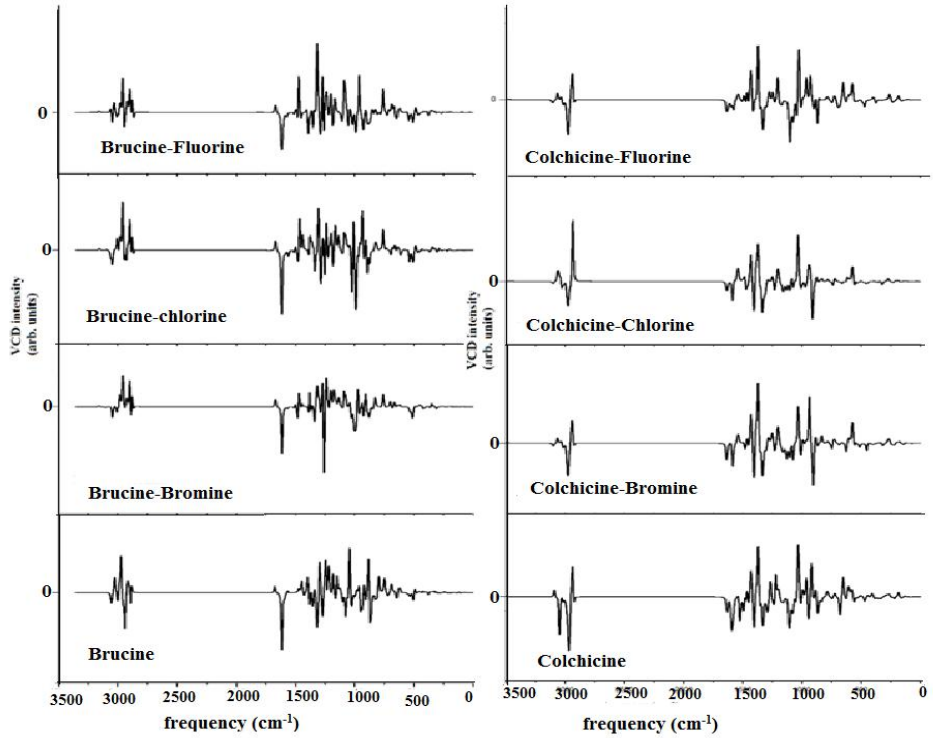

Figure 7.9 VCD spectra of brucine and colchicine

7.3.5 UV-Visible spectroscopy

The experimental and theoretical UV-Visible Spectroscopy was done to study the characteristics of the excited states of colchicine molecules by electronic absorption of radiation. The experimental UV-Visible spectrum of colchicine was recorded in methanol and theoretical UV-Visible spectrum was obtained in the gas phase by the TD-DFT method (B3LYP/6-311++g(d, p). The bandgap energy is calculated using E=hc/λ[51]. The excited electronic states, excitation energies, oscillator strengths, absorption wavelengths of colchicine were shown in table 4 and the comparative UV-Visible spectrum of colchicine is shown in figure 7.10. Figure 7.10 shows three absorption bands at 360 nm, 347 nm, and 329 nm. The maximum absorbed peak appears at 360 nm with an oscillator strength f = 0.2801, bandgap 3.4417 eV and HOMO-LUMO with 93% is responsible for n→π* transition. The other two bands at 347 and 329 nm have a maximum contribution from H-1 and a minor contribution from HOMO. These two bands can be assigned to mixed transitions including n→π* and π→π*.

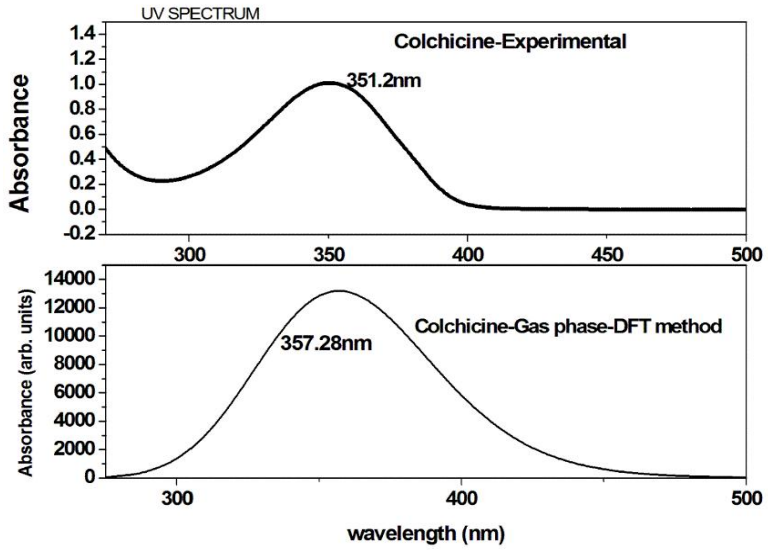

Figure 7.10 Theoretical and experimental UV spectra of colchicine

Table 7.4 Theoretical and experimental UV spectral characteristics of colchicine

States	λ_{obs} (nm)	λ_{cal} (nm)	f	E (cm^{-1})	Composition (%)
S1	351.2	360.24	0.28	27759.18	Singlet-A HOMO->LUMO (93%) HOMO->L+1 (2%)
S2		347.24	0.025	28798.02	Singlet-A H-1->LUMO (73%) H-3->LUMO (3%), H-1->L+1 (8%), HOMO->LUMO (4%), HOMO->L+1 (9%)
S3		329.78	0.039	30322.41	Singlet-A H-1->L+1 (51%), HOMO->L+1 (41%)

7.3.6 Frontier molecular orbital studies

The charge transfer characteristics of molecules are typically calculated by the pattern and energies of a molecule's HOMO (electron-donating nucleophile) and LUMO (electron-accepting electrophile) and Frontier Molecular Orbital Studies (FMO) provide data on the stability of a molecule from the energy gap between them[52][53]. If the energy difference between HOMO and LUMO is greater, the molecule's stability and chemical hardness will be greater and vice versa. The molecule is more chemically reactive and softer for a lower value of the energy difference[54]. The FMO diagram of the brucine is reported by N. Islam *et al.*[15]. From the HOMO-LUMO diagram of colchicine shown in figure 7.11, the highest occupied molecular orbitals (E_{HOMO}= -5.936 eV) and the lowest unoccupied molecular orbital (E_{LUMO}= -2.287 eV)

of colchicine are primarily concentrated over seven carbon rings, including the contribution of the carbonyl group and the methoxy substituent present on the seven-membered rings. This HOMO-LUMO colchicine diagram is shown in Figure 7.11. In addition, in the case of HOMO, the aromatic ring is evenly distributed by the electron density while the aromatic sextet makes a small contribution as the LUMO. The energy difference between HOMO-LUMO and colchicine is estimated at 3,649 eV and 4,831 eV for brucine.

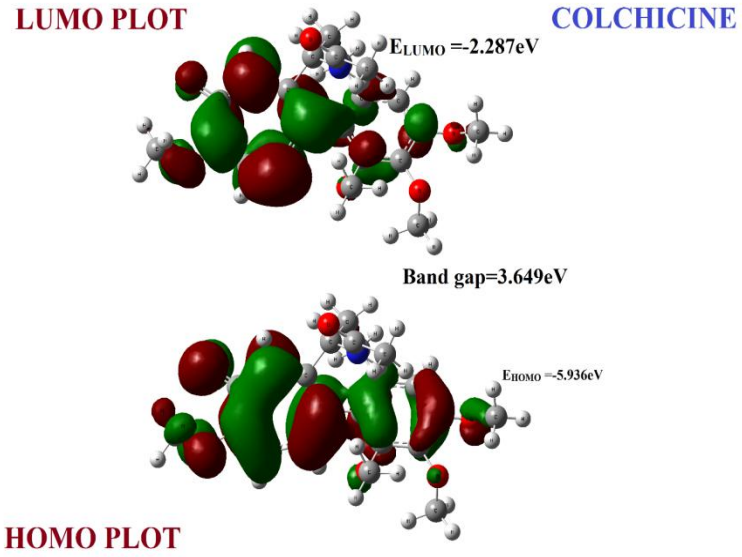

Figure 7.11 HOMO LUMO plot for colchicine

Table 7.5 shows the typical parameters that characterize the molecular chemical stability of brucine and colchicine. The energy band gap to the frontier molecular orbitals of brucine is greater than that of colchicine. Electron affinity values show that colchicine is more reactive than brucine, which is evident from the electronegativity values of brucine and colchicine. The chemical hardness of brucine is higher than that of colchicine. Colchicine's electrophilicity (G) is much higher than that of brucine, which suggests that the ability for colchicine to accept an electron pair is much greater than that of brucine. The full data reveals that colchicine is more stable than brucine.

Table 7.5 Stability parameters from frontier molecular orbitals of brucine and colchicine by B3LYP/6-311++G (d, p) method

Stability parameters	Colchicine	Brucine
E_{HOMO}	-5.936 eV	-5.576 eV
E_{LUMO}	-2.287 eV	-0.745 eV
Ionization potential (IP)	5.936 eV	5.576 eV
Electron affinity (EA)	2.287eV	0.745 eV
Energy gap (ΔE)	3.649 eV	4.831 eV
Electronegativity (χ)	4.11eV	3.161 eV
Chemical potential (V)	-4.11eV	-3.161 eV
Chemical hardness (η)	1.824 eV	2.4155 eV
Chemical softness (S)	0.548 eV	0.414 eV
Electrophilicity (ω)	4.63 eV	2.068 eV

7.3.7 Molecular electrostatic potential

The ideas about molecular shape, size, and also the neutral, negative, and positive electrostatic potential areas of the molecules are obtained from molecular electrostatic potential surfaces (MEP) and are expressed in the form of colour coding. It also offers information about how electronic and nuclear charges are distributed in a molecule. When MEP values are mapped to the surface of the electron density, one obtains a descriptive illustration of the reactivity of the molecule with respect to electrophilic and nucleophilic attack. With regard to electrophilic attacks, molecular areas characterized by negative MEP values are considered to be electrophilic-sensitive, whereas molecular areas characterized by positive MEP values are considered to be nucleophilic-sensitive. The MEP map is framed on the optimized geometry of brucine and colchicine to examine the chemical reactivity of the molecule and is shown respectively in Figures 7.12 and 7.13. The red colour in the MEP surface map indicates the electrophilic attack, or the maximum negative part and the blue colour indicates the nucleophilic part, or the maximum positive part[55]. The potential decreases in the

blue-green-yellow-orange-red order. Based on the results provided in Figure 7.12, it can be seen that there are differences between brucine and colchicine molecules in the maximal and minimal MEP values. While the difference between brucine and colchicine molecules 'minimum MEP values is 3 kcal/mol, the difference between their maximum MEP values is large and is equal to ~16 kcal/mol. MEP surfaces, therefore, indicate that the sensitivity of brucine and colchicine molecules to electrophilic attacks is rather similar, but the sensitivity to nucleophilic attacks appears to be quite different in favour of colchicine molecules. Red and purple colour locations on the MEP surfaces of brucine and colchicine molecules indicate sensitivity to electrophilic attacks of mostly oxygen atoms. The lowest MEP values suggest that oxygen atom locations could be sensitive to electrophilic attacks.

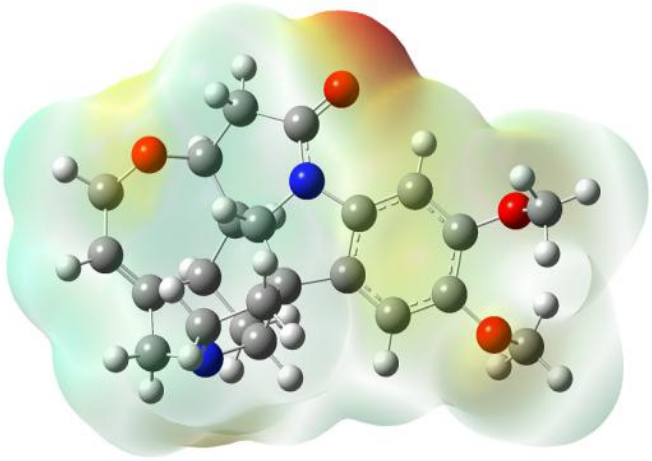

Figure 7.12 Molecular electrostatic potential surface of brucine

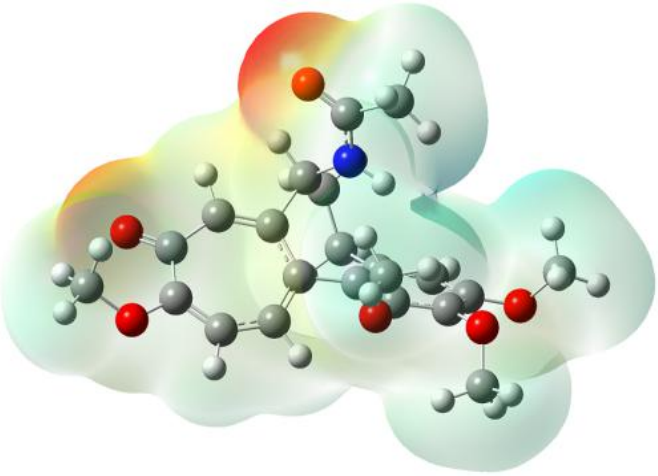

Figure 7.13 Molecular electrostatic potential surface of colchicine

7.3.8 Natural bond orbital (NBO) analysis

NBO analysis using NBO 3.1 program [31] to understand the effects of hyper-conjugation and its effect on inter-and intra-molecular interactions by providing information on both virtual and filled orbital spaces. The interaction between the idealized Lewis structure and the empty non-Lewis orbital is due to perturbation of the second order, corresponding to the brucine and colchicine intra-molecular bonds. Tables 7.6 and 7.7 show the second-order perturbation theory analysis of the Fock matrix for the intramolecular bonds of brucine and colchicine, and the Lewis and non-Lewis's orbitals are given in tables 7.8 and 7.9.

Table 7.6 Second-order perturbation theory analysis of Fock matrix in NBO basis corresponding to the intramolecular bonds of brucine

Donor(i)	Type	ED/e	Acceptor(j)	Type	ED/e	$E_{(2)a}$	$E_{(j)}$-$E_{(i)b}$	$F_{(ij)c}$
O_2-C_{21}	π	1.98804	C_{16}-C_{20}	σ*	0.02201	1.23	0.7	0.026
N_6-C_{21}	σ	1.98717	N_6-N_8	σ*	0.03055	1.26	1.1	0.033
-	-		N_6-C_{19}	σ*	0.03559	2.43	1.23	0.049
C_7-C_9	σ	1.96695	C_7-C_{14}	σ*	0.03252	1.76	1.01	0.038
C_8-C_{10}	σ	1.96994	C_7-C_8	σ*	0.03069	1.23	0.94	0.03
-	-		C_{10}-C_{11}	σ*	0.02944	1.25	0.96	0.031
C_{10}-C_{16}	σ	1.97867	C_7-C_8	σ*	0.03069	2.75	0.95	0.046
-			C_{11}-C_{12}	σ*	0.01634	1.27	0.96	0.031
C_{17}-C_{18}	σ	1.97866	C_{17}-C_{23}	σ*	0.02004	3.48	1.29	0.06
-		-	C_{23}-C_{24}	σ*	0.02701	3.96	1.02	0.057
C_{19}-C_{25}	π	1.65381	C_{14}-C_{22}	π*	0.36841	20.35	0.29	0.068
-		-	C_{26}-C_{27}	π*	0.42197	22.06	0.27	0.07
C_{20}-C_{21}	σ	1.98167	N_6-C_{19}	σ*	0.03559	4.25	1.04	0.06
C_{22}-C_{26}	σ	1.97241	O_4-C_{27}	σ*	0.02782	3.78	1.01	0.055
-		-	C_7-C_{14}	σ*	0.03252	4.72	1.12	0.065
-		-	C_{14}-C_{22}	σ*	0.02216	3.75	1.3	0.062
-		-	C_{26}-C_{27}	σ*	0.04497	3.97	1.26	0.063

C_{23}-C_{24}	σ	1.98447	C_{17}-C_{18}	σ*	0.03449	4.61	1.03	0.062
-		-	C_{17}-C_{23}	σ*	0.02004	3.29	1.31	0.059
C_{25}-C_{27}	σ	1.97091	O_3-C_{26}	σ*	0.02767	3.84	1	0.055
-		-	N_6-C_{19}	σ*	0.03559	5.8	1.11	0.072
-		-	C_{19}-C_{25}	σ*	0.02152	3.3	1.29	0.058
-		-	C_{26}-C_{27}	σ*	0.04497	4.1	1.26	0.064
C_{26}-C_{27}	σ	1.97997	C_{22}-C_{26}	σ*	0.02492	3.87	1.29	0.063
-		-	C_{25}-C_{27}	σ*	0.02543	3.79	1.3	0.063
C_{26}-C_{27}	π	1.6618	C_{14}-C_{22}	π*	0.36841	19.95	0.3	0.069
-		-	C_{19}-C_{25}	π*	0.38698	18.49	0.29	0.067
LPO1	π	1.96725	C_{10}-C_{16}	σ*	0.03891	6.63	0.64	0.059
-	-		C_{23}-C_{24}	σ*	0.02701	6.04	0.69	0.058
LPO2	σ	1.97428	N_6-C_{21}	σ*	0.0794	2.03	1.11	0.043
-	-		C_{20}-C_{21}	σ*	0.05742	2.2	1.04	0.043
-	π	1.87338	N_6-C_{21}	σ*	0.0794	25.26	0.68	0.118
-	-		C_{20}-C_{21}	σ*	0.05742	18.71	0.61	0.097
LPO3	σ	1.96337	C_{26}-C_{27}	σ*	0.04497	5.99	1.06	0.071
-	-		C_{26}-C_{27}	π*	0.42197	1.17	0.52	0.025
-	π	1.91741	C_{22}-C_{26}	σ*	0.02492	4.31	0.93	0.057
-	-		C_{26}-C_{27}	π*	0.42197	8.04	0.38	0.054
LPO4	σ	1.96285	C_{26}-C_{27}	σ*	0.04497	6.03	1.05	0.071
-	π	1.91634	C_{25}-C_{27}	σ*	0.02543	4.19	0.95	0.057
-	-		C_{26}-C_{27}	π*	0.42197	8.16	0.38	0.055
LPN5	σ	1.89312	C_7-C_9	σ*	0.04091	2.81	0.59	0.037
-	-		C_{17}-C_{18}	σ*	0.03449	6.79	0.65	0.06
LPN6	σ	1.64786	O_2-C_{21}	π*	0.29278	57.86	0.26	0.112
-	-		C_8-C_{10}	σ*	0.03087	3.8	0.61	0.047
-	-		C_{19}-C_{25}	π*	0.38698	33.15	0.29	0.089

Table 7.7 Second-order perturbation theory analysis of Fock matrix in NBO basis corresponding to the intramolecular bonds of colchicine

Donor(i)	Type	ED/e	Acceptor(j)	Type	ED/e	$E_{(2)a}$	$E_{(j)}$-$E_{(i)b}$	$F_{(ij)c}$
O_6-C_{22}	π	1.99394	O_6-C_{22}	σ*	0.04584	1.63	0.47	0.027
C_8-C_9	σ	1.973	N_7-C_{22}	σ*	0.07388	1.55	1.05	0.036
N_7-C_{22}	σ	1.99045	N_7-C_8	σ*	0.03535	1.59	1.15	0.038
C_{13}-C_{15}	σ	1.96899	O_2-C_{19}	σ*	0.02576	3.3	1.01	0.052
-		-	C_{12}-C_{13}	σ*	0.03069	3.84	1.25	0.062
-		-	C_{15}-C_{19}	σ*	0.04215	3.87	1.26	0.062
C_{13}-C_{15}	π	1.67005	C_{12}-C_{16}	σ*	0.02077	20.1	0.29	0.069
-		-	C_{19}-C_{20}	π*	0.41913	18.96	0.27	0.066
C_{15}-C_{19}	σ	1.97573	C_{13}-C_{15}	σ*	0.03501	4.38	1.27	0.067
-		-	C_{19}-C_{20}	σ*	0.04303	3.94	1.28	0.064
C_{16}-C_{20}	σ	1.97273	O_2-C_{19}	σ*	0.02576	4.16	1	0.058
-		-	C_{19}-C_{20}	σ*	0.04303	3.79	1.26	0.062
C_{17}-C_{21}	σ	1.97978	C_{11}-C_{17}	σ*	0.0216	3.95	1.29	0.064
C_{19}-C_{20}	σ	1.97629	C_{15}-C_{19}	σ*	0.04215	3.83	1.28	0.063
-		-	C_{16}-C_{20}	σ*	0.024	3.77	1.29	0.062
C_{19}-C_{20}	π	1.66027	C_{12}-C_{16}	π*	0.34442	17.41	0.3	0.065
-		-	C_{13}-C_{15}	π*	0.4154	21.67	0.29	0.072
C_{21}-C_{24}	σ	1.98281	C_{23}-C_{24}	σ*	0.02375	3.42	1.29	0.059
C_{23}-C_{24}	π	1.97747	O_5-C_{21}	π*	0.35773	21.57	0.27	0.069
-		-	C_{14}-C_{18}	π*	0.26433	20.8	0.3	0.072
LPO1	σ	1.95407	C_{13}-C_{15}	π*	0.4154	2.16	0.5	0.032
-		-	C_{15}-C_{19}	σ*	0.04215	5.41	1.04	0.067
LPO1	π	1.92209	C_{13}-C_{15}	σ*	0.03501	5.2	0.93	0.063
-		-	C_{13}-C_{15}	π*	0.4154	7.09	0.39	0.052
LPO2	σ	1.95163	C_{15}-C_{19}	σ*	0.04215	5.49	1.04	0.068
-		-	C_{19}-C_{20}	σ*	0.04303	2.3	0.5	0.034
-	π	1.9309	C_{15}-C_{19}	σ*	0.04215	1.81	0.93	0.037

-		-	C_{19}-C_{20}	σ*	0.04303	5.43	0.94	0.064
-		-	C_{19}-C_{20}	π*	0.41913	5.61	0.39	0.046
LPO3	σ	1.96058	C_{19}-C_{20}	σ*	0.04303	7.42	1.05	0.079
-	π	1.89667	C_{16}-C_{20}	σ*	0.024	3.2	0.92	0.049
-	-		C_{19}-C_{20}	π*	0.41913	13.79	0.36	0.069
LPO4	σ	1.96552	C_{21}-C_{24}	σ*	0.07204	7.08	0.98	0.075
-	π	1.80778	C_{23}-C_{24}	π*	0.26872	29.2	0.33	0.089
LPO5	σ	1.97829	C_{21}-C_{24}	σ*	0.07204	1.87	1.14	0.042
-	π	1.90042	C_{17}-C_{21}	σ*	0.04895	14.37	0.73	0.092
-	-		C_{21}-C_{24}	σ*	0.07204	16.83	0.69	0.097
LPO6	σ	1.97679	N_{7}-C_{22}	σ*	0.07388	2.15	1.12	0.044
-	π	1.86973	N_{7}-C_{22}	σ*	0.07388	22.84	0.69	0.113
LPN7	σ	1.69811	O_{6}-C_{22}	σ*	0.04584	2.42	0.72	0.04
-	-		O_{6}-C_{22}	π*	0.27382	49.51	0.31	0.111
-	-		C_{8}-C_{9}	σ*	0.02679	4.03	0.6	0.047
-	-		C_{8}-C_{11}	σ*	0.03535	6.43	0.62	0.06

[a]E(2) means the energy of hyper-conjugative interactions (stabilization energy in kcal/mol)

[b]Energy difference (a.u) between donor and acceptor i and j NBO orbitals

[c]F(i,j) is the Fock matrix elements (a.u) between i and j NBO orbitals

Table 7.8 NBO results showing the formation of Lewis and non-Lewis orbitals: brucine

Bond (A-B)	ED/e[a]	EDA%	EDB%	NBO	s%	p%
πO_{2}-C_{21}	1.98804	68.28	31.72	0.8263($sp^{99.99}$)O+	0.68	99.32
-		-	-	0.5632($sp^{99.99}$)C	0.6	99.4
σN_{6}-C_{21}	1.98717	63.78	36.22	0.7987($sp^{1.86}$)N+	34.98	65.02
-		-	-	0.6018($sp^{2.23}$)C	30.92	69.08
σC_{7}-C_{9}	1.96695	51.65	48.35	0.7187($sp^{2.93}$)C+	25.46	74.54
-		-	-	0.6954($sp^{2.82}$)C	26.15	73.85
σ C_{8}-C_{10}	1.96994	50.12	49.88	0.7079($sp^{2.68}$)C+	27.18	72.82

-		-	-	$0.7063(sp^{3.01})C$	24.93	75.07
σ C_{10}-C_{16}	1.97867	51.27	48.73	$0.7160(sp^{2.86})C+$	25.92	74.08
-		-	-	$0.6981(sp^{2.48})C$	28.73	71.27
σ C_{17}-C_{18}	1.97866	50.92	49.08	$0.7136(sp^{2.28})C+$	30.49	69.51
-		-	-	$0.7006(sp^{2.57})C$	28.02	71.98
π C_{19}-C_{25}	1.65381	50.21	49.79	$0.7086(sp^{1.00})C+$	0.01	99.99
-		-	-	$0.7056(sp^{99.99})C$	0.02	99.98
σ C_{20}-C_{21}	1.98167	51.13	48.87	$0.7150(sp^{2.87})C+$	25.82	74.18
-		-	-	$0.6991(sp^{1.74})C$	36.47	63.53
σ C_{22}-C_{26}	1.97241	50.24	49.76	$0.7088(sp^{1.89})C+$	34.61	65.39
-		-	-	$0.7054(sp^{1.62})C$	38.19	61.81
σ C_{23}-C_{24}	1.98447	50.01	49.99	$0.7072(sp^{2.17})C+$	31.55	68.45
-		-	-	$0.7070(sp^{2.36})C$	29.77	70.23
σ C_{25}-C_{27}	1.97091	49.91	50.09	$0.7064(sp^{1.89})C+$	34.61	65.39
-		-	-	$0.7078(sp^{1.60})C$	38.41	61.59
σ C_{26}-C_{27}	1.97997	50.01	49.99	$0.7072(sp^{1.69})C+$	37.24	62.76
-		-	-	$0.7071(sp^{1.69})C$	37.16	62.84
π C_{26}-C_{27}	1.6618	50.84	49.16	$0.7130(sp^{99.99})C+$	0.01	99.99
-		-	-	$0.7012(sp^{99.99})C$	0.01	99.99
n_1O_1	1.96725	-	-	$sp^{1.00}$	50.02	49.98
-	-0.5886					
n_2O_1	1.92992	-	-	$sp^{99.99}$	0.11	99.89
-	-0.2891					
n_1O_2	1.97428	-	-	$sp^{0.63}$	61.5	38.5
-	-0.6717					
n_2O_2	1.87338	-	-	$sp^{1.00}$	0	100
-	-0.2406					
n_1O_3	1.96337	-	-	$sp^{1.74}$	36.56	63.44
-	-0.5018					
n_2O_3	1.91741	-	-	$sp^{7.68}$	11.52	88.48
-	-0.3574					
n_1O_4	1.96285	-	-	$sp^{1.82}$	35.49	64.51
-	-0.4921					

n_2O_4	1.91634	-	-	$sp^{6.87}$	12.71	87.29
-	-0.3627					
n_1N_5	1.89312	-	-	$sp^{6.59}$	13.17	86.83
-	-0.2541					
n_1N_6	1.64786	-	-	$sp^{49.11}$	2	98
-	-0.2596					

[a] ED/e is expressed in a.u.

Table 7.9 NBO results showing the formation of Lewis and non-Lewis orbitals: colchicine

Bond (A-B)	ED/ea	EDA%	EDB%	NBO	s%	p%
πO_6-C_{22}	1.99394	68.88	31.12	0.8300(sp23.82)O+	4.03	95.97
-		0.42043		0.5578(sp27.20)C	3.55	96.45
σC_8-C_9	1.973	51.09	48.91	0.7148(sp2.70)C+	26.91	73.09
-		0.59763		0.6994(sp2.78)C	26.48	73.52
σN_7-C_{22}	1.99045	62.61	37.39	0.7913(sp1.71)N+	36.86	63.14
-		0.82779		0.6115(sp2.15)C	31.72	68.28
σC_{13}-C_{15}	1.96899	50.91	49.09	0.7135(sp1.98)C+	33.59	66.41
-		0.71638		0.7006(sp1.58)C	38.82	61.18
πC_{13}-C_{15}	1.67005	51.19	48.81	0.7155(sp99.99)C+	0.01	99.99
-		0.27365		0.6986(sp99.99)C	0.02	99.98
σC_{15}-C_{19}	1.97573	50.05	49.95	0.7075(sp1.70)C+	37.04	62.96
-		0.73243		0.7068(sp1.65)C	37.67	62.33
σC_{16}-C_{20}	1.97273	49.8	50.2	0.7057(sp1.92)C+	34.26	65.64
-		0.71516		0.7085(sp1.65)C	37.8	62.2
σC_{17}-C_{21}	1.97978	50.67	49.33	0.7118(sp1.91)C+	34.33	65.67
-		-0.6854		0.7024(sp1.75)C	36.43	63.57
σC_{19}-C_{20}	1.97629	50.27	49.73	0.7090(sp1.65)C+	37.76	62.24
-		-0.73305		0.7052(sp1.71)C	36.93	63.07
πC_{19}-C_{20}	1.66027	52.44	47.56	0.7241(sp99.99)C+	0.02	99.98
-		0.28195		0.6896(sp99.99)C	0.02	99.98

σC_{21}-C_{24}	1.98281	48.72	51.28	0.6980(sp1.95)C+	33.9	66.1
-		0.69697		0.7161(sp1.78)C	36.02	63.98
πC_{23}-C_{24}	1.68924	52.81	47.19	0.7267(sp99.99)C+	0.02	99.98
-		-0.2754		0.6870(sp1.00)C	0.01	99.99
n_1O_1		1.95407		sp2.08	32.44	67.56
-		0.49383				
n_2O_1		1.92209		sp6.28	13.74	86.26
-		0.38746				
n_1O_2		1.95163		sp2.04	32.88	67.12
-		-0.5004				
n_2O_2		1.9309		sp6.36	13.58	86.42
-		0.38834				
n_1O_3		1.96058		sp1.91	34.32	65.68
-		0.49701				
n_2O_3		1.89667		sp8.45	10.59	89.4
-		0.36217				
n_1O_4		1.96552		sp1.66	37.65	62.35
-		0.51961				
n_2O_4		1.80778		sp61.93	1.59	98.41
-		-0.3141				
n_1O_5		1.97829		sp0.56	64.01	35.99
-		0.68094				
n_2O_5		1.90042		sp1.00	0	100
-		0.23466				
n_1O_6		1.97679		sp0.60	62.58	37.42
-		0.67065				
n_2O_6		1.86973		sp99.99	0.05	99.95
-		0.23386				
n_1N_7		1.69811		sp1.00	0	100
-		0.25424				

a ED/e is expressed in a.u.

In the brucine molecule, the interactions of C_{10}-C_{16} from O_1 of $n_2(O_1)\rightarrow\sigma^*$ (C_{10}-C_{16}), C_{26}-C_{27} from O_3 of $n_2(O_3)\rightarrow\pi^*(C_{26}$-$C_{27})$, N_6-C_{21} from O_2 of $n_2(O_2)\rightarrow\sigma^*$ (N_6-C_{21}), C_{26}-C_{27} from O_4 of $n_2(O_4)\rightarrow\pi^*(C_{26}$-$C_{27})$, C_{17}-C_{18} from N_5 of $n_1(N_5)\rightarrow\ \sigma^*(C_{17}$-$C_{18})$ and O_2-C_{21} from N_6 of $n_1(N_6)\rightarrow\pi^*$ (O_2-C_{21}) are the important hyper conjugative interactions (intra-molecular) with stabilization energies, 6.63, 25.26, 8.04, 8.16, 6.79 and 57.86 kJ/mo. The natural orbital hybrid with p-character, higher energy, and low brucine occupancy numbers are n_2 (O_1), n_2 (O_2), n_2 (O_3), and n_2 (n_2) (O_4). The corresponding energy values and low occupation numbers are respectively, -0.28906, -0.24058, -0.35736, -0.36270 a.u. and 1.92992, 1.87338, 1.91741, 1.91634. The low-energy orbitals are n_1 (O_1), n_1 (O_2), n_1 (O_3), and n_{11} (O_4). The respective energy and high occupancy numbers are -0.58858, -0.67171, -0.50175, -0.49211 a.u. 1.96725, 1.97428, 1.96337, 1.96285, and 1.96725. Therefore, a nearly pure p-type lone pair orbital participates in the donation of electrons to $n_2(O_1)\rightarrow$ (C_{10}-C_{16}) σ^*, $n_2(O_2)\rightarrow(N_6$-$C_{21})\ \sigma^*$, $n_2(O_3)\rightarrow\pi^*(C_{26}$-$C_{27})$, ($O_4$) $n_2\rightarrow\pi^*(C_{26}$-$C_{27})$, ($N_5$) $n_1\rightarrow\sigma^*$ (C_{17}-C_{18}) and $n_1(_{N6})$ Interactions of $\pi^*(O_2$-$C_{21})$. The higher the stabilization energy values of the second-order, the higher the molecule conjugation from the interaction between electron acceptors and donors.

The significant intra-molecular hyper conjugative interactions in the colchicine molecule are C_{13}-C_{15} from O_1 of $n_2(O_1)\rightarrow\pi^*(C_{13}$-$C_{15})$, C_{19}-C_{20} from O_2 of $n_2(O_2)\rightarrow\pi^*(C_{19}$-$C_{20})$, C_{19}-C_{20} from O_3 of $n_2(O_3)\rightarrow\ \pi^*(C_{19}$-$C_{20})$, C_{23}-C_{24} from O_4 of $n_2(O_4)\rightarrow\pi^*$ (C_{23}-C_{24}), C_{21}-C_{24} from O_5 of $n_2(O_5)\rightarrow\sigma^*(C_{20}$-$C_{24})$, N_7-C_{22} from O_6 of $n_2(O_6)\rightarrow\sigma^*(N_7$-$C_{22})$, O_6-C_{22} from N_7 of $n_1(N_7)\rightarrow\sigma^*(O_6$-$C_{22})$ with stabilization energies, 7.09, 5.61, 13.79, 29.20, 16.83, 22.84 and 49.51 KJ/mol. The natural hybrid orbital with significant p-characters, high energies, and low occupation numbers are n_2 (O_1), $n_2(O_2)$, $n_2(O_3)$, $n_2(O_4)$, $n_2(O_5)$, and $n_2(O_6)$ in the colchicine molecule. 1.92209, 1.93090, 1.89667, 1.80778, 1.90042, 1.86973 and -0.38746, -0.38834, -0.36217, -0.31410, -0.23466, -0.23386 a.u. are the respective occupation numbers and energies. The low-energy high-occupancy orbital numbers for the colchicine molecule are $n_1(O_1)$, $n_1(O_2)$, $n_1(O_3)$, $n_1(O_4)$, $n_1(O_5)$, and n_1 (O_6). These orbital energies are -0.49383, -0.50040, -0.49701, -0.51961, -0.68094, -0.67065 and -0.67065 a.u. with high occupancy numbers 1.95407, 1.95163, 1.96058, 1.96552, 1.97829 and 1.97679 respectively. Thus, in colchicine, a pure p-type lone pair orbital participates in the electron donation to the

$n_2(O_1)\rightarrow\pi^*(C_{13}\text{-}C_{15})$, $n_2(O_2)\rightarrow\pi^*(C_{19}\text{-}C_{20})$, $n_2(O_3)\rightarrow\pi^*(C_{19}\text{-}C_{20})$, $n_2(O_4)\rightarrow\pi^*(C_{23}\text{-}C_{24})$, $n_2(O_5)\rightarrow\sigma^*(C_{20}\text{-}C_{24})$, $n_2(O_6)\rightarrow\sigma^*(N_7\text{-}C_{22})$ and $n_1(N_7)\rightarrow\sigma^*(O_6\text{-}C_{22})$ interaction. The significant intra-molecular interaction between the molecules provides evidence that, due to intra-molecular hyperconjugation interactions, the molecules are highly stable. The higher values of the title compounds' second-order perturbation energies predict strong hyper-conjugative interaction between the lone pair of electrons containing the orbital and the neighboring C=O anti-bonding orbital.

7.3.9 Nonlinear optical properties

A molecule's NLO properties provide useful information for its use in optoelectronic application [11]and are due to the differential interaction between light and materials. In various electronic devices, such as televisions, light-emitting diodes, etc., these properties are very important. Organic compounds dominate traditional semiconductor electronics nowadays. For this purpose, the polarizability and hyperpolarizability information obtained from the Raman frequency calculations can be used. 4.239 Debye, 4.196×1023, 3.323×1030, 23.746×1037 e.s.u for brucine and 6.094 Debye, 4.124×1023, 2.880×1030, 25.168×1037 e.s.u for colchicine, respectively,
are the dipole moment, polarizability, first hyperpolarizability, and second hyperpolarizability values. To compare the NLO properties of the compounds of interest, the organic material urea is typically considered a standard material. The first hyperpolarizability values of brucine and colchicine are 25.56 and 22.15 times those of urea,[56] indicating that it is possible to develop title compounds with the potential to show very high NLO properties for use in organic electronics.

7.3.10 Light harvesting efficiency

Light-harvesting efficiency (LHE) parameter can be used to predict the efficiency of a compound as a potential photosensitizer in dye-sensitized solar cells (DSSC)’s [57]. For arbitrary halogen substitutions in the benzene ring, the LHE values for brucine and colchicine showed that both brominated brucine and colchicine had more LHE values than for other halogen substitutions. The methyl group attached to the carbon atoms C_{27} and C_{24} of brucine and colchicine respectively is replaced by the halogen atoms fluorine, bromine, and chlorine to find the LHE of halogenated

substitution in brucine and colchicine. Figures 7.14 and 7.15 show the simulated UV spectra of brucine and chlorinated brucine.

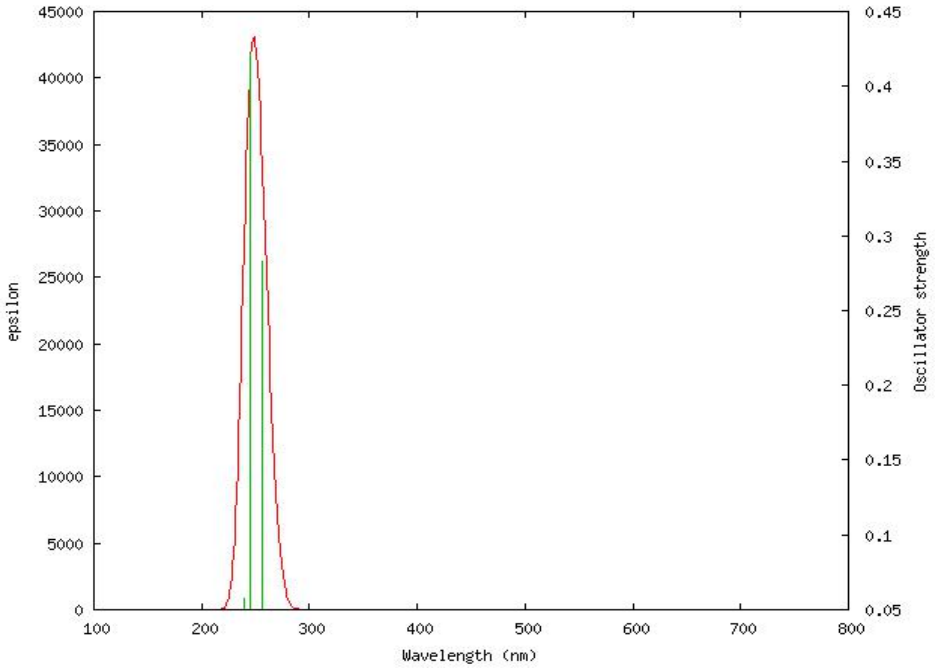

Figure 7.14 Simulated UV spectra of brucine

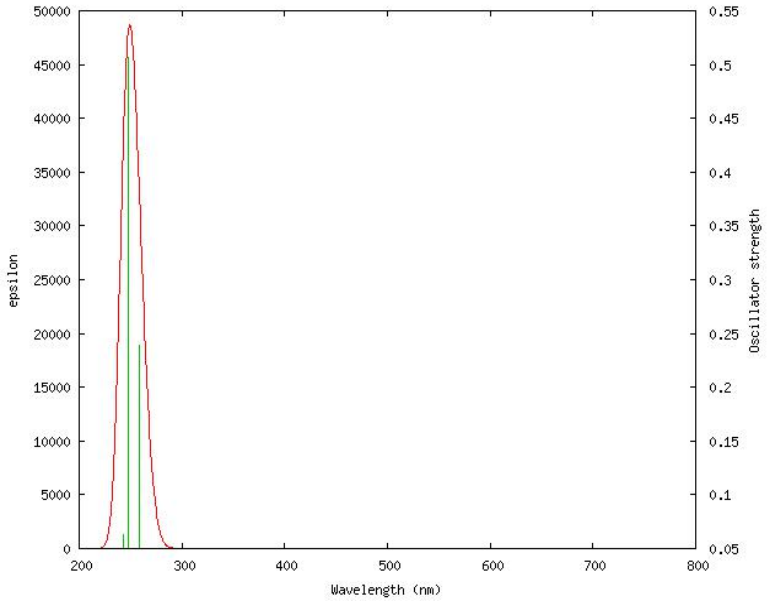

Figure 7.15 Simulated UV spectra of chlorinated Brucine

The TD-DFT calculations show three significant electronic transitions with oscillator strengths of 0.2831, 0.4221, and 0.0575, respectively, at 256.6, 245.6, and 239.5 nm. The first transition is between HOMO-1to LUMO (22%), HOMO to LUMO (34%), HOMO to LUMO+1 (11%). The second is due to HOMO-1 to LUMO (16%),

HOMO-1 to LUMO+1 (17%), HOMO to LUMO (18%), HOMO to LUMO+1 (24%), and third is due to H-1 to LUMO+2 (24%), HOMO to LUMO+1 (11%), HOMO to LUMO+ 2 (35%). The LHE values for brucine for various transitions are 0.4789, 0.6216, and 0.1240, respectively. Table 7.10 shows the LHE values for brucine and colchicine and their different halogen substitutions.

Table 7.10 Light Harvesting Efficiency of brucine, colchicine and their halogen substitutions

Sample	Energy (cm^{-1})	Wavelength (nm)	Osc. Strength	LHE
Brucine	38969.75	256.61	0.2831	0.4789
	40711.92	245.63	0.4221	0.6216
	41745.13	239.55	0.0575	0.124
Fluorinated brucine	37693.78	265.2958	0.2788	0.4737
	40322.35	248.0014	0.5002	0.6839
	41034.55	243.6971	0.0611	0.1312
Chlorinated brucine	38707.62	258.3471	0.2388	0.423
	40380.43	247.6447	0.5064	0.6884
	41110.36	243.2477	0.0632	0.1354
Colchicine	28416.72	351.9055	0.5873	0.7414
	30697.67	325.7576	0.3231	0.5248
	32509.21	307.6052	0.0039	0.0089
Fluorinated colchicine	29939.51	334.0068	0.4841	0.672
	33288.34	300.4054	0.0444	0.0972
	33610.97	297.5219	0.3402	0.5431
Chlorinated colchicine	38707.62	258.3471	0.2388	0.423
	40380.43	247.6447	0.5064	0.6884
	41110.36	243.2477	0.0632	0.1354
Brominated colchicine	37193.71	268.8627	0.2411	0.426
	39789.22	251.3244	0.6424	0.7722
	40871.62	244.6685	0.0006	0.0014

There are also three transitions corresponding to wavelengths 265.29, 248.00, and 243.69 nm with oscillations of 0.2788, 0.5002, and 0.0611 respectively in the case of compounds with fluorine in the side aromatic ring (table 7.10). For the first transition, the major contribution is due to HOMO-1 to LUMO (42%) and HOMO to LUMO (33%) and for the second HOMO-1 to LUMO (11%), HOMO-1 to LUMO+1 (39%), HOMO to LUMO+1 (32%) and finally for the third, HOMO-1 to LUMO+2 (18%), HOMO to LUMO+2 (56%). The theoretically calculated LHE values, respectively, are 0.4737, 0.683, and 0.1312. Once again, the TD-DFT analysis shows three λ_{max} oscillations slightly lower than the fluorinated derivative, but higher than the unsubstituted brucine oscillation). The electronic transitions in this derivative occur at 258.34, 247.644, and 243/24 nm of oscillator strength of 0.2388. 0.5064 NS 0.0632, respectively. The major contributions to the electronic spectra are due to HOMO-1 to LUMO (42%), HOMO-1 to LUMO+1 (26%), HOMO to LUMO (12%) for the first, HOMO-1 to LUMO (32%), HOMO-1 to LUMO+1 (38%), HOMO to LUMO+1 (14%) for the second and HOMO to LUMO+2 (64%), HOMO to LUMO+3 (11%) for the third. The LHE data provided in Table 7.11 shows 0.423, 0.68884, and 0.1354, which is a clear indicator of the gradual increase in the efficiency of light-harvesting. For brominated brucine, there is a redshift from other halogenated compounds with electronic excitations at 268.86, 251.32, and 244.66 nm having 0.2411. 0.6424 and 0.000, respectively. The electrons participate in HOMO-1 to LUMO (33%), HOMO to LUMO (55%) for the first transition, HOMO-1 to LUMO+1 (34%), HOMO to LUMO+1 (56%) for the second, and HOMO-1 to LUMO+2 (27%), HOMO to LUMO+2 (40%) for the third. The LHE values also indicate an increase in the compounds' harvesting power. For the various transitions, the values are 0.4260, 0.7722, and 0.0014. It can therefore be concluded that the brominated brucine has more LHE than the others.

The different electronic transitions and the LHE of this compound's various halogenated derivatives are also analyzed, and the results are discussed as follows. At 351.90, 325.75, and 307.60 nm. Pure colchicine showed three major electronic transitions with oscillator strengths of 0.5873, 0.323, and 0.0031, respectively. The first transition near-visible range is HOMO to LUMO (94%), the second HOMO to LUMO+1 (86%), and the third HOMO-3 to LUMO (31%), HOMO-3 to LUMO+1

(45%). The molecule shows good light-harvesting efficiency, as evident from the values 0.7414, 0.5248, and 0.008, respectively. Fluorinated colchicine shows wavelength 334.00, 300.40, and 297.52 having oscillator strength 0.4841, 0.0444, and 0.3402 respectively. The data shows that on fluorination there is a blue wavelength shift. The first transition is HOMO to LUMO (90%), the second HOMO-6 to LUMO (10%), HOMO-6 to LUMO+1 (33%), HOMO-3 to LUMO+1 (14%), HOMO to LUMO+1 (10%), and the third HOMO to LUMO+1 (69%). Fluorination decreased the intensity of the HOMO to LUMO transition. The light-harvesting values are 0.4260, 0.7722, and 0.0014.

A further blue shift with values of 258.34, 247.64, and 243.25 nm with oscillator strengths of 0.2388, 0.5064, and 0.0632 is observed when substituted with chlorine. The LHE values, which are higher than the fluorinated analogue, are 0.2388, 0.5064, and 00632. The transitions are due to HOMO to LUMO (90%), H-6 to LUMO (10%), HOMO-6 to LUMO+1 (33%), HOMO-3 to LUMO+1 (14%), HOMO to LUMO+1 (10%) & HOMO to LUMO+1 (69%) respectively. In the case of brominated analogue, excitations with oscillator strengths of 0.2411, 0.6424, and 0.0006 with corresponding LHE values of 0.4260, 0.7722, and 0.0014 are at 268.86, 251.32, and 244.67 nm. The brominated system, therefore, has more LHE among the colchicine analogues,

7.3.11 Molecular docking

The docking calculations were carried out in the Schrodinger suite using the quantum computational software Maestro (V18.4).[58][59]. The ligand, through weak non-covalent interactions, binds at the active sites of the substrate. Table 7.11 shows the binding affinity, nature, and distance of the interaction of docked ligands (brucine and colchicine) with the amino acids of the proteins selected. Figures 13-18 are shown in the docked ligand and ligand interaction diagram of brucine and colchicine for various cancer proteins. Brucine showed the lowest binding affinity of -8.218 kcal/mol to cancer protein (PDBID 5JMJ) interacting with amino acid TRY55 at a distance of 1.9 A through hydrogen bond, while colchicine showed a lowest binding affinity of -5.298 kcal/mol with cancer protein (PDBID 3 S7 S) and interaction with aminoacid ALA438 through hydrogen bond at 2.11 A. Colchicine showed a binding affinity of -

4.68 kcal/mol to cardiovascular protein (5G3 N) and interacted via hydrogen bond at a distance of 2.03 A with amino acid VAL30.

Table 7.11 Binding affinity, nature of the interaction of docked ligands with various proteins

Ligand	PDBID of Protein	Docking Score	Nature of	Length of interaction	Interacted
		kCal/mol	Interaction	(A)	Amino-acid
Brucine	5JM5	-8.218	H BOND	1.9	TRY55
			H BOND	2.63	GLN222
	3U9U	-3.809	H BOND	1.97	SER43
			H BOND	2.06	THR94
	4AOW	-2.895	H BOND	1.79	ARG155
			H BOND	2.3	GLN20
	5NWH	-2.469	H BOND	2.25	ARG51
Colchicine	3S7S	-5.298	H BOND	2.11	ALA438
	5NQR	-4.5	H BOND	2.12	ALA195
			H BOND	1.77	ARG196
			H BOND	2.63	ARG51
	3U9U	-4.24	H BOND	1.98	THR94
			H BOND	2.36	SER43
	1BHJ	-4.2	H BOND	2.24	THR599
	1JNX	-2.387	H-BOND	2	HIE1822
Colchicine	(Cardiovascular) 5G3N	-4.684	H BOND	2.03	VAL30

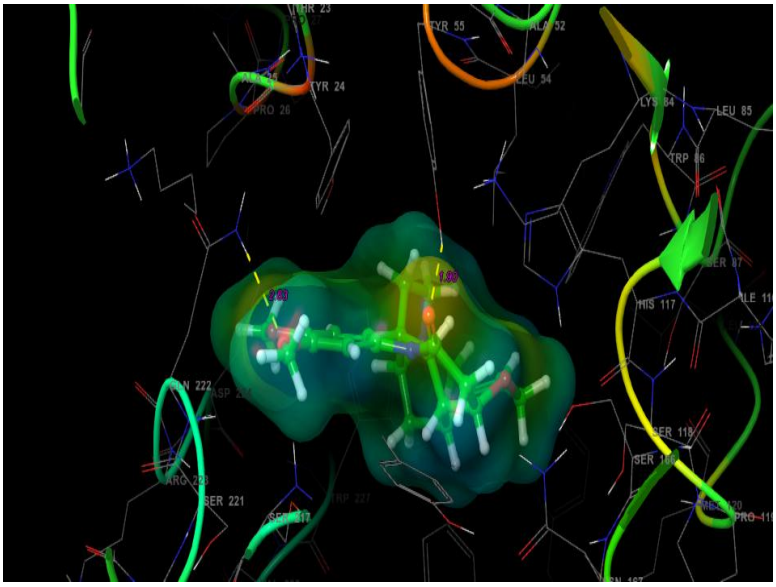

Figure 7.16 Molecular docking of brucine (yellow dotted lines) showing the hydrogen bond interactions with protein PDBID 5JM5

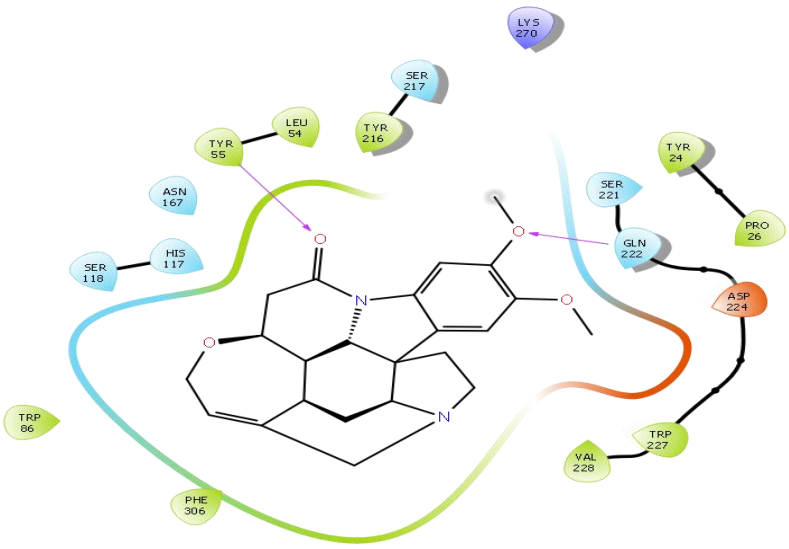

Figure 7. 17 ligand interaction diagram of brucine with protein PDBID 5JM5

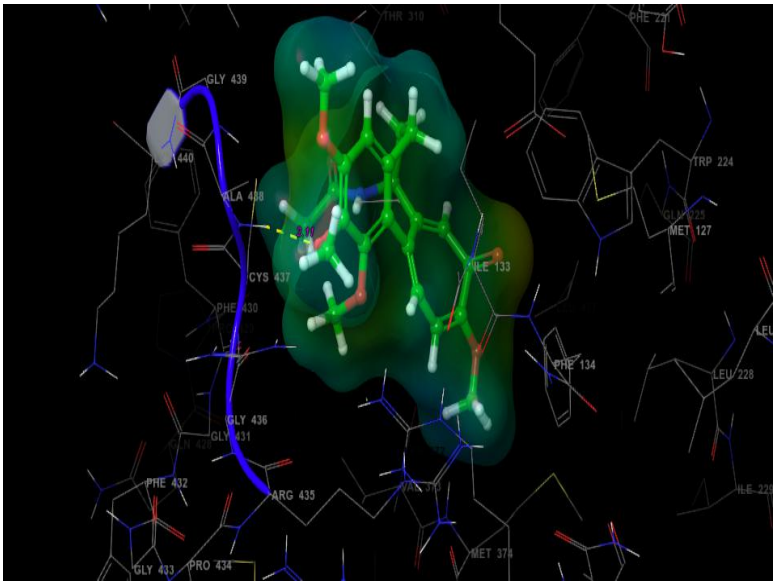

Figure 7.18 Molecular docking of colchicine (yellow dotted line) showing the hydrogen bond interactions with 3S7S

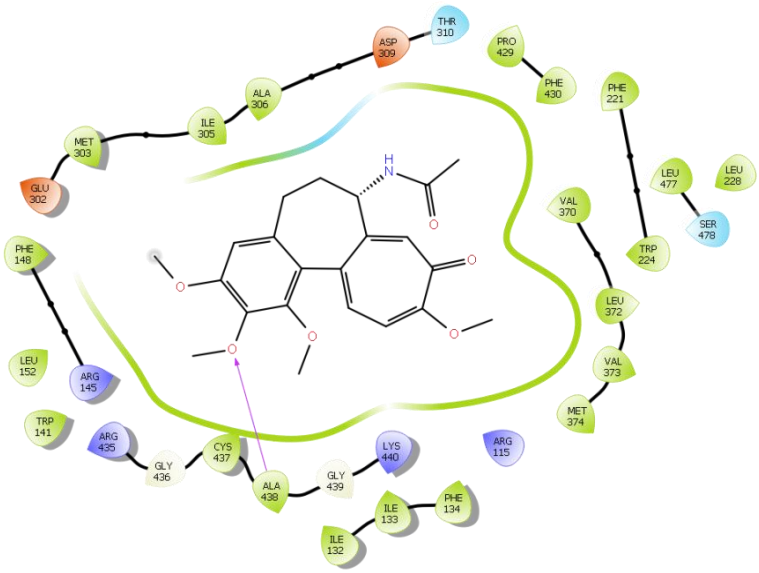

Figure 7.19 Ligand interaction diagram of colchicine with 3S7S

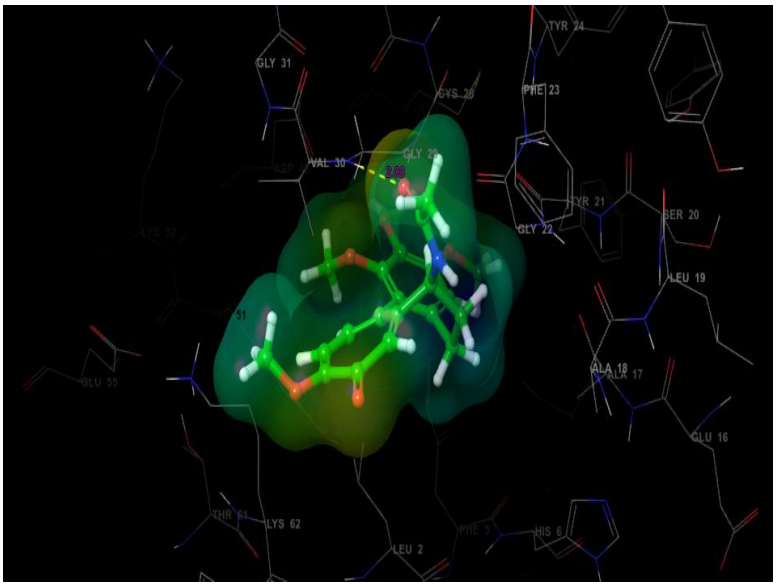

Figure 7. 20 Molecular docking of Colchicine (yellow dotted line) showing the hydrogen bond interactions with cardiovascular protein 5G3N

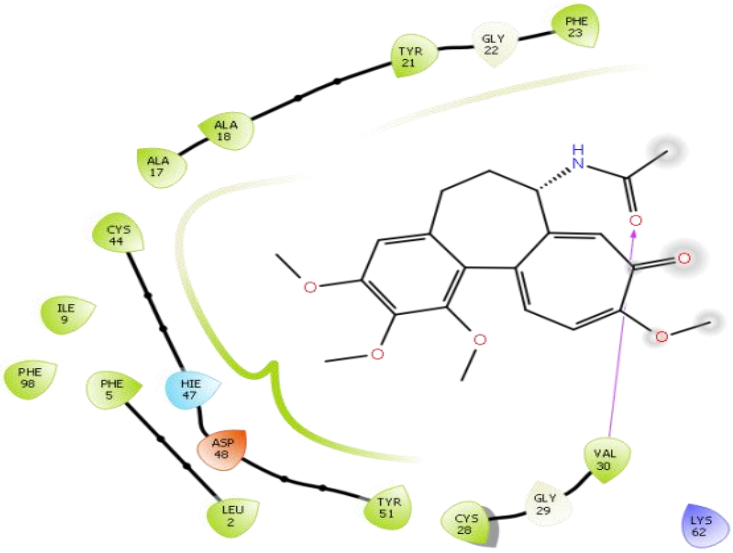

Figure 7.21 Ligand interaction diagram of colchicine with cardiovascular protein 5G3N

7.4 Conclusions

Molecular structure, vibrational spectra, UV, NBO, NLO, HOMO-LUMO, and molecular docking studies of anti-cancerous alkaloids brucine and colchicine were done using Density Functional Theory (DFT) method at the B3LYP/6-311G++(d, p) level using Gaussian-09 software and were supported by experiments. The results obtained from the quantum computational DFT method agree well with the experimental results. Conformational analysis of each of the title molecules was done

by relaxed potential energy scans at two arbitrary selected dihedrals. The vibrational assignments of the title molecules were obtained from FT-IR and FT-Raman spectra by theoretical and experimental methods. From the MEP surfaces obtained by the DFT method, the difference between the minimal MEP values of brucine and colchicine molecules is 3 kcal/mol, the difference between their maximal MEP values is large and is equal to 16 kcal/mol. The sensitivity towards electrophilic attacks of brucine and colchicine molecules is rather similar, however, sensitivity towards nucleophilic attacks seems to be quite different in favor of colchicine molecules. The TD-DFT theory calculations of the electronic structures and electronic absorption spectra of colchicine were studied and observed in the UV-VIS spectrum of colchicine, that the maximum absorbed peak appears at 360 nm and bandgap 3.4417 eV corresponding to transition HOMO-LUMO with 93% cause n-π* transition.

HOMO-LUMO energy gap for colchicine is calculated as 3.649 eV and 4.831 eV for brucine, while colchicine is found to be more chemically reactive than brucine, while chemical hardness is more for brucine than that for colchicine. Electrophilicity (G) of colchicine is much higher than that of brucine, which means the tendency to accept an electron pair is much higher for colchicine than that of brucine. NBO analysis on title molecules was performed and a very strong intramolecular hyper-conjugative interaction was observed with greater stabilization energy in both brucine and colchicine. The significant intra-molecular interaction between the molecules provides evidence that the molecules are highly stable due to intramolecular hyperconjugation interactions. The NBOs analysis predicts strong hyper conjugative interaction between the lone pair electron orbital of nitrogen and the C=O anti-bonding orbital in brucine. From the VCD spectra, CH_2 and CH_3 groups were found to act as markers of a configuration having right polarization and left polarization respectively for the halogen substitutions of the title molecules. The stretching modes of aromatic rings and carbonyl stretching modes in combination with CH_2 and CH_3 groups stretching modes at stereogenic centers generate VCD bands in the range 11400–1100 cm @1 are good markers of the configuration showing right polarization and left polarization for halogen-substituted brucine which are remarkably efficient configuration markers for these chiral molecular systems enabling them for chiral applications. The first order hyperpolarizability values are greater than that of urea molecule by 25.56 and 22.15

times for brucine and colchicine respectively, thereby enabling the title molecules for NLO applications. From LHE calculations of brucine and colchicine with halogen substitutions, the brominated system was found to possess higher values of LHE. Molecular docking shows that brucine showed the lowest binding affinity of -8.218 kcal/mol with cancer protein with PDBID 5JMJ, while colchicine showed the lowest binding affinity of 5.298 kcal/mol with cancer protein with PDBID 3S7S and also showed a binding affinity of 4.68 kcal/mol with cardiovascular protein 5G3N. Thus, the molecular docking results points out that the reported facts that brucine and colchicine have anti-cancer effects.

References

[1] S. Li, X.-P. Wang, In vitro and in vivo evaluation of novel NGR-modified liposomes containing brucine, Int. J. Nanomedicine. 12 (2017) 5797.

[2] J. Teske, J.-P. Weller, U.-V. Albrecht, A. Fieguth, Fatal intoxication due to brucine, J. Anal. Toxicol. 35 (2011) 248–253.

[3] A. Rathi, N. Srivastava, S. Khatoon, A.K.S. Rawat, TLC determination of strychnine and brucine of strychnos nux vomica in Ayurveda and homeopathy drugs, Chromatographia. 67 (2008) 607–613.

[4] W. Yin, T.-S. Wang, F.-Z. Yin, B.-C. Cai, Analgesic and anti-inflammatory properties of brucine and brucine N-oxide extracted from seeds of Strychnos nux-vomica, J. Ethnopharmacol. 88 (2003) 205–214.

[5] J.-M. Qin, P.-H. Yin, Q. Li, Z.-Q. Sa, X. Sheng, L. Yang, T. Huang, M. Zhang, K.-P. Gao, Q.-H. Chen, Anti-tumor effects of brucine immuno-nanoparticles on hepatocellular carcinoma, Int. J. Nanomedicine. 7 (2012) 369.

[6] M. Serasanambati, S.R. Chilakapati, J.R. Vangavaragu, D.R. Chilakapati, Inhibitory effect of gemcitabine and brucine on MDA MB-231human breast cancer cells, Int. J. Drug Deliv. 6 (2014) 133.

[7] H. Vernon, The Neck Disability Index: state-of-the-art, 1991-2008, J. Manipulative Physiol. Ther. 31 (2008) 491–502.

[8] A. Bayes-Genis, Y. Adler, A.B. De Luna, M. Imazio, Colchicine in pericarditis, Eur. Heart J. 38 (2017) 1706–1709.

[9] G. Cocco, D.C.C. Chu, S. Pandolfi, Colchicine in clinical medicine. A guide for internists, Eur. J. Intern. Med. 21 (2010) 503–508.

[10] Z.-Y. Lin, C.-H. Kuo, D.-C. Wu, W.-L. Chuang, Anticancer effects of clinically acceptable colchicine concentrations on human gastric cancer cell lines, Kaohsiung J. Med. Sci. 32 (2016) 68–73.

[11] K. Mohee, J. Zhang, J.G. Cleland, A.L. Clark, 161 Use of colchicine in cardiovascular diseases–a systematic review, (2015).

[12] H. Alkadi, M.J. Khubeiz, R. Jbeily, Colchicine: a review on chemical structure and clinical usage, Infect. Disord. Targets (Formerly Curr. Drug Targets-Infectious Disord. 18 (2018) 105–121.

[13] R. Bhushan, D. Gupta, Resolution of (±)-ibuprofen using (−)-brucine as a chiral selector by thin layer chromatography, Biomed. Chromatogr. 18 (2004) 838–840.

[14] N.B. Malkar, V.G. Kumar, Optical resolution of (±)-Threo-9, 10, 16-trihydroxy hexadecanoic acid using (−) brucine, J. Am. Oil Chem. Soc. 75 (1998) 1461–1463.

[15] N. Islam, S. Niaz, T. Manzoor, A.H. Pandith, Theoretical investigations into spectral and non-linear optical properties of brucine and strychnine using density functional theory, Spectrochim. Acta Part A Mol. Biomol. Spectrosc. 131 (2014) 461–470.

[16] A. Bialonska, Z. Ciunik, Racemic resolution of N-protected alanine by strychnine and brucine versus donor/acceptor capability, CrystEngComm. 6 (2004) 276–279.

[17] H. Schneider, Mechanisms of molecular recognition: investigations of organic host–guest complexes, Angew. Chemie Int. Ed. English. 30 (1991) 1417–1436.

[18] A. Afzal, M.S. Thayyil, P.A. Sivaramakrishnan, M.K. Sulaiman, K.P.S. Hussan, C.Y. Panicker, K.L. Ngai, Dielectric spectroscopic studies in supercooled liquid and glassy states of Acemetacin, Brucine and Colchicine, J. Non. Cryst. Solids. 508 (2019) 33–45. https://doi.org/10.1016/j.jnoncrysol.2019.01.008.

[19] S. Kim, J.K. Lee, S.O. Kang, J. Ko, J.-H. Yum, S. Fantacci, F. De Angelis, D. Di Censo, M.K. Nazeeruddin, M. Grätzel, Molecular engineering of organic sensitizers for solar cell applications, J. Am. Chem. Soc. 128 (2006) 16701–16707.

[20] G.J. Hedley, A. Ruseckas, I.D.W. Samuel, Light harvesting for organic photovoltaics, Chem. Rev. 117 (2017) 796–837.

[21] R.D. 0. Gaussian 09 M.J. Frisch, G.W. Trucks, H.B. Schlegel, G.E. Scuseria, M.A. Robb, J.R. Cheeseman, G. Scalmani, V. Barone, B. Mennucci, G.A. Petersson, H. Nakatsuji, M. Caricato, X. Li, H.P. Hratchian, A.F. Izmaylov, J. Bloino, G. Zheng, J.L., No Title, .

[22] X.-Y. Meng, H.-X. Zhang, M. Mezei, M. Cui, Molecular docking: a powerful approach for structure-based drug discovery, Curr. Comput. Aided. Drug Des. 7 (2011) 146–157.

[23] S. Armaković, S.J. Armaković, S. Koziel, Optoelectronic properties of curved carbon systems, Carbon N. Y. 111 (2017) 371–379.

[24] M. Samadizadeh, S.F. Rastegar, A.A. Peyghan, The electronic response of nano-sized tube of BeO to CO molecule: a density functional study, Struct. Chem. 26 (2015) 809–814.

[25] A. Reisi-Vanani, M. Safipoor, Investigation of carbon monoxide adsorption onto sumanene (C21H12) decorated with Li+ ions toward its elimination, Curr. Appl. Phys. 17 (2017) 1382–1395.

[26] A. Reisi-Vanani, Z. Shabani, Evaluation of the hydrogen adsorption onto Li and Li+ decorated circumtrindene (C36H12): A theoretical study, Int. J. Hydrogen Energy. 42 (2017) 22973–22986.

[27] R.A. Friesner, J.L. Banks, R.B. Murphy, T.A. Halgren, J.J. Klicic, D.T. Mainz, M.P. Repasky, E.H. Knoll, M. Shelley, J.K. Perry, Glide: a new approach for rapid, accurate docking and scoring. 1. Method and assessment of docking accuracy, J. Med. Chem. 47 (2004) 1739–1749.

[28] T.A. Halgren, R.B. Murphy, R.A. Friesner, H.S. Beard, L.L. Frye, W.T. Pollard, J.L. Banks, Glide: a new approach for rapid, accurate docking and scoring. 2. Enrichment factors in database screening, J. Med. Chem. 47 (2004) 1750–1759.

[29] D.C. Young, A practical guide for applying techniques to real-world problems, Comput. Chem. New York. 9 (2001) 390.

[30] A. Frish, A.B. Nielsen, A.J. Holder, Gauss View User Manual, Gaussian Inc, Pittsburg, PA. (2001).

[31] E.D. Glendening, A.E. Reed, J.E. Carpenter, F. Weinhold, NBO, version 3.1; Gaussian, Inc. Pittsburgh, PA. (2003).

[32] http://www.rcsb.org, No Title, .

[33] R.S. Williams, R. Green, J.N.M. Glover, Crystal structure of the BRCT repeat region from the breast cancer-associated protein BRCA1, Nat. Struct. Biol. 8 (2001) 838–842.

[34] M. Hollmén, P. Liu, K. Kurppa, H. Wildiers, I. Reinvall, T. Vandorpe, A. Smeets, K. Deraedt, T. Vahlberg, H. Joensuu, Proteolytic processing of ErbB4 in breast cancer, PLoS One. 7 (2012) e39413.

[35] B.D.G. Page, N.C.K. Valerie, R.H.G. Wright, O. Wallner, R. Isaksson, M. Carter, S.G. Rudd, O. Loseva, A.-S. Jemth, I. Almlöf, Targeted NUDT5 inhibitors block hormone signaling in breast cancer cells, Nat. Commun. 9 (2018) 1–14.

[36] S. Jain, W.B. Drendel, Z. Chen, F.S. Mathews, W.S. Sly, J.H. Grubb, Structure of human β-glucuronidase reveals candidate lysosomal targeting and active-site motifs, Nat. Struct. Biol. 3 (1996) 375–381.

[37] D. Ghosh, J. Lo, D. Morton, D. Valette, J. Xi, J. Griswold, S. Hubbell, C. Egbuta, W. Jiang, J. An, Novel aromatase inhibitors by structure-guided design, J. Med. Chem. 55 (2012) 8464–8476.

[38] D. Ruiz Carrillo, R. Chandrasekaran, M. Nilsson, T. Cornvik, C.W. Liew, S.M. Tan, J. Lescar, Structure of human Rack1 protein at a resolution of 2.45 Å, Acta Crystallogr. Sect. F Struct. Biol. Cryst. Commun. 68 (2012) 867–872.

[39] F. Giordanetto, D. Pettersen, I. Starke, P. Nordberg, M. Dahlström, L. Knerr, N. Selmi, B. Rosengren, L.-O. Larsson, J. Sandmark, Discovery of AZD2716: a novel secreted phospholipase A2 (sPLA2) inhibitor for the treatment of coronary artery disease, ACS Med. Chem. Lett. 7 (2016) 884–889.

[40] S.K. Tripathi, R. Muttineni, S.K. Singh, Extra precision docking, free energy calculation and molecular dynamics simulation studies of CDK2 inhibitors, J. Theor. Biol. 334 (2013) 87–100.

[41] L.L.C. S. Schrödinger Release 2018-4: LigPrep New York, NY, 2018, No Title, .

[42] L.L.C. S. Schrödinger Release 2018-4: Glide New York, NY, 2018., No Title, .

[43] L. Lessinger, T.N. Margulis, The crystal structure of colchicine. A new application of magic integers to multiple-solution direct methods, Acta Crystallogr. Sect. B Struct. Crystallogr. Cryst. Chem. 34 (1978) 578–584.

[44] B. Schammé, M. Mignot, N. Couvrat, V. Tognetti, L. Joubert, V. Dupray, L. Delbreilh, E. Dargent, G. Coquerel, Molecular relaxations in supercooled liquid and glassy states of amorphous quinidine: dielectric spectroscopy and density functional theory approaches, J. Phys. Chem. B. 120 (2016) 7579–7592.

[45] X.C. T.B. Freedman D.A. Young, D.L. Elmer, L.A. Nafie, Density functional, J.P.C.A. 106 (2002). theory calculations of vibrational circular dichroism in transition metal complexes: identification of solution conformations and mode of chloride ion association for (+)-tris(ethylenediaminato)cobalt(III), No Title, .

[46] A.H. Pandith, N. Islam, Z.F. Syed, S. Rehman, S. Bandaru, A. Anoop, Density functional theory prediction of geometry and vibrational circular dichroism of bridged triarylamine helicenes, Chem. Phys. Lett. 516 (2011) 199–203.

[47] N. Norani, H. Rahemi, S.F. Tayyari, M.J. Riley, Conformational stabilities, infrared, and vibrational dichroism spectroscopy studies of tris (ethylenediamine) zinc (II) chloride, J. Mol. Model. 15 (2009) 25–34.

[48] L.A. Nafie, Vibrational Circular Dichroism—A New Tool for the Solution-State Determination of the Structure and Absolute Configuration of Chiral Natural Product Molecules, ChemInform. 40 (2009) .

[49] C. 1-C.A. in N. DilipKondepudi Editor(s): Prasad L. Polavarapu, Chiral Analysis (Second Edition), Elsevier, 2018,Pages 3-28, No Title, .

[50] L.T. Kuhn, K. Motiram-Corral, T.J. Athersuch, T. Parella, M. Pérez-Trujillo,

Simultaneous Enantiospecific Detection of Multiple Compounds in Mixtures using NMR Spectroscopy, Angew. Chemie Int. Ed. 59 (2020) 23615–23619.

[51] S.M. Hiremath, A. Suvitha, N.R. Patil, C.S. Hiremath, S.S. Khemalapure, S.K. Pattanayak, V.S. Negalurmath, K. Obelannavar, Molecular structure, vibrational spectra, NMR, UV, NBO, NLO, HOMO-LUMO and molecular docking of 2-(4, 6-dimethyl-1-benzofuran-3-yl) acetic acid (2DBAA): Experimental and theoretical approach, J. Mol. Struct. 1171 (2018) 362–374.

[52] J. Prashanth, G. Ramesh, J. Laxman Naik, J. Kishan Ojha, B. Venkatram Reddy, Molecular geometry, NBO analysis, Hyperpolarizability and HOMO-LUMO energies of 2-azido-1-phenylethanone using Quantum chemical calculations, Mater. Today Proc. 3 (2016) 3761–3769. https://doi.org/ https://doi.org/10.1016/j.matpr.2016.11.025.

[53] G. Ramesh, B.V. Reddy, Spectroscopic investigation on structure (monomer and dimer), molecular characteristics and comparative study on vibrational analysis of picolinic and isonicotinic acids using experimental and theoretical (DFT & IVP) methods, J. Mol. Struct. 1160 (2018) 271–292.

[54] F.A.M. Al-Omary, Y.S. Mary, C.Y. Panicker, A.A. El-Emam, I.A. Al-Swaidan, A.A. Al-Saadi, C. Van Alsenoy, Spectroscopic investigations, NBO, HOMO–LUMO, NLO analysis and molecular docking of 5-(adamantan-1-yl)-3-anilinomethyl-2, 3-dihydro-1, 3, 4-oxadiazole-2-thione, a potential bioactive agent, J. Mol. Struct. 1096 (2015) 1–14.

[55] M. Raja, R.R. Muhamed, S. Muthu, M. Suresh, Synthesis, spectroscopic (FT-IR, FT-Raman, NMR, UV–Visible), NLO, NBO, HOMO-LUMO, Fukui function and molecular docking study of (E)-1-(5-bromo-2-hydroxybenzylidene) semicarbazide, J. Mol. Struct. 1141 (2017) 284–298.

[56] C. Adant, M. Dupuis, J.L. Bredas, Ab initio study of the nonlinear optical properties of urea: Electron correlation and dispersion effects, Int. J. Quantum Chem. 56 (1995) 497–507.

[57] Z. Wang, Y. Cui, K. Hara, Y. Dan-oh, C. Kasada, A. Shinpo, A high-light-harvesting-efficiency coumarin dye for stable dye-sensitized solar cells, Adv. Mater. 19 (2007) 1138–1141.

[58] N.G. Haress, F. Al-Omary, A.A. El-Emam, Y.S. Mary, C.Y. Panicker, A.A. Al-Saadi, J.A. War, C. Van Alsenoy, Spectroscopic investigation (FT-IR and FT-Raman), vibrational assignments, HOMO–LUMO analysis and molecular docking study of 2-(Adamantan-1-yl)-5-(4-nitrophenyl)-1, 3, 4-oxadiazole, Spectrochim. Acta Part A Mol. Biomol. Spectrosc. 135 (2015) 973–983.

[59] H. Claußen, C. Buning, M. Rarey, T. Lengauer, FlexE: efficient molecular docking considering protein structure variations, J. Mol. Biol. 308 (2001) 377–395.

CHAPTER 8
SUMMARY AND PROSPECTS

8.1 Summary

The motivation of research in this thesis was based on the following facts, that the molecular dynamics of the amorphous state challenge our present knowledge of the physicochemical properties of the amorphous phase of low water-soluble pharmaceuticals as they were avoided for commercial use despite the life-saving potential of some of them, to study molecular dynamics of diverse glass formers for providing new insights to researchers engaged in research of the unresolved glass transition problem, and to explore untapped plant-derived anticancer drugs by experimental and theoretical characterization using the quantum computational methods. Recently quantum computational methods, modelling and simulations were used in research and they have several advantages, and evaluation of such innovative methods are of immense value in research. Several researchers have characterized the molecular dynamics of pharmaceuticals in supercooled liquid and glassy states and established a correlation between primary and secondary relaxations and physicochemical stability of the amorphous state. Experimental evaluation of such correlations is of great practical value despite challenges due to the long-time scales and non-ergodic nature of glasses. In the present work, thermal and dielectric behaviour of seven low water-soluble pharmaceuticals were critically investigated with thermogravimetric analysis (TGA), differential scanning calorimetry (DSC), and broadband dielectric spectroscopy (BDS) (10^{-2} to 10^{7} Hz). A piece of diverse information about the shape of dielectric loss spectra, relaxation strength, and the temperature dependence for structural or conductivity and secondary relaxation time was determined through the dielectric measurements. Melting, cold crystallization, and glass transition temperature from the DSC measurements. The structural and conductivity relaxations observed in the investigated orientationally disordered crystals display non-Debye or non-exponential relaxation characteristics in the frequency domain and showing strong or slight deviations from thermally activated behaviour i.e., non-Arrhenius temperature dependence.

In chapter 3, anticancerous plant-derived alkaloids namely brucine and colchicine and non-alkaloid acemetacin were characterized in supercooled liquid and glassy states by broadband dielectric spectroscopy. These two molecules are larger and complex in structure and their study is of significance for researchers. Various

significant parameters related to the stability of the glassy phase like T_g, fragility, temperature dependence of β_{KWW} were deduced from the temperature dependence of relaxation time and found many similarities between that of brucine and colchicine. Two types of secondary relaxation were observed simultaneously in a temperature range below T_g in glassy brucine which is first ever observed in a pharmaceutical. All three samples obeyed Paluch's anti-correlation and the origin of secondary relaxation was identified by the DFT method in colchicine and acemetacin.

In chapter 4, molecular dynamics of amorphous bezafibrate were studied and is compared with same-class drug, pure fenofibrate and binary mixture of fenofibrate (PS800-fenofibrate) as any similarity in glassy dynamics between these two are of great value for researchers involved in glass transition. Chemically, both these title fibrate drugs have molecular structures which differ only by their attached groups on the main skeleton, i.e., amide and carboxylic acid in bezafibrate, while keto and esters in fenofibrate. The effect of mixing polymer PS800 to pure fenofibrate have decreased the β_{KWW} value of pure fenofibrate from 0.7 to 0.36 thereby increasing rapidly the distribution of structural relaxation times and hence decreasing the stability of the supercooled liquid phase even though there has been no effect on fragility. The presence of PS800 shifted the molecular dynamics above T_g, and T_g is shifted to a higher temperature by 25K. Due to the difference in the attached groups in bezafibrate and fenofibrate, no prominent similarities in molecular dynamics were observed between them. Moreover, the origin of secondary relaxation, i.e., the relevant molecular sub-group that causes the observed secondary relaxation was identified by the DFT method using the dihedral scan method and Gaussian software.

Molecular dynamics in the supercooled liquid and glassy states of acetohexamide and piroxicam were discussed in chapters 5 and 6 respectively. Both these samples, acetohexamide and piroxicam. Both the samples acetohexamide and piroxicam showed conductivity relaxation below and above T_g and the structural relaxation was masked by conductivity above T_g whereas the secondary relaxation was resolved in permittivity formalism in both samples. Modulus formalism was used to study the molecular dynamics above T_g and dielectric permittivity formalism was used to study molecular dynamics below T_g in both samples. The relaxation times of secondary relaxations in both modulus and permittivity formalism are found to be

similar and is a case of translational rotational coupling which was also observed in amlodipine besylate. Such behaviour was rarely observed in pure pharmaceuticals and hence this study serves as a great resource for researchers in glassy dynamics. The relevant molecular sub-group that causes the observed secondary relaxation was identified by the B3LYP/6-311g (d, p) level of theory in both acetohexamide and piroxicam.

Chapter 7 discusses optimized geometry, FTIR, FT-Raman spectroscopy, vibrational circular dichroism, UV-Visible spectroscopy, frontier molecular orbital analysis, non-linear optical properties, molecular electrostatic potential surface, and molecular docking studies of brucine and colchicine using Density Functional Theory (DFT) method at the B3LYP/6-311G++(d, p) level using Gaussian-09 software. The results obtained from the theoretical FTIR, Raman, and UV-VIS spectra agree well with the experimental results. HOMO-LUMO energy gap for colchicine is calculated as 3.64 eV and 4.83 eV for brucine, while colchicine is found to be more chemically reactive than brucine, while chemical hardness is more for brucine than that for colchicine. Electrophilicity (G) of colchicine is much higher than that of brucine, which means the tendency to accept an electron pair is much higher for colchicine than that of brucine. NBO analysis on title molecules was performed and a very strong intramolecular hyper-conjugative interaction was observed with greater stabilization energy in both brucine and colchicine. The significant intra-molecular interaction between the molecules provides evidence that the molecules are highly stable due to intramolecular hyperconjugation interactions. The NBOs analysis predicts strong hyper conjugative interaction between the lone pair electron orbital of nitrogen and the C=O anti-bonding orbital in brucine. From the VCD spectra, CH_2 and CH_3 groups were found to act as markers of a configuration having right polarization and left polarization respectively for the halogen substitutions of the title molecules. Molecular docking shows that brucine showed the lowest binding affinity of 8.218 kCal/mol with cancer protein with PDBID 5JMJ, while colchicine showed the lowest binding affinity of 5.298 kCal/mol with cancer protein with PDBID 3S7S.

8.2 Future prospects

(1) Low water-soluble plant-derived drugs brucine and colchicine were found to be stable in amorphous phase from our study, so we are planning to explore similar drugs with low water solubility to explore their potential.

(2) We plan to do BDS experiments in a broader frequency range of 10^{-2} Hz to few Giga Hertz to explore relaxations in liquid state in elevated pressure, which may help us to resolve Johari-Goldstein β relaxation.

(3) We intend to use advanced differential scanning calorimetry to study enthalpy changes and temperature-controlled X-Ray diffractometer to complement the BDS results especially below T_g.

(4) We intend to investigate the molecular dynamics in the supercooled liquid and glassy states of more interesting systems having industrial applications like polymers, ionic liquids, plastic crystals etc.

(5) We will develop strategies to utilize these findings in the future to better understand and address challenges in technology applications such as the development of amorphous pharmaceuticals, efficient electrolytes, supercapacitors etc.

(6) We plan to use advanced quantum computational tools using DFT, modelling and simulations to characterize unexplored drugs, and materials having industrial applications.

LIST OF PUBLICATIONS

1. Dielectric relaxation studies in super-cooled liquid and glassy phases of anti-cancerous alkaloid: Brucine, **A Afzal**, M Shahin Thayyil, M K Sulaiman, and A R Kulkarni. Indian Journal of Physics, Volume 92, Issue 5, pp.565-573 Pub Date: May 2018, DOI:10.1007/s12648-017-1139-3

2. Dielectric spectroscopic studies in supercooled liquid and glassy states of Acemetacin, Brucine and Colchicine. **Aboothahir Afzal**, M. Shahin Thayyil, P.A. Sivaramakrishnan, M.K. Sulaiman, K.P. Safna Hussan, C. Yohannan Panicker, K.L. Ngai, Journal of Non-Crystalline solids, 2019, DOI: https://doi.org/10.1016/j.jnoncrysol.2019.01.008

3. Anti-Cancerous Brucine and Colchicine: Experimental and Theoretical Characterization **Aboothahir Afzal**, * Mohamed Shahin Thayyil, Mohammad Shariq, Yohannan Sheena Mary, Kaippallil Sundaresan Resmi, Renjith Thomas, Nasarul Islam, and Ajithan Jyothi Abinu DOI: https://doi.org/10.1002/ slct.201902698

4. Molecular Dynamics in the Supercooled Liquid and Glassy States of Bezafibrate and binary mixture of Fenofibrate Aboothahir Afzal, P.A. Sivaramakrishnan; Sailaja Urpayil; Simone Capaccioli, Mohamed Shahin Thayyil, Journal of Non-Crystalline Solids 550 (2020) 120407 DOI: https://doi.org/10.1016/j.jnoncrysol.2020.120407

5. Growth, molecular structure and characterization of L-Isoleucinium hydrogen maleate hemihydrate (LIM) NLO single crystal by density function theory A. Hemalatha, Aboothahir Afzal, S. Muthu, M. Raja, S. Senthil, Materials Today: Proceedings 2020, DOI: https://doi.org/10.1016/j.matpr.2020.07.462

6. Thermal and dielectric studies on orientationally disordered crystal: Cyclobutanol, Nighil Nath M P, Mohamed Shahin Thayyil, Aboothahir Afzal, G. Govindaraj, Indian Journal of Physics, 2021